



HAL
open science

Device integration of the CoBiSS spectrometer and modélisation of (L)SPR chip for the detection through CoBiSS

Rohit Prasad

► **To cite this version:**

Rohit Prasad. Device integration of the CoBiSS spectrometer and modélisation of (L)SPR chip for the detection through CoBiSS. Micro and nanotechnologies/Microelectronics. Université de Technologie de Troyes, 2017. English. NNT : 2017TROY0031 . tel-02964835

HAL Id: tel-02964835

<https://theses.hal.science/tel-02964835>

Submitted on 12 Oct 2020

HAL is a multi-disciplinary open access archive for the deposit and dissemination of scientific research documents, whether they are published or not. The documents may come from teaching and research institutions in France or abroad, or from public or private research centers.

L'archive ouverte pluridisciplinaire **HAL**, est destinée au dépôt et à la diffusion de documents scientifiques de niveau recherche, publiés ou non, émanant des établissements d'enseignement et de recherche français ou étrangers, des laboratoires publics ou privés.

Thèse
de doctorat
de l'UTT

Rohit PRASAD

**Device Integration of the CoBiSS
Spectrometer and Modelisation of
(L)SPR Chip for the Detection through
CoBiSS**

Spécialité :

Matériaux, Mécanique, Optique et Nanotechnologie

2017TROY0031

Année 2017

THESE

pour l'obtention du grade de

DOCTEUR de l'UNIVERSITE DE TECHNOLOGIE DE TROYES

Spécialité : MATERIAUX, MECANIQUE, OPTIQUE ET NANOTECHNOLOGIE

présentée et soutenue par

Rohit PRASAD

le 30 novembre 2017

Device Integration of the CoBiSS Spectrometer and Modelisation of (L)SPR Chip for the Detection through CoBiSS

JURY

M. P.-M. ADAM	PROFESSEUR DES UNIVERSITES	Président
M. É. BOURILLOT	MAITRE DE CONFERENCES	Directeur de thèse
M. A. GARCIA-MARTIN	INVESTIGADOR CSIC	Examineur
M. B. GUIZAL	PROFESSEUR DES UNIVERSITES	Rapporteur
M. É. LESNIEWSKA	PROFESSEUR DES UNIVERSITES	Rapporteur
M. R. VINCENT	ENSEIGNANT CHERCHEUR UTT	Directeur de thèse



UNIVERSITE DE TECHNOLOGIE DE TROYES

DOCTORAL THESIS

Device integration of the CoBiSS spectrometer, and modelisation of (L)SPR chip for detection through CoBiSS

Author:
Rohit PRASAD

Supervisor:
Dr. Rémi VINCENT, LNIO,
UTT
Dr. Eric BOURILLOT, ICB

*A thesis submitted in fulfillment of the requirements
for the degree of Doctor of Philosophy*

in the speciality

Materials, Mecanics, Optics and Nanotechnology

Realized in

Labex Action

January 29, 2018



UNIVERSITE DE TECHNOLOGIE DE TROYES

Abstract

Materials, Mecanics, Optics and Nanotechnology
Labex Action

Doctor of Philosophy

Device integration of the CoBiSS spectrometer, and modelisation of (L)SPR chip for detection through CoBiSS

by Rohit PRASAD

As the world is moving towards Internet of Things, an optical detection device is presented that can be utilized in this domain. This device can be used to do tests that use optical detection for analysis like monitoring of Health of a person by doing a blood test or other medical analysis and also be used to monitor environment by testing water or air in cities, mountains, factories, rivers and so on for a practical purpose. To create this optical detection device, a combination of spectrometer named Coupled Bi-Directional Sampling Spectrometer (CoBiSS) [Patent number WO2009127794A1] and Surface Plasmon Resonance (SPR) Chip has been used. For the optical integration, a new analysis of the sampling in the spectrometer CoBiSS is presented. Followed by, Device and Optical Integration of CoBiSS has been done to remove all the moving parts. It was necessary to make the device small that can be handheld and portable. For ease of use a Graphical User interface was developed. For detection, CoBiSS was added with a chip of SPR. A modelisation of SPR chip was done to maximize its sensitivity. A new Localized Surface Plasmon Resonance (LSPR) chip has been proposed to work with CoBiSS. Optimization of LSPR chip has been performed to maximize the sensitivity. A new definition for the calculation of Sensitivity has been proposed. This device needs the addition of functionalization on (L)SPR Chip for detection and a final application. This device could be an ideal “Thing” in Internet of Things.

KEYWORDS: Systems integration, Optical spectrometers, Optical detectors, Integrated optics, Photonics, Nanophotonics, Surface Plasmon Resonance, Visible spectroscopy, near field optics.

Acknowledgements

First of all, I would like to express my gratitude to all of the defense committee members, for accepting the invitation to be part of the committee and for the constructive remarks and comments on my PhD work.

I would like to thank my supervisors Dr. Rémi VINCENT and Dr. Eric BOURILLOT for offering me a great chance to work for LABEX ACTION C/o Laboratoire de Nanotechnologies et Instruments Optiques (LNIO), where I enjoyed a wonderful experience with highly talented people and abundant research resources. Thank you for your delighting guidance, suggestions and encouragements that kept me on the correct path and allowed me to pursue new directions throughout the 4 years and 3 months of my PhD work.

Special Thanks to Abdelhamid HMIMA for being an excellent group member with whom I've had the great pleasure to work. I would like to thank Dr. Yassine HADJAR, Dr. Sylvain BLAIZE, Dr. Aurelien BRUYANT and Pr. Hichem SNOUSSI for their advice in the Project CoBiSS. I am really indebted to so many things that I've learnt from this inspiring and supportive team. I would like to thank the team of Centre de Calcul Romeo for allowing the use of the supercomputer and helping the team with the installation and usage of the Simulation Software from Lumerical Solutions Inc. I would like to thank SATT Grand Est for partially financing the Project CoBiSS and Resolution Spectra Systems for supplying the camera and helping the team with its special requirements.

Thanks to all the erstwhile F111 members Dr. Wei Geng, Hind Kadiri, Dr. Nancy Rahbany and Lina Riachy for helping me in the initial years of my PhD.

Special Thanks to David Legrand, Dr. Anisha Gokarna-Barreau and Dr. Joseph Maraé Djouda for helping me throughout the PhD.



Contents

Abstract	iii
Acknowledgements	v
1 Introduction	1
1.1 Working of CoBiSS Spectrometer	5
1.2 Aim	10
1.3 Initial Result	10
1.4 Organization	12
2 Sampling of the confined interferogram	15
2.1 Scattering of the propagative evanescent wave	15
2.1.1 Evanescent wave scattering of a small particle in the dipolar approximation	17
2.1.1.1 Radiation diagram of a dipole and Influence of the air-glass interface	19
2.2 Scattering of the Evanescent Standing Wave (ESW) with FDTD calculation	23
2.2.1 The evanescent standing wave (ESW)	23
2.2.1.1 Introduction to Finite Difference Time Domain	25
2.2.2 At the position of the local minimum intensity of the ESW	27
2.2.3 At the position of the local maximum intensity of the ESW	27
2.2.3.1 Spectral dependence of the radiation pattern for a Rectangular Nano-Wire (RNW) 150 nm x 100 nm	29
2.3 Conclusion	32
3 Integration of the Device	33
3.1 Introduction	33
3.2 Requirements	34
3.3 Integration	35
3.3.1 Laser	35
3.3.2 Camera	37
3.3.3 Controlling Camera and Laser together	37
3.3.4 Lomb Scargle Method	41
3.3.5 Calculation using Micro-spectrometer	44
3.3.6 Calculation Robustness	46

3.3.7	Calculation of Multiple wavelengths	49
3.3.8	Graphical User Interface	51
3.3.9	Motherboard	54
3.3.9.1	OS Installation for the Deployment board	54
3.3.9.2	Code Compilation methods	55
3.4	Conclusion	55
4	Detection trough SPR and LSPR	57
4.1	Introduction	59
4.1.1	Surface Plasmons	60
4.1.2	Local Surface Plasmons	60
4.1.3	Coupling of Light and Surface Plasmons	62
4.1.4	Sensitivity	65
4.1.5	RCWA Calculation	67
4.2	Plasmonic Gold Slab for SPR-chip	69
4.2.1	Sensitivity in the case of gold slab	71
4.3	Plasmonic "W" structure for LSPR-chip	74
4.3.1	Sensitivity calculation	80
4.4	Conclusion	83
5	Conclusion and Prospects	85
6	French Summary	91
Appendix A	Selection of Nano Particle for CoBiSS	115
A.1	Shape	115
A.2	Selection of Material of Nano-Particle	118
A.3	Length variation of Nano-Particle	120
A.4	Height variation of Nano-Particle	122
A.5	Test of selected Nano-Particle in Dimer formation	125
A.6	Conclusion	126
A.7	Determination of Width of Nano Particle	127
Appendix B	"W" tip - Effect of Peak and Trench	131
Appendix C	Consideration of Devices	133
C.1	Motherboard	133
C.2	Camera	135
C.3	Laser	136
Appendix D	OS Selection and Installation for the Development board	139

Appendix E Article Published

List of Figures

1.1	Requirements and Area of Application for Internet of Things	2
1.2	Market Scope of Internet of Things	2
1.3	Explanation of CoBiSS	6
1.4	Working of CoBiSS	7
1.5	2D sampling principle of CoBiSS	8
1.6	Positioning of Camera with Glass Slab	11
1.7	Example of images found by varying height	11
2.1	A plane wave arrived at an angle of 45° towards the right from the glass side and evanescent wave is formed at the surface. A nano particle's series of complex interactions taking place between the particle and the substrate.	16
2.2	A plane wave arrived at an angle of 45° towards the right from the glass side and evanescent wave is formed at the surface.	16
2.3	Evanescent wave scattering for TM and TE waves.	18
2.4	Polarizability calculation for Gold particle. The green curve indicates the polarizability of a Gold particle at a distance of infinity from the interface. The blue curve indicates the polarizability of the particle touches the interface	19
2.5	Dipole-substrate geometry.	20
2.6	Radiation Diagram of a dipole in Air.	21
2.7	Radiation Diagram in the plane XZ and a Dipole is placed perpendicular to the interface.	22
2.8	Radiation Diagram in the plane XZ and a Dipole is placed parallel to the interface.	23
2.9	Two lasers are placed at an angle of 45° towards the left and the right in glass and evanescent wave is formed at the surface of intersection. . . .	24
2.10	Normalized intensity of the standing wave above and below the interface at $z = 0$ where on the left side we observe the Maximum of the ESW and on the Right side we observe the Minimum of the ESW.	25
2.11	Explanation of FDTD Method	26

2.12	Intensity (left figure) and Near field (right figure) induced ($\mathbf{E} = \mathbf{E}_{Total} - \mathbf{E}_{ESW}$) by the presence of a rectangular gold NP of length (d) = 150 nm and height (h) = 100 nm at the position of a local minimum in intensity of the ESW at 600 nm.	28
2.13	Radiation pattern of the rectangular gold NP of length (d) = 150 nm and height (h) = 100 nm at the position of a local minimum in intensity of the ESW	28
2.14	Near field induced by the presence of a rectangular gold NP of length (d) = 150 nm and height (h) = 100 nm at the position of a local maximum in intensity of the ESW $\mathbf{E} = \mathbf{E}_{Total} - \mathbf{E}_{ESW}$	29
2.15	Constructive interference: Radiation pattern a rectangular gold NP of length (d) = 150 nm and height (h) = 100 nm at the position of a local maximum / minimum in intensity of the ESW $\mathbf{E} = \mathbf{E}_{Total} - \mathbf{E}_{ESW}$	30
2.16	Radiation Pattern as a function of wavelength for gold rectangular nano-particle of length = 150 nm and height = 100 nm in destructive interference	30
2.17	Radiation Pattern as a function of wavelength for gold rectangular nano-particle of length = 150 nm and height = 100 nm in constructive interference.	31
2.18	Total Intensity as a function of wavelength for a nano-particle of length = 150 nm and height = 100 nm. Comparison of particle in destructive and constructive interference.	32
3.1	Block diagram of a code controlling the USB port of motherboard and communicating to a laser	36
3.2	Flow chart of the code that controls the Laser	36
3.3	Block diagram of a code controlling the USB port of motherboard and communicating to a camera and also saving an Image	37
3.4	Flow chart of the code that controls the Camera	38
3.5	Block diagram of a code controlling the USB ports of motherboard and communicating to a laser and a camera and also saving an Image from the camera	39
3.6	Flow chart of the code that controls the Laser and Camera together	40
3.7	Conversion of 2D array of nanostructure to 1D	41
3.8	Calculation of a spectrum (right) using an Image (left) with the help of lomb scargle method. The incident wavelength used was 660 nm.	43
3.9	Initial Graphical User Interface image when the software is started.	47
3.10	Initial Graphical User Interface image when the software is started.	48
3.11	Graph showing the efficiency of Micro spectrometer method when used with CoBiSS as compared to the spectral analyzer	49

3.12	Graph showing the efficiency of Micro spectrometer method when used with CoBiSS as compared to the commercial spectrometer	50
3.13	Graph showing the efficiency of Micro spectrometer method when used with CoBiSS as compared to the commercial spectrometer	50
3.14	Block diagram of a Graphical User Interface code controlling the USB ports of motherboard and communicating to a laser and camera and also displaying an Image	53
3.15	Initial Graphical User Interface image when the software is started. . . .	53
3.16	Graphical User Interface image when then calculation of an image is performed to give the wavelength-intensity spectrum using Lomb Scargle Calculation.	54
4.1	CoBiSS modified for the Detection of SPR	58
4.2	Shift of Resonance from the initial state to functionalized Gold Layer and ultimately when an analyte interacts with the functionalized Gold Layer	58
4.3	Epsilon value of Gold is plotted from the values present in the Lumerical's FDTD software for Gold (Johnson and Christy) with the help of function getfddindex.	60
4.4	Illustration of Surface Plasmons wave, taken from [93].	60
4.5	Localized Surface Plasmons and Field amplification in and around the near Field of the Nanoparticle	61
4.6	Coupling of light and surface Plasmons using attenuation of Total Internal Reflection	62
4.7	Dispersion curve of light in (vacuum and glass) and surface plasmons and coupling condition	65
4.8	Graph shows the Sensitivity calculation method.	66
4.9	Diffraction of a plane wave on an infinite periodic array of metallic nanowires along the x-axis, of thickness t and period $\Lambda = w + g$, between two semi-infinite homogeneous media.	68
4.10	A Gold slab is used for the calculation of reflectance for SPR analysis. Width of Gold Slab varies from 10 nm to 50 nm. The light is incident at an angle of 45° from glass towards Gold slab.	69
4.11	Graphs showing the effect of reflectance with the variation of wavelength for determining the optimum thickness of Gold Slab.	70
4.12	A Gold slab is used for the calculation of reflectance for SPR analysis. Width of Gold Slab is fixed at 30 nm. A layer of material is added on top of the gold layer which have different Refractive index from 1.00 to 1.05 respectively. The light is incident at an angle of 45° from glass towards Gold slab.	71

4.13	Graph showing the effect of reflectance with the variation of wavelength for multiple refractive index of layer above gold slab that varies from 1 to 1.05 respectively.	72
4.14	Sensitivity of a gold slab as a variation of refractive index.	72
4.15	Reflectance as a function of the refractive index of the superstrat for multiple wavelengths for Gold Slab having a thickness of 43.5 nm.	73
4.16	Sensitivity as a function of the refractive index of the superstrat for multiple wavelengths for Gold Slab having a thickness of 43.5 nm.	73
4.17	CoBiSS modified for the Detection of SPR with modified "W" structure with $2 \times \text{Radius} = \text{Diameter} = 10 \text{ nm}$	74
4.18	Graph showing the effect of reflectance with the variation of wavelength for multiple widths of W-structure that varies from 10 nm to 60 nm with an curvature radius of 5 nm.	75
4.19	Graph showing the effect of diffraction grating along with reflectance with the variation of wavelength for multiple widths of W-structure that varies from 10 nm to 60 nm.	76
4.20	Graph showing the effect of reflectance with the variation of wavelength for multiple length of W-structure for the most optimized thickness with a radius of curvature of 5 nm.	77
4.21	Graph showing the effect of reflectance with the variation of wavelength for multiple length of W-structure for the most optimized thickness. . .	78
4.22	Graph showing the effect of reflectance with the variation of wavelength for multiple length of W-structure for the thickness of gold layer as 25 nm.	78
4.23	Near Field calculation of "W" structure of length 600 nm and thickness of gold layer as 25 nm and Intensity values are present in dB ($10 \log_{10} \frac{I}{I_0}$).	79
4.24	Sensitivity analysis for W structure with structure length of 600 nm and radius of curvature of 0 nm. Graph shows the effect of reflectance with the variation of wavelength for multiple refractive index of layer above gold "W" structure that varies from 1 to 1.05 respectively.	80
4.25	Graph shows the Sensitivity of "W" structure with no radius of curvature on the edges as the variation of refractive index	81
4.26	Graph showing the effect of reflectance with the variation of refractive index for multiple wavelengths for "W" structure having a length of 600 nm and thickness of 25 nm.	82
4.27	Graph showing the effect of sensitivity with the variation of refractive index for multiple wavelengths for "W" structure having a length of 600 nm and thickness of 25 nm.	82
6.1	Exigences et domaine d'application de l'Internet des choses	92
6.2	Marché de l'Internet des choses	93

6.3	Explication de CoBiSS	96
6.4	Méthode de travail de CoBiSS	97
6.5	Explication du fonctionnement de CoBiSS	98
6.6	Le positionnement de la caméra avec Verre Slab	99
6.7	Exemple d'images trouvée par hauteur variable	99
6.8	Dipole-substrate geometry.	100
6.9	Radiation Diagram of a dipole in Air.	100
6.10	Radiation Diagram in the plane XZ and a Dipole is placed perpendicular to the interface.	101
6.11	Radiation Diagram in the plane XZ and a Dipole is placed parallel to the interface.	101
6.12	Normalized intensity of the standing wave above and below the interface at $z = 0$	102
6.13	Diagramme de rayonnement pour la nano-particules d'or rectangulaire de longueur = 150 nm et hauteur = 100 nm dans une interférence destructive qui change en fonction de la longueur d'onde de la courbe d'intensité	102
6.14	Diagramme de rayonnement pour la nano-particules d'or rectangulaire de longueur = 150 nm et hauteur = 100 nm dans une interférence constructive qui change en fonction de la longueur d'onde de la courbe d'intensité	103
6.15	Intensité totale en fonction de la longueur d'onde pour une nano-particule de longueur = 150 nm et hauteur = 100 nm. Comparaison des particules dans l'interférence destructive et constructive.	103
6.16	Diagramme du code qui contrôle le laser et l'appareil photo ensemble .	105
6.17	Calcul d'un spectre à l'aide d'une image à l'aide de la méthode de lomb scargle. La longueur d'onde utilisée était de 660 nm.	106
6.18	Calcul de Microspectrometre	107
6.19	l'image graphique de l'utilisateur de l'interface quand alors le calcul d'une image est réalisée pour donner le spectre de longueur d'onde d'intensité en utilisant Calcul de Lomb Scargle.	108
6.20	CoBiSS modifié pour la détection de SPR	109
6.21	Graphique montrant l'effet de la réflectance avec la variation de la longueur d'onde pour l'indice de réfraction multiple de la couche au-dessus de la dalle d'or qui varie de 1 à 1,05 respectivement.	110
6.22	Analyse de sensibilité pour la structure W avec une longueur de structure de 600 nm et un rayon de courbure de 0 nm. Le graphique montre l'effet de la réflectance avec la variation de la longueur d'onde pour l'indice de réfraction multiple de la couche au-dessus de la structure en or "W" qui varie de 1 à 1,05 respectivement.	111

A.1	The image representing the forms of the particles.	116
A.2	Radiation pattern of different nano-particles are considered where the surface area is $15,000 \text{ nm}^2$. Rectangular particle with a $b=150 \text{ nm}$ and $h=100 \text{ nm}$, sphere of radius = 69.10 nm , Triangle1 of $b=200$ and $h=150$ and Triangle2 of $b=100 \text{ nm}$ and $h=100 \text{ nm}$ are considered where b and h means base and height respectively.	117
A.3	Total intensity is calculated for different nano-particles are considered where the surface area is $15,000 \text{ nm}^2$ when observed in air. Rectangular particle with a $b=150 \text{ nm}$ and $h=100 \text{ nm}$, sphere of radius = 69.10 nm , Triangle1 of $b=200$ and $h=150$ and Triangle2 of $b=100 \text{ nm}$ and $h=100 \text{ nm}$ are considered where b and h means base and height respectively.	118
A.4	In this calculation a rectangular particle of base 150 nm and height 100 nm is considered. The rectangular particle of different materials like Gold, Platinum, Chromium, Silver and Aluminum are used for simulation.	119
A.5	In this calculation a rectangular particle of base 150 nm and height 100 nm is considered. The rectangular particle of different materials like Platinum, Chromium, Silver and Aluminum are used for simulation.	119
A.6	In this calculation a rectangular particle of base 150 nm and height 100 nm is considered. The rectangular particle of different materials like Gold, Platinum, Chromium, Silver and Aluminum are used for simulation. Total Intensity of each material is calculated when observed in air.	119
A.7	Radiation pattern of a gold rectangular nano-particle of 100 nm in height is used and radiation diagrams are plotted for different base of $50, 100, 150, 200$ and 250 nm respectively.	120
A.8	Total intensity plot of a gold rectangular nano-particle of 100 nm in height is used and radiation diagrams are plotted for different base of $50, 100, 150, 200$ and 250 nm respectively.	121
A.9	Radiation pattern of a gold rectangular nano-particle of 150 nm in height is used and radiation diagrams are plotted for different base of $50, 100, 150, 200$ and 250 nm respectively.	121
A.10	Total intensity plot of a gold rectangular nano-particle of 150 nm in height is used and radiation diagrams are plotted for different base of $50, 100, 150, 200$ and 250 nm respectively.	121
A.11	Radiation pattern of a gold rectangular nano-particle of 100 nm in base is used and radiation diagrams are plotted for different height of $50, 100, 150, 200$ and 250 nm respectively.	123
A.12	Total intensity plot of a gold rectangular nano-particle of 100 nm in base is used and radiation diagrams are plotted for different heights of $50, 100, 150, 200$ and 250 nm respectively.	123

A.13 Radiation pattern of a gold rectangular nano-particle of 150 nm in base is used and radiation diagrams are plotted for different height of 50, 100, 150, 200 and 250 nm respectively.	124
A.14 Total intensity plot of a gold rectangular nano-particle of 150 nm in base is used and radiation diagrams are plotted for different heights of 50, 100, 150, 200 and 250 nm respectively.	124
A.15 Radiation pattern of two nano-particles of length = 75 nm and height 100 nm are used and the distance between the two are varied from 10,20,30,40 and 50 nm respectively.	125
A.16 Total Intensity calculation of two nano-particles of length = 75 nm and height 100 nm are used and the distance between the two are varied from 10,20,30,40 and 50 nm respectively in air.	126
A.17 Gold Nano-particle where $L = 150$ nm and $H = 100$ nm with a variation of depth as 50,100,150,200 nm and plotted in XZ plane at the center . . .	127
A.18 Gold Nano-particle where $L = 150$ nm and $H = 100$ nm with a variation of depth as 50,100,150,200 nm and plotted in YZ plane at the center . . .	128
A.19 Nano - particle vs Camera Positioning	128
B.1 Singularities present at the level of the structure	131
B.2 Plasmon Polariton	132

List of Tables

3.1	Basic Electronic Integration Requirements	34
C.1	Motherboard Comparison	134
C.2	Camera Comparison	135
C.3	Laser Comparison	136

List of Abbreviations

IOT	I nternet O F T hings
CoBiSS	C oupled B i-Dimensional S ampling S pectrometer
RFID	R adio-Frequency I dentification
WiFi	W ireless F idelity
LiFi	L ight F idelity
IP network	I nternet P rotocol
LTE	L ong-Term E volution
CPU	C entral P rocessing U nit
HVAC	H eating, V entilation and A ir C onditioning
FTS	F ourier T ransform S pectroscopy
TIR	T otal I nternal R eflection
BS	B eam S plitter
CCD	C harge-Coupled D evice
CMOS	C omplementary M etal– O xide– S emiconductor
FDTD	F inite-Difference T ime-Domain
ESW	E vanescent S tanding W ave
SPR	S urface P lasmon R esonance
MNP	M etallic N ano- P articles
LSP	L ocal S urface P lasmons
SPP	S urface P lasmons P olitrons
RAM	R andom A ccess M emory
RIU	R efractive I ndex U nit
USB	U niversal S erial B us
LAN	L ocal A rea N etwork
GPIO	G eneral-Purpose I nput/ O utput
i2c	I nter- I C
IC	I ntegrated C ircuits
BIOS	B asic I nput/ O utput S ystem
ARM	A dvanced R ISC M achines
PDA	P ersonal D igital A ssistant
IR	I nfra- R ed
UV	U ltra- V iolet
GUI	G raphical U ser I nterface
PGM	P ortable G ray M ap

List of Symbols

N_x	Number of Nano-Particles along X axis	
N_y	Number of Nano-Particles along Y axis	
P_x	Longitudinal Period	
P_y	Transverse Period	
N_{max}	Total Number of Sampling Points	
T	Time Period	
P_{SI}	Sampling Interval	
L_s	Sampling Distance	
λ	Wavelength	/m
D	Diameter	m
P	power	W ($J s^{-1}$)
p	p polarization	
s	s polarization	
θ	angle of incidence	Degree ($^\circ$)
θ_1	initial angle of incidence for this case in Glass	Degree ($^\circ$)
$t(\theta_1)$	transmittance coefficients at θ_1	
\tilde{n}	the effective refractive index between glass and air (1.52 in our case)	
k_1	wave number in medium 1	
k_2	wave number in medium 2	
x	the x axis	
z	the z axis	
γ	the decay constant = $k_2 \sqrt{\tilde{n}^2 \sin^2 \theta_1 - 1}$	
n_1	refractive index in glass	
n_2	the refractive index in air	
θ_2	refracted angle in air.	
ω	angular frequency	rad
τ	time delay	
t_j	time at a position j	
X_j	value of pixel intensity at a point j	

*Dedicated To My Mother &
The Loving Memory of My Father*

Chapter 1

Introduction

In the time where we live, everyone constantly and regularly uses Internet or World Wide Web and it has become a basic part of our lives. The Internet that we use is the global system of interconnected computer networks. It is a network of networks that consists of millions interconnected computers comprising of private, public, academic, business, and government networks of local to global scope. These computers are linked by a broad array of electronic, wireless, and optical networking technologies. The Internet has no centralized governance [1].

As the reach of internet increased, the inter-networking of physical devices also started to grow and this leads to the creation of more interconnected physical devices is known as Internet of things (IoT). They are also known as "Connected devices" or "Smart devices". These connected devices are generally embedded with electronics, software, sensors, actuators, and network connectivity that enable these objects to collect and exchange data [2, 3, 4, 5]. This means that to work in this area, one needs the knowledge of the fields of embedded systems, wireless sensor networks, control systems, automation as seen from the Figure (1.1) [6].

This allows the objects to be sensed and/or controlled remotely across existing network infrastructure[7], creating opportunities for more direct integration of the physical world into computer-based systems, and resulting in improved efficiency, accuracy and economic benefit [8, 9, 10, 11, 12, 13, 14].

In the years to come, Smart Devices will play an important roll in our daily lives and will become an integral part of our lives. First of all, let us see the economic ramifications and how these devices are increasing, followed by different technologies that are developed for data transfer and finally the areas where these devices can be used.

The Economic Aspect of these devices shows that, the experts have estimated that, the IoT will consist of almost 50 billion objects by 2020 [15]. ABI Research have also estimated that more than 30 billion devices will be wirelessly connected to the internet of things by 2020 [16]. This can also be visualized by the growth chart of internet of things and its prediction for years to come as seen in the Figure 1.2 [6].

Due to this economic growth in this area, a lot of companies and consortiums have started developing or have developed new methods of communications that can ease

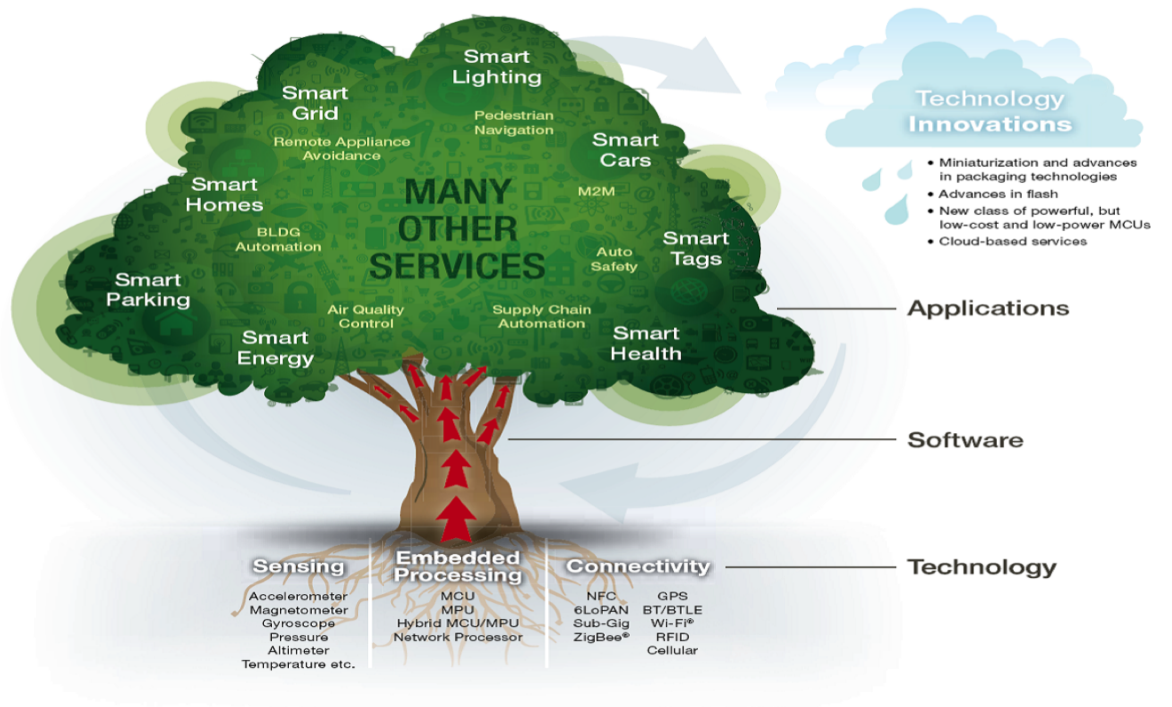


FIGURE 1.1: Requirements and Area of Application for Internet of Things

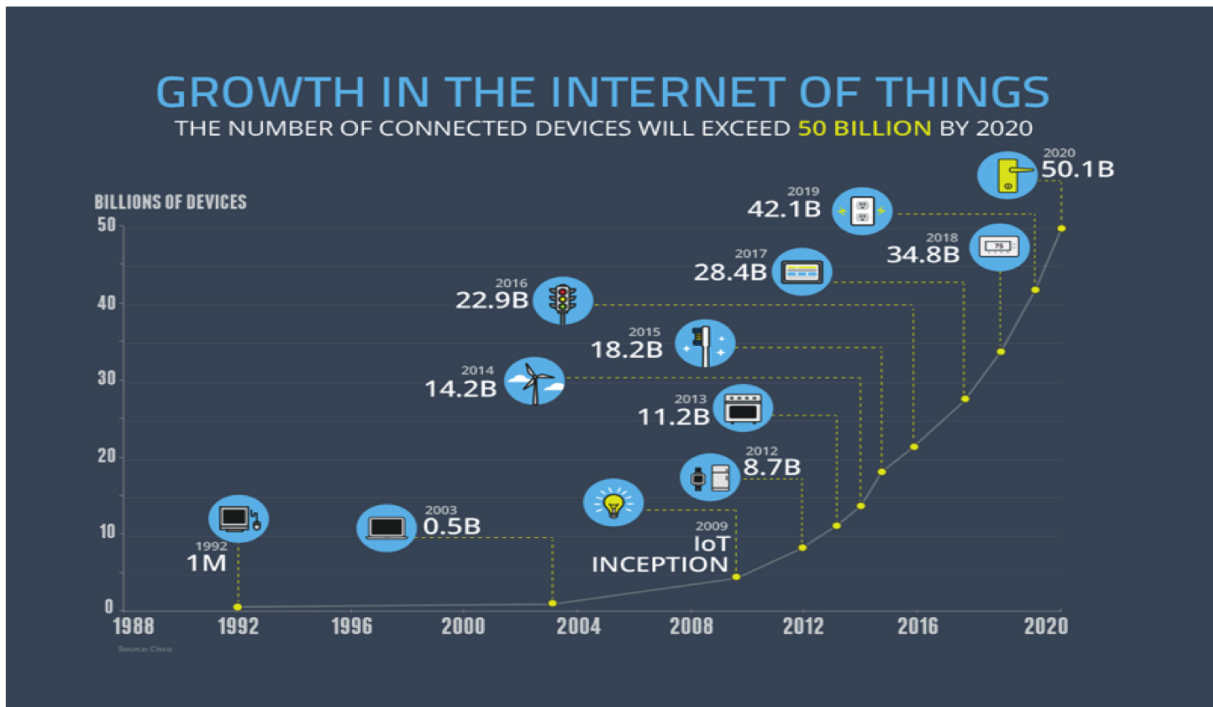


FIGURE 1.2: Market Scope of Internet of Things

the communication problem and the devices can connect to other devices using technologies like RFID and near-field communication, the Optical technologies like Li-Fi, Cisco's 40 Gbit/s bidirectional optical technology (BiDi [17]), Bluetooth low energy, Low energy wireless IP networks, ZigBee, LTE-Advanced, WiFi-Direct, HaLow, Home-Plug, Ethernet. From all the technologies mentioned, there are some that cannot be used directly to connect to internet but can communicate to each other, but if a device needs to connect to internet then it needs to take into account the old infrastructure that has been developed. So, the devices that need to connect to the internet directly will need to use the basic developed technologies like Low energy wireless IP networks, LTE-Advanced, Ethernet, Satellite connection.

Using these technologies, a lot of products are being or will be developed that use network embedded devices with limited CPU, memory and power resources. It means that IoT finds applications in nearly every field [18]. One can also say that "Things," in "Internet of Things", can refer to a wide variety of devices that will affect different areas of research and technological advancements.

The potential applications for Internet of Things is in both Defense and Civilian Sector.

Potential applications like securing borders, automated facial and bio-metric systems to check immigration, automated start/ fire and forget systems that can keep a country secure. There are also application in remote surveillance and activity monitoring, automated drones that do not need human interference along with creation of a platform that lead to potential removal of friendly fire in a combat zone among others that can be used in Defense Sector of a country.

In Civilian Sector the potential applications are shown in the Figure (1.1). One of the potential application is Smart Homes. In this scenario the devices will be used in home automation and security such as the control and automation of lighting, heating (like smart thermostat), ventilation, air conditioning (HVAC) systems, and appliances such as washer/dryers, ovens or refrigerators/freezers that use Wi-Fi for remote monitoring. IoT systems could also be responsible for performing actions like Intelligent shopping systems, sensing and automatically controlling HVAC system, electricity and energy management, as well as transportation systems [19].

Internet of things has led to creation of Smart Industries that is the devices can also aid in Network control and management of manufacturing equipment, asset and situation management like local environment monitoring for some industries, or manufacturing process control for smart manufacturing [20]. Digital control systems and asset management via predictive maintenance, statistical evaluation, can lead to the creation of Smart Grid, thereby enabling real-time energy optimization.

This Smart Grid along with integration of communications, control, and information processing across various transportation systems, that is, dynamic interaction

between components of a transport system enabling inter and intra vehicular communication, smart traffic control, smart parking, electronic toll collection systems, logistic and fleet management, vehicle control along with driver less cars, and safety and road assistance leads to creation of Smart Cities [21].

To create Smart City, one needs huge number of devices connected together by linking devices of smart grid, traffic management, monitoring and controlling operations along with structural conditions of urban and rural infrastructures like bridges, railway tracks, on- and offshore- wind-farms. It can also help in Fog computing by getting real time data. In the smart city project one can also add the applications like security, energy and fleet management, digital signage, public Wi-Fi, paperless ticketing among others [22].

The Smart City is not complete till one can do environmental monitoring and integration of health care services.

One of the major issues in smart city is also monitoring the Environment. The IoT typically can use sensors to assist in environmental protection [23] by monitoring air or water quality [15], atmospheric or soil conditions [24] and can even include areas like monitoring the movements of wildlife and their habitats [25].

In health care services, we have already seen a boom in sensors that are used to monitor health like blood pressure and heart rate monitors to advanced devices capable of monitoring specialized implants, such as pacemakers or advanced hearing aids [21]. Specialized sensors can also be equipped within living spaces to monitor the health and general well-being of senior citizens, while also ensuring that proper treatment is being administered and assisting people regain lost mobility via therapy as well [26]. Other consumer devices to encourage healthy living, such as, connected scales or wearable heart monitors, are also a possibility with the IoT [27].

Our work, that is presented in this thesis, can also lead to a possible creation of an optical detection device that can be used to monitor the Environment and also be used to monitor Health of a person. Usually, a device that is capable of doing a blood test or water pollutant or air testing or other medical analysis uses an optical detector for analysis.

An optical detector is routinely used to identify the chemical composition of matter, that is, molecules and also determines its physical structure. A measurement using optical detector is obtained by detecting a change in state or response of the radiating object [28].

Our optical detector that will be introduced in this thesis is a combination of Surface Plasmons Resonance (SPR) Chip and a spectrometer named Coupled Bi-Directional Sampling Spectrometer (CoBiSS) [Patent number WO2009127794A1]. The other SPR detectors that are present today are systems like Biacore SPR systems (created by GE) [29], Spreeta (created by Texas Instruments) [30], SWIFT (created by Floralis) [31],

SPIRIT (Created by Seattle Sensor Systems) [32]. This SPR technique can most effectively detect trace amounts of pollutants or contaminants till a level of a few molecules [33]. This SPR chip as explained in Chapter 4 is generally small in size. The SPR chip could use a Spectrometer which is an apparatus to measure a spectrum or a graph that shows intensity or phase of light as a function of wavelength or frequency.

In present day, we are required to develop a more precise optical detector and spectrometer or lamdameter, that are not heavy. These devices should not have moving parts. This makes it a problem for other optical devices to be used in real world and real time applications. It is also important that the devices are immune to external perturbation.

While keeping this problem a new Spectrometer was developed and is known as Coupled Bi-Directional Sampling Spectrometer (CoBiSS) [Patent number WO2009127794A1] to create a device. This device initially had a lot of moving parts as it was designed to be used in the laboratory but it had a great potential. This device has been modified to remove all the constraints like movable parts (presented in the thesis). This device could be the next generation of the spectrometer and can revolutionize the Environmental and Health care system globally. The working of CoBiSS spectrometer is explained in Section 1.1.

This device could also play an important role in Medical and Healthcare department even in environmental monitoring as this could be used to enable remote monitoring and automated emergency notification and deployment services in Smart City and Remote areas.

1.1 Working of CoBiSS Spectrometer

Now, the basic working of an Ultracompact Fourier Transform Spectrometer (FTS), that is, also known as CoBiSS [35-38], that is based on bi-dimensional (2D) spatial sampling of a confined interferogram as shown in Figure (1.3).

In the figure (1.4), A light beam issued from an input collimated beam is split into two beams say Laser 1 and Laser 2 by a nonpolarizing cube beam splitter (BS). Each part of the laser light is the same as we are using 50:50 beam splitters. Let us call a portion of the laser, which is moving on the right as Laser Beam 1 (F1) and on the other side as Laser Beam 2 (F2), see figure (1.4).

When F1 interacts with the surface of the prism where there is difference in refractive index (between glass prism and air), total internal reflection (TIR) takes place. TIR condition is fulfilled since the angle of incidence $\theta = 45^\circ$ is greater than the critical angle of glass/air interface. When the total internal reflection takes place a portion of wave propagates towards the right side. Similarly when F2 interacts with the surface

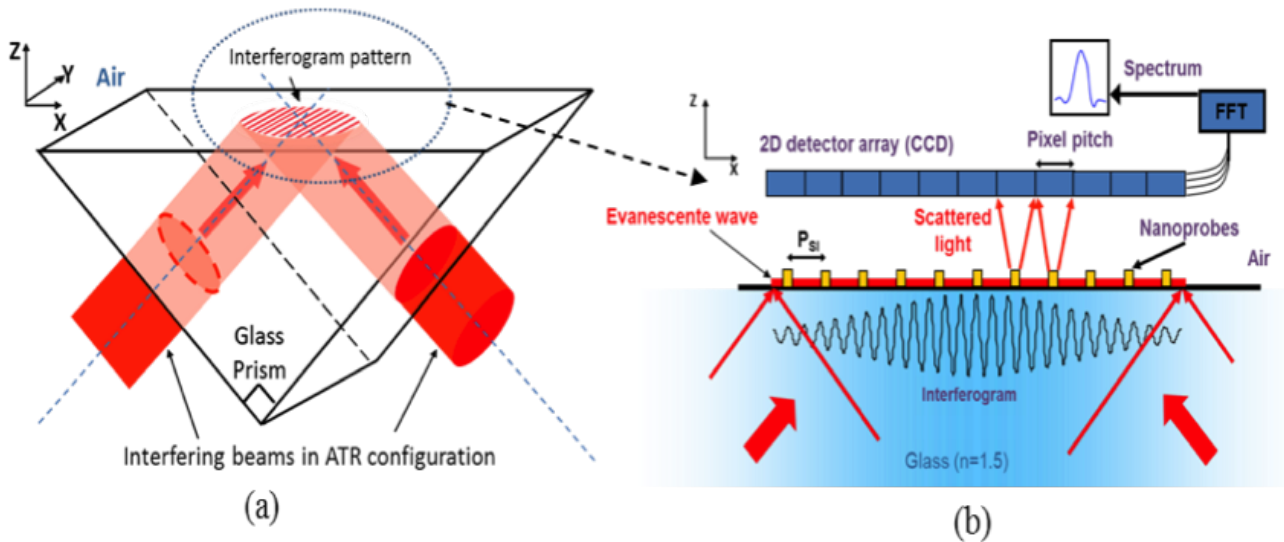


FIGURE 1.3: Explanation of CoBiSS

of prism the portion of wave propagates on the left side. Ultimately, the addition of the two waves gives us a standing wave.

The evanescent fields created by the F1 and F2 leads to creation of Evanescent Standing Wave (ESW). The ESW on the planes of interaction lacks the intensity and it diminishes exponentially as we go further in the air. The maximum intensity is at the surface of the interaction. This takes place in the 3 facets of prisms, that is, on the left, right and the top surface as seen in the figure (1.4).

This light source which is splitted into two collimated beams (seen in Figure (1.4)) interferes in TIR configuration on an optical prism's top facet (Fig.(1.4a)). The evanescent part of the interferogram is sampled using a 2D array of scattering optical near field nanoprobe deposited on the prism surface (Fig. (1.4b)). The scattered light is then detected in the far field using a 2D photo detector array (Camera) and finally the 2D image is uploaded in a Matlab script to perform a Fourier Transformation on the sampled interferogram.

The 2D sampling principle of CoBiSS is shown in Figure (1.5). The Figure (1.5A) sketches the projection principle on the longitudinal x axis. The 2D array of nanostructures is made of N_x lines with a longitudinal period P_x . Each line contains N_y nanoprobe equally spaced by P_y (transverse period). The total number of the interferogram sampling points is $N_{Max} = N_x \times N_y$. The interference lines are parallel to the transverse y axis and the spatial distribution along the x axis is a periodic function with a period T given by

$$T = \lambda_0 / (2\tilde{n} \sin(\theta)) \quad (1.1)$$

where, λ_0 is the laser wavelength, \tilde{n} is the glass refractive index and θ is the incidence angle. For instance, let us consider wavelength (λ_0) as 600 nm, angle of incidence (θ) as 45° and glass refractive index (\tilde{n}) as 1.52, then the calculated value of $T = 279.12$ nm.

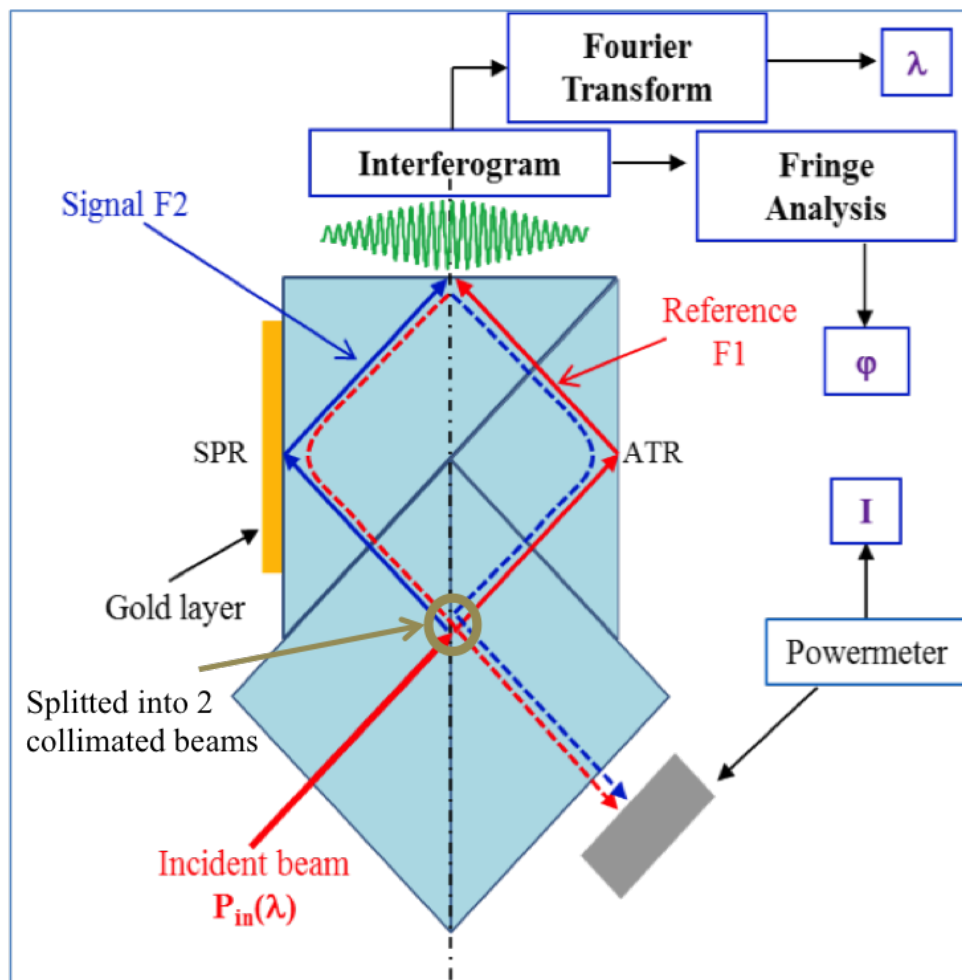


FIGURE 1.4: Working of CoBiSS

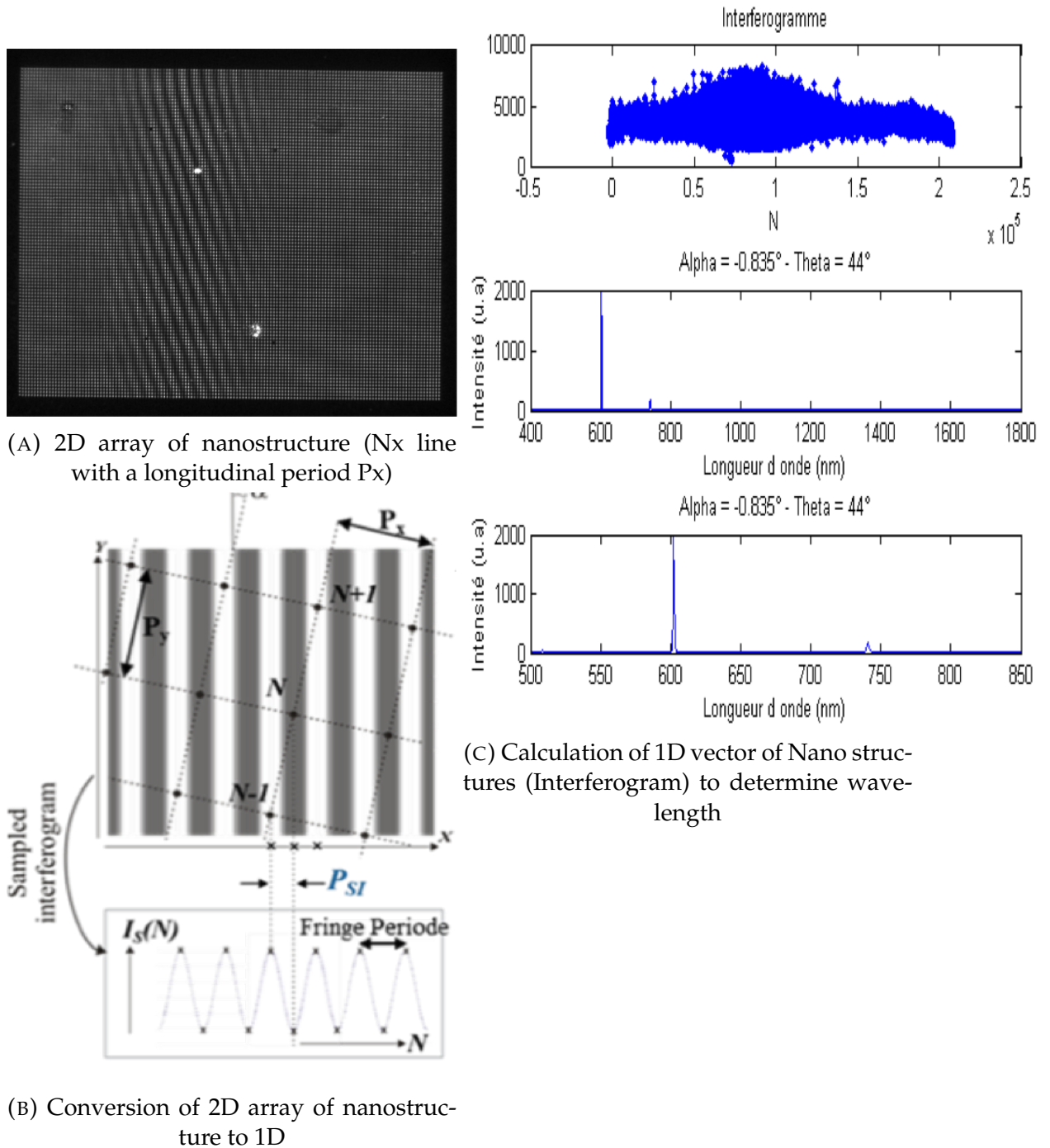


FIGURE 1.5: 2D sampling principle of CoBiSS

The configuration where the N_x lines are parallel to the fringe lines features a sampling interval P_{SI} equal to the longitudinal period P_x . In the tilted configuration shown in Figure (1.5B), the 2D array of nanoprobe is rotated in the (x0y) plane by an angle α . In such configuration, the interferogram is sampled in agreement with the Shannon criterion [39] regardless of the pitch of the 2D nanoprobe array which could be much larger than the interferogram period T . Assuming fringe lines are parallel to the transverse y axis, we get the theoretical sampling interval $P_{SI} = P_y \sin(\alpha)$, is seen in Figure 1.5B, and the sampling distance $L_S = (N_{Max} - 1)P_{SI}$.

Each nano-probe $N(x_N, y_N)$ scatters a number of photons proportional to the local intensity of the evanescent wave and the corresponding intensity I_N is stored. The Figure (1.5A) shows the 2D image acquired by a CCD camera through a microscope objective. This image is uploaded in a Matlab script where we apply a projection for each nanoprobe parallel to the fringe lines. We then obtain an intensity distribution along the x axis (sampled interferogram) and perform a 1D Fourier transformation to recover the spectrum as shown in the Figure (1.5C). The CoBiSS spectrum was obtained using 14000 channels (sampling points), corresponding to a nanoprobe array with the following parameters: $\alpha = 1^\circ$; $N_x = 100$; $N_y = 50$; $P_x = P_y = 1.5\mu m$; and gold nanoprobe diameter $D = 120$ nm. The theoretical spectral resolution $\delta\lambda = (\lambda_0)^2 / (2\tilde{n} \sin(\theta)L_S)$ is equal to 1.4 nm around 780 nm with $\theta = 45^\circ$ and $n = 1.517$ (BK7 prism).

The interferometric configuration used in [35] is not suitable for measuring wide band spectrums since the corresponding interferogram collapses around the zero optical path difference (ZOPD) due to a low coherent length for a wide band input light source [38]. According to CoBiSS principle, the ZOPD must coincide with the center of the 2D array of nanoprobe inscribed on the prism surface. This is a big issue since the size of the sampling length can be only some hundred microns and therefore one has to ensure an interferometric configuration with an optical path difference smaller than few tens of a micron.

This configuration is novel mainly for three reasons:

1. Contrary to the configuration described in [35], this one presents one input.
2. The interference paths take place inside a glass bulk and therefore increases noise immunity for phase shifts measurements.
3. An intensity monitoring is possible using the output beam which is the merged transmitted F1 and reflected F2 beams after one roundtrip (half of the input intensity is collected for a 50/50 BS).

For the purposes of this thesis, the Figure 1.3a will be known as Evanescent Standing Wave (ESW) configuration where no nano particles are present.

1.2 Aim

The main aim is to create a portable optical detection device which uses ESW configuration to do SPR calculations figure 1.4 and can also be used for environmental testing, medical testing in cities, mountains, factories, rivers and so on for a practical purpose, that is, in wireless sensing of environment as one of the example. It means that the device needs to be small handheld and portable. It should be a rugged device which can be deployed even in the harshest condition. This also means that the device should not have any movable parts and all the parts need to be fixed.

The ultimate aim of this thesis is to create or give most optimized solution(s) for future production for a first working prototype which has no moving parts and can be created without using too many custom parts. This would help in the reduction of cost.

1.3 Initial Result

Initially, one thought the process will be rather simple to convert the setup of CoBiSS to a device.

Earlier the description of working of CoBiSS spectrometer was given in Section 1.1 where one used a microscope to get an image of an interference pattern that was irradiated by the nano-particles or nano-probes. As it is, this setup can not be used as a device in real world applications. This setup has too many moving parts and needs a lot of calibration with the microscope therefore it was imperative to remove the microscope (to start with) and to replace a camera CCD/CMOS 2D array without any focus and lenses.

For this purpose, few new glass slabs were made to match 1 nano-particle in 3 pixels and 1 nano-particle per pixel by varying the distance between each nano-particle and always respecting the Shannon's Sampling Condition.

We placed these slabs on CoBiSS configuration with the help of a gel having same refractive index. We placed a camera on top of this whole setup. We moved the camera from the closest position to furthest position without touching the surface of nano-particles as shown in Figure 1.6.

As we moved from just above the surface to the 5 cm, we started seeing multiple images as we increased the height / position of the camera from the surface of prism. This can be visualized using few images in Figure (1.7).

After visualizing these images(Figure (1.7)) and other results, it became clear that one needs to understand this in detail. To understand these images, one can propose that it comes from Diffraction gratings and from the Talbot effect.

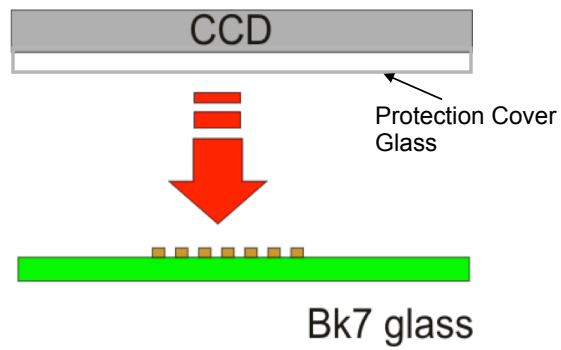
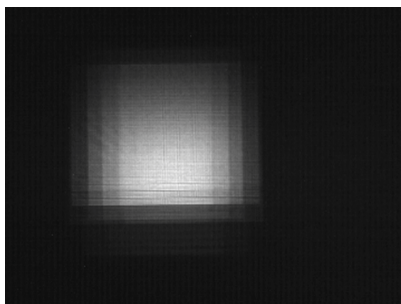
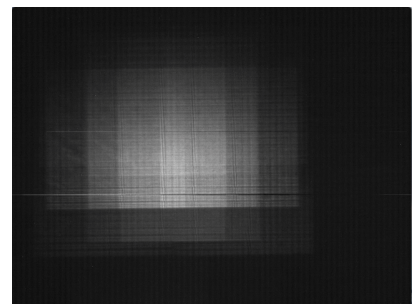


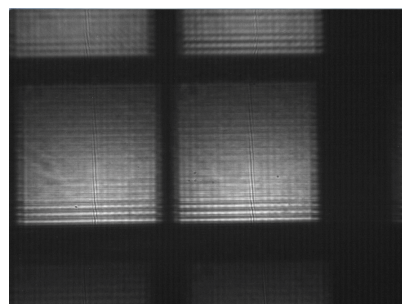
FIGURE 1.6: Positioning of Camera with Glass Slab



(A) Closest Position 1



(B) Intermediate height



(C) farthest height

FIGURE 1.7: Example of images found by varying height

We also saw as the images at the closest point are not crisp and we realized the camera has a small covering of glass which is located above the camera CCD/ CMOS sensor as a protection cover.

This protector cover changes the observation results. One cannot determine the thickness nor the refractive index of camera's protective cover. Now, new cameras were purchased which have no Glass Cover and also a company named Resolution Spectra Systems started to collaborate with us to position our glass slab with nano-particles at a specific distance to the camera (without any glass slab).

For a camera without a protective layer, one needs to precisely understand the working and positioning of nano-structures among other aspects of integration. To do this one needed to start from the basics to the end product. This thesis covers this distance. The flow or how each chapter adds value to the final integrated product is explained in Section 1.4

1.4 Organization

The total integration process to create this product is divided into Three parts, namely, optical integration of CoBiSS spectrometer followed by electronic integration of this spectrometer and then a SPR Chip is designed specifically for this spectrometer.

The optical integration constitutes the working of all the aspects of optics related to CoBiSS spectrometer in this thesis and are present from Chapter 2. This chapter deals with the following :

- To understand radiation pattern of a dipole (a particle of extremely negligible size) behaves when it is present near or at the interface of glass and air.
- Understanding irradiation pattern when a nano-particle interacts with evanescent standing wave. A study is done to find the correct nano-particle, that is , material, form and size of particle will be suited to increase the intensity of the light coming in the air so that the camera can capture it (be it minimum light or the maximum light). A spectral study is performed to see the changes in the radiation of the said nano particle as a function of wavelength.

As the device had to be made compact and transportable, the electronic integration of the device was done. The electronic integration deals with all the electronic connections, data processing and transmission of data. This can be found in Chapter 3.

The first integration model and is described in Chapter 3 and it contains:

- A selection of a few electronic devices is performed with the help of our matching criterion. Comparison tables for these devices is also shown.

- Using those selected devices (specially microprocessor and its development kit) we created a code which could be control other devices like camera, laser and do necessary calculations. Also, the code was optimized to run faster on the ARM processor. This was done as we cannot use Matlab on ARM processors or if we try then they are really slow (not optimized).
- A description of the calculation methods are presented. This method is like a function to convert the image into a wavelength value.
- To complete this device, an autonomous program was made for its real time functioning and also a small Graphic User Interface (GUI) was created for ease of use.

After the spectrometer was complete, we created a new SPR Chip design that is best suited to work with this system and is showcased in Chapter 4.

This chapter includes the following:

- The most optimum thickness of Gold slab is found.
- A new structure named "W" is presented and most optimum parameters for development are found. A variation of this structure with rounded borders is also explored.
- A comparison of sensitivity analysis of Gold slab and Gold "W" structure is performed by taking their most optimized parameters.

As a new trend emerging in the area of Internet of Things, we coded the wireless communication capabilities for this device to communicate between the device which is next to it and also between device and central server. A small description of where these capabilities can be used is present in the Conclusion section of this thesis.

Chapter 2

Sampling of the confined interferogram

The working of CoBiSS spectrometer (presented in 1.1) is based on the principle of confined interferogram sampling and is shown in Figure (1.4). A light beam that is issued from a light source is split into two collimated beams with the help of a beam splitter. These beams interfere in Total Internal Reflection configuration on an optical prism facet as shown in Figure (1.3(a)). The evanescent part of the interferogram is sampled using a two-dimensional array of scattering optical near-field nanoprobe that are deposited on the prism surface Figure (1.3(b)). The scattered light is then detected in the far-field with the help of a two-dimensional photo-detector array by creating a two-dimensional image. Finally, this two-dimensional image is uploaded in a Matlab script to perform a Fourier transformation on the sampled interferogram.

To understand this, in detail, we present a simplified model of diffusion where a small probe is used to analyze a propagating evanescent wave scattering over this small probe and is represented as a small induced dipole that is emitting in far field. Afterwards, a numerical method (FDTD) is used for analysis and optimization of parameters for the fabrication of the compact prototype.

In this first section, we will present the case of nanoprobe scattering by a unique incident propagative wave[38], which will be followed by the case of nanoprobe scattering by the evanescent standing wave in the section two, which represent the working of the cobiss spectrometer, and conclude.

2.1 Scattering of the propagative evanescent wave

The spatial sampling of the evanescent standing wave is realized by a nanoprobe (a metallic particle) scattering the near field into the far-field (toward the CCD camera). This scattering into the far-field emerges from a series of complex interactions taking place between the particle and the substrate as seen in Figure (2.1).

In the CoBiSS system, the light is "impinging" the Glass-Air interface at an angle of incidence of $\theta_1 = 45^\circ$, i.e., above the critical angle of 41.12° as seen in the Figure (2.2). This implies that the Total Internal Reflection (TIR) takes place at this interface

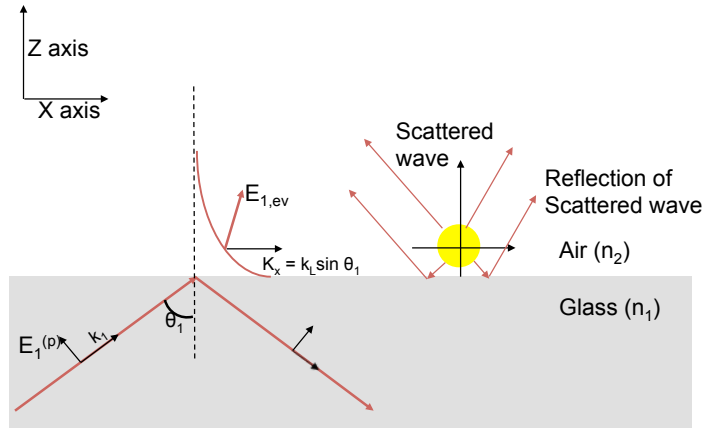


FIGURE 2.1: A plane wave arrived at an angle of 45° towards the right from the glass side and evanescent wave is formed at the surface. A nano particle's series of complex interactions taking place between the particle and the substrate.

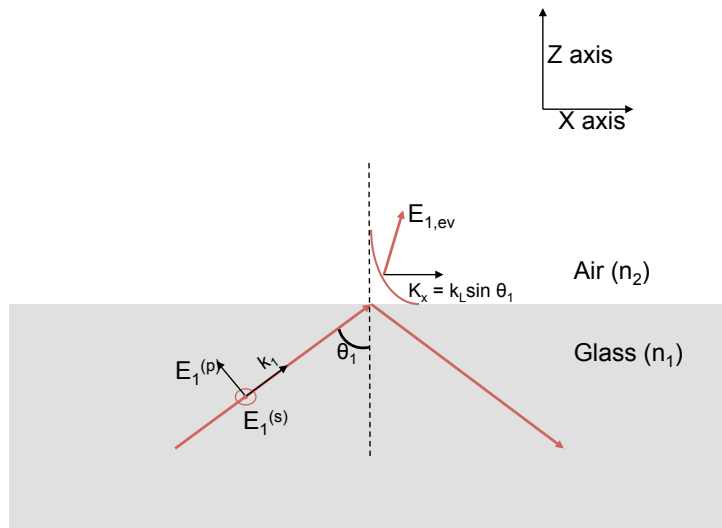


FIGURE 2.2: A plane wave arrived at an angle of 45° towards the right from the glass side and evanescent wave is formed at the surface.

and therefore leads to a creation of a pure evanescent wave on the side of Air (refer to Figure (2.2)). Here, we will describe, the characteristics of the field.

First let us consider, the laser has an Electric Field E_1 and that is incoming from the glass medium. This Field can be p polarized (p) or s polarized (s) or both. As this field will strike the interface of glass (n_1) and air (n_2), the effective refractive index is represented by \tilde{n} (1.52 in our case). This field also strikes the interface with an angle, therefore the initial angle of incidence in Glass is represented by θ_1 and angle of refraction is represented by θ_2 .

As we are fulfilling the criteria of total internal refection, the evanescent wave $\mathbf{E}_{1,ev}(\mathbf{r}, \omega)$ is given by [40],

$$\mathbf{E}_{1,ev}(\mathbf{r}, \omega) = \begin{bmatrix} -iE_1^{(p)}t^p(\theta_1)\sqrt{\tilde{n}^2 \sin^2 \theta_1 - 1} \\ E_1^{(s)}t^s(\theta_1) \\ E_1^{(p)}t^p(\theta_1)\tilde{n} \sin \theta_1 \end{bmatrix} e^{i \sin(\theta_1)k_1 x} e^{-\gamma z} e^{i\omega t} \quad (2.1)$$

where $t(\theta_1)$ represents transmittance coefficients at θ_1 , k_1 represents wave number in medium 1, k_2 represents wave number in medium 2, x represents the x axis, z represents the z axis, γ represents the decay constant $= k_2 \sqrt{\tilde{n}^2 \sin^2 \theta_1 - 1}$. Where t_s , and t_p represent the transmittance coefficients for s and p polarized light which are given by the Fresnel equation as follows

$$t_s = \frac{2n_1 \cos \theta_1}{n_1 \cos \theta_1 + n_2 \cos \theta_2} \quad (2.2)$$

$$t_p = \frac{2n_1 \cos \theta_1}{n_2 \cos \theta_1 + n_1 \cos \theta_2} \quad (2.3)$$

In our case of total internal reflection, the value of θ_2 becomes 90° . Therefore the Fresnel coefficients can be rewritten as: $t_s = 2$, $t_p = 2\frac{n_1}{n_2} = 2\tilde{n}$.

The ratio of amplitude of evanescent field's x-component to its z-component is compared at a wavelength of 600 nm as it is the average wavelength of the visible to Near Infra Red zone of 400 nm to 800 nm and the angle of incidence of the beam is 45° . The ratio is found to be 0.366 or 36.65 %. It is important to notice, for this wavelength and angle, the x-component of the evanescent field is non-negligible, and is 1/3 of the total field and this will play an important role in the comprehension of the energy transfer towards the camera's pixel.

We have explored the scattering of a dipole, or a particle small enough to behave as a dipole, and its radiation pattern that is generated from the Evanescent wave.

2.1.1 Evanescent wave scattering of a small particle in the dipolar approximation

In this section, we will describe some elements of the scattering process of the evanescent wave by a small particle. In this case, one of the prominent feature is the evanescent nature of the incoming wave's field that interacts at the level of the nanoparticle. Its strong spatial dependence (evanescent characteristics), has several consequences for excitation of the mode at the level of the nanoparticle, see for a description of the modification of the scattering cross section and modal excitation [41, 42].

In the small particle approximation, i.e., by considering that the scatterer to be small enough so that it can be treated as an electric dipole, we have a simple description in term of dipolar moment. Indeed, the dipole moment \mathbf{p} induced in the particle by

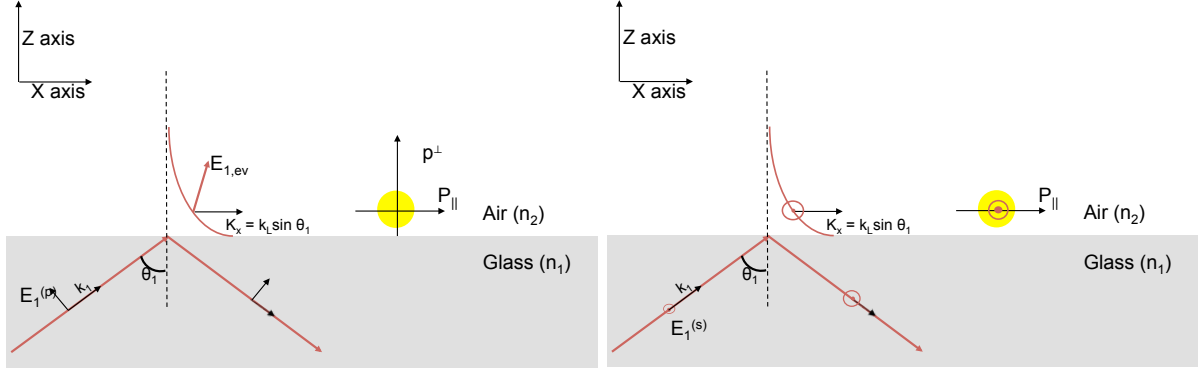


FIGURE 2.3: Evanescent wave scattering for TM and TE waves.

the exciting local field $\mathbf{E}_{1,ev}(\mathbf{r}, \omega)$ (from eq. (2.1) at its position \mathbf{r} is being expressed as follows [46],

$$\mathbf{p}(\mathbf{r}, \omega) = \epsilon_0 \boldsymbol{\alpha}(\mathbf{r}, \omega) \mathbf{E}_{1,ev}(\mathbf{r}, \omega) \quad (2.4)$$

with $\boldsymbol{\alpha}(\mathbf{r}, \omega)$ being the polarizability. In the case of small spherical particle in vacuum, it is express in the quasi-static approximation by a diagonal tensor $\boldsymbol{\alpha}(\mathbf{r}, \omega) = \alpha_0 \mathbf{I}$ with \mathbf{I} the diagonal unity tensor, and α_0 the static polarizability

$$\alpha_0 = 3V \frac{\epsilon - 1}{\epsilon + 2} \quad (2.5)$$

with the volume of the nanoparticle $V = 4\pi R^3/3$ of radius R . In front of a dielectric interface, the polarizability is modified and can be express in the image dipole approach[44, 45] depending on the direction. In the TM configuration, the Electric field is p-polarized and the induced dipole creates a polarizability that is both parallel (α_{\parallel}) to the interface (x direction) and perpendicular (α_{\perp}) to the interface (z-direction) see Figure (2.3). Whereas, in the TE configuration, the induced dipole's polarizability is parallel to the interface, that is, x and y-direction (α_{\parallel}).

The polarizability can be calculated as follows:

$$\boldsymbol{\alpha}(\omega) = \begin{pmatrix} \alpha_{\parallel} & 0 & 0 \\ 0 & \alpha_{\parallel} & 0 \\ 0 & 0 & \alpha_{\perp} \end{pmatrix} \quad (2.6)$$

with

$$\alpha_{\perp}(\mathbf{r}, \omega) = \frac{\alpha_0}{1 - \frac{\alpha_0 \beta}{16\pi z^3}} \quad (2.7)$$

$$\alpha_{\parallel}(\mathbf{r}, \omega) = \frac{\alpha_0}{1 - \frac{\alpha_0 \beta}{32\pi z^3}} \quad (2.8)$$

And $\beta = (\epsilon_s - 1)/(\epsilon_s + 1)$, with ϵ_s the dielectric constant of the substrate.

Let us illustrate some effects related to the presence of the dielectric interface (glass), for the polarizability of a gold particle having a radius of 5 nm for two distances from the interface for both parallel and perpendicular orientation of the field. Calculation of polarizability for both parallel and perpendicular orientation are done based on equation (2.6-2.8), where the gold particle is placed at a distance of $z = 5\text{nm}$ in air from the interface and secondly, we place the particle at a distance of $z = \infty$ in air from the interface (static polarizability : α_0) for the calculation of polarizability where the wavelengths that are considered are in the visible spectrum, i.e. between 400 and 800 nm. In this approximation, we observe in Figure (2.4) a change in amplitude of the relative polarizability when compared to the vacuum case i.e. α_0 in quasi-static. From the Figure (2.4), we observe no shift of the resonance when the dipole is placed in the presence of the substrate. This is as expected from the quasi-static approximation. But in the presence of the substrate, we should expect a shift when the radiative correction is performed. This is due to the limitation of the quasi-static model, which doesn't take into account the radiative correction [43]. This simple example also gives us a locally

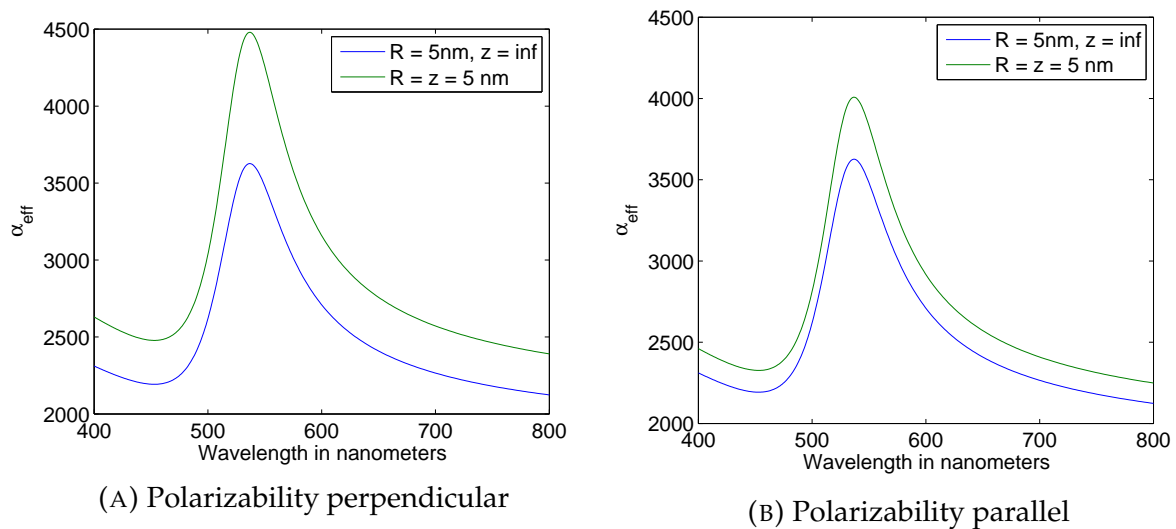


FIGURE 2.4: Polarizability calculation for Gold particle. The green curve indicates the polarizability of a Gold particle at a distance of infinity from the interface. The blue curve indicates the polarizability of the particle touches the interface

induced dipole and also permits us to describe the radiation diagram. This simplistic model permits us to interpret a some of the phenomenons related to the transfer of energy by the nano-antennas. This is described in the following sub-chapters.

2.1.1.1 Radiation diagram of a dipole and Influence of the air-glass interface

In this part, we present the radiation pattern of an electric dipole that is placed near the interface, in a simple description [47, 48, 49]. This is an approximated model. The

dipole is placed near the surface and its radiation pattern is observed which is calculated by observing the scattered power in a small solid angle ($d\Omega$). The measure of the

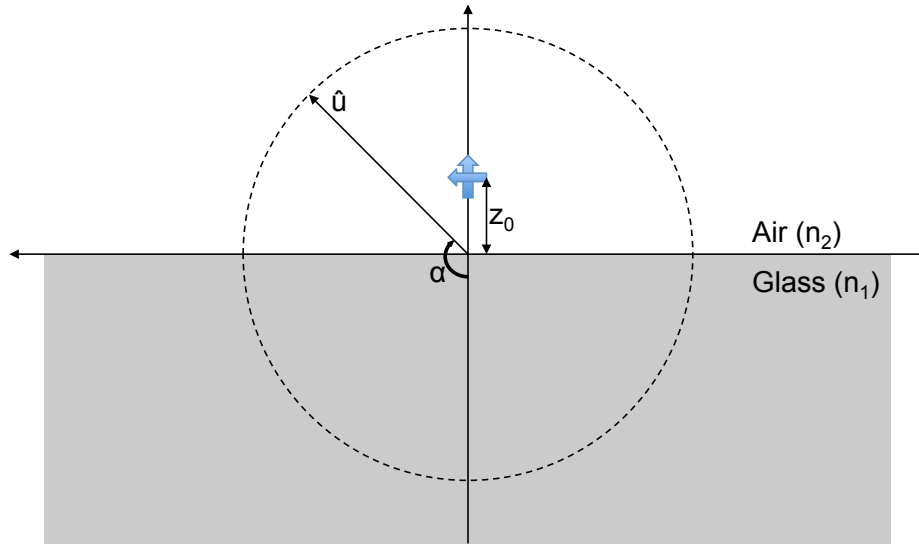


FIGURE 2.5: Dipole-substrate geometry.

radiating power is done by measuring the field at a distance of 1 meter from the center of the particle. This circle can be in the same plane that is in XZ plane as seen in Figure (2.5) or in the perpendicular plane to XZ plane. Here, we restrict our calculation for the plane XZ and the two orientations of the dipole that correspond to a parallel dipole and a perpendicular dipole to the X axis (both seen in Figure (2.5)). The radiation pattern for a radiating electric dipole is calculated by observing the scattered power in a small solid angle ($d\Omega = \sin \alpha d\alpha$). The calculation of scattering within a small solid angle $d\Omega$ and is obtained by the averaged pointing vector

$$\langle \mathbf{P} \rangle = (\mathbf{E}_{scat} \times \mathbf{H}_{scat}) = \frac{1}{2} \sqrt{\frac{\epsilon_0 \epsilon}{\mu \mu_0}} E_{scat}^2 \quad (2.9)$$

The scattered power passing through the element of surface $dA = r^2 \sin \alpha d\alpha$ is given by the Equation (2.10),

$$dP_{scat}(\alpha) = \langle \mathbf{P} \rangle r^2 \sin \alpha d\alpha = \frac{1}{2} \sqrt{\frac{\epsilon_0 \epsilon}{\mu \mu_0}} |\mathbf{E}_{scat}|^2 r^2 \sin \alpha d\alpha \quad (2.10)$$

which becomes,

$$\frac{dP}{d\alpha} = \frac{r^2 \sin \alpha}{2} \sqrt{\frac{\epsilon_0 \epsilon}{\mu \mu_0}} |\mathbf{E}_{scat}|^2 \quad (2.11)$$

For the calculation of analytical radiation diagrams of a dipole as described in [48, 49], requires the terminologies like power distribution in vacuum ($P_{\infty}^{(s,p)}(\alpha_2)$) followed by Fresnel coefficient for reflectance and transmittance ($R_{2,1}^{(s,p)}(\alpha_2)$ and $T_{2,1}^{(s,p)}(\alpha_2)$ respectively). To calculate the exact radiating power that is present in the same plane as in XZ plane, the radiating power for each solid angle is:

1. Power Distribution in Vacuum (w.o. the interface, or far from it) In vacuum, the

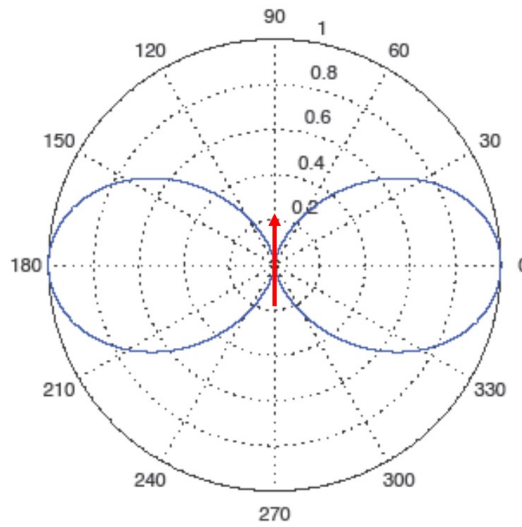


FIGURE 2.6: Radiation Diagram of a dipole in Air.

dipolar radiation is described by the far-field expression of the dipole

$$P_{\infty}^{(p)}(\alpha) = \frac{3}{8\pi} \sin^2(\alpha) \quad (2.12)$$

The radiation pattern of a dipole in far field is shown in Figure (2.6).

2. Power Distribution in Glass

$$P^{(s,p)}(\alpha_1) = P_{\infty}^{(s,p)}(\alpha_2) T_{2,1}^{(s,p)}(\alpha_2) \frac{d\Omega_2}{d\Omega_1} \quad (2.13)$$

3. Power Distribution in Air

$$P^{(s,p)}(\alpha_2) = P_{\infty}^{(s,p)}(\alpha_2) R_{2,1}^{(s,p)}(\alpha_2) \frac{d\Omega_2}{d\Omega_1} \quad (2.14)$$

2.1.1.1.1 Electric Dipole placed Perpendicular to the surface of Interaction First, one needs to properly understand the placement of the dipole (refer to Figure (2.5)) that is it is placed 1 nm above the surface of the interaction in Air and Perpendicular to the surface of Interaction.

By simplifying the equations (2.13) and (2.14) for this case, the new equations will become:

- Radiation Diagram in Air

$$P_e(\alpha_2) = \frac{3}{8\pi} \frac{\sin^2 2\alpha_2}{(\tilde{n} \cos \alpha_1 + \cos \alpha_2)^2} \quad (2.15)$$

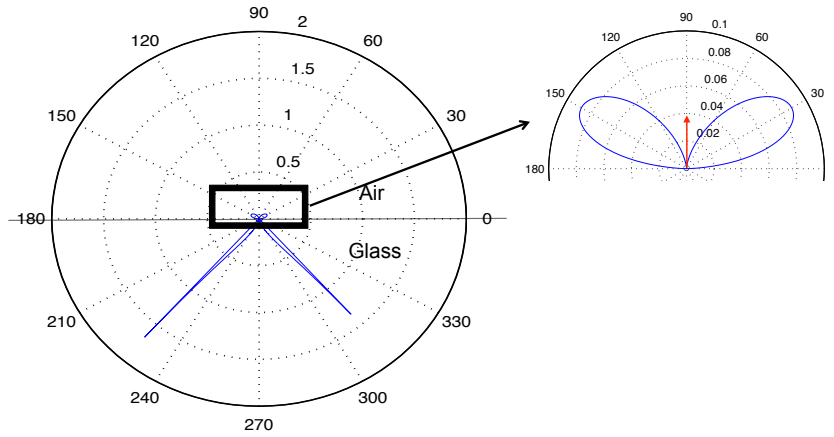


FIGURE 2.7: Radiation Diagram in the plane XZ and a Dipole is placed perpendicular to the interface.

- Radiation Diagram in Glass

$$P_e(\alpha_1) = \frac{3}{8\pi\tilde{n}^3} \frac{\sin^2 2\alpha_1}{(\tilde{n} \cos \alpha_2 + \cos \alpha_1)^2} \quad (2.16)$$

Using the results of these equations for an electric dipole that is oriented perpendicular to the plane of interaction, the radiation diagram can be seen in the Figure (2.7). In this Figure (2.7), on the left hand side one sees the radiation diagram of all the angular positions that means that light present in Air and Glass. Whereas on the right side we see a zoomed radiation pattern that is present in the medium Air. Our work is mostly confined to see the radiation diagrams in the medium Air as the camera will only receive the light that is present in air.

2.1.1.1.2 Electric Dipole placed Parallel to the surface of Interaction the dipole is now placed parallel to the surface of interaction. One needs to refer to Figure (2.5) where the dipole is placed 1 nm above the surface of the interaction in Air. By simplifying the equations (2.13) and (2.14) for this case, the new equations will become:

- Radiation Diagram in Air

$$P_e(\alpha_2) = \frac{3\tilde{n}^2}{2\pi} \frac{\cos^2 \alpha_2 \cos^2 \alpha_1}{(\tilde{n} \cos \alpha_1 + \cos \alpha_2)^2} \quad (2.17)$$

- Radiation Diagram in Glass

$$P_e(\alpha_1) = \frac{3}{2\pi\tilde{n}} \frac{\cos^2 \alpha_1 \cos^2 \alpha_2}{(\cos \alpha_2 + \tilde{n} \cos \alpha_1)^2} \quad (2.18)$$

Using the results of these equation for an electric dipole that is oriented perpendicular to the plane of interaction, the radiation diagram can be seen in the Figure (2.8).

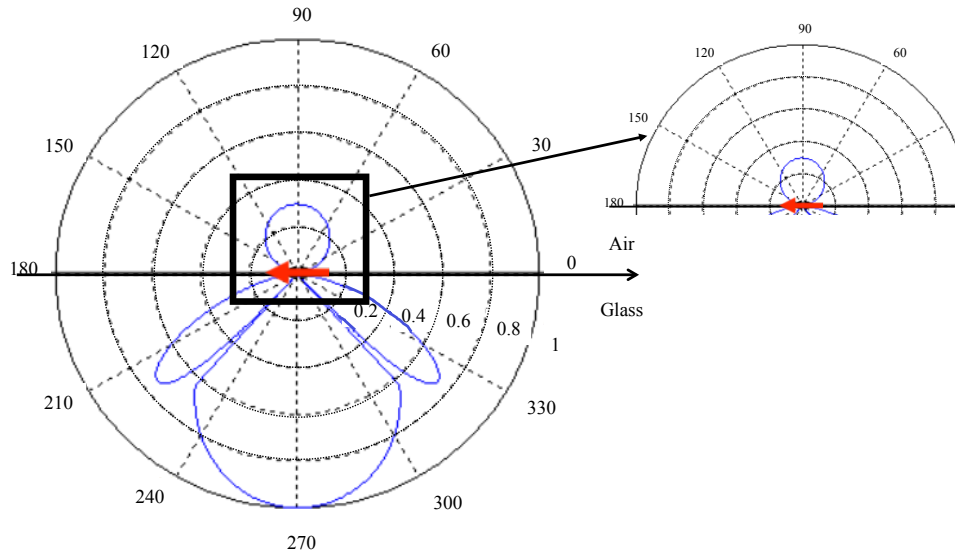


FIGURE 2.8: Radiation Diagram in the plane XZ and a Dipole is placed parallel to the interface.

2.2 Scattering of the Evanescent Standing Wave (ESW) with FDTD calculation

In previous section, we have discussed the radiation pattern of a nano-particle coming in interaction with a single evanescent wave, in dipolar and quasi-static, to cite few of them [41, 42]. To go further than the simple picture, as we have described previously, the ESW configuration calculation is explained. We make use of a commercial FDTD calculation, Lumerical's FDTD Solution for the simulation of the local minimum and maximum of the ESW and the nanoparticle (selection presented in Appendix A). A Rectangular Nano-Wire (RNW) of length 150 nm and a height of 100 nm is selected. For this nanoparticle the near field analysis along with radiation diagram are presented in the local maxima and minima. A study of spectral dependence is also presented for the wavelengths of 400 nm to 800 nm.

So far and up to our knowledge, the calculation of the scattering by a nanoparticle for evanescent standing wave hasn't been realized. This study reveals a counter intuitive results, that is, there could be more power scattered in the upper direction from the lower local intensity of the standing wave as compared to the local maximal intensity. This has the consequence to inverse the contrast of the sampling image of the standing wave as captured by the CCD camera.

To start, the calculation of the evanescent standing wave (ESW) has been presented.

2.2.1 The evanescent standing wave (ESW)

In the Figure (2.9), the Electric field of beam F1 is represented by $\mathbf{E}_1(\mathbf{r}, t)$ and the Electric field of beam F2, see Figure (1.4) direction is given by $\mathbf{E}_2(\mathbf{r}, t)$ where both have the

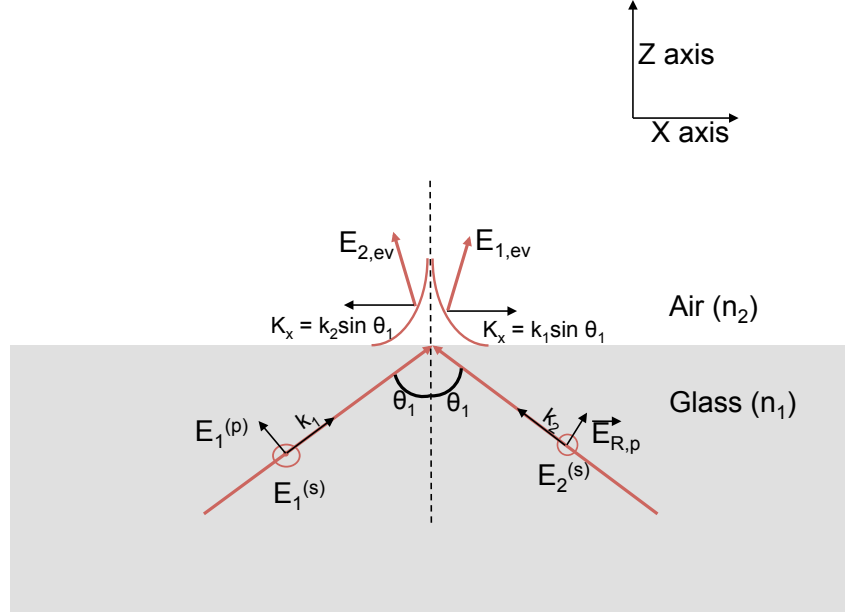


FIGURE 2.9: Two lasers are placed at an angle of 45° towards the left and the right in glass and evanescent wave is formed at the surface of intersection.

magnitude of amplitude as E_1 . The equations of both electric fields are represented as:

$$\mathbf{E}_1(\mathbf{r}, t) = \mathbf{E}_1 e^{i\mathbf{k}_1 \cdot \mathbf{r} + i\omega t} \quad (2.19)$$

$$\mathbf{E}_2(\mathbf{r}, t) = \mathbf{E}_2 e^{i\mathbf{k}_2 \cdot \mathbf{r} + i\omega t} \quad (2.20)$$

And for the evanescent part

$$\mathbf{E}_{1, \text{ev}}(\mathbf{r}, t) = \begin{bmatrix} -iE_1^{(p)} t^p(\theta_1) \sqrt{\tilde{n}^2 \sin^2 \theta_1 - 1} \\ E_1^{(s)} t^s(\theta_1) \\ E_1^{(p)} t^p(\theta_1) \tilde{n} \sin \theta_1 \end{bmatrix} e^{i \sin(\theta_1) k_1 x} e^{-\gamma z} e^{i\omega t} \quad (2.21)$$

Using equations (2.19), (2.20) and (2.21), the Evanescent Standing Wave $\mathbf{E}_{ESW} = \mathbf{E}_{1, \text{ev}} + \mathbf{E}_{2, \text{ev}}$ that is created is:

$$\mathbf{E}_{ESW}(x, z, t) = 2e^{-\gamma z} \begin{bmatrix} -iE_1^{(p)} t^p(\theta_1) \sqrt{\tilde{n}^2 \sin^2 \theta_1 - 1} \cos(k_1 x \sin \theta_1) \\ E_1^{(s)} t^s(\theta_1) \cos(k_1 x \sin \theta_1) \\ iE_1^{(p)} t^p(\theta_1) \tilde{n} \sin \theta_1 \sin(k_1 x \sin \theta_1) \end{bmatrix} e^{i\omega t} \quad (2.22)$$

The intensity of the standing wave is given by the equation:

$$I_{ESW} = 2\epsilon_0 \tilde{n}^2 e^{-2\gamma z} \left[\left(E_1^{(s)} t^s(\theta_1) \right)^2 \cos^2(k_1 x \sin \theta_1) + \left(E_1^{(p)} t^p(\theta_1) \right)^2 (\tilde{n}^2 \sin^2 \theta_1 - \cos^2(k_1 x \sin \theta_1)) \right] \quad (2.23)$$

An example of standing wave in p-polarization calculated at 600 nm is shown in Figure (2.10) that illustrates the constructive or destructive interference of the two propagat-

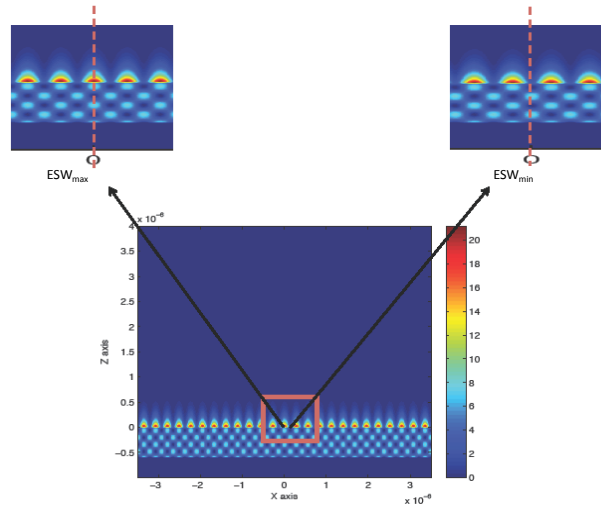


FIGURE 2.10: Normalized intensity of the standing wave above and below the interface at $z = 0$ where on the left side we observe the Maximum of the ESW and on the Right side we observe the Minimum of the ESW.

ing evanescent wave. In order to realize the spatial sampling of the interferogram, the extraction of the near field intensity should be different depending on the local intensity. Therefore in the following, we will consider only the two extremum position, i.e. the maximum and minimum intensity.

2.2.1.1 Introduction to Finite Difference Time Domain

Finite Difference Time Domain (FDTD) [53] [52] method is one of the full wave techniques used to solve problems in electromagnetics. It is the simplest method because the idea behind FDTD is to discretize the electromagnetic problem of Maxwell's equations, in both time and space. It can accurately tackle wide range of problems. The accuracy of the calculations and errors depends on the implementation of the FDTD computational code. This calculation method is computationally expensive as it uses a huge amount of memory and computation time.

This method employs finite differences as approximations to both the spatial and temporal derivatives that appear in Maxwell's equations (specifically Ampere's and Faraday's laws). Consider the Taylor series expansion of the function $f(x)$ expanded about the point x_0 with an offset of $\pm\delta/2$:

$$f\left(x_0 + \frac{\delta}{2}\right) = f(x_0) + \frac{\delta}{2}f'(x_0) + \frac{1}{2!}\left(\frac{\delta}{2}\right)^2 f''(x_0) + \frac{1}{3!}\left(\frac{\delta}{2}\right)^3 f'''(x_0) + \dots \quad (2.24)$$

$$f\left(x_0 - \frac{\delta}{2}\right) = f(x_0) - \frac{\delta}{2}f'(x_0) + \frac{1}{2!}\left(\frac{\delta}{2}\right)^2 f''(x_0) - \frac{1}{3!}\left(\frac{\delta}{2}\right)^3 f'''(x_0) + \dots \quad (2.25)$$

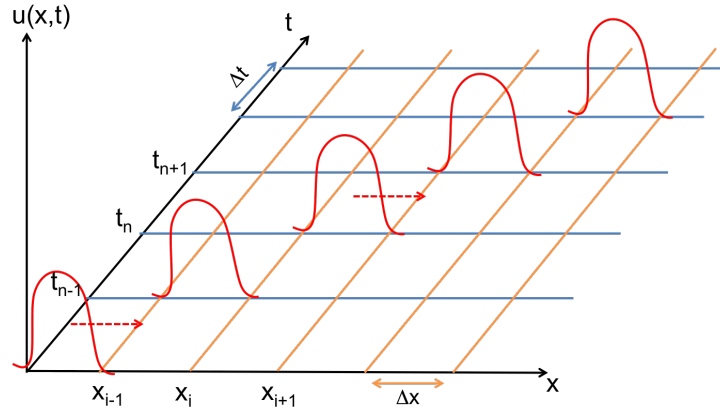


FIGURE 2.11: Explanation of FDTD Method

where the primes indicates differentiation. Subtracting the second equation from the first yields

$$f\left(x_0 + \frac{\delta}{2}\right) - f\left(x_0 - \frac{\delta}{2}\right) = \delta f'(x_0) + \frac{2}{3!} \left(\frac{\delta}{2}\right)^3 f'''(x_0) + \dots \quad (2.26)$$

Dividing by δ produces,

$$\frac{f\left(x_0 + \frac{\delta}{2}\right) - f\left(x_0 - \frac{\delta}{2}\right)}{\delta} = f'(x_0) + \frac{1}{3!} \left(\frac{\delta}{2}\right)^2 f'''(x_0) + \dots \quad (2.27)$$

This on the left hand side is the derivative function at the point x_0 and approximating it with central difference approximation gives:

$$\frac{df(x)}{dx} \Big|_{x_0} \approx \frac{f\left(x_0 + \frac{\delta}{2}\right) - f\left(x_0 - \frac{\delta}{2}\right)}{\delta} \quad (2.28)$$

In the method of finite differences, if the sample points are increased or higher order of derivatives are used for calculation of FDTD then it can lead to greater computational accuracy.

This FDTD Algorithm was first proposed by Kane Yee who employed second-order central differences method. His proposed algorithm is described as follows [51]:

1. Replace all the derivatives in Ampere's and Faraday's laws with finite differences. Discretize space and time so that the electric and magnetic fields are staggered in both space and time.
2. Solve the resulting difference equations to obtain updated equations'' that express the (unknown) future fields in terms of (known) past fields.

3. Evaluate the magnetic fields one time-step into the future so they are now known (effectively they become past fields).
4. Evaluate the electric fields one time-step into the future so they are now known (effectively they become past fields).
5. Repeat the previous two steps until the fields have been obtained over the desired duration.

2.2.2 At the position of the local minimum intensity of the ESW

At the position of the minimum of the standing wave see eq. (2.23), i.e. at $k_1 x \sin \theta_1 = 0[\pi]$, and using eq. (2.22), we can expressed the local field at this position by

$$\mathbf{E}_{ESW}(x, z, t) = 2e^{-\gamma z} \begin{bmatrix} -iE_1^{(p)} t^p(\theta_1) \sqrt{\tilde{n}^2 \sin^2 \theta_1 - 1} \\ E_1^{(s)} t^s(\theta_1) \\ 0 \end{bmatrix} e^{i\omega t} \quad (2.29)$$

which give in the p-polarization case, a field purely polarized in the x-direction. Therefore the nanoparticle centered in that position, will be polarized along this direction, and consequently the radiation pattern will have a specific feature. As an example, a Near field simulation for the rectangular gold nano particle of length 150 nm and height 100 nm was done at a position of a "deep" in the standing wave, this has been illustrated in figure (2.12), where the incoming field standing field has been removed, i.e. $\mathbf{E} = \mathbf{E}_{Total} - \mathbf{E}_{ESW}$. This nano particle was placed on top of the glass air interface for a wavelength of 600 nm. For the case of ESW_{min} , the Figure (2.12) represents the near Field Intensity. It is observed that the mode excited in that case, is related to an edge mode of the particle with hotspot at the four edges of the particle. A plot of the electric field show the global dipolar character of this mode. We observe two induced dipoles are formed at the edges of the particle that are parallel to the interface and gives the radiation diagram present in Figure (2.13). This figure illustrates well the polarization along the x-direction of the nanoprobe, creating an induced dipole moment that is irradiating in the far field along the z-direction. This is as expected from the dipole radiation above the Air-Glass interface, as illustrated in the beginning of the chapter (see Figure (2.8) and the equations (2.17) and (2.18)) for a dipole parallel to the interface and above the interface.

2.2.3 At the position of the local maximum intensity of the ESW

Similarly, at the position of the maximum of the standing wave, i.e. at the position of the ESW_{max} (refer Figure (2.14)) and eq (2.23) $k_1 x \sin \theta_1 = \pi/2[\pi]$, the local field is given

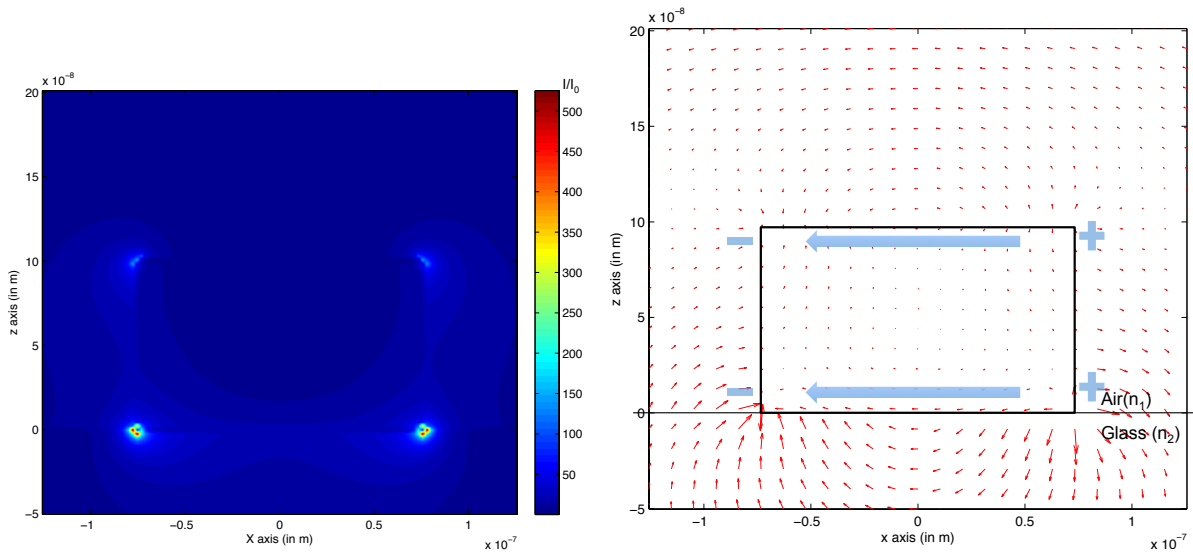


FIGURE 2.12: Intensity (left figure) and Near field (right figure) induced ($\mathbf{E} = \mathbf{E}_{Total} - \mathbf{E}_{ESW}$) by the presence of a rectangular gold NP of length (d) = 150 nm and height (h) = 100 nm at the position of a local minimum in intensity of the ESW at 600 nm.

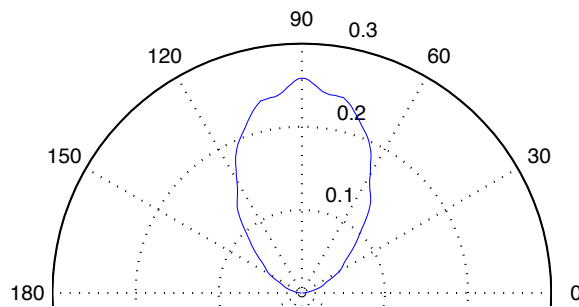


FIGURE 2.13: Radiation pattern of the rectangular gold NP of length (d) = 150 nm and height (h) = 100 nm at the position of a local minimum in intensity of the ESW

by a field purely oriented in the z-direction, as follows

$$\mathbf{E}_{ESW}(x, z, t) = 2e^{-\gamma z} \begin{bmatrix} 0 \\ 0 \\ \pm i E^{(p)} t^p(\theta_1) \tilde{n} \sin \theta_1 \end{bmatrix} e^{i\omega t} \quad (2.30)$$

We observe the creation of a dipolar behavior in the particle that is perpendicular to the interface and gives the radiation diagram (refer to Figure (2.15)). This is as expected from the dipole radiation above the Air-Glass interface, as illustrated in the beginning of the chapter, see Figure (2.8) and the equations for a dipole perpendicular to the interface and above the interface.

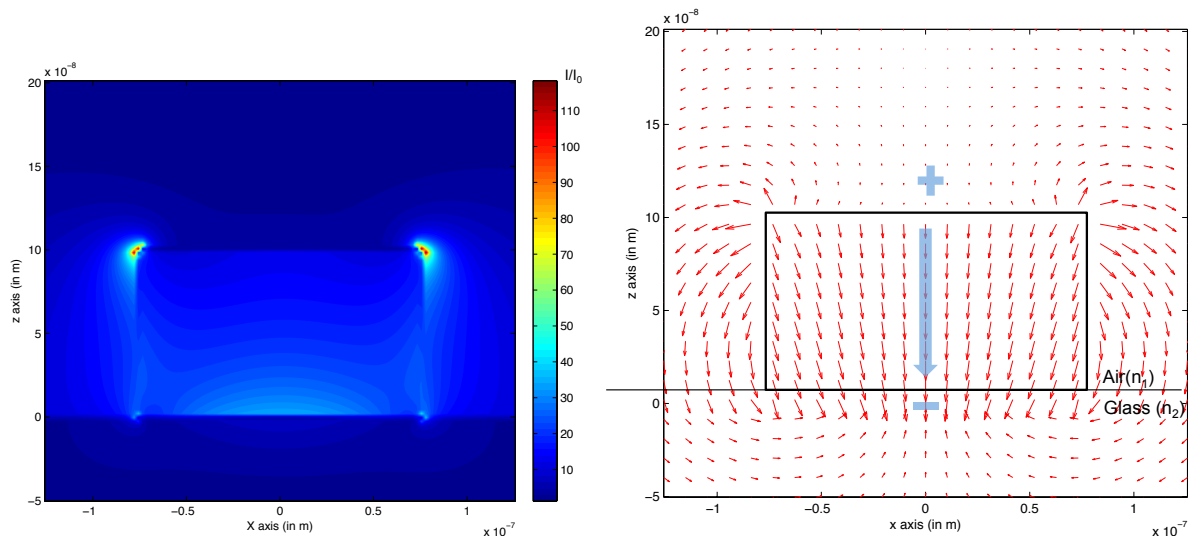


FIGURE 2.14: Near field induced by the presence of a rectangular gold NP of length (d) = 150 nm and height (h) = 100 nm at the position of a local maximum in intensity of the ESW $\mathbf{E} = \mathbf{E}_{Total} - \mathbf{E}_{ESW}$

In ESW_{max} case, the rectangular particle is in an area where the intensity of the ESW is the maximum. The near field intensity of the scattering intensity plot can be seen in Figure (2.14). An angular plot is made to understand the flow of electric field. We observed that an effective induced dipole is formed at the center of the particle. The far field radiation diagram is also present in the Figure (2.15).

While explaining the results of radiation diagrams for particle at positions ESW_{min} and ESW_{max} , the results shows a similarity with the radiation patterns of parallel and perpendicular dipole above a substrate.

2.2.3.1 Spectral dependence of the radiation pattern for a Rectangular Nano-Wire (RNW) 150 nm x 100 nm

Here, we realize calculations for a Gold Rectangular Nano-Wire (RNW) with a base length of 150 nm and height of 100 nm. For each wavelength from 400 to 800 nm, the calculation of maximum intensity that irradiated by a particle in air is performed. This

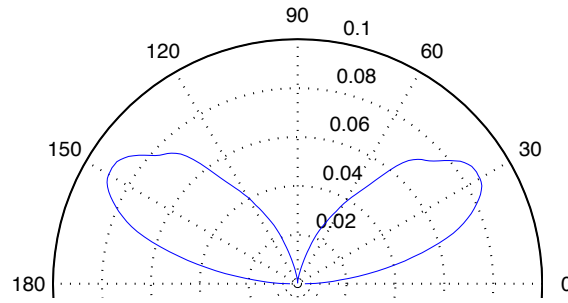


FIGURE 2.15: Constructive interference: Radiation pattern a rectangular gold NP of length (d) = 150 nm and height (h) = 100 nm at the position of a local maximum / minimum in intensity of the ESW $\mathbf{E} = \mathbf{E}_{Total} - \mathbf{E}_{ESW}$

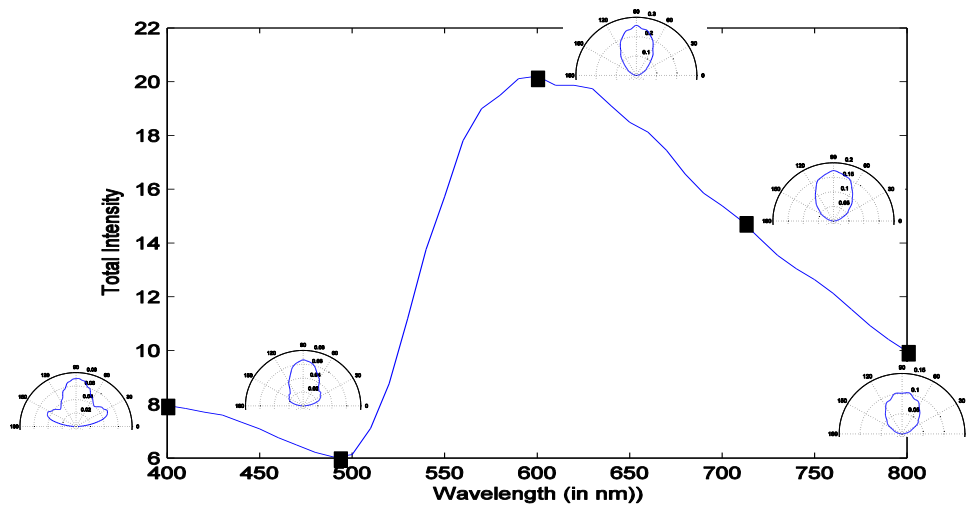


FIGURE 2.16: Radiation Pattern as a function of wavelength for gold rectangular nano-particle of length = 150 nm and height = 100 nm in destructive interference

is done with the help of the radiation diagram. After calculating the radiation diagram (in air), we integrate the values of intensity for each wavelength. The Figure 2.18 shows the plot between the wavelength and total intensity irradiated by the particle in air. This graph (Figure 2.18) is also represents the comparison of total intensity irradiated in air by a particle present in ESW_{min} and ESW_{max} . From Figure (2.16) and (2.17), we observe that the general feature of the radiation pattern is relatively stable as a function of the wavelength. The stability of the radiation pattern for the standing wave is a good news as long as we are looking for an independent extraction of the wavelength. This indicates the origin of the radiation diagram pattern and we see it is mainly coming from the local field direction of the standing wave $\mathbf{E}_{ESW}(x)$ which depends critically on the lateral x -position.

Some distortion are also present in the radiation diagram of Figure (2.16) for destructive configuration when compared to the ideal dipolar radiation pattern above interface. These distortions are observed for wavelength around and below 500 nm, i.e. for a ratio of size to wavelength of $150/500 > 1/4$, which can be interpreted as an

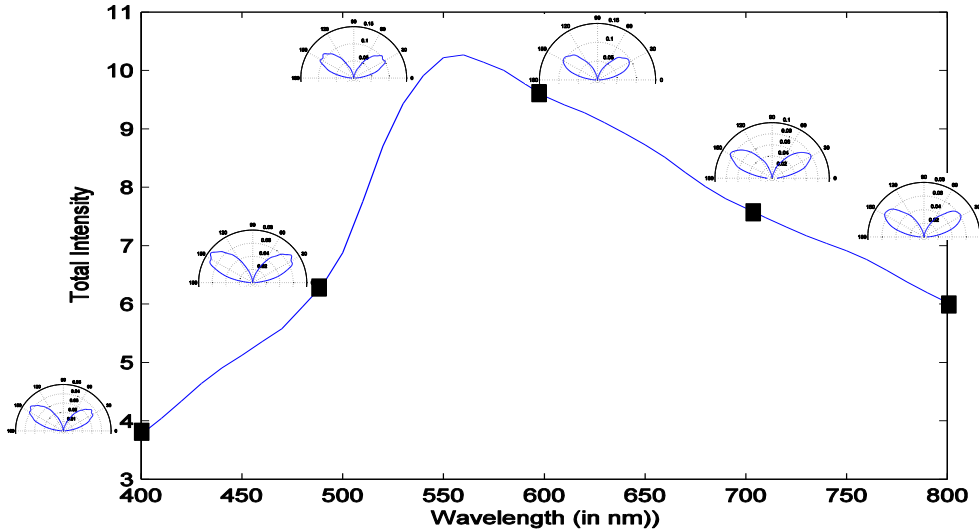


FIGURE 2.17: Radiation Pattern as a function of wavelength for gold rectangular nano-particle of length = 150 nm and height = 100 nm in constructive interference.

effect of the variation of local ESW over the length of the nanoparticle.

With the help of this Figure (2.18), for particle in destructive interference, we observe the least irradiation by this nano-particle is at a wavelength of 490 nm and the maximum is at 600 nm.

For the ESW_{min} , the case that corresponds to the polarization along the x-direction (in length), we observe that there is a red shift of the resonance due to the interaction of nano particle and the substrate. This red shift changes the resonance from 560 to 600 nm, when comparing with same nanoparticle with incoming planewave field in vacuum. Quinten had shown in the case of spheres made up of silver with a radius of 100 nm and placed on the glass [41], he observes a shift in the resonance for effective diffusion cross section. This red-shift for dipolar modes is of similar range of around 25 nm. We should note that the method of calculation presented in the article neglects the modification of polarizability that comes from the interaction of particle and substrate. The calculation method takes into account the excitation due to the evanescent wave and compares its excitation with a plane wave. For example, in the calculation of the cross section, we can observe a very large shift.

As a results, the position of minimum of intensity in the standing wave results in a maximum of radiation in the direction toward the camera. This result is important for the correct analysis of the sampling of the evanescent standing wave. Indeed, it implies that the contrast given by the image camera is the opposite of the one that we sampled.

In any case, we observe that for a very small zone of wavelengths i.e. between 480 and 530 nm, the total intensity irradiated by a particle in air is greater for a nano-particle is present in constructive interference rather than destructive interference. To

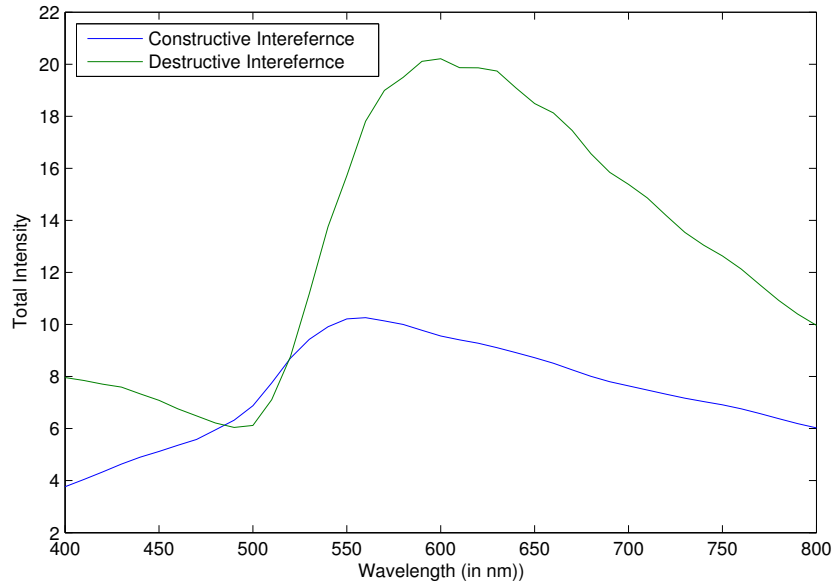


FIGURE 2.18: Total Intensity as a function of wavelength for a nanoparticle of length = 150 nm and height = 100 nm. Comparison of particle in destructive and constructive interference.

remove this disadvantage and to create a system where only ESW_{min} plays an important role, one needs to use lasers between the wavelengths 530 to 800 nm (as per the graph 2.18).

2.3 Conclusion

Initially, a description of working of FDTD has been provided. Theoretical aspects of evanescent waves has been covered. The analytical calculations of evanescent wave scattering in a dipole approximation is covered. Dipole interaction with an interface of air and glass has been explained. This explanation shows how different types of dipole that is s-polarized and p-polarized irradiate the light.

A particle of 150 nm X 100 nm (l X b) could be an ideal choice. For this nano particle, a small study was done to understand the range of wavelengths in which we could use this particle.

This analysis reveal an interesting effect, it is possible to control the local field direction, locally and evanescently at the level of one nanoparticle. Therefore, allowing us to probe the local evanescent response of a nanoparticle as a function of the wavelength and the local polarization direction. For instance, by changing the zero of OPD, we can sample all the local direction, and analyze the absorption, and the radiation direction for a particle on top of a substrate.

Chapter 3

Integration of the Device

Until now the optical integration of CoBiSS was discussed. Now, it is time to discuss about the electronic and software integration.

In this chapter, first of all let me introduce you to why we need electronic integration (3.1) then it is followed by the requirements of all parts are needed to build a prototype of CoBiSS (3.2). A small comparison of devices is done in the section (C) before the final choices to purchase the parts is done.

After, the final parts for the electronic integration were chosen, the final integration process will start (3.3).

3.1 Introduction

As we know these days everything is getting connected. We are moving towards an age where devices that can think or at least take basic decisions on its own and can be deployed wherever needed. These devices need to be robust which can work in any conditions or can be adapted for a specialized environment. These devices need to be small and autonomous which doesn't need any other external devices to work after the device has been deployed.

First of all, electronic integration is a long drawn process which requires us to create a working prototype. The first version of the prototype is generally large in size but made with the parts that are generally present in the market without using too many customized solution. Then later on after the first prototype is validated and tested then further versions of prototype are made when the size is made smaller and at the end only the customized solution is present which is adapted for this specific device.

Here we are generally going to talk about making the first version of the prototype and to test its accuracy. To test this device , we have put a small touch screen which can be used by the user to control the system for specific calculations.

3.2 Requirements

As described in the Introduction of this thesis about the device CoBiSS, we would require products like camera, motherboard along with Lasers specifically for the electronic integration. The exact features that are required by these parts are described in the Table 3.1.

TABLE 3.1: Basic Electronic Integration Requirements

S. NO.	Name of Device	Basic Requirements
1	Camera	<ol style="list-style-type: none"> 1. Works with Linux Operating System 2. Should have USB / LAN connection
2	Laser	<ol style="list-style-type: none"> 1. Small Form factor 2. Works with Linux Operating System 3. Should have USB or GPIO or i2c
3	Motherboard	<ol style="list-style-type: none"> 1. Small Form factor 2. Works with Linux Operating System 3. Should have USB or GPIO for connection 4. Should have Wi-Fi and Ethernet 5. Preferred if it has on-board memory 6. Should be battery operated 7. Preferred if it can be attached to touch screen for demonstration
4	Pressure and Temperature Sensor	<ol style="list-style-type: none"> 1. Small Form factor 2. Works with Linux Operating System 3. Should have USB or GPIO or i2c

Finally, for the purposes of testing and integration the following parts were chosen and they are described in Appendix C. From the list of items chosen, the following were used for the purposes of testing and comparison.

1. Motherboard

- Pandaboard ES
- Udo0 Quad

2. Camera

- The imaging Source - DMM22BUC-ML
- The imaging Source - DMM42BUC-ML
- The imaging Source - DMM72BUC-ML
- FRAMOS -GC 1392 XMB -BL-NM -40
- RSS Supplied Camera

3. Laser

- RGB Laser Systems - MiniLas Evo 785:
- RGB Laser Systems - MiniLas Evo 660:
- Thor Labs - CPS 172 :

3.3 Integration

Now, as the electronic devices / parts for the integration are selected. Using these, we need to integrate every part for it to function unanimously. This will create an fully autonomous device which a user can operate without doing any configurations and going in detail how a device works.

We would start by integrating one part at a time till all the parts can be clubbed together and finally create a GUI for the simple application and for testing. Initially, we start with integrating Laser with the Linux operating system, followed by camera and so on. We have tried to create a small software which can work with all the Linux operating systems and can be compiled for Intel/AMD or ARM boards directly on the boards. This code tries to remove the problem faced during the architecture compatibility.

3.3.1 Laser

Here, a small code was created which is used to control the Laser using USB.

A simple block diagram is described in Figure (3.1) explains how the code when executed can open the USB connection that is present in the motherboard and talk to the USB port.

A flow diagram presented in the Figure (3.2) that explains how the code can start the laser by setting the power output, followed by changing the power as per user needs and finally making the power output as zero and disconnecting it the USB. If the USB is not disconnected and reinitialized each time when the code runs, it can create problems for executing the code as the operating system thinks that the USB connection is always is in use and open even though the code has stopped working.

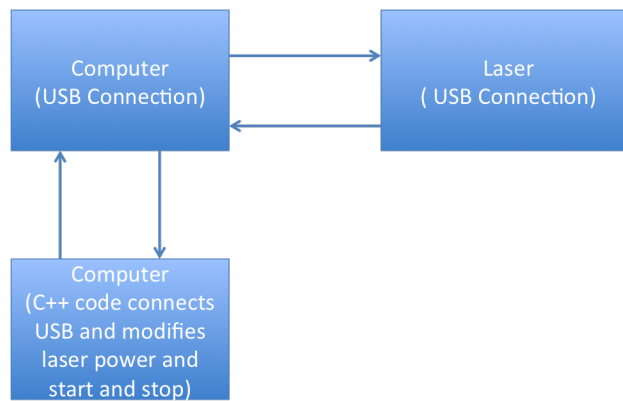


FIGURE 3.1: Block diagram of a code controlling the USB port of motherboard and communicating to a laser

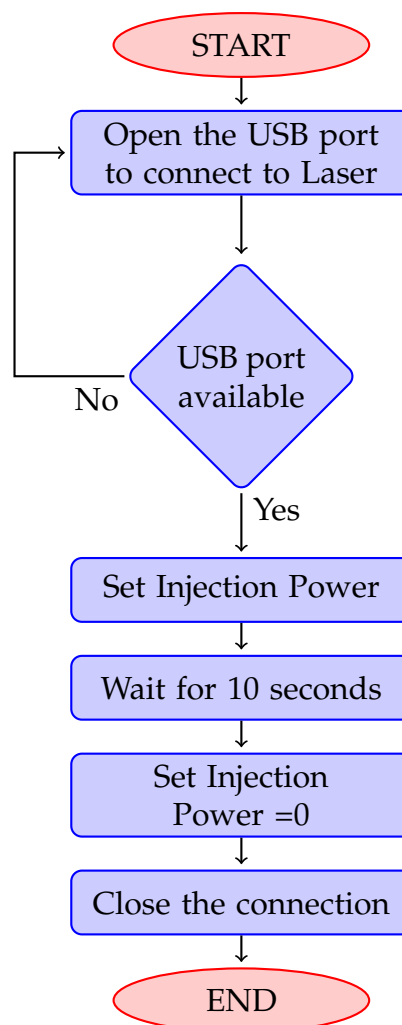


FIGURE 3.2: Flow chart of the code that controls the Laser

3.3.2 Camera

During this portion of integration we create a USB connection with a camera, followed by capturing an image and saving an image. A simple block diagram is described in the Figure (3.3). A flow diagram (refer Figure (3.4)) is also created to show case the exact procedure followed during the coding process.

The usage of an external library known as Video4Linux (v4l) was used. This package is a generic tool which can control most of the cameras present in the industry for the purposes Web Camera (as most of them are embedded in laptops or are USB based for different devices). Most of the packages like OpenCV other development libraries for the purposes of Image Acquisition and processing uses Video4linux as one of the base packages in Linux Operating System.

Here, for saving the images PGM 5 format is used. This image format was chosen as it is the closest format to writing a text document with all the values and it does not need any special encoding procedure or libraries. Using this format, we get unchanged data which was never encoded or compressed as done by other formats. The only drawback is that of the memory used by the system while saving is extremely large when compared to other formats like tiff, jpeg, png.

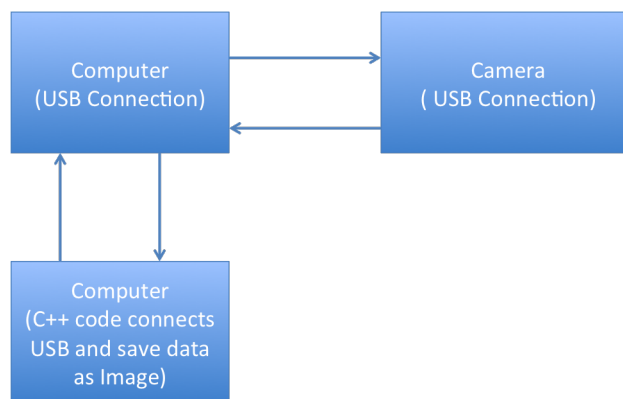


FIGURE 3.3: Block diagram of a code controlling the USB port of motherboard and communicating to a camera and also saving an Image

3.3.3 Controlling Camera and Laser together

The merger of two codes, namely, laser and camera was performed. A simple Integration block diagram is explained in the Figure (3.5).

In this case we first connect the laser then the camera. This is followed by activating / modifying the power output value of the laser. We wait for 5) seconds before starting the image capture from the camera. We wait for some time for the laser to stabilize, in this case 5 seconds. The camera capture of images is implemented and we leave the first two images as the camera also needs to stabilize. Afterwards, the image is saved in the PGM 5 format. This can be showcased in the flow chart presented in the Fig. 3.6

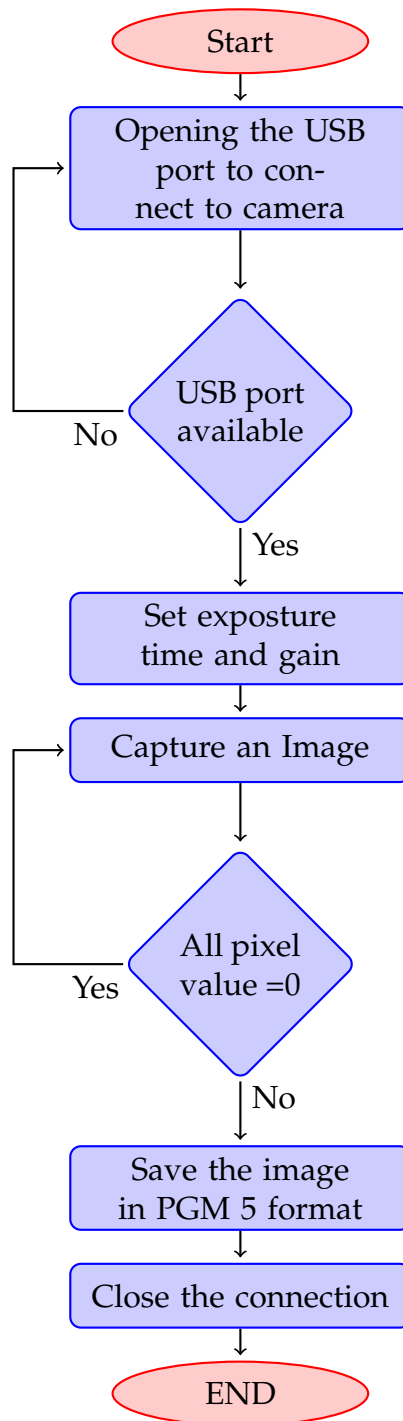


FIGURE 3.4: Flow chart of the code that controls the Camera

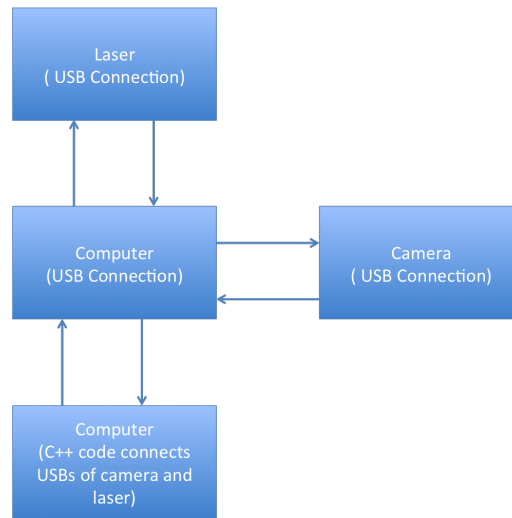


FIGURE 3.5: Block diagram of a code controlling the USB ports of motherboard and communicating to a laser and a camera and also saving an Image from the camera

The image captured using this code is for the configuration of CoBiSS is present on the left side of the Figure (3.8).

This code plays an important role, specially while creating the GUI application and even greater while creating the software for the device that is WiFi enabled and to give the functionality of Wireless sensor in a sensor network. This is the last part of code that is required for physical communication with other devices like camera and laser. Now, It is time to understand the signal and data analysis procedure. It can be showcased in the following sub sections.

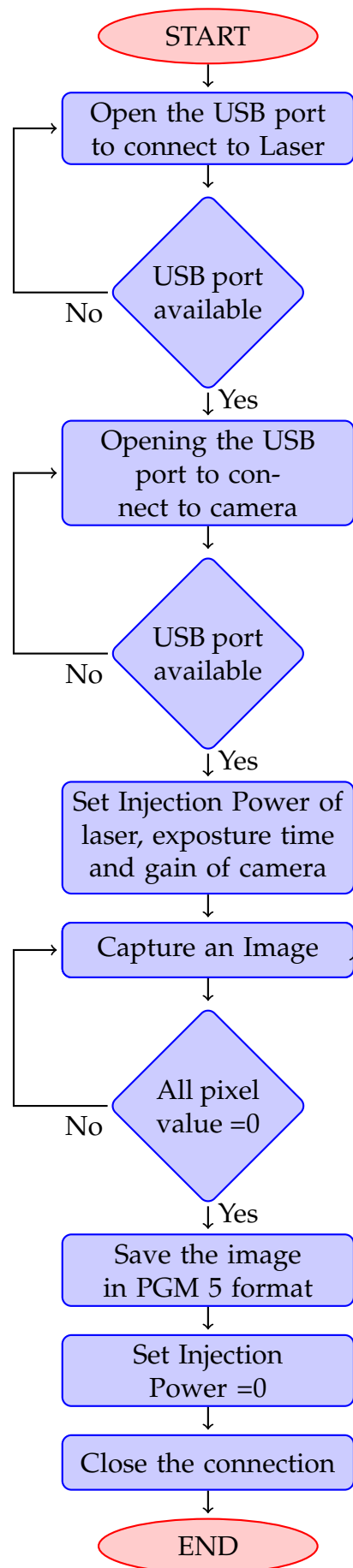


FIGURE 3.6: Flow chart of the code that controls the Laser and Camera together

3.3.4 Lomb Scargle Method

This calculation method is named after the researchers who have perfected a case where normal Fourier transform can not be used. For the Fourier transform to be valid, it requires that all the distance in x and y direction are periodic and have a constant distance. This method deals is used for non periodic transformation. This calculation procedure is based on least square fit of sinusoids to data obtained. This method is highly effective for the data which has a large distribution of noise.

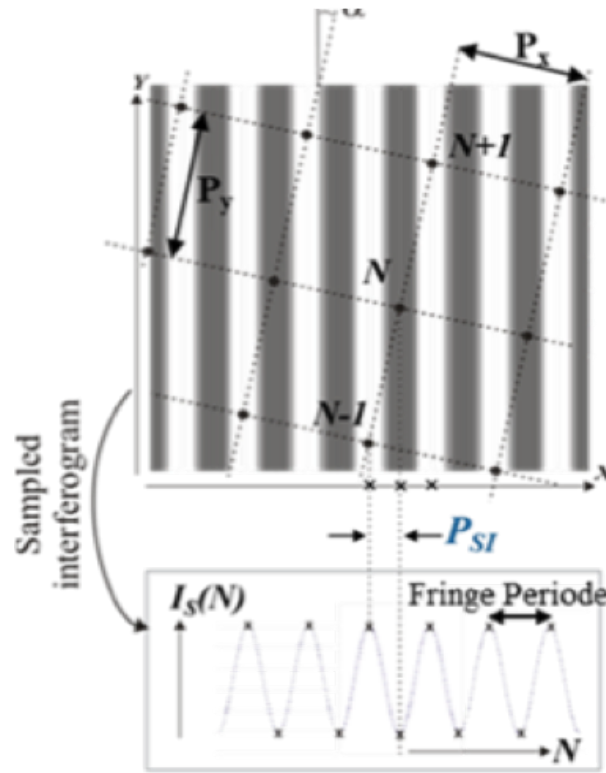


FIGURE 3.7: Conversion of 2D array of nanostructure to 1D

As in our case, we have the evanescent standing wave which interacts with the nano-particles to give the radiation pattern. These evanescent standing waves are sinusoidal in nature can be seen from the sample Figure (3.7). In the case of CoBiSS, the nano particles do not have the same distance between them. The distance in X and Y direction may be the same in their respective directions.

$$\tan 2\omega\tau = \frac{\sum_j \sin 2\omega t_j}{\sum_j \cos 2\omega t_j} \quad (3.1)$$

The calculation formula for the lomb scargle method is given by:

$$P_x(\omega) = \frac{1}{2} \left(\frac{\left[\sum_j X_j \cos \omega(t_j - \tau) \right]^2}{\sum_j \cos^2 \omega(t_j - \tau)} + \frac{\left[\sum_j X_j \sin \omega(t_j - \tau) \right]^2}{\sum_j \sin^2 \omega(t_j - \tau)} \right) \quad (3.2)$$

where, τ = time delay , ω = frequency , t_j = time at a position j, X_j = value of pixel intensity at a point j are the parameters for the calculation.

As we have described the basic formulation, now let us see with an example of image that we received from the microscope which is present in the Figure (3.8). This image is with a laser of wavelength equal to 660 nm in the configuration of CoBiSS with a microscope present with a magnification of 4.

Now using this image, the starting and ending pixels are located from the position 89 to 530 pixel in the x and from 32 to 474 pixel in y- direction, as shown in the Fig (3.8).

As we know that our pattern contains rectangular nano particles of which are 100 in X direction and 100 in Y direction. For this sample calculation they are equally placed at a distance of 1.5 microns. Now, a new matrix is created which uses these edge points to locate the nano particle's position in the image and copies the value of these points into a new matrix.

Using this matrix, the calculation of lomb scargle is performed. This method should give us a wavelength of the laser injected, for our case 660 nm. This calculation gives us the correct result as seen in the Figure (3.8). It means this calculation method is able to detect the wavelength injected from the image.

Please note that this method only works when there is a microscope present but when we tried using the images captured by the camera that was directly placed on top of the particle at a distance of 10 microns, these calculation method failed to give correct results. To eliminate this problem, we found a new method which is explained subsequently.

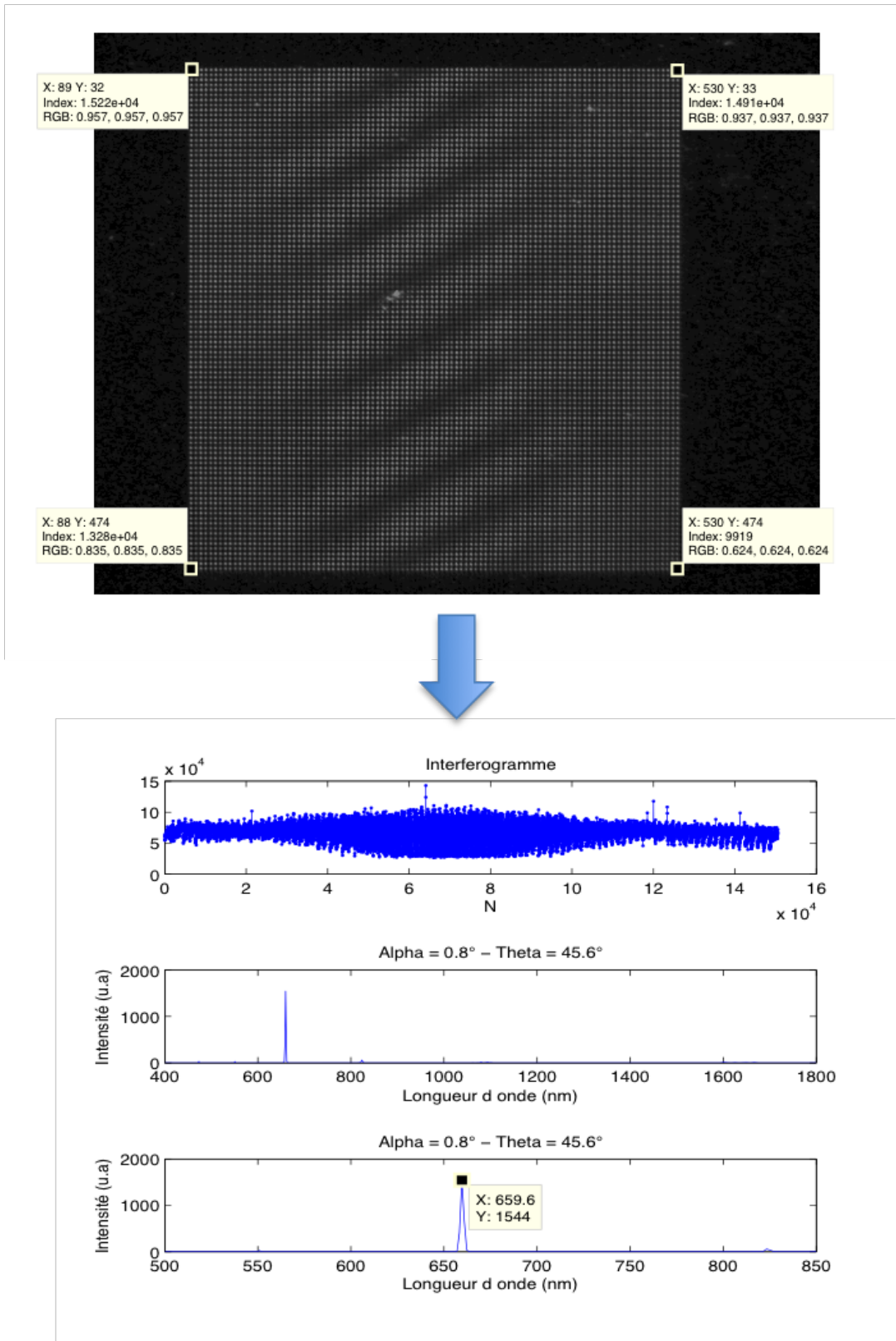


FIGURE 3.8: Calculation of a spectrum (right) using an Image (left) with the help of lomb scargle method. The incident wavelength used was 660 nm.

3.3.5 Calculation using Micro-spectrometer

This calculation method is useful for calculating or determining the wavelength from an image. This method is patented as Evanescent wave microspectrometer (Patent number US 9459149 B2). Presently, we have a very sensitive cameras which have a large number of pixels and the cost of camera CCD or CMOS chips are constantly decreasing. As the number of pixels are increasing, the size of each pixel is decreasing but still it is bigger than the distance between the two nano particles. One can use this method as a method of image processing where it can transform the data of images to micro-spectrometer.

The possible advantages of this method are :

- Price - relatively less as camera are available in a large quantity
- High Resolution - As number of pixels increases, more data can be collected
- Compact
- Configurable - Can be made to process concerned area in an image

The main principle is to functionalize the image (intensity) sensor in order to add a transfer function for each pixel's different spectral variation. Using this method, it is possible to move from the information present in a form of an intensity distribution in space (pixel information) to the wavelength space. This can be obtained by properly calibrating the system and by using an adaptive signal processing techniques.

To understand this method in detail, the data processing elements are explained below: Let us consider a spectrum $\psi(\lambda)$ on any one value on the spectral range $[\lambda_{min}, \lambda_{max}]$ and with a discretization of $\Delta\lambda$. One can decompose $\psi(\lambda)$ on the basis of the functions $\delta_i(\lambda)$, where $\delta_i(\lambda) = 1$ for $\lambda = \lambda_i + \Delta\lambda/2$ otherwise $\delta_i(\lambda) = 0$. The expression can be obtained as,

$$\psi(\lambda) = \sum_i^N a_i \delta_i(\lambda) \quad (3.3)$$

One can also write in the vector form, in the functional space of λ_i

$$[A] = \begin{bmatrix} a_1 \\ \cdot \\ \cdot \\ \cdot \\ a_i \\ \cdot \\ \cdot \\ \cdot \\ a_N \end{bmatrix} \quad (3.4)$$

The signal distribution on the set of pixels can be described by a vector P whose components p_i are the intensities associated with each pixel.

$$[P] = \begin{bmatrix} p_1 \\ \cdot \\ \cdot \\ p_i \\ \cdot \\ \cdot \\ \cdot \\ p_{N_{pixels}} \end{bmatrix} \quad (3.5)$$

Let's recall the transformation function f which links the signal distribution of pixels P to the spectral distribution ψ

$$[P] = f([\psi]) \quad (3.6)$$

As f is a linear transformation through the origin, the relationship in the matrix form becomes,

$$[P] = R[\psi] \quad (3.7)$$

where R is the response of the system. Once when the matrix R is known, with the help of calibration, the measurement of the unknown spectrum $[\psi]$ can be derived from the signal distribution over the pixels $[P]$, after the calculation of the inverse of the matrix R ,

$$[\psi] = R^{-1}[P] \quad (3.8)$$

This method is simple in principle and it works but it has a small problem. The problem is that it is sensible to the noise and may not exactly work.

Hence, to correct this problem and increase the efficiency of this method, one can use the Equation (3.7), and find the least square non negative error as denoted by the Equation (3.9).

$$\epsilon = \min \|R[\psi] - [P]\|^2 \quad (3.9)$$

After understanding this method, let's see some results obtained by this method. A small area where the nano particles are present are illuminated using a laser in CoBiSS configuration. One sees images like the images present on the left side of Figure (3.9)

and (3.10). These two images are taken with the initial wavelength of laser at 782 and 798 nm respectively.

For the calibration purposes, we took the several images in the CoBiSS configuration by varying the wavelength from 752 to 848 nm. The images that were taken had a wavelength difference of 4 nm as the spectral width of laser is 2 nm.

These images were used to define the base comparison wavelength. Two images were taken for those wavelengths where we did not have the base comparison data, for example at 782 nm and 798 nm. After the transformation, the results are shown on the right side of the Figure (3.9) and (3.10). For example, the image obtained from the laser of wavelength at 782 nm gave a peak at 780 nm as the wavelength inserted is between 780 and 784 and the image corresponds well to the calculation. But in this case the image is more inclined towards the wavelength of 780 nm (Figure (3.9)). This might have arisen from the noise or might be the pixel value difference is less for the image with a wavelength of 780 nm. Let's see the second example of the image received by the laser at 798 nm. Here, one sees the wavelengths are almost equally distributed between 796 and 800 nm. This result can be symbolized as an almost ideal result. Here, the ideal result means that the wavelength distribution between 796 and 800 nm should have the correction index as 0.5 and 0.5 .

3.3.6 Calculation Robustness

In the previous subsection 3.3.5, one see that the calculation of Micro Spectrometer works correctly. While exploring the limits of the work, we found that the calculation depends on Intensity of the pixels. This creates a problem as we would like to find the wavelength of any laser without having to bother about the power injected by the laser. This method will work till the camera pixels are not saturated by the power of laser and till we are working the operational wavelength of the system.

In this method first we normalize all the intensities of the pixels in the area of interest. This means that we select the area which we will be using for Micro Spectrometer calculations and normalize the same.

To normalize the intensities, we would require maximum (I_{Max}) and minimum (I_{Min}) intensity in the area of interest and the equation for normalizing each pixel in the area of interest will be :

$$I_{Normalized} = \frac{I_{Pixel} - I_{Min}}{I_{Max} - I_{Min}} \quad (3.10)$$

After normalization and saving all the normalized intensity values in the database, we can do the same for doing measurement calculations. For measurement calculations, we can inject any laser which has intensity less than the threshold of camera and in the operating region. When this new laser gives us an image, we first select

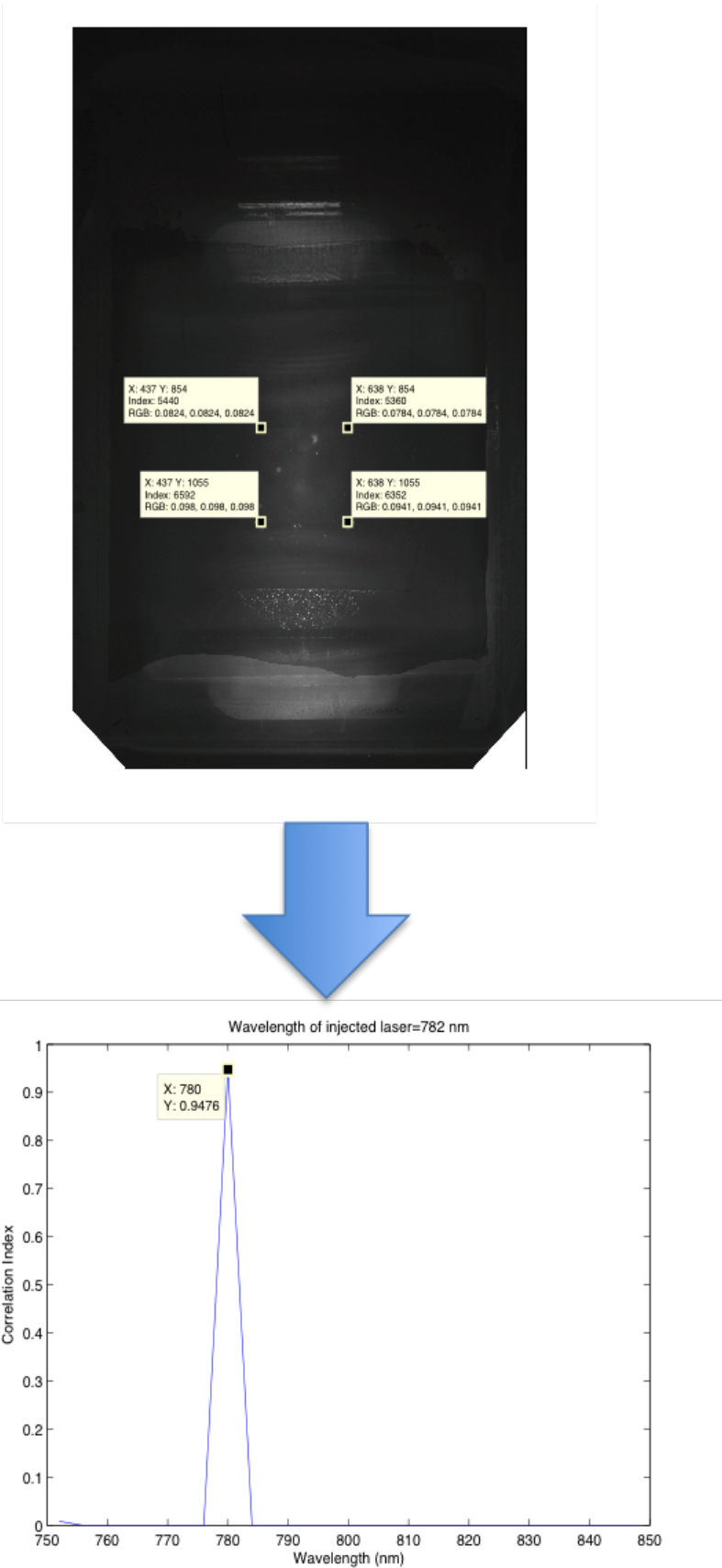


FIGURE 3.9: Initial Graphical User Interface image when the software is started.

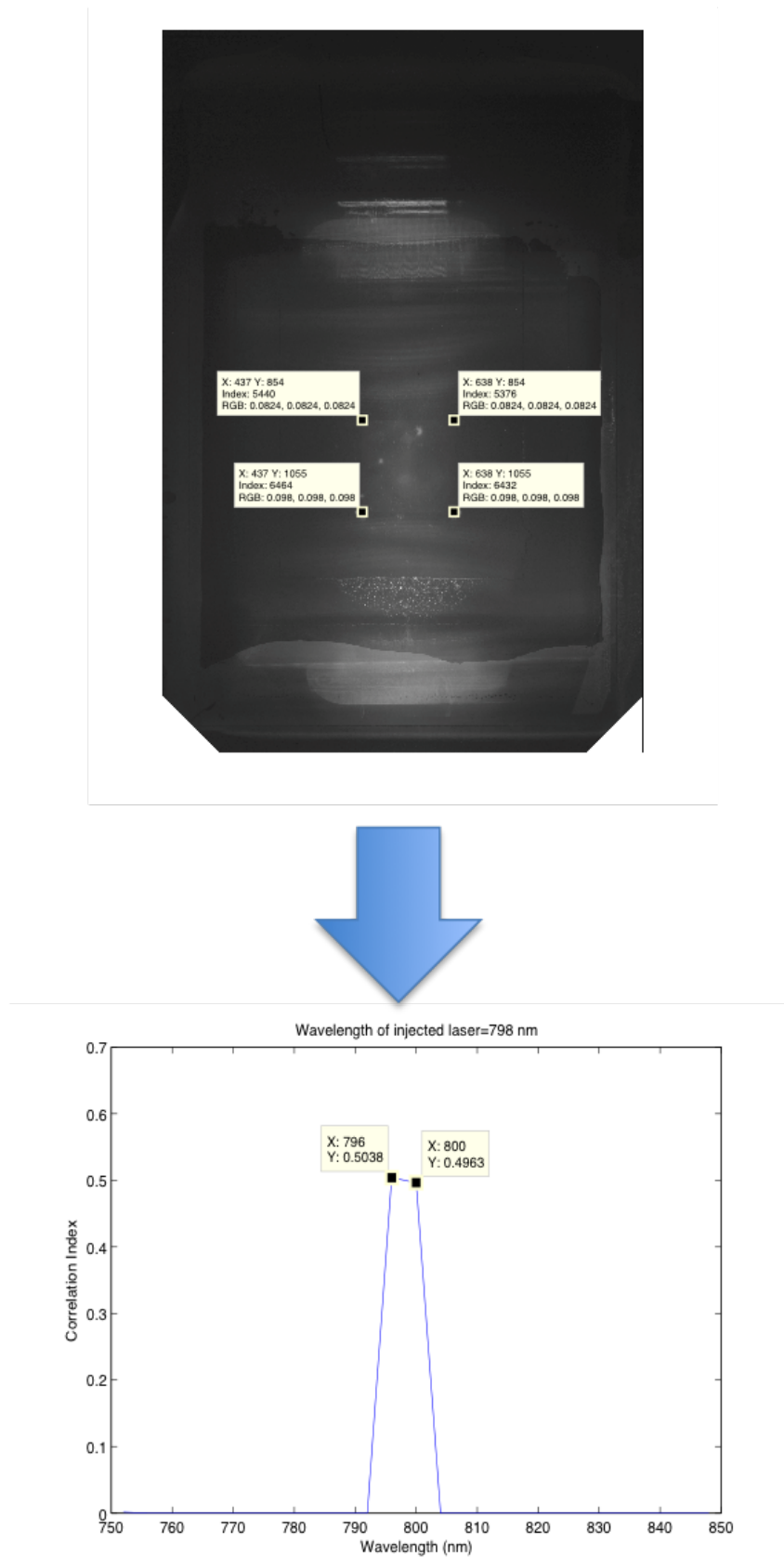


FIGURE 3.10: Initial Graphical User Interface image when the software is started.

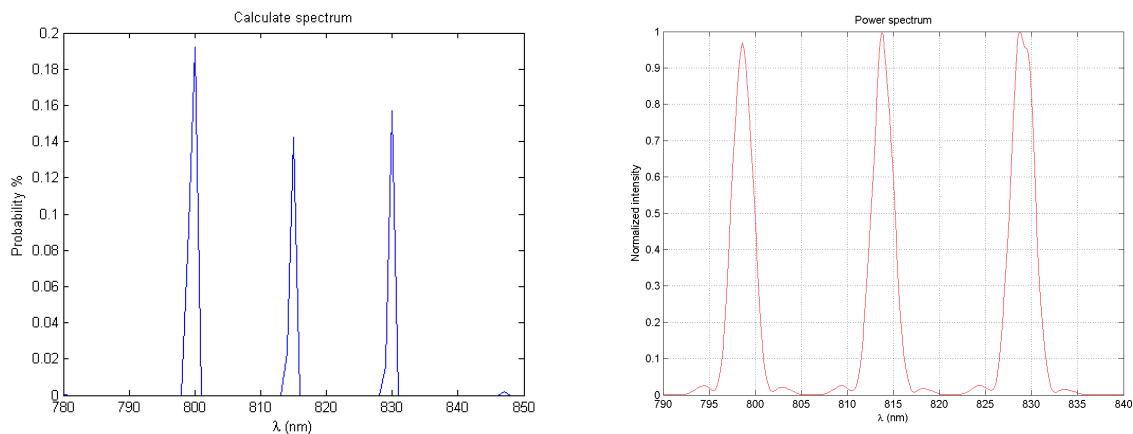
the region of interest and normalize the same before proceeding to Micro Spectrometer calculation.

We have tested our calculations by doing this change and we are able to correctly determine the wavelength without worrying about the power injected by the laser.

3.3.7 Calculation of Multiple wavelengths

In the previous subsection 3.3.5, one see that the calculation of Micro Spectrometer works correctly. In the previous cases, the calculations are done for a single laser that has been transmitted. Now, some tests were preformed by passing multiple lasers wavelength along with different or same intensities.

To start we took one of the the simplest cases where we have three different wavelengths with the same wavelength as can be seen from the image of spectral analysis present in the Figure (3.11b). When this combination is passed through CoBiSS and the image is analyzed with the help of Micro spectrometer method the results obtained are seen in the Figure (3.11a).



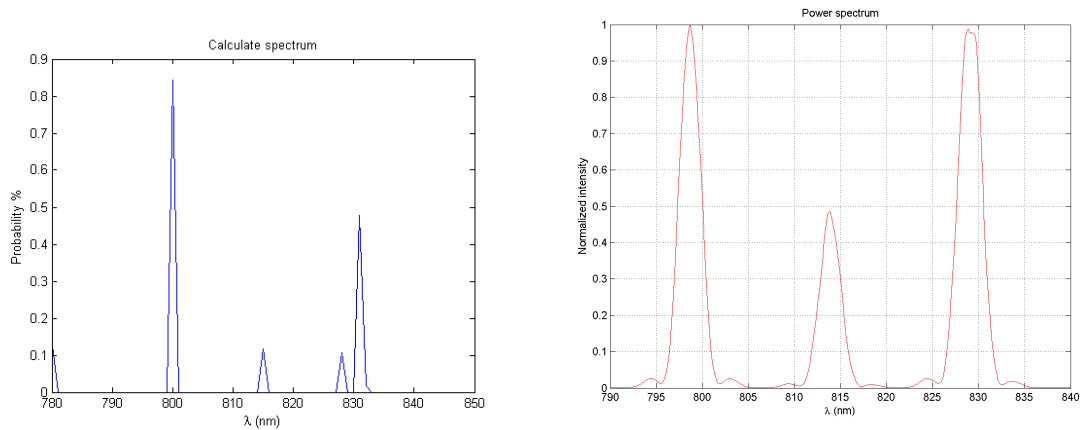
(A) 3 different Laser wavelengths as calculated (B) 3 different Laser wavelengths as viewed by a commercial spectrometer.

FIGURE 3.11: Graph showing the efficiency of Micro spectrometer method when used with CoBiSS as compared to the spectral analyzer

Here, we see that the Micro spectrometer method has given an accurate result in terms of finding the wavelength but not the amount of intensity.

In another experimental result, we kept the same three wavelengths but we changed the intensity of the middle wavelength to 50 % as compared to the other two wavelengths. This can be seen from the Figure (3.13b). We again passed these wavelengths through the CoBiSS spectrometer and the results found by it is shown in the Figure (3.12a).

Here, we again see that the Micro spectrometer method has given a result which shows the three wavelengths but it has also given a residual error wavelength. With

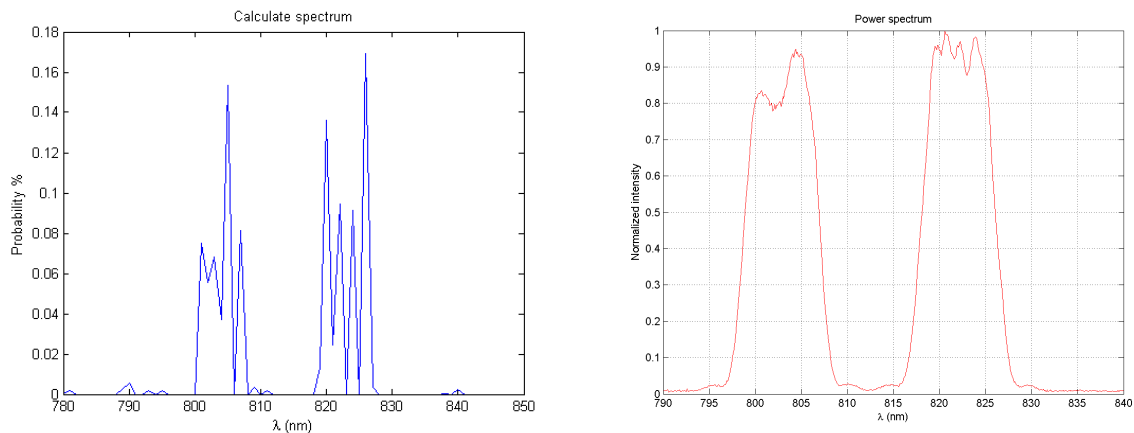


(A) 3 different Laser wavelengths as calculated by Micro-spectrometer Method (B) 3 different Laser wavelengths as viewed by a commercial spectrometer.

FIGURE 3.12: Graph showing the efficiency of Micro spectrometer method when used with CoBiSS as compared to the commercial spectrometer

this result we again see that the wavelength can be found easily but not the amount of intensity.

In the third case of experimental setup we created 2 large band lasers and that can be seen in the figure (3.13b). We passed this laser in CoBiSS spectrometer and found to give us a result as shown in Figure (3.13a).



(A) 2 large band different Laser wavelengths as calculated by Micro-spectrometer Method (B) 2 large band different Laser as viewed by a commercial spectrometer.

FIGURE 3.13: Graph showing the efficiency of Micro spectrometer method when used with CoBiSS as compared to the commercial spectrometer

Here, we again see that the Micro spectrometer method has given a result which shows the 2 multiple large band wavelengths along with featuring multiple individual wavelengths in a large band spectrum and we also see small errors in wavelength. With this result we again see that the wavelength can be found easily but not the amount of intensity.

3.3.8 Graphical User Interface

Till now, you have read about the development of interfaces of laser, camera and also the image and signal processing techniques.

Here, all the different developments are clubbed together to form a small Graphical Software which can be used for testing and seeing the result at the same time rather than running different codes. It is created for ease of use for everyone and should not just be limited for computer experts.

Block diagram of the code is present in the Figure (3.14) but the explanation of how this software works (refer to Figures (3.15) and (3.16)) is explained in the following points :

- **Start Screen** : This is the first screen that one sees when the application is started (see Figure (3.15)). On the top we see all the buttons that can be used in the application while working it. On the left we have a blank screen where the images will be shown in real time from the capture of images by camera and on the right side, one can use it to see the interferogram calculation. When the device (pandaboard) is started, the operating system is modified to directly open this application by default.
- **Start Button** : As soon as this button is clicked, the code executes the command to start the laser and the camera. As the camera and laser, both, are placed in 2 different USB ports, each having unique ids. Both, USB ports are opened one after the other and the initial configurations are applied. (described in previous sections). The only modification, here, is that the camera does not stop until the user desires it. The images come in real time for the purposes of visualization to the left side of the screen (refer Figure (3.16)). These sets of incoming images can be used for configuring and setting up of the devices. This button gets deactivated so that it cannot be clicked again by mistake but it activates the Stop button.
- **Stop Button** : After this button is clicked, the code closes the camera and laser and also closes the USB connections for these devices. Here, the image that is seen on the left hand side of the screen (refer Figure (3.16)) is saved in the memory for further calculations, if required. After this code is executed the Stop button will deactivate itself and Start button gets activated for further use.
- **Upload Button** : A sample image that was obtained from CoBiSS configuration is saved for testing the code of Lomb scargle. This button was created for programming purposes as sometimes, it was not possible to test the real setup. When this button is clicked, it checks if the camera and laser are active or not. If they are on then it calls the function that deals with Stop button first and then it reads

and writes all the information (pixel data) on the same variable that was used for talking live images (from integrated camera). The image is displayed on the left side of the screen (refer Figure (3.16)). If this button is clicked then the image data which was saved after the end of Stop button will be erased.

- **Graph Button** : This button is only activated when there is an image present on the left side of the screen (refer Figure (3.16)). When this button is clicked, it takes the matrix / image that is present on the left side of screen and uses it for image / signal processing. The result of the image / signal processing is displayed as a graph of interference pattern. Here, the X axis is the wavelengths (zone of calculation) and y axis has an arbitrary value of Intensity. This value depends on the code used, as for Micro-spectrometer calculation the maximum value is 1.
- **Save Button** : When this button is clicked, it gives a menu to a user to select if they want to save the image captured or the graph plotted or both. If one selects image captured or graph then it gives the user an option to enter the name of the file using the touch screen panel by activating the touch keyboard. It also gives the option of format for the images to be saved as text file for values only or PNG image. When both are selected then one needs to enter 2 names for image and for the graph to be saved respectively.
- **New Button** : When this button is clicked, it checks if laser and camera are on or off. If they are on, then it calls the close button function and then finally the start screen function. It is used to clear all the data present on the screen. It makes the application look like it has just started.
- **Exit Button** : This button is used to close the application. The code is modified for the touch screen device, where , it doesn't just close the application but also turns off the device (Pandaboard).

Please note that the software is adapted for the size of the tablet screen of 7 inches (800 X 600 pixels) and made to work with touch screen. All the essential buttons are modified to suit the size of the finger tips as the software is used with an touch screen interface.

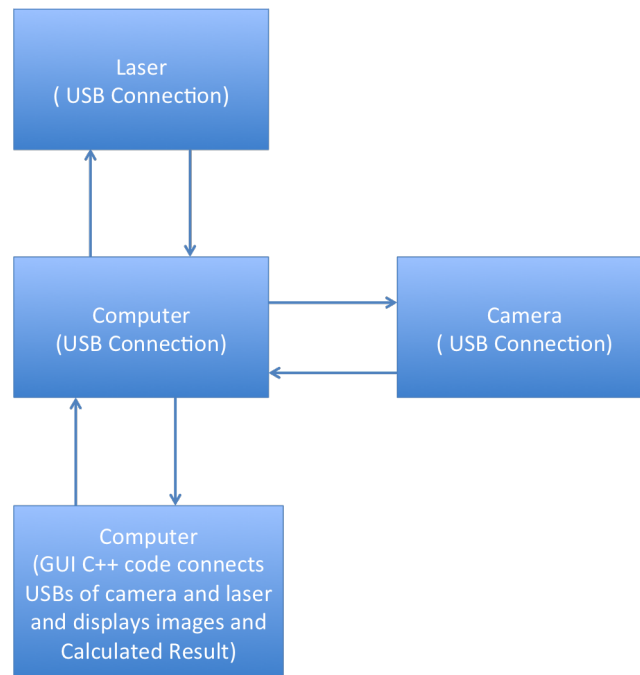


FIGURE 3.14: Block diagram of a Graphical User Interface code controlling the USB ports of motherboard and communicating to a laser and camera and also displaying an Image

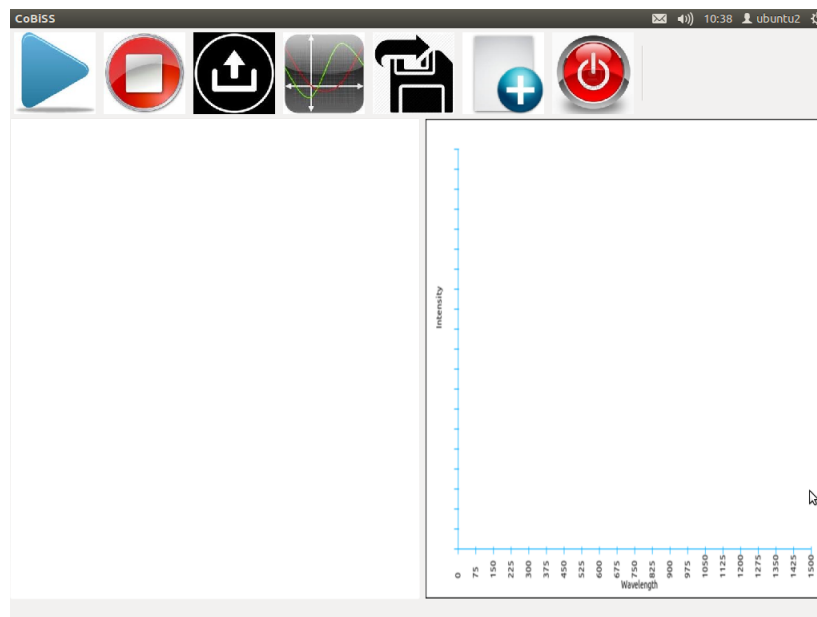


FIGURE 3.15: Initial Graphical User Interface image when the software is started.

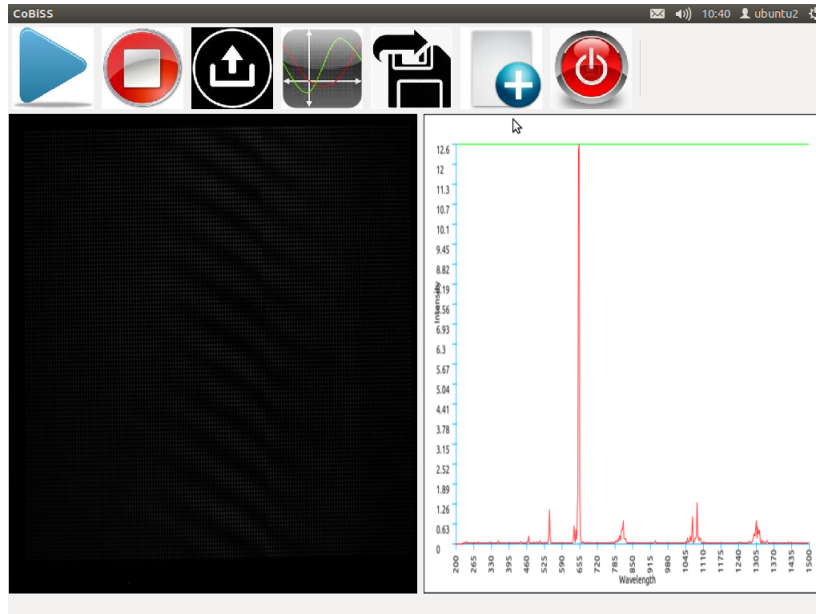


FIGURE 3.16: Graphical User Interface image when the calculation of an image is performed to give the wavelength-intensity spectrum using Lomb Scargle Calculation.

3.3.9 Motherboard

In the previous subsections we have created all the codes for development and deployment, now its time to make the ARM motherboard ready for the same.

The integration of motherboard is divided into the following parts:

- Installation of Linux Operating System for the Development board (Present in Appendix D).
- Installation of Linux Operating System for the Deployment.
- Installation of necessary packages for the development / deployment of the software created.

3.3.9.1 OS Installation for the Deployment board

The following are the steps for the installation of chipsee modified Ubuntu 2011.04 :

- Copy all the files present in the CD provided by them into a folder. for example create a new folder named "chipsee-cd" at the location "root" or "/" in linux.
- Insert the SD MMC card on the Linux computer. As new Linux operating System uses the block location "/dev/mmcblk0"
- As new Linux operating system after 2012 have changed the nomenclature of the partitions of their devices like hard disk, SD MMC card etc. It is required to edit the script file provided by chipsee named "mkscard.sh". In this script file, one

needs to modify the following

```
${device}1 to ${device}p1 and similarly other places like  
${device}2 to ${device}p2 .
```

- For copying the files to the SD MMC card use the following commands:

```
$cd /chipsee-cd$sudo chmod +x mkcard.sh$sudo ./mkcard.sh  
--device /dev/mmcblk0
```

Now the SD MMC card is ready to install ubuntu on the Pandaboard with the touch screen of Chipsee.

3.3.9.2 Code Compilation methods

The required libraries are needed to be installed on pandaboard to make the GUI and to run all the features like controlling the camera, saving the png file and so on.

```
$sudo apt-get update
```

```
$sudo apt-get build-essential v4l-utils libwxgtk2.8-dev libwxgtk2.8-dbg  
lib png-dev
```

3.4 Conclusion

In this chapter, we have tried to integrate the optical portion with the electronics devices and along with controlling and computing device. We have compared different types of cameras, lasers and motherboards available in the market. Using this comparison, we have chosen a few devices that were used in the electronic integration. Using the chosen devices, the computing part was coded to control and get input data from different devices like camera and laser. As we chose Pandaboard as motherboard (computing hardware), a small instruction set is also been provided for the installation of Ubuntu OS.

In the computational part, we have discussed the Lomb Scargle method and also Micro Spectrometer method for calculation of wavelength from an image. We have integrated this code in the computational part just after a control and image recovery instruction set.

A GUI was created on top of this code for ease of use and to show data in real time. This helped in creating a stand alone device that can be used by anyone.

Chapter 4

Detection through SPR and LSPR

In the previous chapter, we have integrated a device to form a CoBiSS spectrometer. In this chapter, we will add the capability of sensing with the help of the Surface Plasmon Resonance (SPR) to the CoBiSS spectrometer, where this device will enable us to measure the concentration of a type of liquid or gas or to detect chemical agents [70]. This will depend on the functionalization performed. The functionalization can be performed with the help of Polyethylene glycol films [71], Teflon films [70, 72], Tungsten trioxide [73, 74] and others [70]. SPR is widely used technique in the field of biomedical [75] where the testing for the gases and bio-molecules are performed. Some analytes that can be tested in Gaseous and liquid states like Carbon Dioxide (CO_2) [76, 77], Heavy Metal ions (Pb_2^+) [70, 78, 79], Methane (CH_4) [71, 80], Alcohol [71], Bacterias [81] and so on. In this work, the detection of chemical agents that are present in air takes priority and will be working on exploring this area as a wireless device could be made to detect environmental pollution. First of all, let us understand how this detection can be done using CoBiSS. As you can see in the Figure (4.1), a gold slab is present on the left side of the prism. The light beam coming from the left side interacts with the gold (functionalized) layer creating attenuated Total Internal Reflection at the interface of prism and gold slab. This light after the interaction with Gold slab gets modified and this modified light is passed to the top surface of the prism. This modified light interacts with the light source coming from the right hand side and gives us a modified standing wave. This wave will have a different phase and also the intensity when compared to a non gold (functionalized) slab present interferogram (refer to Figure (4.2) [87] as an example). As we use multiple wavelengths, data collected will give the exact wavelength where the slab and prism are resonant. The data that is collected is taken as a base reference.

Using this Functionalized Gold Layer, we add a small amount of liquid (refer to Figure (4.2C) [87] as an example). The new interferogram that we obtain has shifted a small amount. We take the difference of interferograms, that is, with and without the liquid and this difference (shift) helps us to reverse calculate the concentration and molecules present in the liquid. A specific molecule has a specific shift in the interferogram.

Before going into detail, the main aim of this work is to compare the reflectance

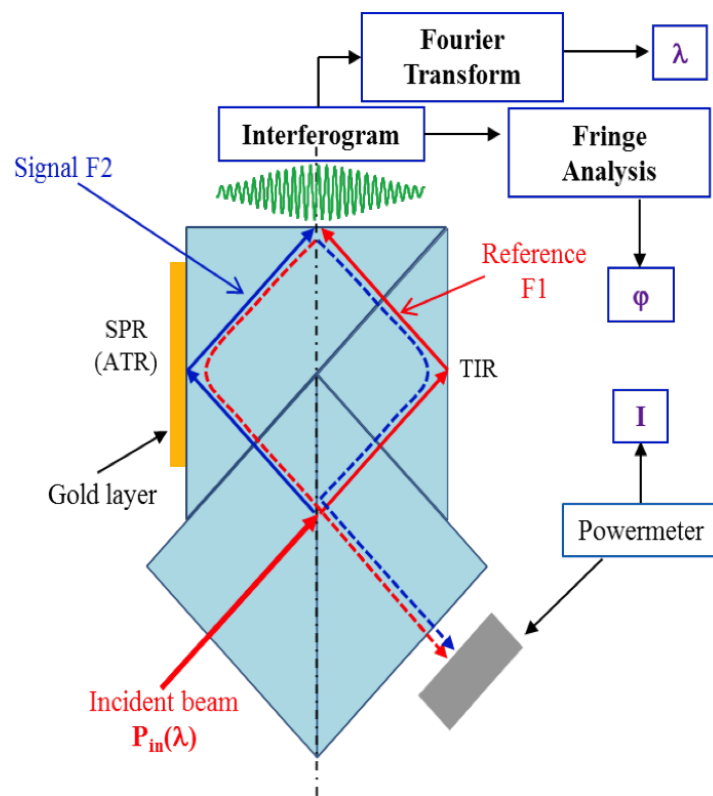


FIGURE 4.1: CoBiSS modified for the Detection of SPR

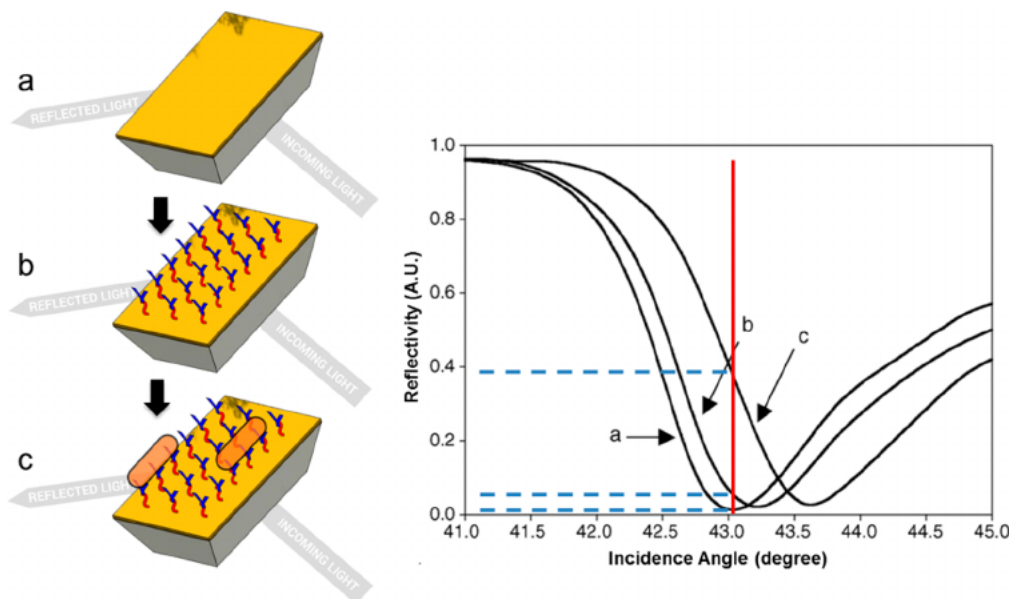


FIGURE 4.2: Shift of Resonance from the initial state to functionalized Gold Layer and ultimately when an analyte interacts with the functionalized Gold Layer

of a gold slab with another structure to determine the best suited structure for the integration with the device. In our case the other structure is shaped as a W with curve endings and for this reason we will call this structure as "W" structure. First of all a gold slab is taken and simulations are done to find the most optimum thickness, that is, the thickness of the gold slab at which the minimum reflectance is present. Later, a few parameters are varied to calculate the dimensional values of the W structure. This was necessary to do as the gold slab has only one variable that is thickness whereas in the "W" structure one can also vary angle of the structure, distance between the 2 ends, etc. The W structure gives more parameters for optimization.

With the optimized dimensions of the two structures the sensitivity analysis for Large spectrum laser and single wavelength laser are performed and compared. To start with the basic concepts of Surface Plasmons, LSPR along with sensitivity is explained in the Introduction.

4.1 Introduction

Surface Plasmons were discovered by R.W. Wood in 1902, who observed some anomalies while performing an experiment on diffraction grating. There was an anomaly with the reflectivity spectrum [88]. At that time the analytical analysis was not that developed and this problem had no solution. Later U. Fano, after forty years, proposed a new solution with an explanation using vectorial calculus for the diffraction. He explained that surface waves moves along the length of the metallic grating [89].

In the year 1957, Ritchie [90] first introduced the notion of surface plasmons where one could guide light at the interface of a metal and dielectric medium. Later in 1965, while working on the anomalies stated by Wood, A. Hassel and A. Oliner proposed a notion of resonance and amplification of fields between the incident light and the surface plasmons. In the year 1968, a new technique to excite the surface plasmons was developed and it used the total internal reflection.

For our calculations, the permittivity value (ϵ_{Gold}) of gold is represented by ($\epsilon_1 + i\epsilon_2$). The permittivity value of Gold is taken from Lumerical's FDTD Solution's material database with the help of the function `getfddtdindex()` [91, 92]. The permittivity values of Gold is plotted in the Figure (4.3).

To understand this in detail, surface plasmons and localized surface plasmons are introduced.

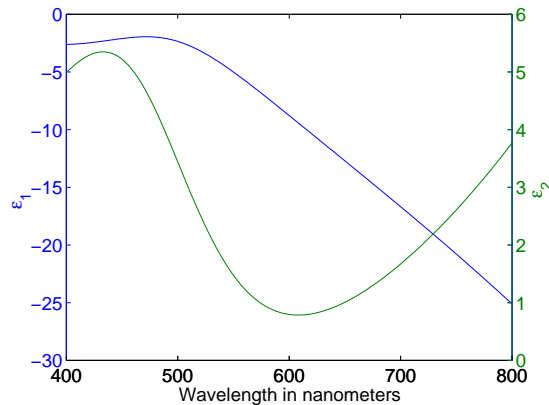


FIGURE 4.3: Epsilon value of Gold is plotted from the values present in the Lumerical's FDTD software for Gold (Johnson and Christy) with the help of function `getfddindex`.

4.1.1 Surface Plasmons

Surface Plasmons are surface electromagnetic modes propagating at the interface between a dielectric and a conducting material, evanescently confined in the perpendicular direction. These waves result in the oscillations of electrons at the interface of the metallic medium resulting in a wave shown in Figure (4.4) [93]. Depending on their wavelength, it depends on the proper frequency between $\omega = 0$ and $\omega = \frac{\omega_p}{\sqrt{1+\epsilon_d}}$.

4.1.2 Local Surface Plasmons

Localized plasmons are non propagating excitations of the conducting electrons of metallic nanostructures that are coupled to the electromagnetic field. Localized surface plasmons are surface electromagnetic modes associated to the collective oscillations of the conducting electrons at the boundaries of Metallic Nano-Particles (MNPs) [94]. These modes can be excited from the scattering problem of the subwavelength conductive particle in an oscillating electromagnetic.

For instance in the case of a metallic spheroid particle, the curved finite shape exerts a restoring force of the driven electrons and is represented by the particle polarizability

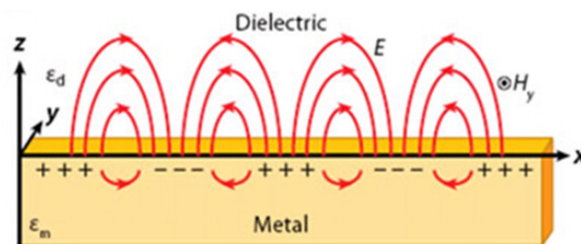


FIGURE 4.4: Illustration of Surface Plasmons wave, taken from [93].

(in quasi-static approximation) as follows

$$\alpha = \frac{\epsilon_{in} - \epsilon_{ext}}{\epsilon_{in} + L(\epsilon_{in} - \epsilon_{ext})} \quad (4.1)$$

where ϵ_{in} is permittivity of metallic particle, ϵ_{ext} is represented as permittivity of the medium, L is depolarization factor which is represented for this particle geometry by[106]:

$$L = \frac{abc}{2} \int_0^\infty \frac{ds}{(s + r_n^2) \sqrt{(s + a^2)(s + b^2)(s + c^2)}} \quad (4.2)$$

Where, a, b, c are the radius / length of the particle along x, y, z axis and r_n is the radius / length of the particle along a selected axis. This leads to resonance that arises from the dielectric constant of the medium. Finally, leading to a field amplification inside the particle and in the near-field zone outside of it. This can be seen from the Figure (4.5)

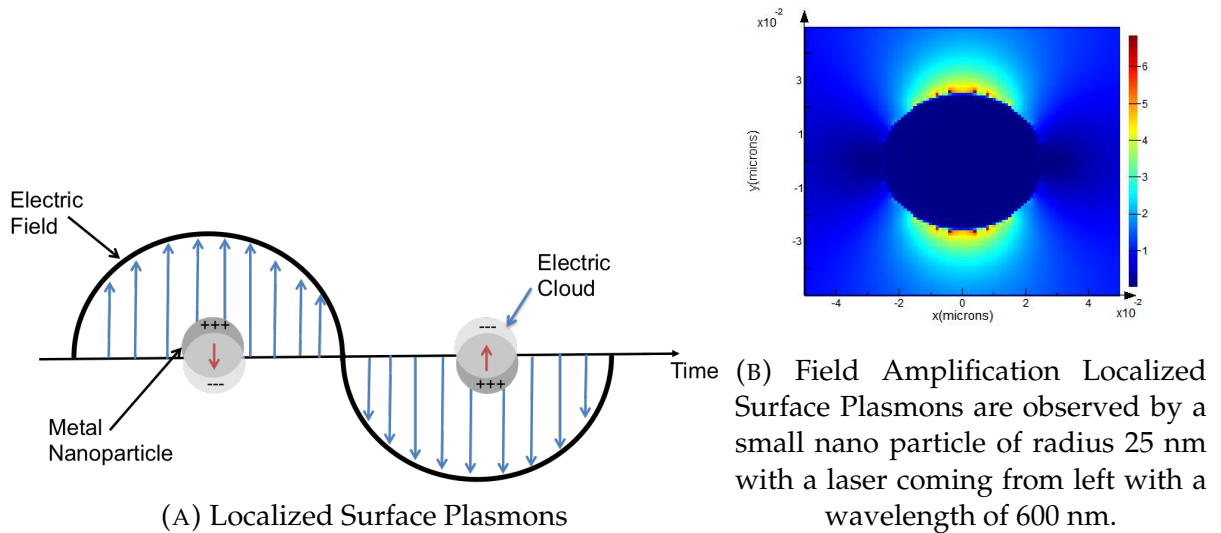


FIGURE 4.5: Localized Surface Plasmons and Field amplification in and around the near Field of the Nanoparticle

From the eq. (4.1), it is clear that the resonance comes from the cancellation of the denominator of the polarizability, i.e.

$$\epsilon_{ext}(\lambda) = \frac{L + 1}{L} \epsilon_{in}(\lambda) \quad (4.3)$$

it becomes clear that the resonance wavelength of the LSP is highly dependent on the geometry of the particle, as well as the refractive index of the surrounding medium. Furthermore, LSP modes provide a highly confined electromagnetic field that can be used to probe a very small volume of matter [95] and also can be applied in optical sensing devices [103].

4.1.3 Coupling of Light and Surface Plasmons

Presently, there are mainly two different methods to couple incoming plane wave with surface Plasmons namely:

- Kretschmann Raether configuration
- Coupling using Diffraction Grating

In this chapter, our interest lies in creating a SPR sensor using CoBiSS (refer Figure (4.1)). For this purpose, the coupling of Light using Total Internal Reflection is only discussed below.

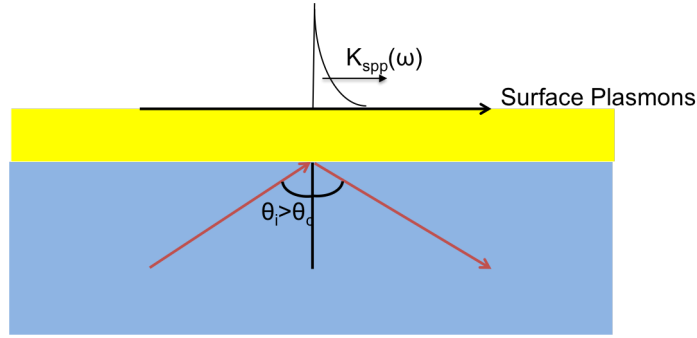


FIGURE 4.6: Coupling of light and surface Plasmons using attenuation of Total Internal Reflection

Today, Kretschmann Raether configuration is the most employed method for exciting the Surface Plasmons. This method was experimentally proven in the year 1968, when A. Otto, and also, E. Kretschmann along with H. Raether created their first coupling devices using Total Internal Reflection. Figure (4.6) shows the setup of coupling in Total Internal Reflection. In this geometry, the guided plane wave and the coupling of Surface plasmons is assured. This is due to the fact that the evanescent wave vector $k_x = \frac{\omega}{c} \sqrt{\epsilon_p} \sin \theta$ created at the upper interface can match the propagating surface plasmon polariton wave vector $k_x^{SPP} = \frac{\omega}{c} Re \left(\sqrt{\frac{\epsilon_d \epsilon_m}{\epsilon_d + \epsilon_m}} \right)$, see Figure (4.6). The incident wave has created an evanescent wave at the surface of metal. This evanescent wave is used for the coupling with surface plasmons. This can be understood by taking the general form of the wave equation [109]. This is described as:

$$\nabla \times (\mathbf{E}) = -\frac{\partial \mathbf{B}}{\partial t} \quad (4.4)$$

$$\nabla \times (\mathbf{H}) = \mathbf{J} + \frac{\partial \mathbf{D}}{\partial t} \quad (4.5)$$

$$\nabla \cdot (\mathbf{D}) = \rho \quad (4.6)$$

$$\nabla \cdot (\mathbf{B}) = 0 \quad (4.7)$$

where, \mathbf{E} is electric field, \mathbf{B} is magnetic field and $\mathbf{H}, \mathbf{J}, \mathbf{D}$ corresponds to magnetic field in the material, electric current density and electrical displacement, respectively and ρ permits us to take into account the free electrical charge density.

Further some more basic relations,

$$\mathbf{B} = \mu_0 \mu_r \mathbf{H} \quad (4.8)$$

$$\mathbf{D} = \epsilon_0 \epsilon_r \mathbf{E} \quad (4.9)$$

$$\mathbf{J} = \sigma \mathbf{E} \quad (4.10)$$

where, μ_0 is magnetic permeability in the air, μ_r is magnetic permeability in a material, ϵ_0 is electric permeability in the air, ϵ_r is electric permeability in a material and σ is conductivity.

The wave equation becomes :

$$\nabla \cdot (\epsilon_0 \epsilon_r \mathbf{E}) = 0 \quad (4.11)$$

$$\nabla \cdot (\mu_0 \mu_r \mathbf{H}) = 0 \quad (4.12)$$

$$\nabla \times \mathbf{E} + \mu_0 \frac{\partial \mathbf{H}}{\partial t} = 0 \quad (4.13)$$

$$\nabla \times \mathbf{H} - \epsilon_0 \epsilon_r \frac{\partial \mathbf{E}}{\partial t} = 0 \quad (4.14)$$

When these equations are simplified by taking into account the specialized case, that is, to understand the behavior of a plane wave at an interface between a metal and a dielectric. This specialized case can also presented in Figure (4.6). With the help of the above equation, the Transversely Magnetic (TM) wave equations are given by:

$$E_z = -\frac{\beta}{\omega \epsilon_0 \epsilon_r} H_y \quad (4.15)$$

$$E_x = -i \frac{1}{\omega \epsilon_0 \epsilon_r} \frac{\partial H_y}{\partial z} \quad (4.16)$$

wave equation can also be written as :

$$\frac{\partial^2 H_y}{\partial z^2} + (k_0^2 \epsilon_i - \beta^2) H_y = 0 \quad (4.17)$$

From this equation, we can determine $H_y(z)$ and from the previous equations we can determine $E_x(z)$ and $E_z(z)$. To determine these values let us take:

$$\kappa_i = \beta^2 - k_0^2 \epsilon_i \quad (4.18)$$

For the case of $z > 0$ (metal (gold) in our case), the equations become:

$$H_y(z) = A_d e^{i\beta x} e^{-\kappa_d z} \quad (4.19)$$

$$E_z(z) = -A_d \frac{\beta}{\omega \epsilon_0 \epsilon_d} \kappa_d e^{i\beta x} e^{-\kappa_d z} \quad (4.20)$$

$$E_x(z) = iA_d \frac{\beta}{\omega \epsilon_0 \epsilon_d} \kappa_d e^{i\beta x} e^{-\kappa_d z} \quad (4.21)$$

For the second case where $z < 0$ (glass in our case), the equations become:

$$H_y(z) = A_m e^{i\beta x} e^{-\kappa_m z} \quad (4.22)$$

$$E_z(z) = -A_m \frac{\beta}{\omega \epsilon_0 \epsilon_m} \kappa_m e^{i\beta x} e^{-\kappa_m z} \quad (4.23)$$

$$E_x(z) = iA_m \frac{\beta}{\omega \epsilon_0 \epsilon_m} \kappa_m e^{i\beta x} e^{-\kappa_m z} \quad (4.24)$$

Here, A_m and A_d are the amplitude of wave in metal and dielectric respectively. At the position where there is an interface between the metal and the dielectric the tangential component of the wave (e_x) needs to be continuous and therefore, we have

$$A_m = A_d \quad (4.25)$$

or

$$\frac{\kappa_m}{\epsilon_m} = \frac{\kappa_d}{\epsilon_d} \quad (4.26)$$

From this equation, if we consider a case with perfect medium that is a medium that has no loss of wave energy when traveling in the material and the imaginary part of the permittivity is null; then we have the propagation constant as:

$$\beta = \frac{\omega}{c} \sqrt{\frac{\epsilon_m \epsilon_d}{\epsilon_m + \epsilon_d}} \quad (4.27)$$

The tangential component of its wave vector, that is, light wave and the coupled plasmon wave k_x becomes:

$$k_x = \beta = \frac{\omega}{c} \sqrt{\frac{\epsilon_m \epsilon_d}{\epsilon_m + \epsilon_d}} \quad (4.28)$$

where, we have ω as frequency of the wave, followed by c that is speed of light, ϵ_m is permittivity of a metal and ϵ_d is permittivity of a dielectric medium.

This allows the coupling of the k_x with the k_{spp} wave. This coupling can be seen from the Figure (4.7).

From this figure, one can see that for a particular medium, that is air, the frequency

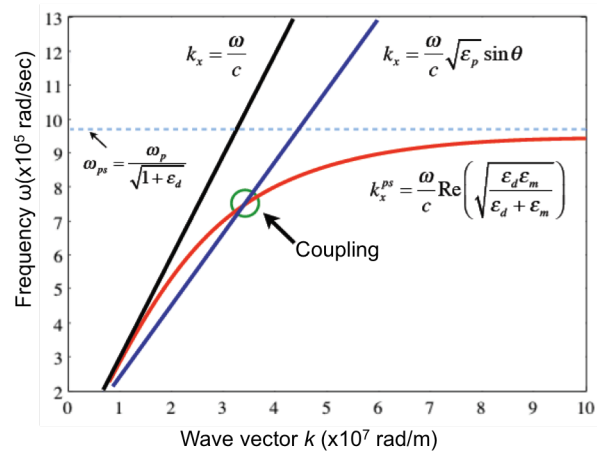


FIGURE 4.7: Dispersion curve of light in (vacuum and glass) and surface plasmons and coupling condition

vs the k_x vector change graph is presented by a black line and for medium glass it is represented in blue. The red curve (k_{ps}) shows the wave vector of surface plasmons. At a particular frequency we find that there is a coupling of surface plasmons and the wave vector of light.

4.1.4 Sensitivity

The definition of sensitivity are used to assess the performance of a sensor as a function of these parameters. The sensor's sensitivity S can be defined as the ratio between the variations of the quantity in question for characterizing plasmon resonance and the variation of Refractive Index Unit (RIU) of the dielectric medium [96]. For the calculation of sensitivity, a large band spectrum laser (Large Wavelength Spectrum Analysis), that is, having a large amount of wavelengths (or spectral band) is used and the sensitivity is calculated by the formula:

$$S(RIU) = \frac{\Delta\lambda_{res}}{\Delta n_d} \quad (4.29)$$

These large band lasers are bulky and very hard to transport. As we are working towards an integrated solution we need lasers that are extremely light, transportable and cost effective. For this purpose, we use single wavelength lasers (Single Wavelength Analysis). To calculate the sensitivity, we propose a new method of calculation and that is:

$$S(RIU) = \frac{\Delta R_{res}}{\Delta n_d} \quad (4.30)$$

According to the modes of interrogation, the sensitivity can be given by [nm/RIU] for eq. (4.29) or [deg/RIU] or [RP/RIU] (with RP: Reflectance Percentage) for eq. (4.30).

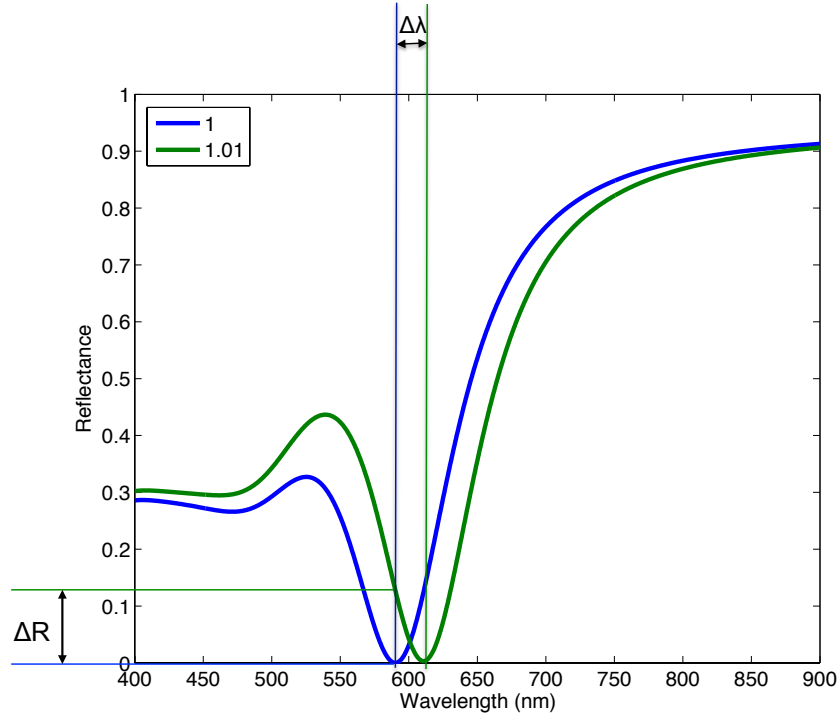


FIGURE 4.8: Graph shows the Sensitivity calculation method.

Therefore, in our work, we have divided the analysis of sensitivity in two different methods, that is, Large Wavelength Spectrum Analysis and Single Wavelength Analysis. To understand the two analysis methods in detail, let us take an example of a gold slab having a thickness of 43.5 nm as shown in Figure (4.8) and that is placed on top of the glass prism. For the measurements, the superstrat's refractive index changes from 1 (air) to 1.01 and the laser is injected at an angle of 45° on the side of glass. The two analysis methods are explained below.

- Large Wavelength Spectrum : From the example stated above and shown in the Figure 4.8, we find the maximum dip for refractive index 1 is present at a wavelength of 590 nm. Similarly, the maximum dip for refractive index 1.01 is present at a wavelength of 611 nm. Using these values, the sensitivity can be calculated from equation 4.29 as follows:

$$S(1.01) = \frac{\lambda_{1.01} - \lambda_1}{n_{1.01} - n_1} = \frac{611 - 590}{1.01 - 1} = 2100[nm/RIU] \quad (4.31)$$

These large band lasers are from manufacturers like opto lasers, Finanium and others.

- Single Wavelength Analysis: One uses a single wavelength to determine the refractive index that is present on top of the gold layer. This is explained from the example stated above and shown in the Figure 4.8. Here, we set the wavelength of the laser as 590 nm (as an example) and the difference of Reflectance values for

a change in refractive index is calculated using the equation 4.30. The sensitivity is calculated as:

$$S(1.01) = \frac{R_{1.01} - R_1}{n_{1.01} - n_1} = \frac{0.1287 - 0}{1.01 - 1} = 12.87[RP/RIU] \quad (4.32)$$

These kind of lasers can be laser diodes manufactured by Thor Labs or specific lasers from RGB systems among other manufacturers.

However, it should be noted that the sensitivity does not provide the information on how precisely one can measure the wavelength's resonance difference.

Presently, there are a lot of SPR and LSPR sensors that are present and a few are presented below. As per the thesis of Kelly [96], a LSPR structure was observed with a sensitivity value of 590 nm/RIU. According to Homola's article on Surface Plasmon Resonance Based Sensors [97], it is said that a sensor can achieve a sensitivity of 7500 nm/RIU. The number of layers and thickness of SiO_2-TiO_2 are varied, the sensitivity changes between 0.69 nm per RIU to 1.25 nm per RIU [98].

To do the sensitivity analysis, we require the Reflectance calculations for each wavelength, refractive index and for some structures, the analytical calculations are a bit complicated or have not been developed yet. Due to that reason we simulate the Reflectance with the help of the Rigorous coupled-wave analysis (RCWA).

4.1.5 RCWA Calculation

Rigorous coupled-wave analysis (RCWA) is a semi-analytical method in computational electro-magnetics that is most typically applied to solve scattering from periodic dielectric structures. The rigorous coupled-wave theory is widely used for diffraction analysis of micro/nanostructured surfaces of arbitrary shapes and dimensions. It is an exact solution of Maxwell's electromagnetic equations and the accuracy of the solution depends solely on the number of retained terms in the space-harmonic expansion of the fields in the diffracting structures. It also satisfies the principle of conservation of energy [99, 100]. It is a Fourier-space method so devices and fields are represented as a sum of spatial harmonics [101, 102]. The following paragraphs outline the principle of rigorous coupled-wave theory for both propagation modes when applied to infinite periodic diffraction gratings.

To study the propagating modes in an infinite periodic grating of thickness t , width w and period Λ between two homogeneous media of permittivities ϵ_1 and ϵ_2 as shown in Figure 4.9. In this Figure, the light or the incident field is a plane wave that impinges on the structure from the substrate (Medium 1) [104], whose wave vector is k forms an incident angle θ_0 respect to the z axis. Plane wave can be written as

$$\psi_{inc}(x, z|\omega) = \psi_0^1 e^{ik_x x} e^{ik_0^1(z+t/2)} e^{-i\omega t} \quad (4.33)$$

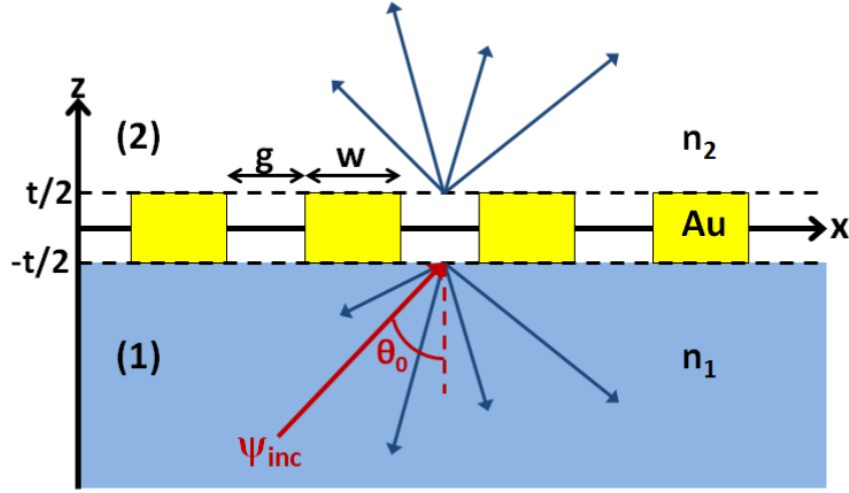


FIGURE 4.9: Diffraction of a plane wave on an infinite periodic array of metallic nanowires along the x-axis, of thickness t and period $\Lambda = w + g$, between two semi-infinite homogeneous media.

where,

$$k_x = \frac{\omega}{c} n_1 \sin \theta_0 \quad (4.34)$$

$$k_0^1 = \frac{\omega}{c} n_1 \cos \theta_0, \quad (4.35)$$

n_1 is the refractive index of the substrate and ψ_0^1 is the amplitude of the incident plane wave.

At the first interface (from medium 1 to the grating region), the plane wave is partially transmitted and reflected. The transmitted part is converted to the diffraction modes of the grating and the reflected fraction is converted into the diffraction orders of the medium 1. The excited modes of the grating reach the second interface (grating medium 2), where they are partially transmitted and converted into the diffracted orders of medium 2 and partially reflected to the modes of grating.

The diffracted order in the adjacent media of the grating can be described the sum of propagative and counter-propagative diffraction orders along z-axis. The diffracted orders can expressed in term of Rayleigh - Fourier expansions with a constant spatial period around a central spatial frequency given by the zeroth order of the incident plane wave (Tishchenko,2005). The expression can be written as

$$\psi^j(x, z|\omega) = \sum_{m=-\infty}^{\infty} e^{ik_{xm}x} \left[A_m^j e^{-ik_m^j(z+h/2)} + B_m^j e^{ik_m^j(z+h/2)} \right] e^{-i\omega t} \quad (4.36)$$

where,

$$k_{xm} = k_x + \frac{2\pi m}{\Lambda} \quad (4.37)$$

$$k_j^m = \sqrt{\left(\frac{\omega}{c}\right)^2 n_j^2 - k_{xm}^2}, \quad (4.38)$$

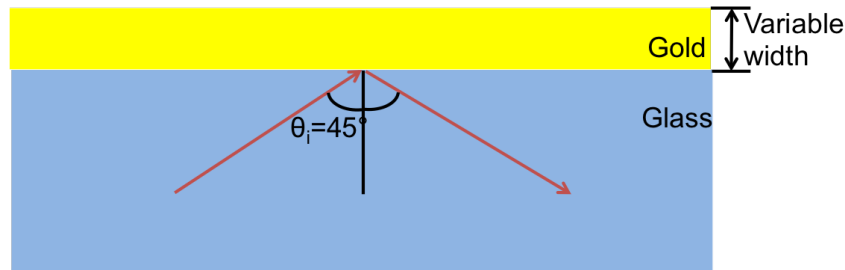


FIGURE 4.10: A Gold slab is used for the calculation of reflectance for SPR analysis. Width of Gold Slab varies from 10 nm to 50 nm. The light is incident at an angle of 45° from glass towards Gold slab.

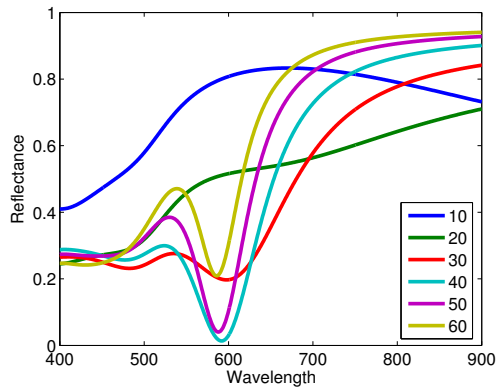
A_m^j, B_m^j are up and down amplitudes, respectively, of each diffracted order, Λ is the period of the structure and the script $j = 1, 2, \dots$ denotes the medium. This is a general expression that can be extended to a multilayered system.

4.2 Plasmonic Gold Slab for SPR-chip

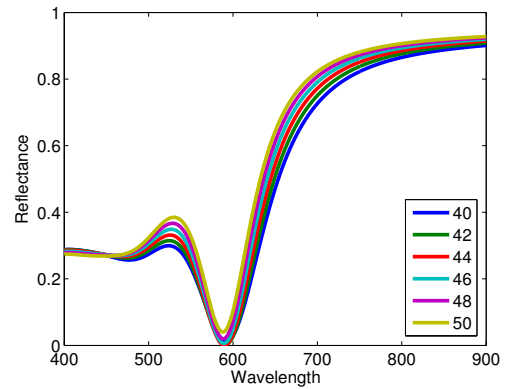
Here, we will find the optimum height (thickness) of the Plasmonic Gold Slab for SPR calculations. We find the optimum height of gold slab, where we the maximum difference in Reflectance. The main aim is to see the maximum dip in the Reflectance and that could increase the value of sensitivity. For this purpose, a few simulations are performed for a gold slab of variable thickness that is deposited on top of the glass of refractive index 1.52 as seen in Fig. (4.10). In these simulations, the thickness of gold slab is varied by starting at 10 to 60 nm.

Figure 4.11a shows the preliminary result of different thickness of gold slab. One can observe the reflectance vs wavelength curve for 10, 20, 30, 40, 50, 60 nm, respectively, as the thickness in gold slab. These thicknesses gives an idea where one can observe the maximum dip in the curve. Using these results, one can visualize that the maximum dip will be present where the thickness is between 40 and 50 nm. To further accurately determine the best optimum thickness of the Gold slab, one needs to do further calculations for the determination of the thickness. For this purpose, we have done simulations for different thicknesses that are 40, 42, 44, 46, 48, 50 nm respectively. The simulated results are shown in the Figure 4.11b. Using these results, one can again narrow the optimum thickness needed to a range between 42 and 44 nm.

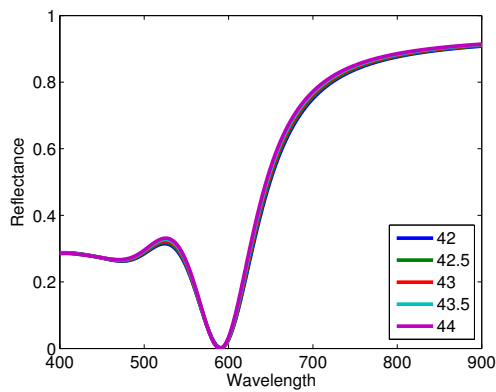
As we have narrowed down the thickness of Gold slab to a range that is 2 nm. We once again did simulations by varying the thickness between 42 and 44 nm and taking the difference between the thicknesses as 0.5 nm. The results that were simulated can be visualized using the Figure 4.11c. Using this Figure, one can not perfectly determine the maximum dip. To solve this problem we have taken a smaller span of wavelength for observation to accurately determine the thickness as can be see in Figure 4.11d.



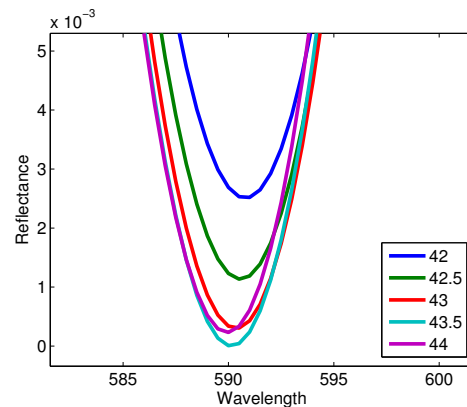
(A) Graph showing the effect of reflectance with the variation of wavelength for multiple widths of Gold Slab that varies from 10 nm to 60 nm.



(B) Graph showing the effect of reflectance with the variation of wavelength for multiple widths of Gold Slab that varies from 40 nm to 50 nm.



(C) Graph showing the effect of reflectance with the variation of wavelength for multiple widths of Gold Slab that varies from 42 nm to 44 nm.



(D) Graph showing the effect of reflectance with the variation of wavelength for multiple widths of Gold Slab that varies from 42 nm to 44 nm. This graph is a enlarged graph in a smaller wavelength period to see the maximum dip.

FIGURE 4.11: Graphs showing the effect of reflectance with the variation of wavelength for determining the optimum thickness of Gold Slab.

Using these results we see the maximum dip and minimum opening is present when the thickness of Gold Slab is 43.5 nm.

Using this simulation results (refer Figure (4.11)), one can see that the maximum interaction between glass and gold slab takes place at a wavelength of 590 nm. The maximum interaction in this configuration is for a gold slab of 43.5 nm.

4.2.1 Sensitivity in the case of gold slab

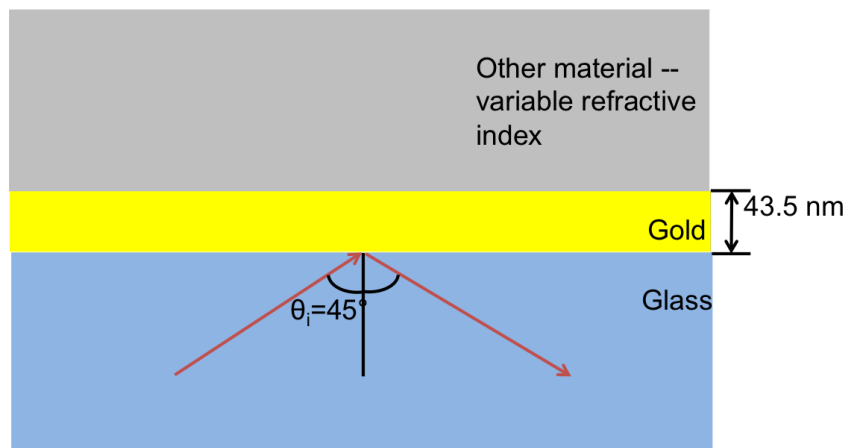


FIGURE 4.12: A Gold slab is used for the calculation of reflectance for SPR analysis. Width of Gold Slab is fixed at 30 nm. A layer of material is added on top of the gold layer which have different Refractive index from 1.00 to 1.05 respectively. The light is incident at an angle of 45° from glass towards Gold slab.

Now, in this section we will discuss the sensitivity of the Gold Slab of thickness 43.5 nm. To start with we need to understand how the sensitivity calculation is performed. Let us consider, the laser positioned at 45° is coming from Glass and interacting with the Gold slab. Above this Gold slab, we have another dielectric material which is air or with an refractive index near air as seen in Figure (4.12). In this case the dielectric material's refractive index is varied from 1.0 to 1.05.

Using the configuration described in Figure (4.12), we keep other parameters as constant that is the angle of incidence of light is taken as 45° and thickness is 43.5 nm of gold slab. We have performed simulations by varying the wavelength of the incident light to visualize the spectral analysis for determining the best wavelength that can be used for final integration. The simulation results are shown in a form of graph for different refractive index vs variable wavelength and is show cased in Figure (4.13).

The analysis of sensitivity is divided into two different parts as presented below.

- **Large Wavelength Spectrum :** From the Figure (4.13), we see how the resonance peak changes with different refractive indexes in the visible spectrum of light. This means that the resonance of the structure changes with the change refractive index. One can observe that the shift of the resonance is towards a larger

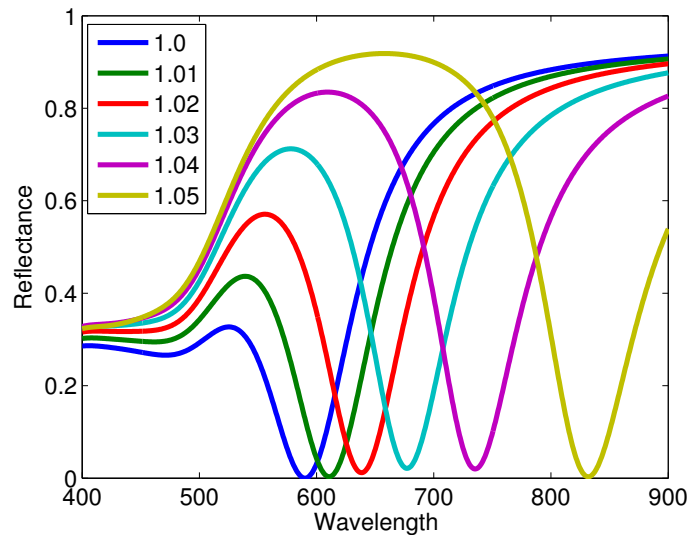


FIGURE 4.13: Graph showing the effect of reflectance with the variation of wavelength for multiple refractive index of layer above gold slab that varies from 1 to 1.05 respectively.

wavelength as compared to resonance peak of the vacuum. For each value of the change in refractive index, its dip frequency is observed and sensitivity is calculated. The sensitivity is presented in the Figure (4.14).

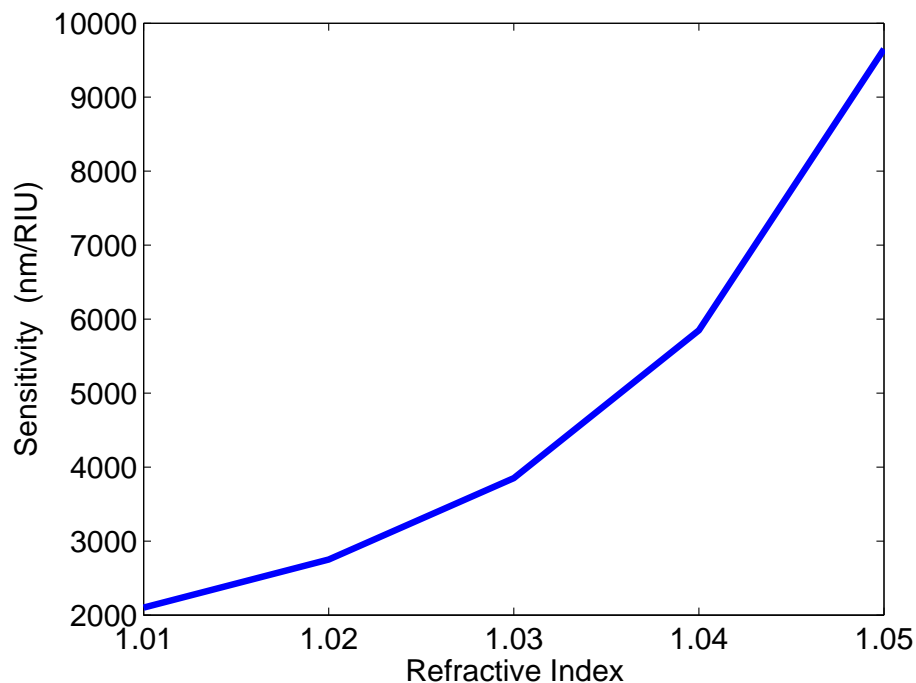


FIGURE 4.14: Sensitivity of a gold slab as a variation of refractive index.

- Single Wavelength Analysis:

In this analysis, we calculate the reflectance values and its sensitivity for each the different wavelengths. The different wavelengths taken are 500 nm, 550 nm, 600

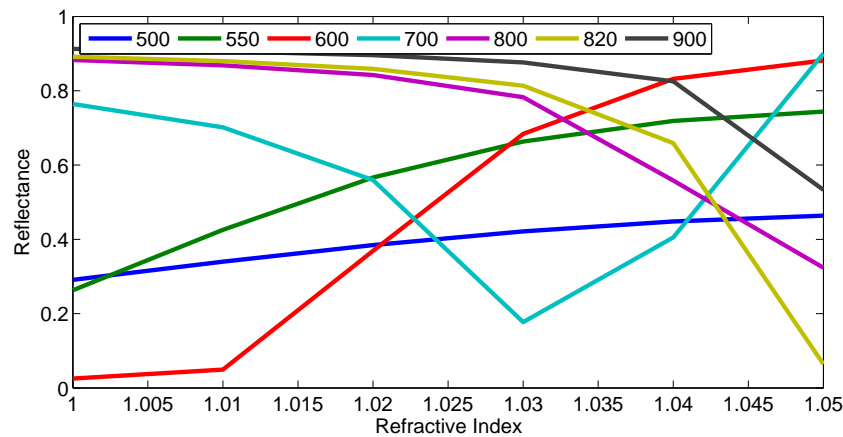


FIGURE 4.15: Reflectance as a function of the refractive index of the superstrat for multiple wavelengths for Gold Slab having a thickness of 43.5 nm.

nm, 700 nm, 800 nm, 820 nm and 900 nm. For each wavelength the sensitivity is calculated with the help of the equation (4.30). The calculated reflectance and sensitivity are plotted in the Figure (4.15) and Figure (4.16) respectively.

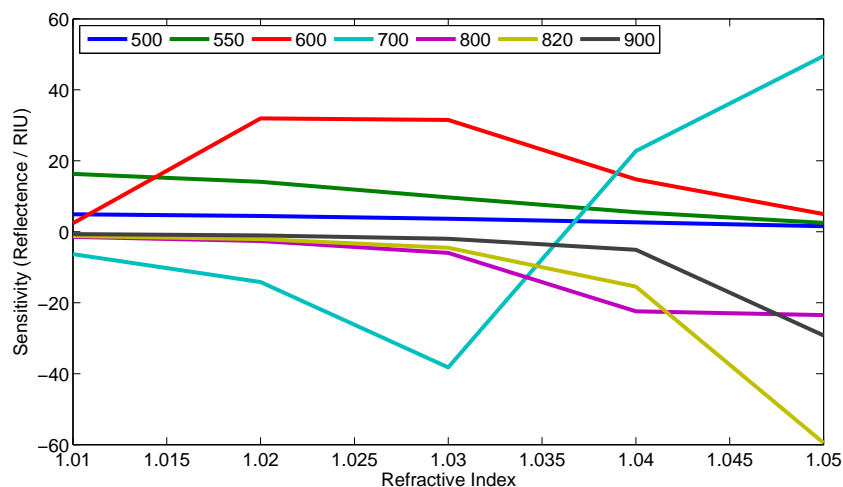


FIGURE 4.16: Sensitivity as a function of the refractive index of the superstrat for multiple wavelengths for Gold Slab having a thickness of 43.5 nm.

One can see that for almost all the wavelengths there is an abrupt increase or decrease in reflectance value as we change the refractive index. There are only a few cases, in which the change is almost linearly constant or decreasing and this can be seen for the wavelengths of 500, 550 and 900 nm.

For this gold slab having a thickness of 43.5 nm, we find that it is more suitable for large Wavelength Spectrum Analysis. We have already discussed in Subsection 2.2.3.1 that the minimum wavelength required for CoBiSS integration is 540 nm. Therefore, we are left with wavelengths of 550 nm or 900 nm for integration.

4.3 Plasmonic "W" structure for LSPR-chip

A new structure that is proposed except for the usual Gold slab, is known as Gold "W structure". For this "W" structure, the opening angle (α) is 32° and the larger segment length is varied from 400 nm to 1000 nm. The radius of curvature of 5 nm is taken for the the peaks and trenches of "W" structure and the thickness is varied. Using this structure LSPR chip can be made as the structure has the peaks and trenches. This structure is deposited on top of the glass of refractive index 1.52 by using a polymer that has the same refractive properties as of glass. This can be seen in Fig. (4.17) where we have made no difference between Glass and the polymer.

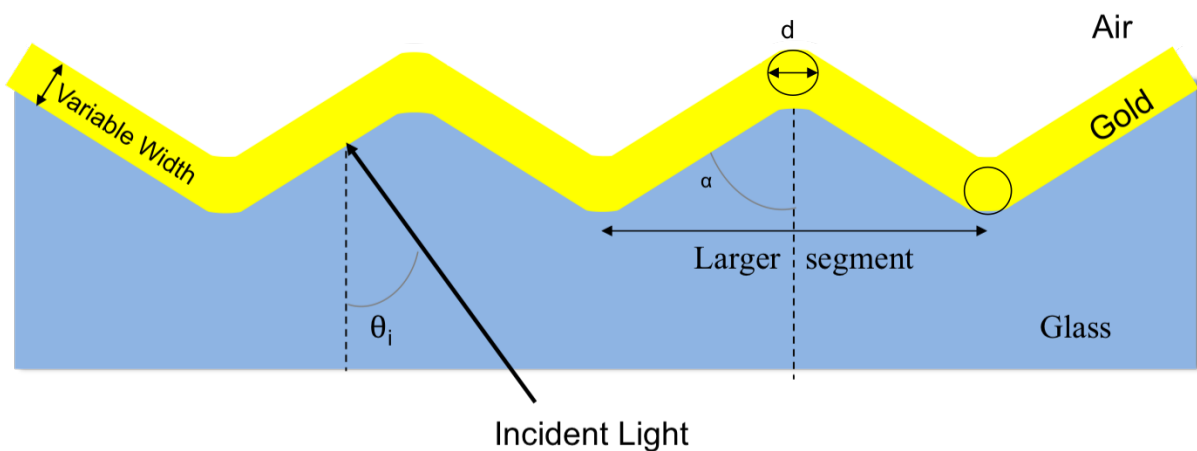


FIGURE 4.17: CoBiSS modified for the Detection of SPR with modified "W" structure with $2 \times \text{Radius} = \text{Diameter} = 10 \text{ nm}$

For the ease of explanation, we will be using four different lengths of the structure that are 400, 600, 800, 1000 nm. A few simulations are performed for this gold "W structure" for all these four specific cases. The thickness of gold that is deposited on top of the glass is varied and taken as 10, 20, 30, 40, 50, 60 nm respectively. For these simulations, the radius of curvature for peak and trenches is taken as 5 nm. This gave us the initial results as seen in Figure (4.18).

A new set of simulations were performed to understand the difference of Reflectance for all the above cases when the radius of curvature for peak and trenches is taken as 0 nm (i.e., exact "W" structure). The simulated results are shown in Figure (4.19).

Figure (4.18) and (4.19) show the results of interaction of gold "W" structure where the graph is plotted for thickness ranging from 10 - 60 nm as a function of wavelength from 400 - 900 nm and reflectance. To interpret these results, we observe that a part of the pattern's characteristics is coming from diffraction. This is made by recording the interference fringes generated at the intersection of two coherent beams of light [113, 114]. This can be related with the formula

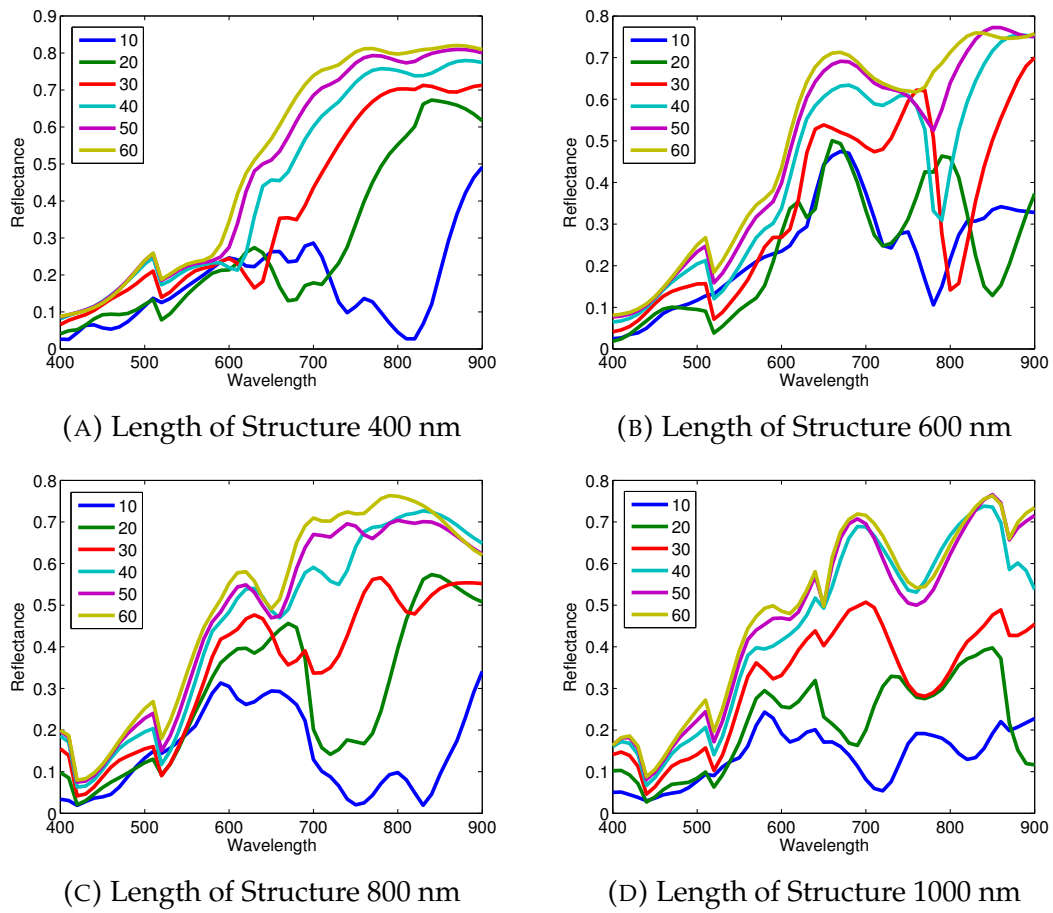


FIGURE 4.18: Graph showing the effect of reflectance with the variation of wavelength for multiple widths of W-structure that varies from 10 nm to 60 nm with an curvature radius of 5 nm.

$$\lambda = n_{sub} (1 + \sin(\theta_{inc})) \left(\frac{\Delta}{m} \right) \quad (4.39)$$

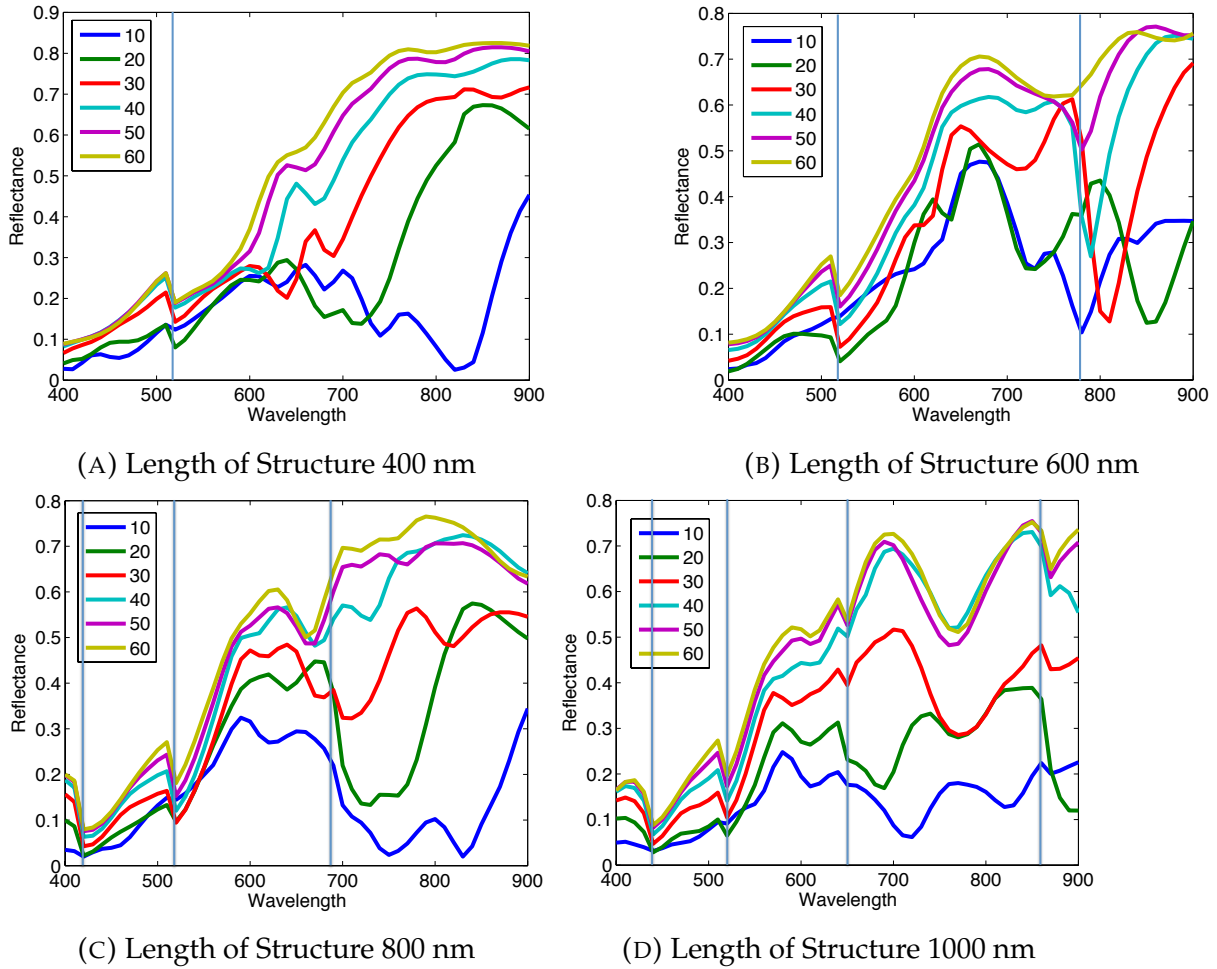


FIGURE 4.19: Graph showing the effect of diffraction grating along with reflectance with the variation of wavelength for multiple widths of W-structure that varies from 10 nm to 60 nm.

The diffraction is calculated from the equation present in (4.39) where, λ is the wavelength of diffraction grating, n_{sub} is refractive index of substrate, θ_{inc} is incident angle, Δ is the length of the structure and finally m represents the diffraction order.

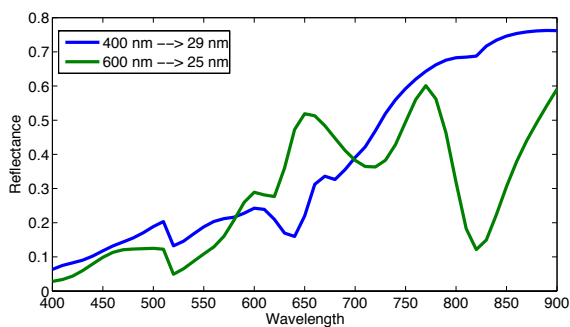
With the help of the equation (4.39), we found that the diffraction wavelengths are as follows:

- For structure length of 400 nm, the diffraction wavelength is 519 nm.
- For structure length of 600 nm, the diffraction wavelengths are 519 and 778 nm.
- For structure length of 800 nm, the diffraction wavelengths are 415, 519 and 691 nm.
- For structure length of 1000 nm, the diffraction wavelengths are 432, 519, 649 and 864 nm.

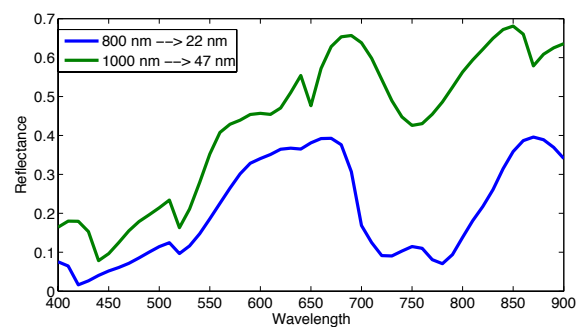
These diffraction wavelengths are also represented in the Figure (4.19) by perpendicular lines at the same wavelength. With these results, we see that the small trenches or dip at those wavelengths in the figures corresponds to the diffraction wavelengths.

As we are interested in finding the most optimum thickness of the gold layer for their respective "W" structure length, we used the results showcased in the Figures (4.18) and (4.19) and performed further analysis. For both structures, we found that the maximum change in reflectance is observed as the following:

- For the structure length of 400 nm, the thickness required for the gold layer is 29 nm.
- For the structure length of 600 nm, the thickness required for the gold layer is 25 nm.
- For the structure length of 800 nm, the thickness required for the gold layer is 22 nm.
- For the structure length of 1000 nm, the thickness required for the gold layer is 47 nm.



(A) The length of structure chosen is 400 and 600 nm along with the most optimized thickness as 25 and 29 nm respectively.

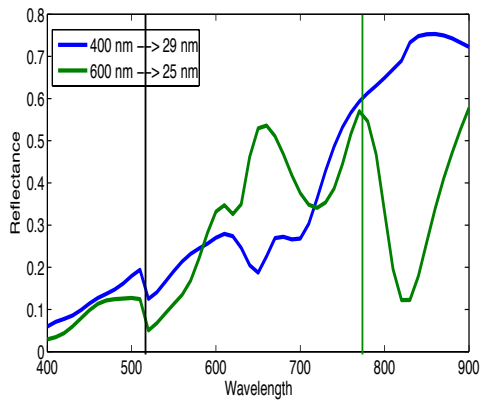


(B) The length of structure chosen is 800 and 1000 nm along with the most optimized thickness as 22 and 47 nm respectively.

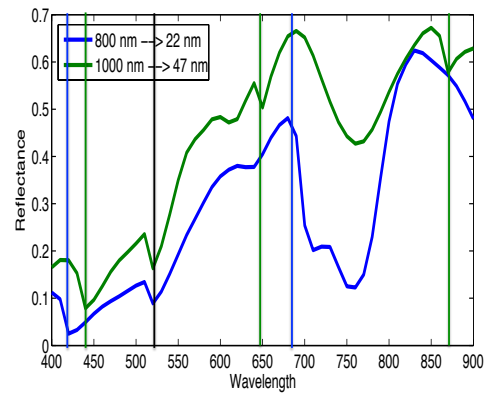
FIGURE 4.20: Graph showing the effect of reflectance with the variation of wavelength for multiple length of W-structure for the most optimized thickness with a radius of curvature of 5 nm.

These results can be seen from the Figure (4.20) and (4.21). In the figure (4.21), the diffraction grating wavelengths are shown with the same color as their respected structure length and the diffraction grating in color black is represented when the two have the same diffraction grating wavelength. Out of these results, we found for both "W" structures, the maximum dip along with 2 distinctive dips are present when the length of the two "W" structures are 600 nm.

Now, let us compare the results that we have for "W" structure and "W" structure without curvature, one can see that there is not much of the difference between the

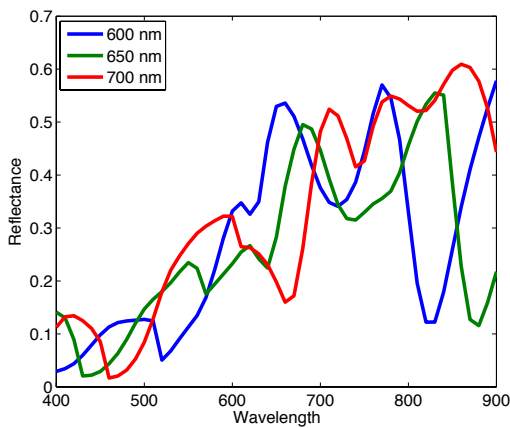


(A) The length of structure chosen is 400 and 600 nm along with the most optimized thickness as 25 and 29 nm respectively.

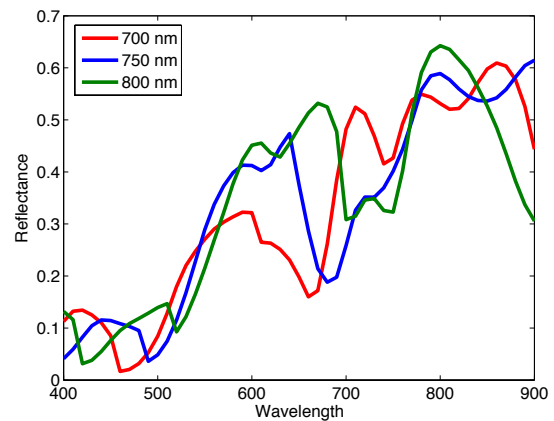


(B) The length of structure chosen is 800 and 1000 nm along with the most optimized thickness as 22 and 47 nm respectively.

FIGURE 4.21: Graph showing the effect of reflectance with the variation of wavelength for multiple length of W-structure for the most optimized thickness.



(A) Length of Structure varies from 600 to 700 nm



(B) Length of Structure varies from 700 to 800 nm

FIGURE 4.22: Graph showing the effect of reflectance with the variation of wavelength for multiple length of W-structure for the thickness of gold layer as 25 nm.

two. This could lead us to say that we can do our simulations without the curvature for similar results.

With this result present in (4.21), we also see a possibility that the dips could be moving when the length of the "W" structure changes from 600 to 800 nm. This might help in seeing that it may be possible that for a specific length of the structure we just obtain one effective dip. To understand this, we simulated the scenario where the thickness of the gold layer was taken as 25 nm and the length of the structure is varied from 600 nm to 800 nm for "W" structure with no curvature. The result of this simulation is presented in the Figure (4.22).

With this result, we observe that the two different dips in the reflectance curve for 600, 650, 700 starts to move closer to each other as can be seen from the Figure (4.22a).

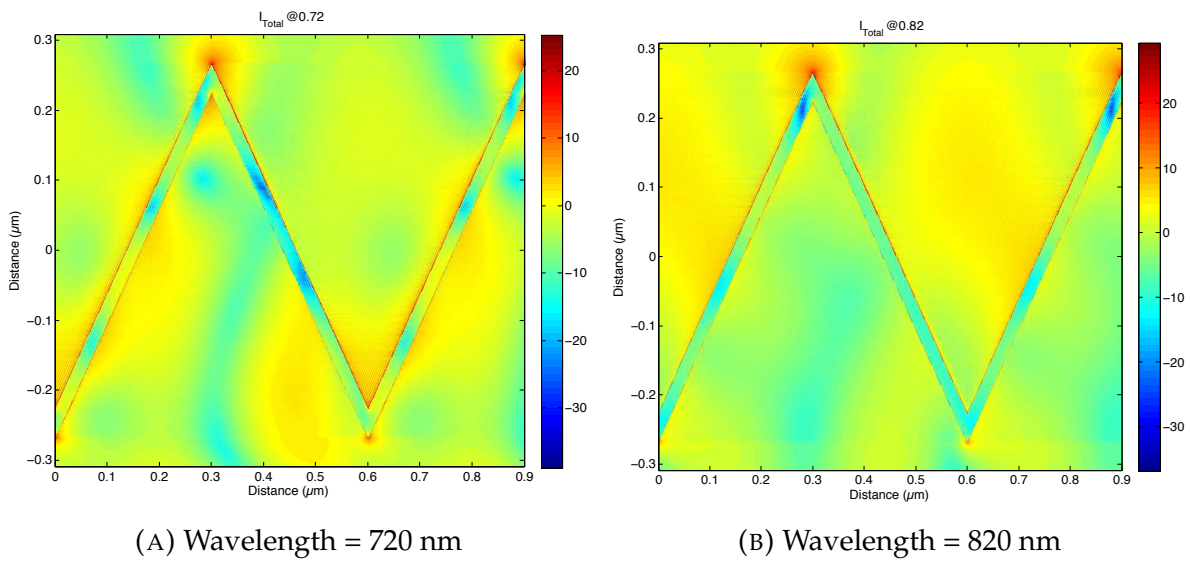


FIGURE 4.23: Near Field calculation of "W" structure of length 600 nm and thickness of gold layer as 25 nm and Intensity values are present in dB ($10 \log_{10} \frac{I}{I_0}$).

In the Figure (4.22b), we observe the simulated results from 700 to 800 nm of structure length. In this scenario, we see that the 750 nm of the structure length has two dips that are almost co incident. This could be interesting as around 750 nm of structure length there is only one dip.

After we have found the most optimized length of the structure and the thickness of the gold layer, let us see the effects of the interaction of light of 720 and 820 nm with the "W" structure in Near field. In the Figure (4.23), the Intensity of Light that was irradiated was measured in decibel (dB). The formula for calculation of decibel is given as:

$$I(dB) = \left(10 \times \log_{10} \frac{I}{I_0} \right). \quad (4.40)$$

This shows that we have a very high amplification factor.

4.3.1 Sensitivity calculation

In this configuration, we find the sensitivity for the structure that has the length of 600 nm as discussed in Section 4.3. We have chosen the most optimal thickness for this case, that is, 25 nm and the sensitivity calculations are preformed by varying the refractive index that is present above the gold "W" structure.

For doing the sensitivity calculations, we have varied the incident wavelength of the laser from 400 to 900 nm and also the refractive index of the material from 1 to 1.05. In this case too the incident laser is placed at an angle of 45° in glass (because of the CoBiSS configuration). The responses, that is, the reflectance that are obtained for these cases are shown in the Figure (4.24). We have also marked the wavelengths of diffraction of the structure in air with black lines.

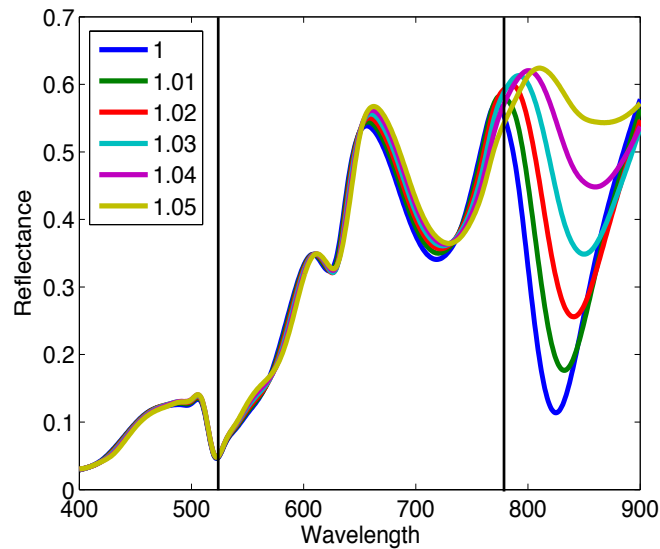


FIGURE 4.24: Sensitivity analysis for W structure with structure length of 600 nm and radius of curvature of 0 nm. Graph shows the effect of reflectance with the variation of wavelength for multiple refractive index of layer above gold "W" structure that varies from 1 to 1.05 respectively.

While looking at the results in the Figure (4.24), we see that there are two different peaks / dips present in the Reflectance curve. One can observe that the Reflectance curve for all different refractive index are the same till the 650 nm but afterwards one starts to see the differences in the curve that can be measured.

Let us consider two zones namely Zone One and Zone Two that are between 650 nm to 760 nm and 760 nm to 900 nm respectively. In the zone One, the amount of dip remains almost the same for all the reflectance calculation when the refractive index is varied but the minimum value of the reflectance increases as there is an increase in refractive index at a particular wavelength. In Zone 2, the amount of dip changes significantly as the refractive index is varied. In this case, as the refractive index increases the amount of dip or the reflectance value decreases. In our case, this zone 2 plays an

important role in finding the sensitivity. The two methods of sensitivity calculation is given below:

- Large Wavelength Spectrum: We calculate the sensitivity for the results that are shown in Figure (4.24). For each value of the change in refractive index, its dip frequency is observed and sensitivity is calculated.

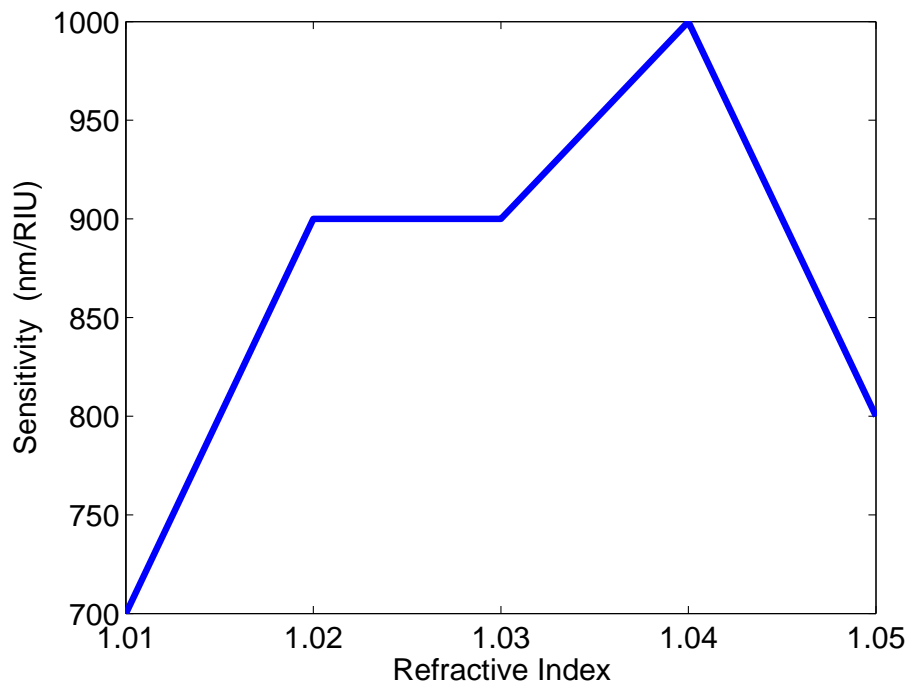


FIGURE 4.25: Graph shows the Sensitivity of "W" structure with no radius of curvature on the edges as the variation of refractive index

The analysis of the sensitivity for all the structures are done when the refractive index of the top layer changes from 1.01 to 1.05 as seen in Figure (4.25).

- Single Wavelength Analysis:

Referring to the Figure (4.27), one sees that the sensitivity value is almost constant or has a tendency to increase or decrease gradually in a linear order except for wavelengths of 820 and 900 nm. If we use one or two different wavelengths like wavelengths at 600 nm and 700 nm we should be able to obtain distinctive patterns or markers. We can even use a wavelength of 820 nm as it gives us an increasing value of sensitivity for small refractive index change. We also see that there are more wavelengths that are present above the threshold wavelength of 540 nm. For this reason it is recommended that the "W" structure be used for single or two wavelength detection.

The exact decision to use which type of structure will depend on the final application of this device.

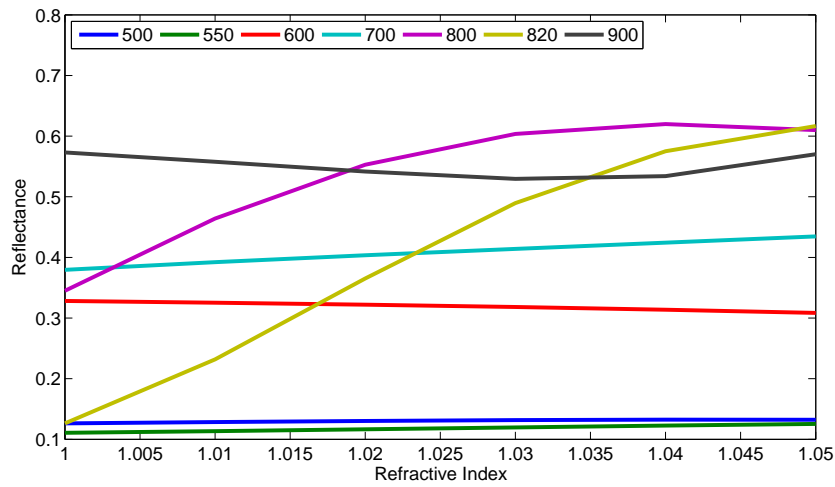


FIGURE 4.26: Graph showing the effect of reflectance with the variation of refractive index for multiple wavelengths for "W" structure having a length of 600 nm and thickness of 25 nm.

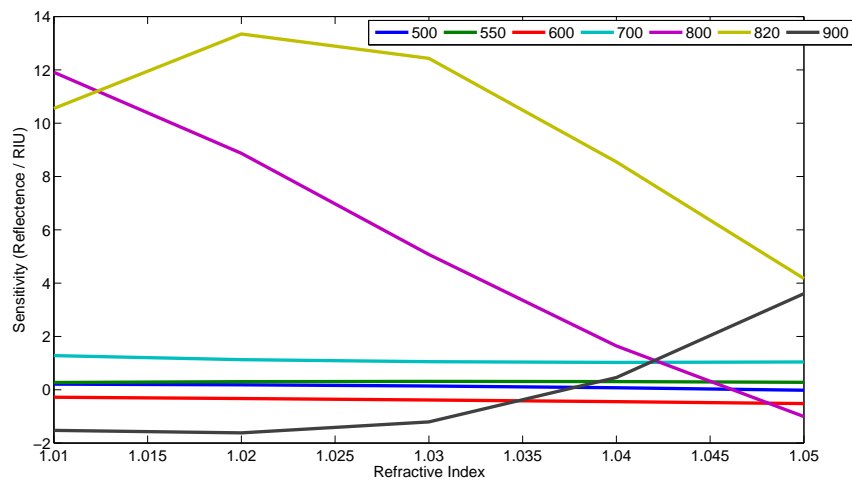


FIGURE 4.27: Graph showing the effect of sensitivity with the variation of refractive index for multiple wavelengths for "W" structure having a length of 600 nm and thickness of 25 nm.

4.4 Conclusion

In this chapter, we have explored the the sensing part of the device. We have written about two different structures, namely, Gold slab and new "W" structure for SPR sensing.

For the Gold slab, we have found the most optimized width of the gold slab and the sensitivity calculations have been performed for that width. We find that this structure is best suited for the usage of Large wavelength spectrum analysis.

We have also discussed the "W" structure where we have determined the most optimized length of the structure and the width of gold layer. We have done the sensitivity calculations for the optimized length of the structure. With the observations presented in the chapter, it is recommended that this "W" structure with the optimizations be used for the Single wavelength analysis.

Chapter 5

Conclusion and Prospects

The main aim of this thesis was to create a device which uses CoBiSS configuration to do SPR calculations and can also be used any where for a practical purpose, that is, in wireless sensing of environment as one of the example. It means that the device needs to be small handheld and portable. It should be a rugged device which can be deployed even in the harshest condition. This also means that the device should not have any movable parts and all the parts need to be fixed.

The ultimate aim of this thesis was to create or give the most optimized solution for future production for a first working prototype which has no moving parts and can be created without using too many custom parts. This would eventually help in the reduction of cost.

To attain this aim, we, initially, thought that the process will be rather simple to convert the setup of CoBiSS to a device. But due to various constraints like finding a camera without a protective layer or a need to precisely understand the working and positioning of nano-structures along with other aspects of integration.

This created a need for us to start from the basics to create the end product. This thesis covers this distance.

Initially, we started by understanding how one can get a nano-particle to irradiate light in our interest area, that is, irradiating towards the top. To understand this we first needed to understand how a dipole (a particle of extremely negligible size) behaves when it is present near or at the interface of glass and air. For this purpose a few analytical calculations of Dipole's interaction with an interface of air and glass were done. With the help of these analytical calculations, we showed how a dipole having perpendicular and parallel orientation with respect to the surface irradiate the light.

This study for our work is the precursor to understand how a nano-particle irradiates light in air as a nano-particle has multiple dipoles present in them. Their interaction might give us an effective dipole or a combination of a few (depending on the size of nano particle) that may lead to simplification in understanding the radiation diagrams of nano particles.

The work was followed by a description of working of FDTD as we have used this simulation method in our work. We also covered the theoretical aspects of evanescent

waves by taking into account the wavelength changes when the refractive index of the dielectric interface changes.

As we are interested in the ESW configuration for CoBiSS, we have explored the theoretical aspects of standing evanescent waves and we have also taken into account the wavelength changes when the refractive index of the dielectric interface changes. Using these calculations we found a particle of 150 nm X 150 nm X 100 nm could be an ideal choice. After selecting this nano particle, a small study was done to understand the range of wavelengths in which we could use this particle.

Now, we have finished the optical integration part now was time to add the electronics and software integration to the mix.

Initially, as the electronics and software integration goes we have tried to make a stand alone device for testing purposes. To do this we tried to integrate the optical portion with the electronics devices and along with controlling and computing device. We compared different types of cameras, lasers and motherboards available in the market. Using this comparison, we have chosen a few devices that were used in the electronic integration. Using the chosen devices, the computing part was coded to control and get input data from different devices like camera and laser. As we chose Pandaboard as motherboard (computing hardware), and Ubuntu OS as the operating system.

We added the computational part, that is, the Lomb Scargle method and also Micro Spectrometer method for calculation of wavelength from an image. We have integrated this code in the computational part just after a control and image recovery instruction set.

A GUI was created on top of this code for ease of use and to show data in real time. All these procedures helped in creating a stand alone device that would be used by anyone.

It was time to add the sensing part in the device. In this sensing part we have focused our work towards SPR and we have worked on two different structures, namely, Gold slab and new "W" structure.

For the Gold slab, we have tried to find the most optimized width of the gold slab and its sensitivity calculations. We have found that this structure is best suited for the usage of Large wavelength spectrum analysis.

We have also discussed the "W" structure with a small curvature where we have tried to find the most optimized length of the structure and the width of gold layer. We have also discussed a small modified version of this "W" structure where there is no curvature on the tips. We have done the sensitivity calculations for the optimized length of the structure. We saw that the change in length and sensitivity remains almost the same. This means that the simulation with pointed tips would yield almost the same result as the modified structure. With these observations as observed for "W" structure, we feel that this structure is optimized for the Single wavelength analysis.

Now, as the Internet of Things is in the rising and all the devices are getting connected to the internet. This made it necessary for this device to be internet of Things ready. To do this, we have added the functionality of network communication into the coding of this device as this device already has a WiFi and LAN adapters present in the computational board (Motherboard).

For this purpose a basic computer network communication is explained along with the basic features of wireless networking. Small Code was developed for the Client Server Network model, Ad hoc network and also for Hybrid network (Wireless Sensor Network). In Client Server Network model, the device can send data to the server/cloud with the help of infrastructural devices like routers, access points, cellular data, satellite data communication. In Ad hoc network, the data flow is from one device or computer to another without the help of access points or infrastructural dependency. In hybrid network, it uses the features of both of the above. It meant to be deployed in remote areas and at least one device or sensor can be connected to the infrastructural devices. A small optimization or improvement was done over hybrid network code for the device to function as a sensor (for operation in real time).

We have created this functionality that enables the device to connect to the Internet but it is just too basic and acts as the backbone to the future development and requires to be improved depending on the final application of this device. This has led us to talk about the future work that is required to create a functional device with all the sensing capabilities. The device would require:

- For the detection and for error reduction, multiple lasers and the calculation that enables calculations of multiple wavelengths simultaneously needs to be added / improved upon.
- For sensing and detection aspects, we can have multiple localized zones and each zone is functionalized for different molecules. These zones will be at specific area for detection calculation. This could improve the capabilities of this device to sense multiple markers/ molecules at the same time. This could effectively reduce the cost.
- For the SPR sensing part, functionalization of the gold slab or "w" structure needs to be done to attract the molecule that will be sensed.
- For the communication part, as we have created the basic wireless networking that is it will act as a backbone, therefore, development in this area is required. To improve this area of development, first of all we need to find the applications this device will function as and accordingly add the additional capabilities.

The last two points will change as per the application area in which the device will eventually be placed. We can understand this by taking a few areas in which this device can be used :

- Industrial IoT: Let us take an example of Coal Mining industry where, the CO emissions are closely monitored. In this example, the device needs to be functionalized to capture CO particles and only one sensing zone is required. For the application, the device needs to communicate with other devices and ultimately to the servers that are present in different location. This will utilize the Wireless sensor network mode and a small sound system needs to be integrated for alarms to work for evacuation.
- Environmental Sensing for Smart Cities: We can have this device functionalized in different localized areas where this device can sense different molecules like CO, NO₂, SO₂, etc from the same device. As the communication part goes for the device, it can be divided into two different scenarios where the device is present in :
 - In Urban Areas: All the networking infrastructure already exists, therefore the device can communicate directly to the servers and send all the data. The device can work in the client server network model.
 - In Rural or Underdeveloped Areas: The networking infrastructure may not be fully developed, the device needs to function in Wireless sensing mode where the device connects in adhoc mode and also few devices act as access points to connect to existing infrastructure. In this case, one can add the functionality of automatic error detection and correction of the device by analyzing the data coming from other devices. This could be necessary as one may not have people equipped to do corrections in the device in remote areas.
- Smart Healthcare: We can have this device functionalized in different localized areas where this device can sense different molecules in the blood with the help of micro fluidics and this can be done from the same device. This device can be created in two different formats:
 - Stand alone device: We can have a small touch screen attached to this device along with the Graphical user application that starts when the user wants and sends the data to their personal cloud and the hospital or doctor with the help of Client server connection.
 - Small device : We can create an application for the mobile phone/ tablets / computer where the sensing part gets attached to the mobile phone and can do the sensing as per the user wish and send the data to their personal cloud, to their doctor.

This could help the people who are busy or far away from the specialists, doctors who can do tests wherever they are present and also the emergency services.

As we know that these areas where this device can be used in Internet of Things have just started and are yet to come into global picture. This will be the future for the IoT and will enable to generate a specific market in itself. As the global market is presently moving towards smart devices and a lot of people and other organizations would be interested in buying these kind of devices.

Chapter 6

French Summary

Intégration du spectromètre CoBiSS et modélisation de puce (L)SPR pour la détection a travers CoBiSS

Résumé : Aujourd'hui l'Internet des Objets (IdO) est en pleine évolution, et le dispositif de détection optique tel que présenté ici pourrait être utilisé dans ce domaine. En effet ces dispositifs pourraient être utilisés pour faire des tests pour une analyse comme la surveillance de la santé d'une personne en faisant un test sanguin ou d'autres analyses médicales et utilisés pour surveiller l'environnement en testant l'eau ou de l'air dans les villes, les montagnes, les usines, les rivières. Pour créer le dispositif, on a utilisé une combinaison du spectromètre nommé Spectromètre d'échantillonnage bi-directionnel couplé (CoBiSS) [Brevet WO2009127794A1] et une puce à résonance de Plasmon de Surface (SPR). Dans le but de l'intégration optique, une nouvelle analyse de l'échantillonnage dans le spectromètre CoBiSS est présentée, suivie de l'intégration du système électronique et optique pour supprimer les pièces mobiles. Il était nécessaire de rendre l'appareil petit et portable. Pour faciliter l'utilisation, une interface graphique a été développée. Pour la détection, une puce SPR a été ajoutée à CoBiSS et une nouvelle puce à résonance de plasmon de surface localisée (LSPR) a été modélisée pour maximiser sa sensibilité. Une nouvelle définition du calcul de sensibilité a été proposée. Cet appareil nécessite l'ajout de fonctionnalisation sur (L)SPR Chip pour la détection et une application finale. Cet appareil pourrait être un « objet » idéale dans l'IdO.

Dans ce temps où nous vivons, chacun utilise Internet ou World Wide Web (WWW) et il est devenu une partie fondamentale de notre vie quotidienne. L'Internet que nous utilisons est le réseau mondial de réseaux informatiques interconnectés. Il s'agit d'un réseau de réseaux qui se compose de millions d'interconnexions. Les ordinateurs qui sont connectés comprennent des réseaux privés, publics, universitaires, commerciaux et gouvernementaux. Ces ordinateurs sont reliés par un large éventail de technologies de réseau électronique, sans fil et optique. L'Internet n'a pas de gouvernance centralisée [1].

Comme l'utilisation de l'Internet a augmenté, la connexion entre le réseau et des périphériques physiques a également commencé à croître. Cela a conduit à la création d'objets interconnectés connus sous "l'Internet des objets (IoT)". Ils sont également appelés "périphériques connectés" ou "périphériques intelligents". Ces dispositifs

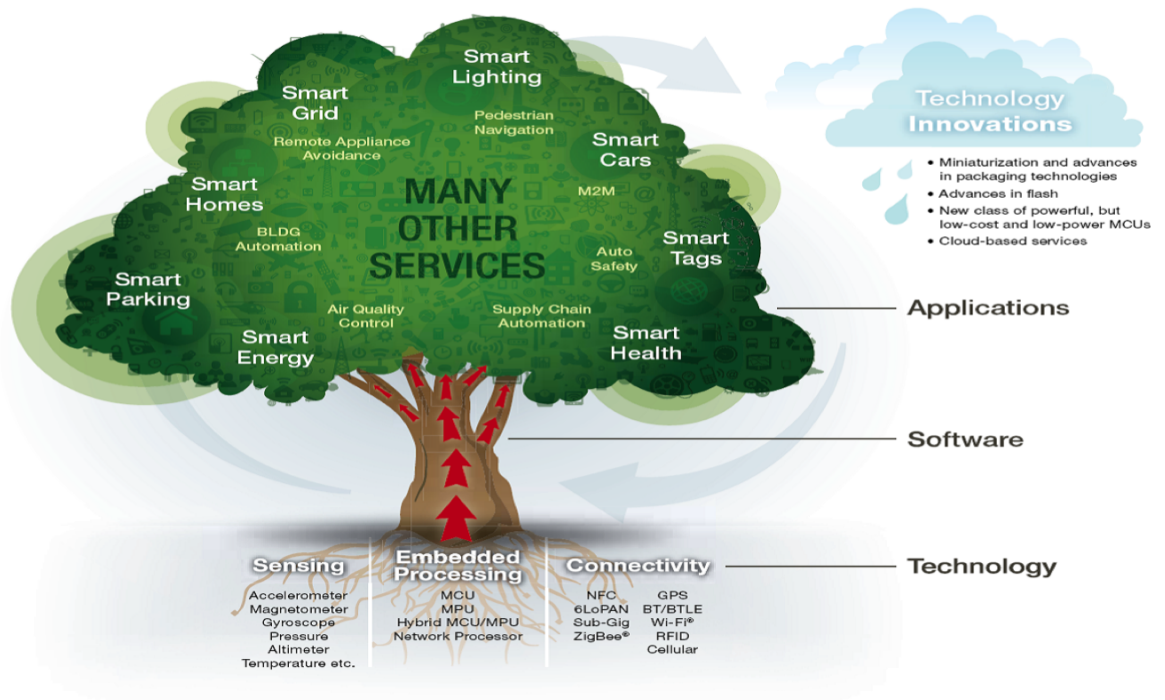


FIGURE 6.1: Exigences et domaine d'application de l'Internet des choses

connectés sont généralement intégrés à l'électronique, aux logiciels, aux capteurs, aux actionneurs et à la connectivité réseau qui permettent à ces objets de recueillir et d'échanger des données [2 - 4]. La figure 6.1 [6] montre l'intérêt de connaître les connaissances dans plusieurs domaines pour pouvoir maîtriser ces objets connectés, en particulier, les systèmes embarqués, des réseaux de capteurs sans fil, des systèmes de contrôle et également de l'automatisation.

Cela permet aux objets d'être détectés et / ou contrôlés à distance avec l'infrastructure réseau existante [7]. Cet avantage crée des opportunités pour une intégration plus directe du monde physique dans les systèmes informatiques et également une amélioration d'efficacité de contrôle, la précision et surtout les avantages économiques [8 - 14].

Dans les années à venir, Smart Devices ou Objets intelligents jouera un rôle important dans notre vie quotidienne. Tout d'abord, par l'intermédiaire des ramifications économiques et comment ces dispositifs augmentent sur une base quotidienne, ensuite, par les différentes technologies développées pour le transfert des données et enfin par les domaines où ces dispositifs peuvent être utilisés.

Les experts de ces dispositifs dans le domaine économique ont estimé que l'IoT concernera près de 50 milliards d'objets autour de 2020 comme le montre la figure 6.2, [15]. ABI Research ont également estimé que plus de 30 milliards d'appareils seront connectés sans fil à Internet des objets d'ici 2020 [16]. Cela peut également être visualisé par le tableau de croissance des IoTs et ses prévisions pour les années à venir.

Pour cette raison de croissance économique, de nombreuses entreprises et consortiums ont commencé à développer ou ont déjà développé de nouvelles méthodes de

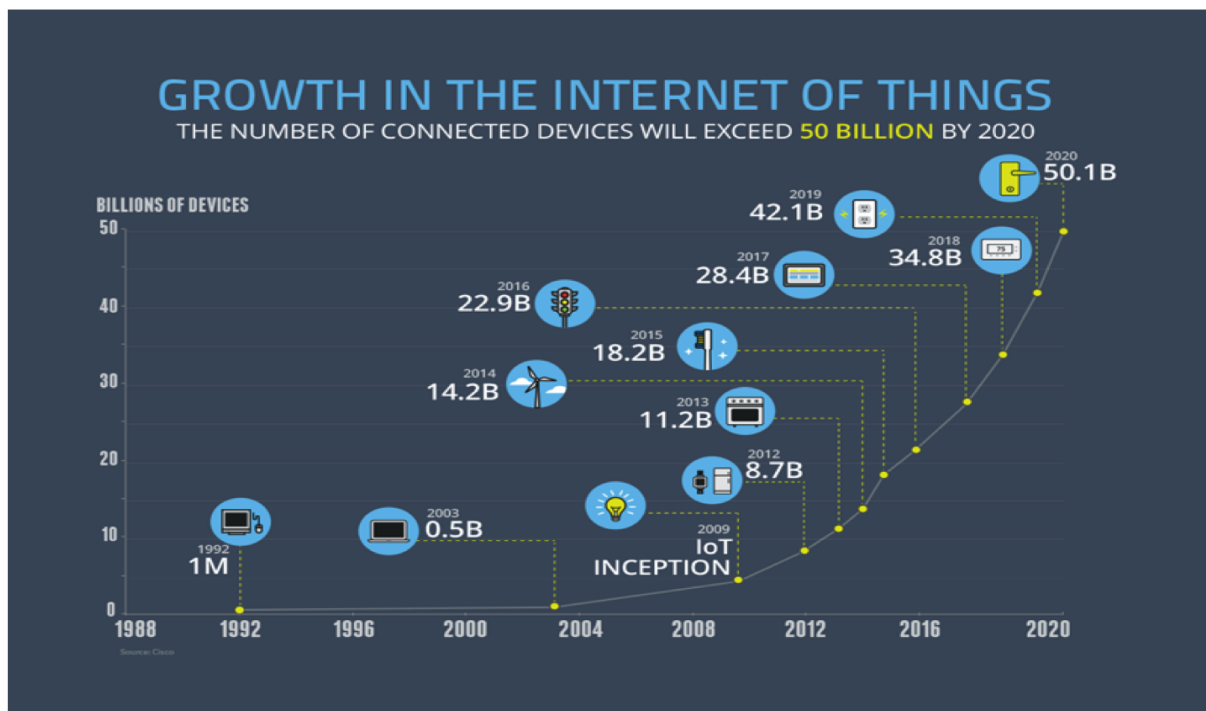


FIGURE 6.2: Marché de l'Internet des choses

communication apportant un soulagement aux problèmes de communication actuels et également permettre à ces dispositifs de se connecter entre eux. Nous citons par exemple, les technologies RFID, Near-Field-Communication, les technologies optiques (Li-Fi, la technologie optique bidirectionnelle de 40 Gbit / s de Cisco (BiDi [17])), la technologie basse consommation Bluetooth, les réseaux IP sans fil basse consommation, ZigBee, LTE-Advanced, WiFi Direct, HaLow, HomePlug, Ethernet. Parmi toutes les technologies mentionnées ci-dessus, il ya certaines qui ne peuvent pas être utilisées directement pour se connecter à Internet, mais peuvent communiquer entre elles. Si un périphérique doit se connecter à Internet, alors, il doit prendre en compte l'ancienne infrastructure qui a été développée. Ainsi, les périphériques qui doivent se connecter directement à Internet devront utiliser les technologies de base développées comme les réseaux IP sans fil à faible consommation d'énergie, LTE-Advanced, Ethernet et connexion par satellite.

Grâce à ces technologies, beaucoup de produits sont ou seront développés et utiliseront des objets embarqués avec des ressources limitées en CPU, mémoire et puissance. Ceci signifie que les IoTs trouvent des applications dans presque tous les domaines. [18]. On peut aussi dire que «Objet», dans IoT peut se référer à une grande variété de dispositifs qui affecteront différents domaines de la recherche.

Les applications potentielles pour les IoTs sont principalement dans le secteur de la défense et dans le secteur civil. Dans le premier, les applications potentielles concernent la sécurisation des frontières, les systèmes faciaux et biométriques automatisés pour contrôler l'immigration, les systèmes automatisés de démarrage / extinction et d'oubli qui permettent de sécuriser un pays. Il existe également des applications dans

la surveillance à distance et la surveillance des activités, les drones automatisés qui n'ont pas besoin d'interférence humaine ainsi que la création d'une plate-forme qui mènent à l'élimination potentielle du feu amical dans une zone de combat et les autres qui peuvent être utilisés dans le secteur de la Défense d'un pays.

Dans le secteur civil, les applications potentielles sont représentées dans la figure 1.1. L'une des applications possibles est les Smart Homes. Dans ce scénario, les dispositifs seront utilisés dans la domotique et la sécurité tels que le contrôle et l'automatisation de l'éclairage, le chauffage (comme le thermostat intelligent), la ventilation, les systèmes de climatisation (HVAC) et les appareils tels que la laveuse / sècheuse, fours ou réfrigérateurs / Congélateurs qui utilisent Wi-Fi pour la surveillance à distance. Les systèmes IoT pourraient également être responsables de l'exécution d'actions telles que les systèmes d'achats intelligents, la détection et le contrôle automatique du système HVAC, la gestion de l'électricité et de l'énergie, ainsi que les systèmes de transport [19].

IoT conduit à la création d'industries intelligentes en les aidant à améliorer le contrôle du réseau, la gestion de l'équipement de fabrication, la gestion des actifs et la situation comme la surveillance de l'environnement local pour certaines industries [20]. Les systèmes de contrôle numérique, la gestion d'actifs via la maintenance prédictive et l'évaluation statistique peuvent conduire à la création des Smart Grid. Ils permettent ainsi une optimisation énergétique en temps réel.

Ce Smart Grid intègre les communications, le contrôle et le traitement de l'information à travers divers systèmes de transport, c'est-à-dire l'interaction dynamique entre les composantes d'un système de transport permettant la communication inter et intra véhicule, le contrôle de la circulation intelligente, le stationnement intelligent, la gestion de la flotte, le contrôle des véhicules avec le conducteur de voitures, la sécurité et l'assistance routière. Tous ces outils mènent directement à la création de villes intelligentes [21].

Pour créer une Smart City, on a besoin d'un grand nombre d'appareils reliés entre eux par des dispositifs de couplage de réseaux intelligents. ces besoins concernent par exemple, la de gestion du trafic en temps réel. Dans le projet smart city, on peut aussi ajouter des applications comme la sécurité, l'énergie, la gestion de flotte, la signalisation numérique, le Wi-Fi public et la billetterie électronique [22].

La ville intelligente n'est pas complète jusqu'à ce que l'on puisse faire la surveillance environnementale et l'intégration des services de soins de santé.

L'un des principaux enjeux dans la ville intelligente est également la surveillance de l'environnement. L'IOT peut généralement utiliser des capteurs pour aider à la protection de l'environnement en surveillant la qualité de l'air ou de l'eau, des conditions atmosphériques ou du sol, et peut même inclure des domaines comme le suivi des mouvements de la faune et de la flore [25].

Dans les services de soins de santé, nous avons déjà vu une expansion des capteurs de surveillance de le domaine de la santé tels que la mesure de pression artérielle, la fréquence cardiaque à des capteurs avancés capables de surveiller les implants spécialisés [21]. On peut également utiliser ces capteurs pour améliorer la santé et le bien-être général des personnes âgées [26]. D'autres capteurs de consommation pour encourager la vie saine, comme des échelles connectées ou des moniteurs de cœur portables, sont également une possibilité avec l'IoT [27].

Notre travail qui est présenté dans cette thèse peut également s'inscrire dans la thématique de la création d'un capteur utilisable pour la surveillance de l'environnement ou de la santé des personnes. En général, un capteur est capable de faire un test sanguin ou un test de polluants d'eau ou d'air ou d'autres analyses médicales qui utilise un détecteur optique pour l'analyse.

Notre capteur optique qui sera introduit dans cette thèse est une combinaison de puce de Résonance de Surface Plasmons (SPR) et d'un spectromètre appelé CoBiSS. Les autres détecteurs SPR présents aujourd'hui sont des systèmes tels que les systèmes Biacore SPR (créés par GE) [29], Spreeta (créé par Texas Instruments) [30], SWIFT (créé par Floralis) [31], SPIRIT (Créé par Seattle Sensor Systems) [32]. Cette technique SPR peut détecter le plus possible des quantités traces de polluants ou de contaminants jusqu'à un certain nombre de molécules [33]. Cette puce SPR comme expliqué dans Chapter 4 est généralement de petite taille. La puce SPR pourrait utiliser avec un Spectromètre qui est un appareil pour mesurer un spectre ou un graphique qui montre l'intensité ou la phase de la lumière en fonction de la longueur d'onde ou de la fréquence.

On développe un détecteur optique et un spectromètre ou lamdameter plus précis, qui ne sont pas lourds. Ces appareils ne devraient pas avoir de pièces qui bouge. C'est un problème pour les autres appareils optiques dans des applications réelles et en temps réel. Il est également important que les capteurs soient immunisés contre les perturbations externes.

On a développé un nouveau Spectromètre et il est connu avec le nom de Spectromètre d'échantillonnage bi-directionnel couplé (CoBiSS) [Numéro de brevet WO2009127794A1] pour créer un capteur. Ce capteur avait initialement beaucoup de pièces mobiles. Il était utilisé en laboratoire mais il avait un grand potentiel. Cet capteur a été modifié pour supprimer toutes les contraintes comme les pièces mobiles (présentées dans la thèse). Cet appareil pourrait être la prochaine génération du spectromètre et peut révolutionner globalement le système de santé et d'environnement. Le fonctionnement du spectromètre CoBiSS est expliqué dans la section 1.1.

Le spectromètre optique est un dispositif pour mesurer un spectre de la lumière. c'est un graphique qui décrit l'évolution de l'intensité de la lumière en fonction de sa longueur d'onde ou de sa fréquence. Plusieurs types de spectromètres, mais ils sont basés généralement sur des techniques d'interférométrie optique très coûteuses

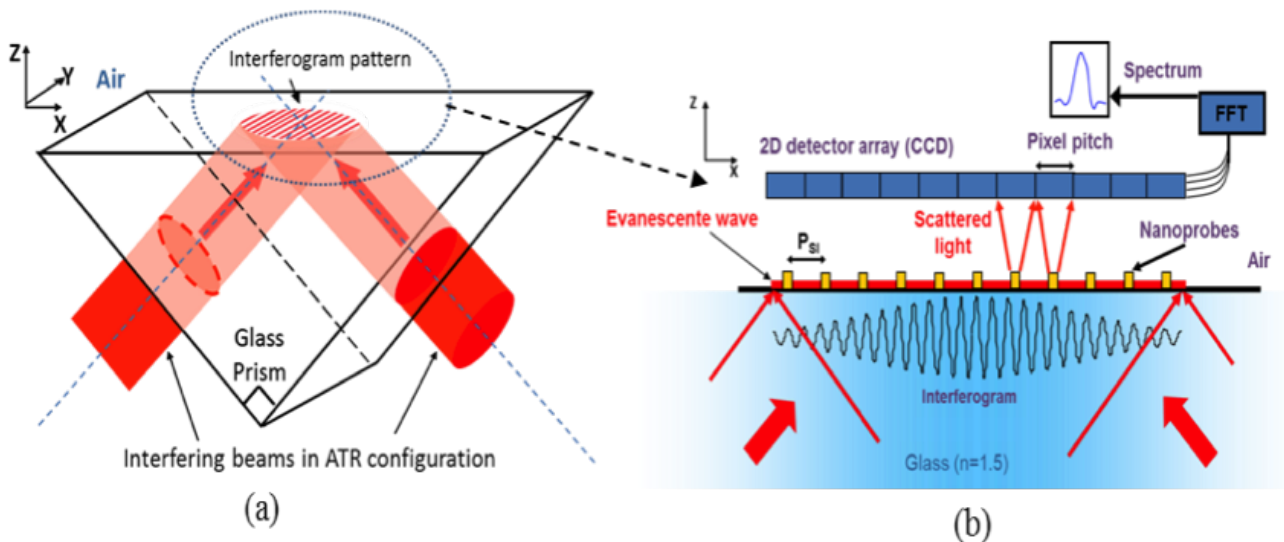


FIGURE 6.3: Explication de CoBiSS

et largement encombrant. En effet la résolution de ces spectromètres dépend en partie de la stabilité en température des éléments interférométrique très sensible. Ce qui rend compliquée leurs utilisation dans une future intégration dans un environnement en temps réel et en IOT.

Pour résoudre ces problèmes de sensibilité, d'encombrement et de résolution spectrale, une équipe de recherche au sein de département LNIO de l'université de technologie de Troyes s'était penchée sur ces questions et a travaillé sur une nouvelle technique de spectromètre. Ces travaux ont conduit au dépôt d'un brevet connu sous le nom de COBISS (Compact Bidirectionnal Sampling Spectrometer [brevet WO2009127794A1]). Cette technologie prometteuse dans sa première version est une démonstration des performances en terme de résolution. L'encombrement reste dans un premier temps non pris en compte (C'est la partie développée dans cette thèse). Dans sa partie tenant en compte l'encombrement, des travaux sont menés actuellement pour tenir en compte de cette contrainte très importante pour l'intégration du système et également pour la commercialisation du spectromètre. Le fonctionnement de ce spectromètre sera décrit dans les paragraphes suivants.

COBISS présente l'avantage d'être potentiellement utilisable dans le domaine de la santé, dans la surveillance d'environnement spécifique et également dans les Smart City. Le principe de fonctionnement de COBISS est basé sur un échantillonnage spatial en deux dimensions de l'interférogramme dû à l'interférence de deux faisceaux lasers à l'interface verre/air d'un prisme [35] [36] [37] [38]. L'image 6.3 décrit le principe de fonctionnement de COBISS. Des nano-structures métalliques déposées sur cette interface jouent le rôle d'un transducteur de champs électromagnétique. Elles transmettent l'information de l'intensité du champ évanescent à un capteur (caméra).

Le fonctionnement du spectromètre utilisé dans ces travaux de thèse est représenté

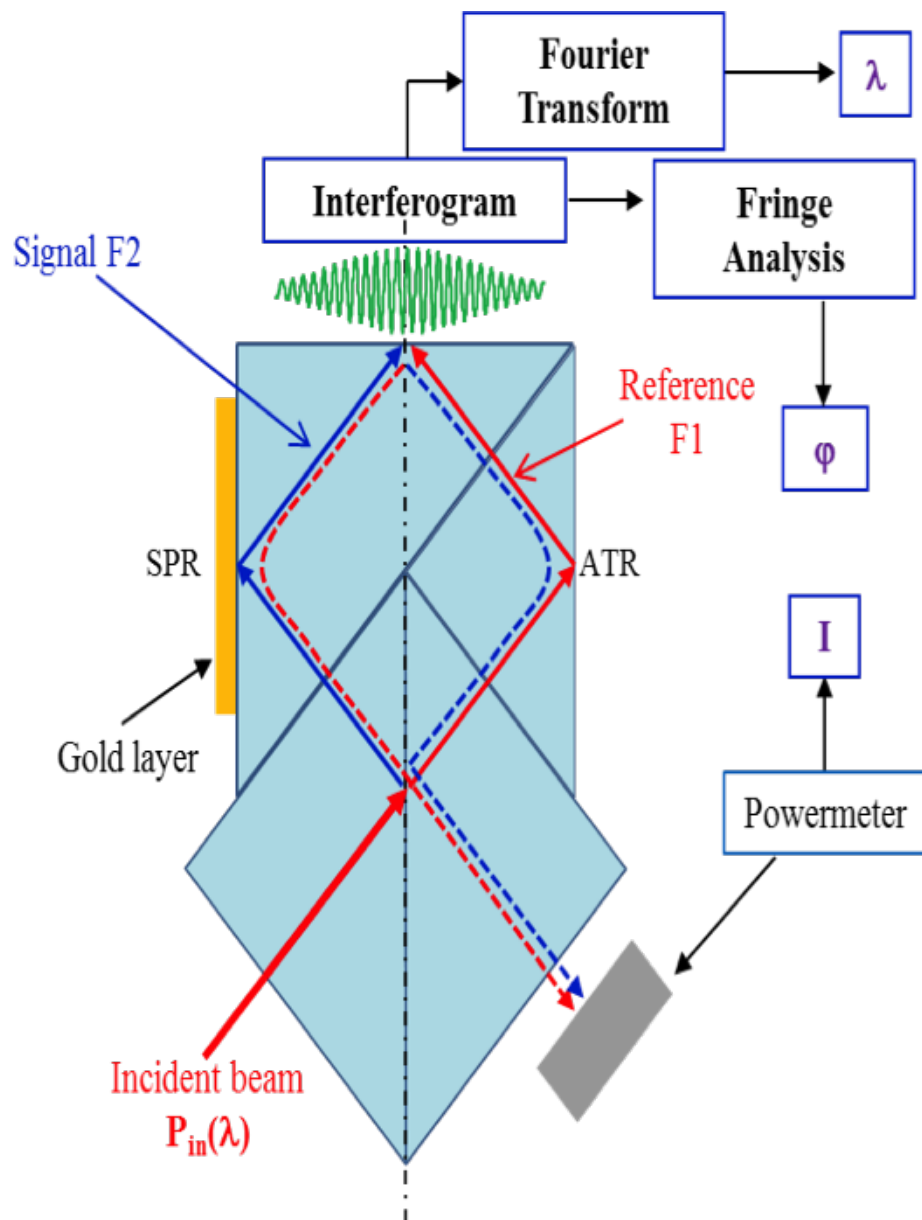


FIGURE 6.4: Méthode de travail de CoBiSS

dans la figure 6.4. le point de départ est un faisceaux laser incident perpendiculairement à un cube séparateur (BS). Ce dernier sépare en deux faisceaux de lumière que nous appelons laser 1 (rouge) et laser 2 (bleu). Les deux lasers se réfléchissent à l'interface verre/air des deux prismes (de gauche et de droite) et se rencontrent à l'interface du prisme de gauche. Les réflexion sur les interfaces verre/air sont des réflexions totale internes (TIR) dues essentiellement à la différence d'indice entre les deux milieux. TIR est remplie lorsque l'angle d'incidence $\theta = 45^\circ$ est supérieur à l'angle critique de l'interface verre / air.

Nous donc deux faisceaux se propageant dans deux sens opposés et une onde stationnaire est ainsi créée et donnant naissance à un interférogramme 2D (présenté en verre dans la figure6.4) sur les trois interfaces où il y a une TIR.

La partie évanescente de l'interférogramme est échantillonnée à l'aide d'un réseau

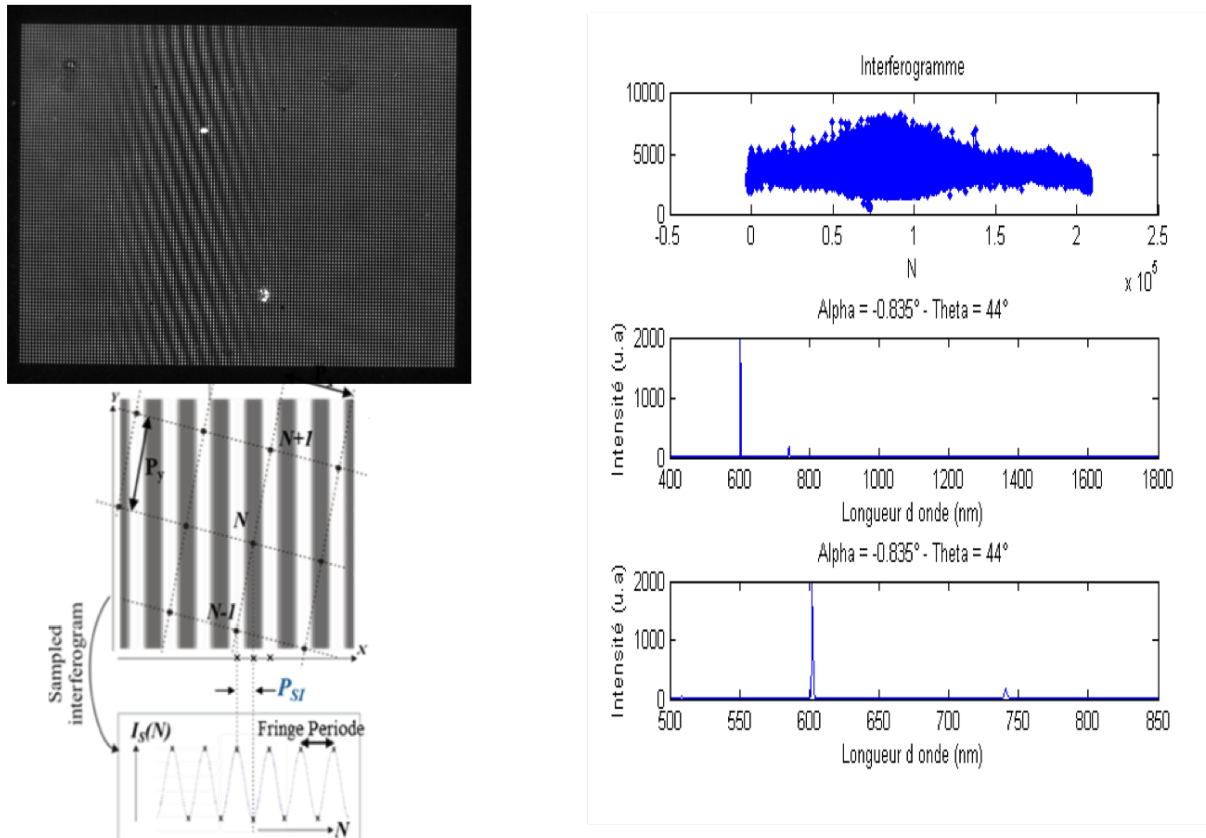


FIGURE 6.5: Explication du fonctionnement de CoBiSS

2D de nano-antennes optiques en champ proche, déposées sur la surface du prisme (Fig.6.3b). La lumière diffusée est alors détectée dans le champ lointain à l'aide d'une matrice de photodétecteurs 2D (Caméra) et enfin l'image 2D est chargée dans un script Matlab pour effectuer une transformation de Fourier sur l'interférogramme échantillonné.

Le système d'imagerie est ici un microscope suivi d'une caméra. Ce système n'est pas adapté pour une intégration et il va être remplacé directement par une approche directe d'une caméra aux nano-antennes métalliques comme le montre la figure 6.6. Nous avons réalisé un test en plaçant la caméra à différentes hauteurs de la surface. Nous avons constaté la présence de plusieurs images du même réseau comme le montre la figure 6.7. Ces images tendent vers une lorsque l'on s'approche à la surface de la caméra.

Dans l'idéal, nous devons avoir une seule image du réseau de nano-structure, mais, avec cette caméra, nous n'avons pas pu l'observer pour deux raisons. La première concerne la présence d'une lamme de verre de protection de la surface du capteur CCD. Ceci nous a empêché d'être le plus proche aux réseaux de nano-structure. Pour la seconde raison, il s'agit en effet de la présence d'interférences entre des nano-particules. Afin de réduire ces interférences, nous avons besoin de trouver la nano-particule la plus optimisée en terme de diffusion de la lumière et de sa directivité. Pour résoudre ces deux problèmes, nous avons travaillé sur une nouvelle caméra sans couche de protection de verre. Cette caméra a des dimensions exactes et nous avons également la

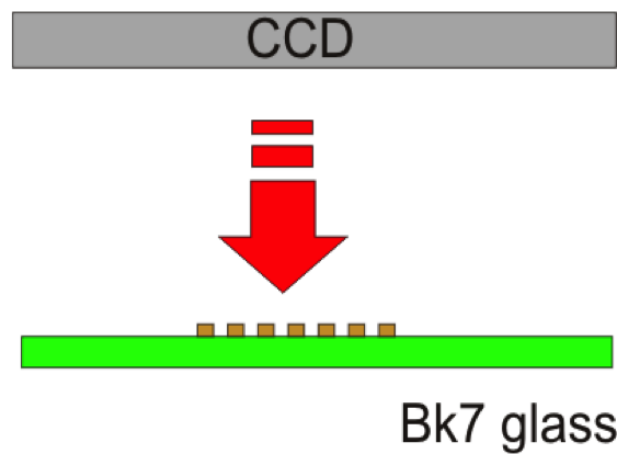
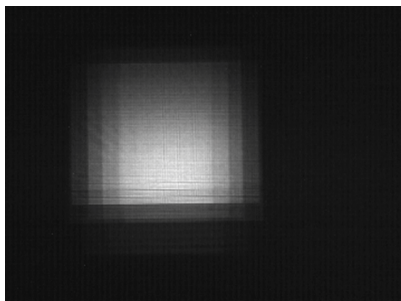
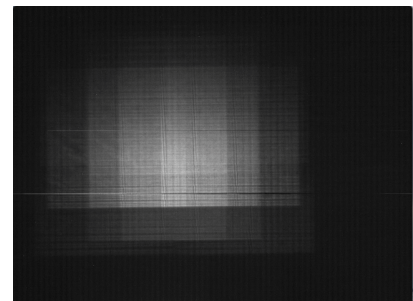


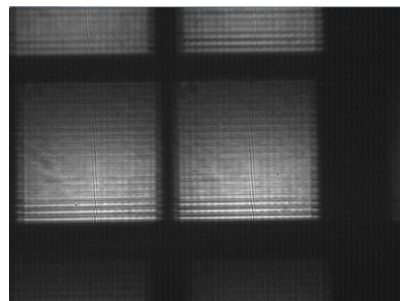
FIGURE 6.6: Le positionnement de la caméra avec Verre Slab



(A) Position la plus proche 1



(B) Hauteur intermédiaire



(C) Hauteur la plus éloignée

FIGURE 6.7: Exemple d'images trouvée par hauteur variable

liste des ses fonctionnalités et le logiciel pour le développement. La question à résoudre maintenant est l'optimisation de la diffusion de lumière des nano-particules.

Pour cela, nous avons dans un premier temps, un besoin de comprendre théoriquement comment un dipôle rayonne la lumière lorsqu'il est placé au-dessus d'une interface et qui est parallèle ou perpendiculaire comme le décrit la figure 6.8. Dans ce scénario, le plan d'observation et le plan où les dipôles sont placés sont les mêmes. Un modèle de calcul théorique a été utilisé pour calculer les diagrammes de rayonnement.

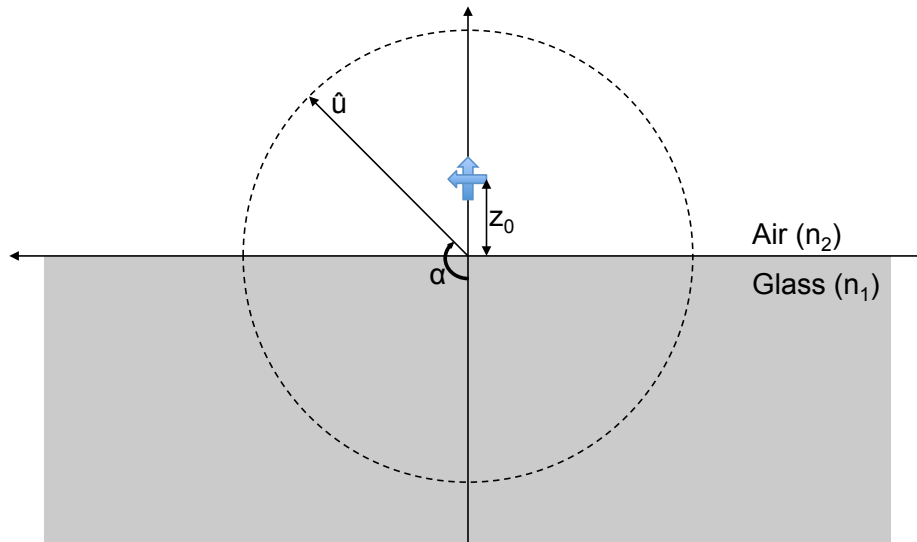


FIGURE 6.8: Dipole-substrate geometry.

Premièrement, on a placé un dipôle très loin de interface en l'air et on observe le Figure 6.9 comme le diagramme de rayonnement. Maintenant, le dipôle est placé très près de la surface d'interaction qui est perpendiculaire à la surface, on voit, dans le Figure 6.10, deux lobes symétriques dans le diagramme de rayonnement.

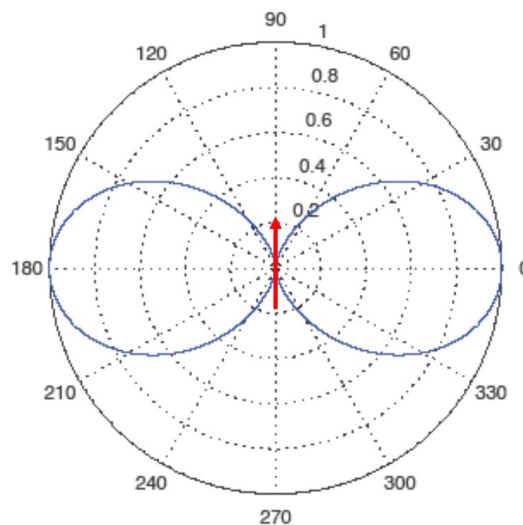


FIGURE 6.9: Radiation Diagram of a dipole in Air.

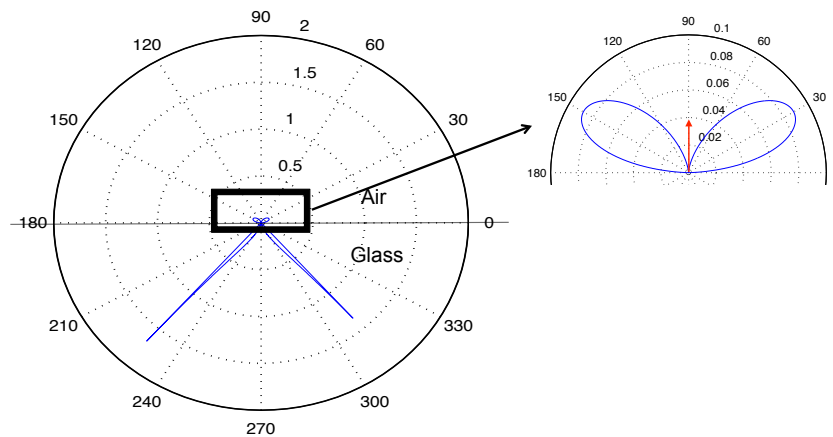


FIGURE 6.10: Radiation Diagram in the plane XZ and a Dipole is placed perpendicular to the interface.

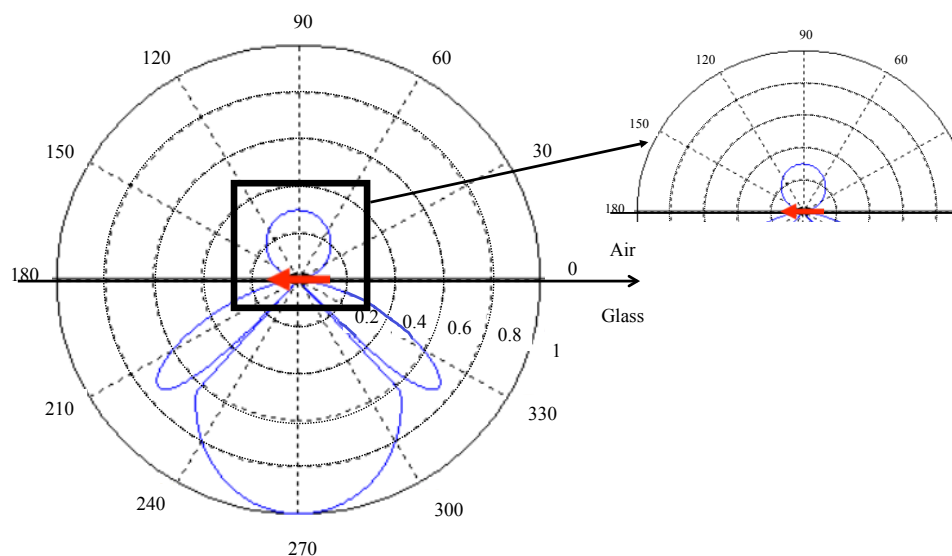


FIGURE 6.11: Radiation Diagram in the plane XZ and a Dipole is placed parallel to the interface.

Le dipôle est placé parallèle à la surface change qui est près de la surface d'interaction, la direction des lobes change également jusqu'à ce qu'elle devienne un lobe central dans le Figure 6.11.

Maintenant, on va aborder le cas où nous avons 2 lasers qui venant des côtés opposés dans le verre. Ces deux lasers sont incidents avec un angle de 45° . Si les deux lasers n'ont pas de différence de phase entre eux, alors une interférence constructive est produite au centre du prisme (voir la figure 6.12). Dans un autre cas, où les deux lasers sont en déphasage, c'est-à-dire que la différence de phase est de 180° . On voit une interférence destructive et cet effet d'interférence destructive comme le montre la figure 6.12. Dans les deux cas, nous plaçons une nano-particule au point 0 qui est le centre du prisme dans l'air.

Avec les études de taille, matériaux et forme, nous avons trouvé que la nano-particule devait être de la forme rectangulaire, en or et avec une longueur de 150 nm

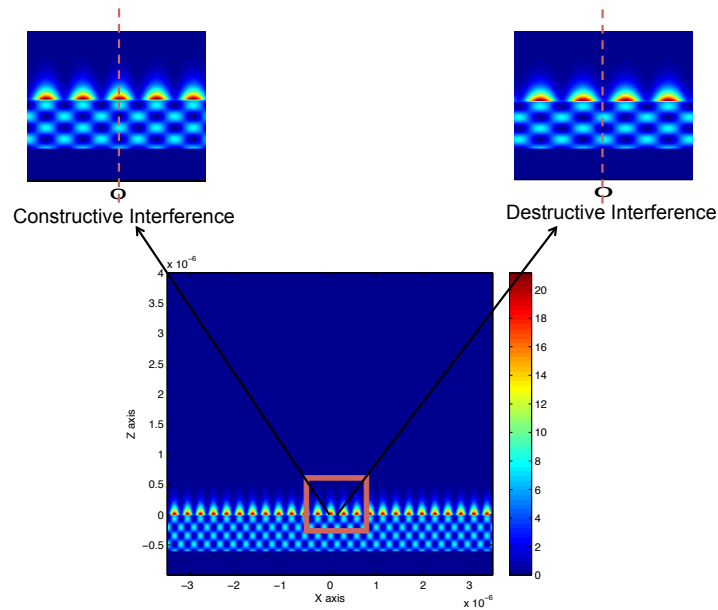


FIGURE 6.12: Normalized intensity of the standing wave above and below the interface at $z = 0$.

et une hauteur de 100 nm.

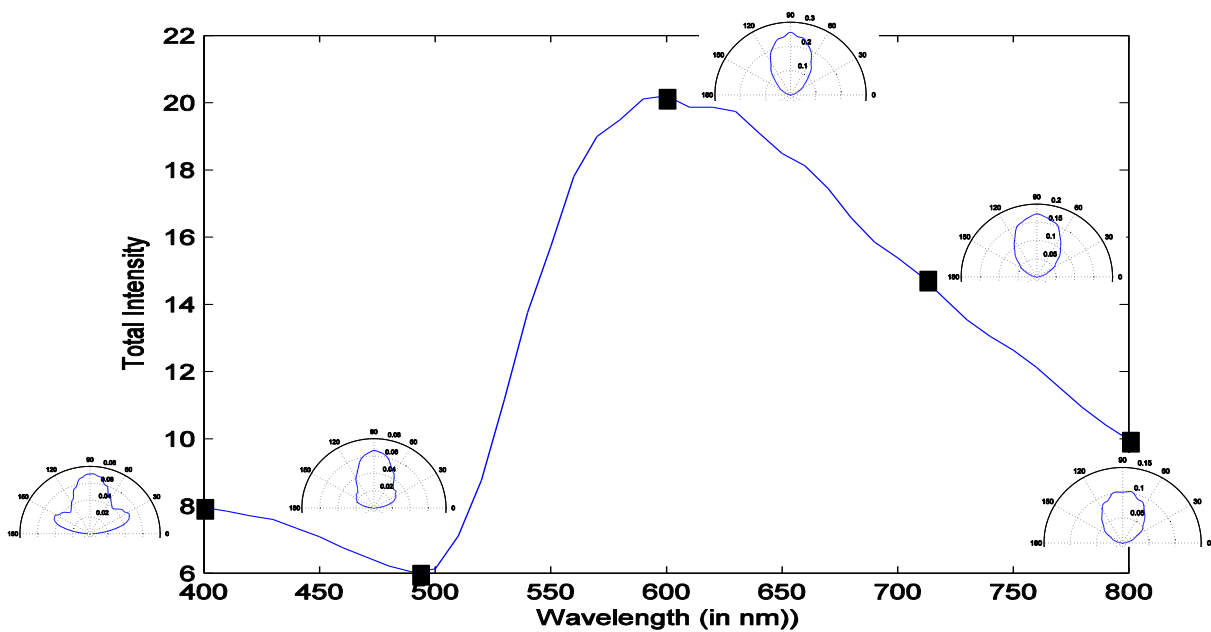


FIGURE 6.13: Diagramme de rayonnement pour la nano-particules d'or rectangulaire de longueur = 150 nm et hauteur = 100 nm dans une interférence destructive qui change en fonction de la longueur d'onde de la courbe d'intensité

Pour cette nano particule sélectionnée, les simulations ont été effectuées en changeant la longueur d'onde du laser de 400 à 800 nm. L'intensité totale avec le changement de diagramme de radiation sont observés pour l'interférence destructive dans la figure 6.13. Nous avons également calculé les simulations pour les interférences construc-

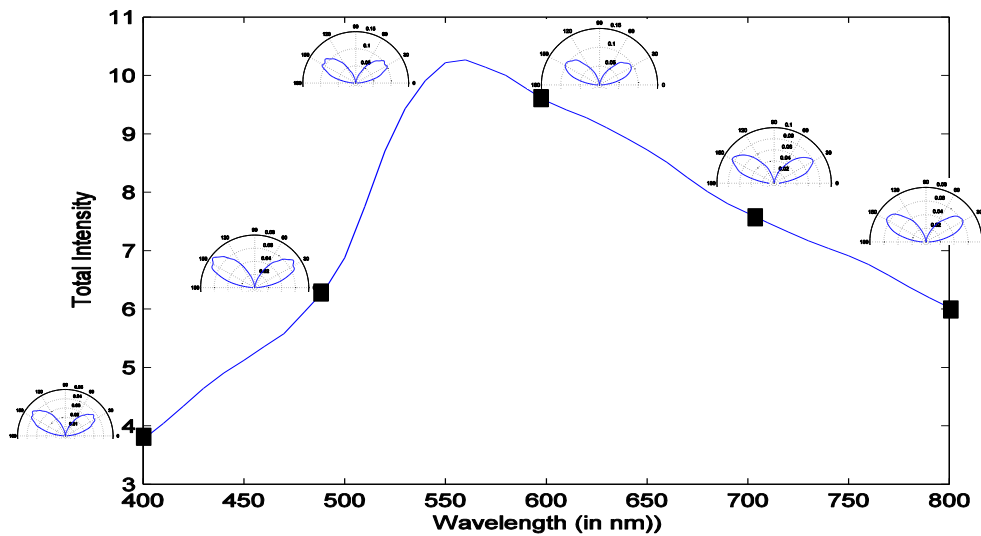


FIGURE 6.14: Diagramme de rayonnement pour la nano-particules d'or rectangulaire de longueur = 150 nm et hauteur = 100 nm dans une interférence constructive qui change en fonction de la longueur d'onde de la courbe d'intensité

tives et l'intensité totale avec le changement de diagramme de radiation est observée pour l'interférence constructive dans la figure 6.14.

Une fois les simulations sur les diagrammes de rayonnement de toutes les longueurs d'onde sont terminées , nous avons calculé

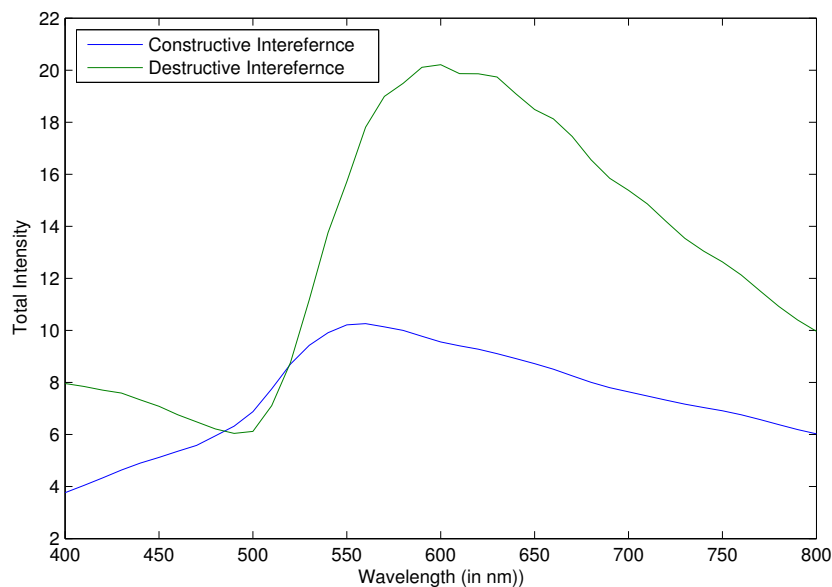


FIGURE 6.15: Intensité totale en fonction de la longueur d'onde pour une nano-particule de longueur = 150 nm et hauteur = 100 nm. Comparaison des particules dans l'interférence destructive et constructive.

Le carte d'intensité present dans la figure 6.15 montre qu'elle est plus grande dans le cas d'interférence destructive et avec presque deux fois la valeur maximale de l'intensité du cas des interférences constructives. Ces différentes courbes nous permettent de bien

choisir la plage de fonctionnement en longueur d'onde de la directivité et de l'intensité les plus optimales.

Une fois que nous avons déterminé les capacités de détection de l'appareil (Spectromètre) avec la particule rechercher, il est temps d'intégrer l'ensemble du dispositif en travaillant ensemble avec l'aide de l'électronique et l'intégration de logiciels. Pour ce travail une petite étude a été faite pour trouver les corrects système embarquées, l'écran tactile, les appareils-photo et les lasers.

Après cette étude, nous avons acheté ce qui suit:

- Camera: Imaging Source cameras (premier essai), camera envoyer par RSS
- Laser: Finanium, MiniLAs Evo
- System Embarqué: Pandaboard ES, UDOO Quad avec écran tactile

Après avoir sélectionné ces périphériques, nous avons créé un logiciel qui utilise le processeur embarqué avec le chipset pour lancer une connexion avec le laser et l'appareil photo. Une fois le laser est lancé et la puissance sélectionnée, la caméra capture l'image de la lumière rayonnée par les reseaux de nanoparticules d'or. Dès que la caméra capture une image différente de celle d'un bruit, le logiciel présent dans le chipset embarqué arrête la caméra et le laser pour réduire l'énergie et la chaleur. Un organigramme de ce processus est illustré à la figure 6.16.

En utilisant cette image de base, d'autres techniques de traitement d'image et de traitement du signal sont appliquées pour le calcul d'images. Initialement, la méthode de Lomb scargle a été utilisée. Un exemple de calcul est illustré à la figure 6.17. Cette méthode est utile quand la distance entre la caméra et la nanoparticule d'or est très proche.

La deuxième méthode qui est plus généralisé est connu comme méthode microspectromètre. Dans cette méthode, l'image capturée est comparée à toutes les images de toutes les longueurs d'onde présentes après une étape de calibration. Le calcul sort l'image la plus proche (ressemblance) à celle que nous cherchons et nous donne ainsi sa longueur d'onde la plus proche de la longueur d'onde que nous recherchons (image déjà présente). Un exemple de cette méthode de calcul est illustré à la figure 6.18. Une petite modification sur ce code a été réalisée pour ajuster automatiquement l'intensité de l'image pour augmenter la robustesse du code.

Il est ensuite important de créer une interface utilisateur graphique (GUI) où toutes les fonctions peuvent être exécutées ensemble et qui soit facile à exécuter pour les utilisateur. Dans cette interface graphique (vue de la Figure 6.19) créé principalement pour faire des tests. Quand le bouton de démarrage est activé ou touché, le laser et l'appareil photo démarrent et le bouton d'arrêt afterwards arrête les deux. Sur le côté gauche, on voit l'image capturée par la caméra et le bouton de calcul effectue le calcul. Nous

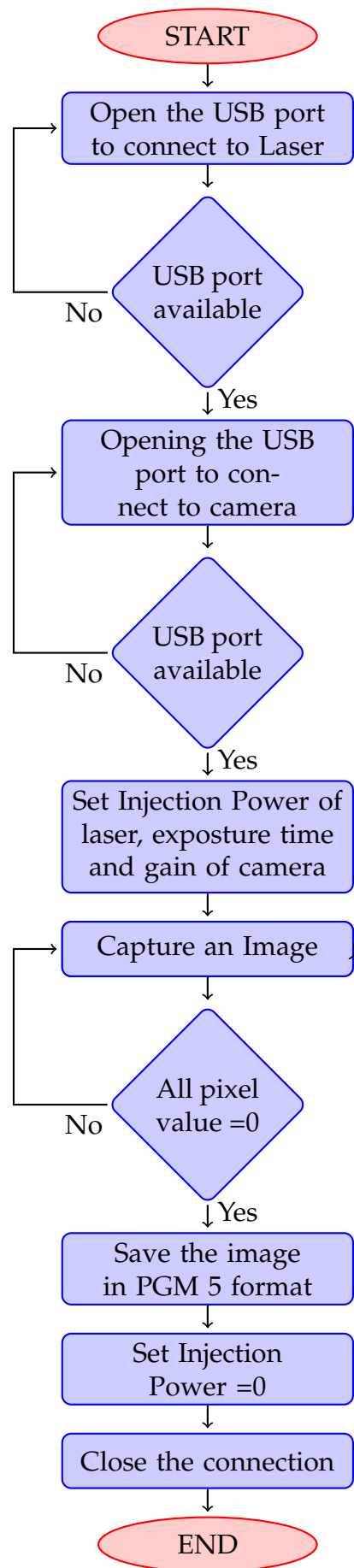


FIGURE 6.16: Diagramme du code qui contrôle le laser et l'appareil photo ensemble

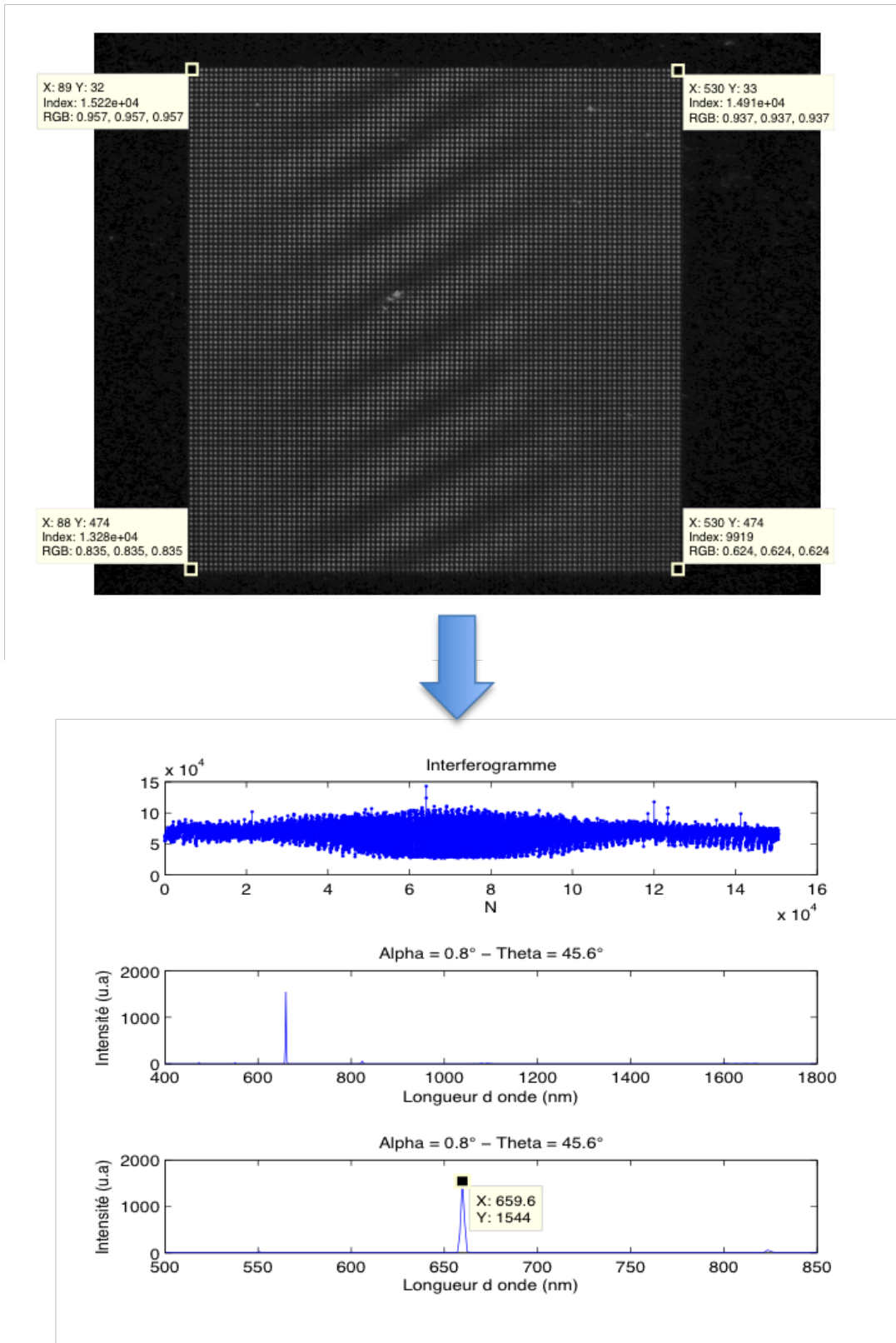


FIGURE 6.17: Calcul d'un spectre à l'aide d'une image à l'aide de la méthode de lomb scargle. La longueur d'onde utilisée était de 660 nm.

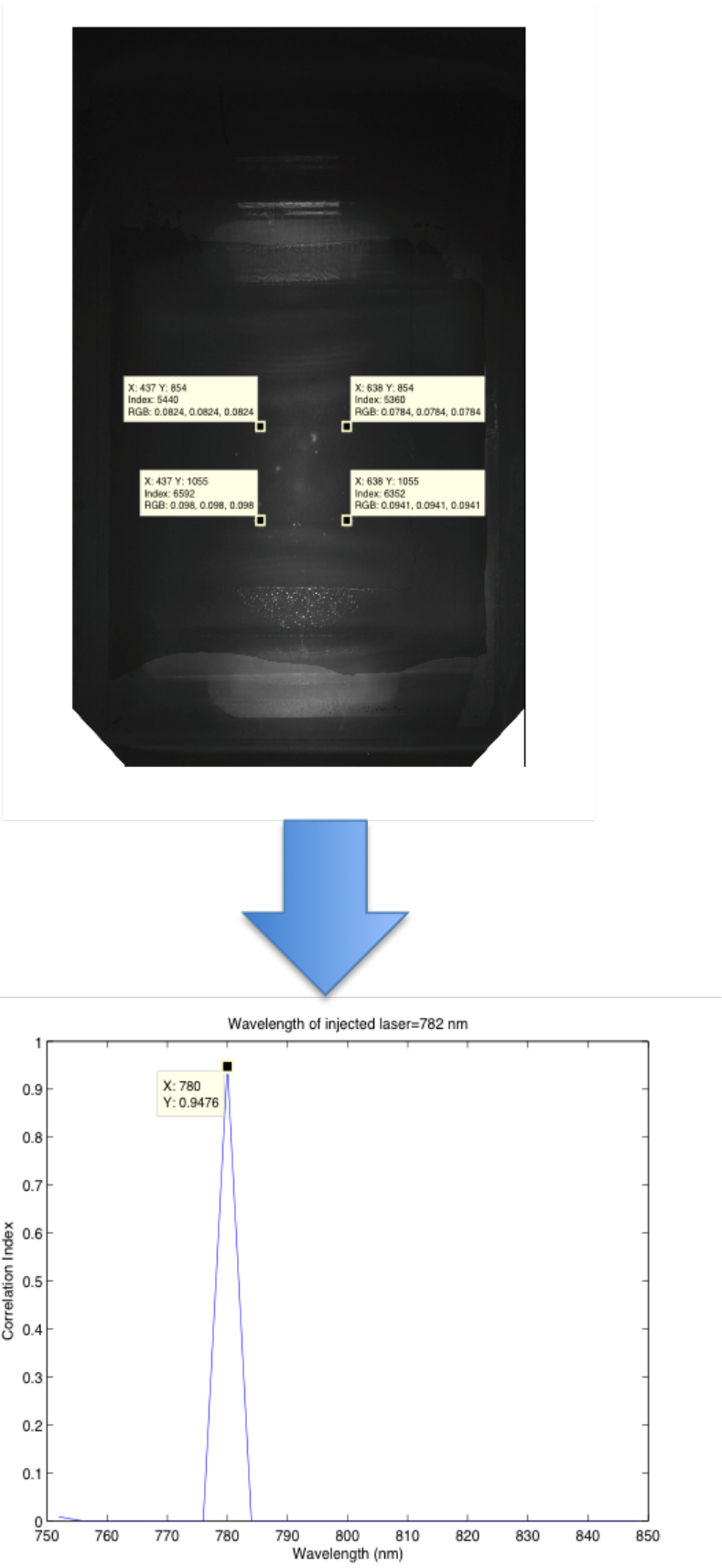


FIGURE 6.18: Calcul de Microspectrometre

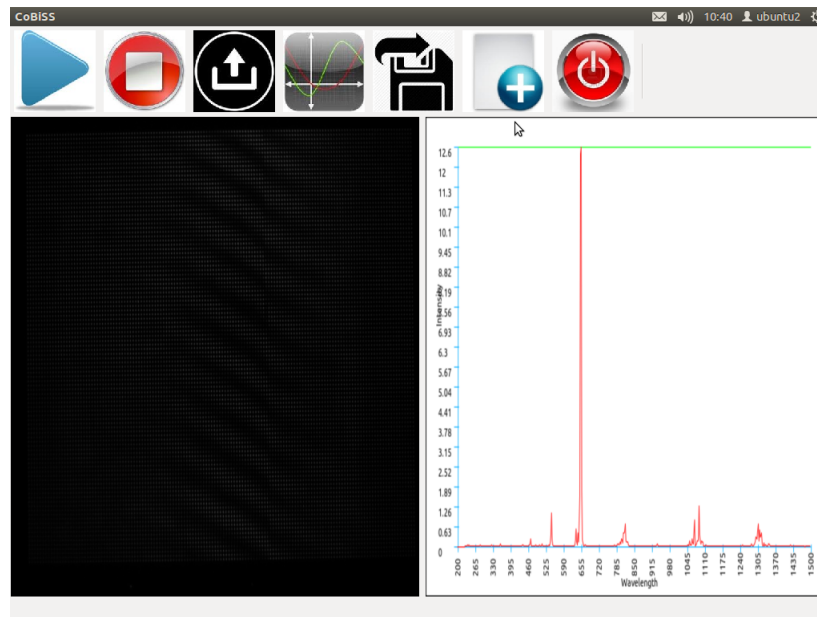


FIGURE 6.19: l'image graphique de l'utilisateur de l'interface quand alors le calcul d'une image est réalisée pour donner le spectre de longueur d'onde d'intensité en utilisant Calcul de Lomb Scargle.

avons ajouté la fonctionnalité de sauvegarde d'image avec le choix du format (png et texte).

Jusqu'à présent, nous avons discuté de l'optimisation du dispositif pour le calcul de longueur d'onde, maintenant nous ajouterons la partie de détection à ce capteur. Pour cette partie, nous utiliserons un capteur SPR qui travaille sur la réflexion interne totale. Cela a été démontré dans la figure 6.20. Pour ce travail nous utiliserons deux structures différentes:

- Gold Slab
- Structure "W"

Les différences principales entre ces deux structures sont:

- Dans la Gold Slab, seule l'épaisseur d'or est variable
- Dans la structure "W", l'angle d'ouverture, la longueur de la structure et l'épaisseur de l'or sont variables.

Comme nous l'avons indiqué dans la Gold slab, il y'a une seule variable qui est présente et qu'est utilisée pour optimiser la réflectance dans le cas d'un laser qui a un angle de 45 en verre. Nous avons essayé d'optimiser le paramètre d'épaisseur de la couche d'or pour cette configuration. A partir des simulations, les résultats indiquent que l'épaisseur optimale est de 43,5 nm.

Dans le cas de la structure "W", il existe trois variables différentes qu'on peut optimiser. Pour nos simulations, l'angle d'ouverture est constant à 32°. Nous avons fait

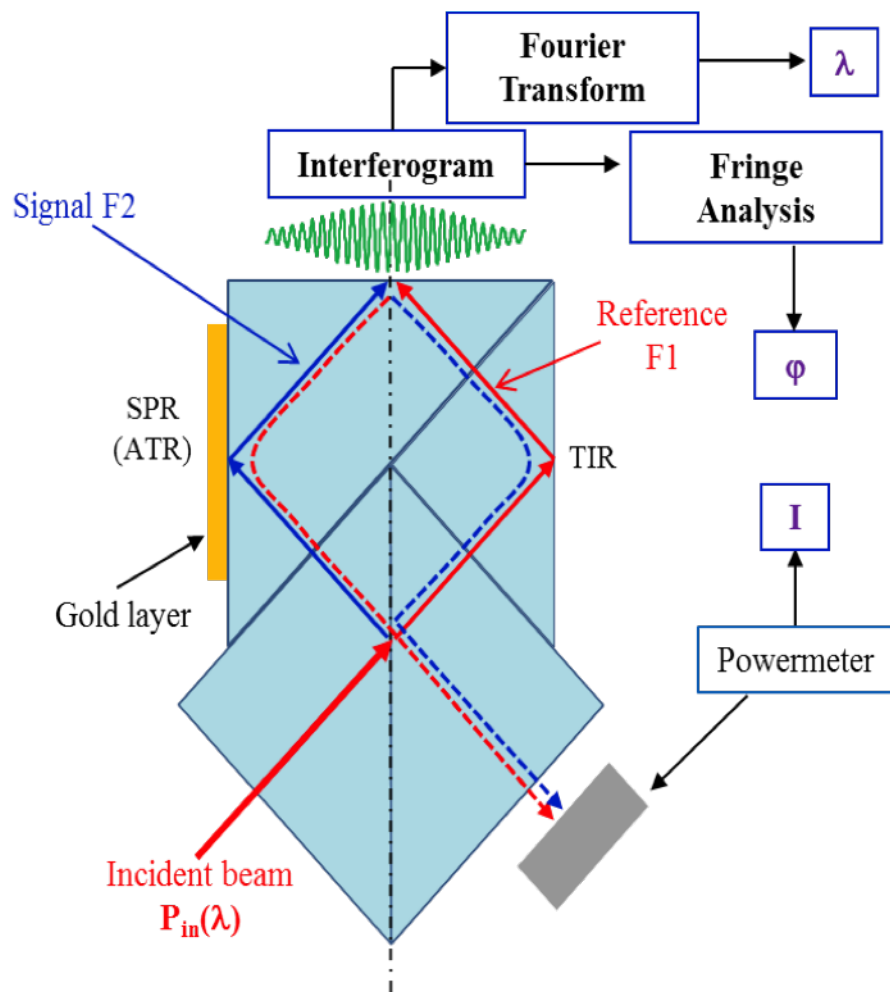


FIGURE 6.20: CoBiSS modifié pour la détection de SPR

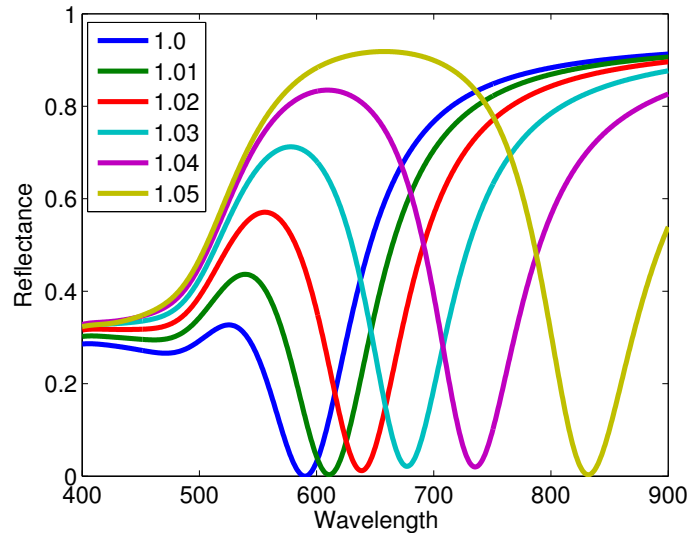


FIGURE 6.21: Graphique montrant l'effet de la réflectance avec la variation de la longueur d'onde pour l'indice de réfraction multiple de la couche au-dessus de la dalle d'or qui varie de 1 à 1,05 respectivement.

varier la longueur de la structure et l'épaisseur de la couche d'or. Nous avons varié la longueur de la structure à 400, 600, 800 et 1000 nm et pour chaque longueur, nous avons essayé de trouver l'épaisseur la plus optimisée de la couche d'or. Ensuite, nous avons comparé la longueur de la structure avec l'épaisseur la plus optimisée de la couche d'or pour déterminer la longueur la plus optimisée de la structure. A partir des résultats des simulations, nous avons trouvé que la longueur de structure la plus optimisée est de 600 nm et avec une épaisseur d'or de 25 nm.

Nous avons aussi simulé une variation de la structure "W", où les bords sont arrondis de 5 nm. C'était nécessaire car aucune fabrication ne donne des bords parfaits. Pour cette structure, nous avons trouvé que la longueur de structure la plus optimisée est de 600 nm et avec une épaisseur de 25 nm. Cela signifie que pour les besoins des simulations nous pouvons utiliser la structure "W".

Après avoir trouvé l'épaisseur et la longueur optimisées pour la structure "W" et l'épaisseur optimisée de la couche d'or, nous avons commencé à travailler sur le calcul de sensibilité. Pour les calculs de sensibilité, nous avons modifié l'indice de réfraction des superstrat de 1 à 1,05. Les résultats pour la couche d'or sont représentés sur la figure 6.21 et pour la structure "W" est représenté sur la figure 6.22.

Ces résultats indiquent que pour une analyse large spectre, on doit utiliser la couche d'or mais pour l'analyse où en utilisant une seule longueur d'onde, la structure "W" est meilleure (expliquer dans le chapitre 4).

Cela crée un dispositif autonome que l'on peut utiliser sans l'Internet, mais comme nous souhaitons tendre vers les IoTs, nous avons ajouté la fonctionnalité d'envoyer les résultats et les images sans fil dans le Appendix ??

Tout ces éléments nous a amené à créer un dispositif qui peut être utilisé pour l'IoT.

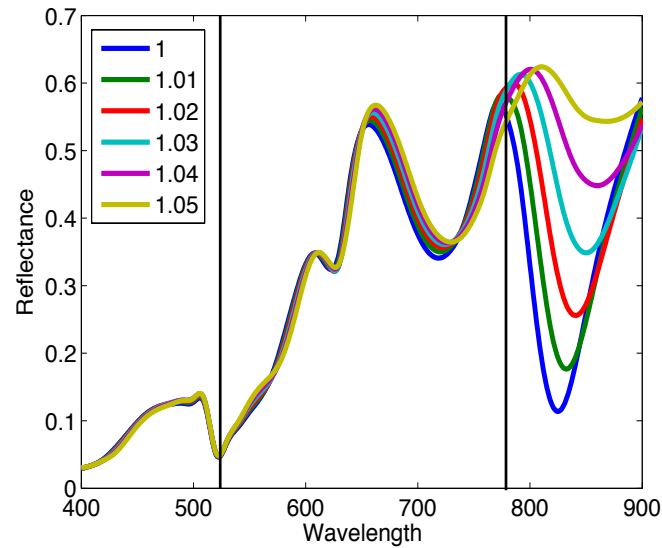


FIGURE 6.22: Analyse de sensibilité pour la structure W avec une longueur de structure de 600 nm et un rayon de courbure de 0 nm. Le graphique montre l'effet de la réflectance avec la variation de la longueur d'onde pour l'indice de réfraction multiple de la couche au-dessus de la structure en or "W" qui varie de 1 à 1,05 respectivement.

Ce dispositif est trop basique et agit comme l'épine dorsale du développement futur. Il nécessite d'être adapté en fonction de l'application finale de ce dispositif. Il est donc très nécessaires pour créer un dispositif fonctionnel avec toutes les capacités de détection d'avoir et d'aborder ces éléments :

- Pour la détection et la réduction des erreurs, plusieurs lasers et le calcul permettant de calculer simultanément plusieurs longueurs d'onde doivent être ajoutés / améliorés.
- Pour les aspects de détection, nous pouvons avoir plusieurs zones localisées et chaque zone est fonctionnalisée pour différentes molécules. Ces zones se trouveront dans une zone spécifique pour le calcul de la détection. Cela pourrait améliorer les capacités de ce dispositif pour détecter plusieurs marqueurs / molécules dans le même temps. Cela pourrait effectivement réduire le coût.
- Pour la partie de détection SPR, la fonctionnalisation de " Gold slab" ou de la structure "W" doit être effectuée pour attirer la molécule à détecter.
- Pour la partie de communication, comme nous avons créé le réseau sans fil de base, nous devons d'abord trouver les applications sur lesquelles ce dispositif fonctionnera et, en conséquence, ajouter les capacités supplémentaires.

Les deux derniers points vont changer selon le domaine d'application dans laquelle le dispositif sera finalement placé. Nous pouvons comprendre cela en prenant quelques domaines dans lesquels cet appareil peut être utilisé:

- Industrial IoT: Prenons un exemple de l'industrie des mines de charbon où les émissions de CO sont étroitement surveillées. Dans cet exemple, le dispositif doit être fonctionnalisé pour capturer des particules de CO et une seule zone de détection est requise. Pour l'application, le périphérique doit communiquer avec d'autres périphériques et finalement avec les serveurs présents dans un autre emplacement. Cela utilisera le mode de réseau de capteurs sans fil et un petit système de son doit être intégré pour les alarmes d'évacuation.
- Détection de l'environnement pour les villes intelligentes: Nous pouvons avoir ce dispositif fonctionnalisé dans différentes zones localisées où ce dispositif peut détecter différentes molécules comme le CO, NO₂, SO₂, etc à partir du même périphérique. Comme la partie de communication va pour le dispositif, il peut être divisé en deux scénarios différents où le dispositif est présent dans:
 - Dans les zones urbaines: Toute l'infrastructure de réseau existe déjà, par conséquent, le dispositif peut communiquer directement avec les serveurs et envoyer toutes les données. Le dispositif peut fonctionner dans le modèle de réseau de serveur de client.
 - Dans les zones rurales ou insuffisamment développés: L'infrastructure de réseau ne peut pas être pleinement développée, l'appareil doit fonctionner dans le mode de détection sans fil lorsque l'appareil se connecte en mode adhoc et aussi quelques dispositifs agissent comme des points d'accès pour se connecter à l'infrastructure existante. Dans ce cas, on peut ajouter la fonctionnalité de détection d'erreur et de correction automatique du dispositif en analysant les données provenant d'autres dispositifs. Cela pourrait être nécessaire car on ne peut pas avoir des gens équipés pour faire des corrections dans le dispositif dans les zones reculées.
- Smart Healthcare: Nous pouvons avoir ce dispositif fonctionnalisé dans différentes zones localisées où ce dispositif peut détecter différentes molécules dans le sang avec l'aide de fluides micro et cela peut être fait à partir du même dispositif. Cet appareil peut être créé dans deux formats différents:
 - Dispositif autonome: Nous pouvons avoir un petit écran tactile attaché à ce dispositif avec l'application d'utilisateur graphique qui commence quand l'utilisateur veut et envoie les données à leur nuage personnel et à l'hôpital ou au docteur avec l'aide de la connexion de serveur de client.
 - Petit appareil: Nous pouvons créer une application pour le téléphone mobile / tablettes / ordinateur où la partie de détection est attachée au téléphone mobile et peut faire la détection selon l'utilisateur souhaitent et envoyer les données à leur nuage personnel, à leur médecin.

Cela pourrait aider les gens occupés ou loins des spécialistes, des médecins qui peuvent faire des tests partout où ils sont présents et aussi pour les services d'urgence.

Comme nous savons que ces domaines où ce dispositif peut être utilisé dans Internet des choses ont juste commencé et sont encore à venir dans l'image globale. Ce sera l'avenir de l'IOT et permettra de générer un marché spécifique en soi. Comme le marché mondial est actuellement en mouvement vers des dispositifs intelligents et un grand nombre de personnes et d'autres organisations serait intéressé à acheter ce genre de dispositifs.

Appendix A

Selection of Nano Particle for CoBiSS

In this section, we try to understand how the nano-particle behaves or resonates with the light (evanescent standing wave) received towards the camera. Here, we try to explore different types of shapes, materials, sizes and formats which are possible for nano-particles with the help of radiation diagrams.

For these calculations, we use constraints like the wavelength, that is, used for the simulation is 600 nm and by using 2 lasers of same wavelength coming from 2 different directions at an angle of 45° , as seen in Figure 2.9. The wavelength of 600 nm is used due to the fact that it is the mean value between the observation wavelength range of 400 nm to 800 nm.

It should also be noted that the FDTD Simulations take a large amount of time and memory, only 2D simulations were performed initially to determine the dimensions of nano-particles. In 2D simulation, the particle's width is considered to be infinite due to this reason the interaction of an s-polarized light will not occur. The simulations were performed for p-polarized light to fix the length, height, shape and material. It still leaves us to determine the width of nano-particle which is done with the help of 3D simulation. While performing these simulations, the mesh size was taken as a constant value of 5 nm for all the directions, that is, X, Y and Z.

In the following, we will present the study which justifies the choice we have made for the nanoparticle in the previous part and for the fabrication.

A.1 Shape

As we have too many parameters to be determined, we have started this journey by determining the shape of the nano-particle to be used. As we know that the volume of the nano-particle needs to be constant for comparison of radiation patterns. Here, as we are using 2D simulation method where the width of the nano-particle is considered infinite. Due to this reason, constant surface area is used for comparison between different radiation diagrams of various shapes.

With 2D simulation, there are only 3 different shapes that can easily be manufactured and shown in the Figure A.1. Those are :

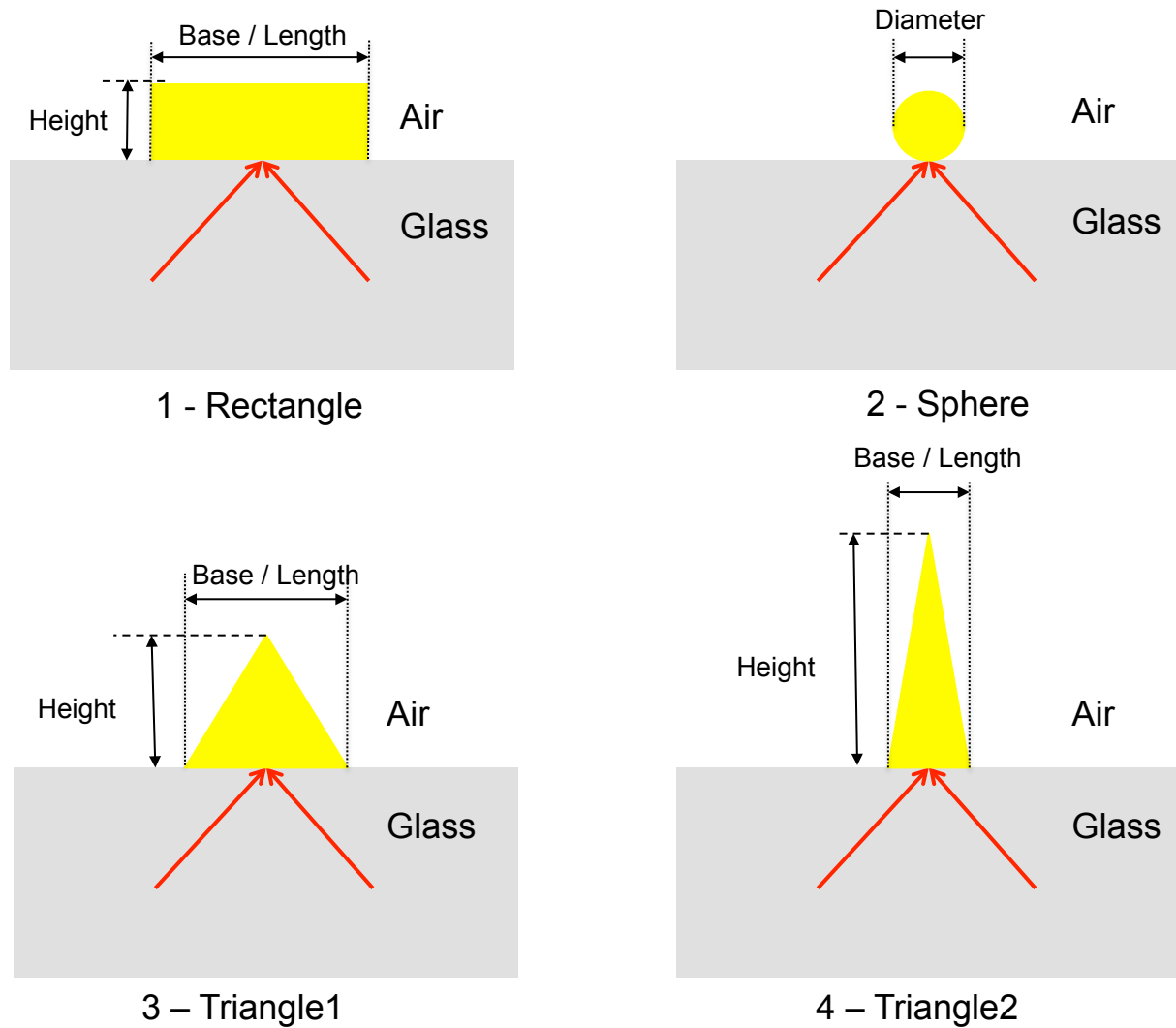


FIGURE A.1: The image representing the forms of the particles.

- Rectangle
- Sphere
- Triangle.

We simulate a rectangle of base 150 nm and height 100 nm respectively. As we have already said that the surface area of these shapes needs to be constant, the radius of sphere becomes 69.10 nm and for triangle there are various possibilities but we are considering only two that are isosceles, namely:

- Triangle1 : The base becomes 200 nm and height is 150 nm.
- Triangle2 : The base becomes 100 nm and height is 300 nm.

The radiation diagrams of these shapes are plotted in the Figure A.2 for destructive and constructive interference. With the observation of these radiation diagrams, one can observe that the destructive interference is more directional towards the top

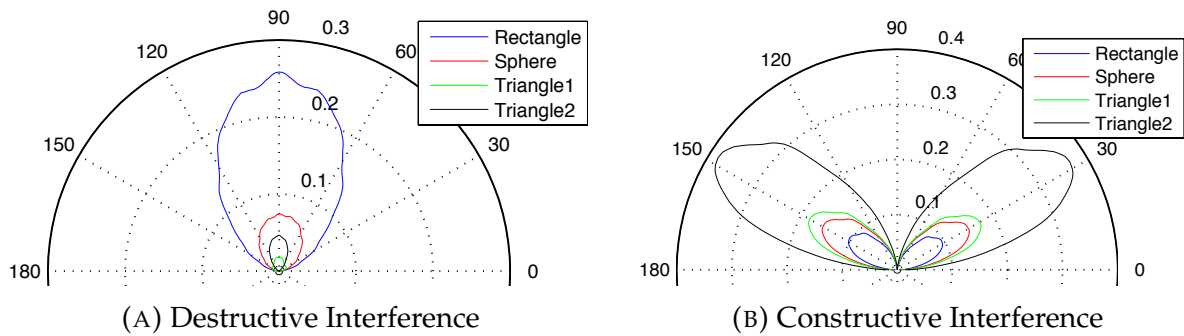


FIGURE A.2: Radiation pattern of different nano-particles are considered where the surface area is $15,000 \text{ nm}^2$. Rectangular particle with a $b=150 \text{ nm}$ and $h=100 \text{ nm}$, sphere of radius = 69.10 nm , Triangle1 of $b=200$ and $h=150$ and Triangle2 of $b=100 \text{ nm}$ and $h=100 \text{ nm}$ are considered where b and h means base and height respectively.

as compared to the constructive interference. As we require the particle to be more directional at 90° of the radiation diagram and we have observed that particles in destructive interference are more directional. Hence, we must maximize the intensity of destructive interference and at the same time minimize the intensity irradiated by the particle in constructive interference.

Now, a plot of total intensities for destructive and constructive interference is calculated by summing up all the intensity irradiated by a particle in all direction on the side of air. In the Figure A.3, the particle form 1 means the particle is rectangle followed by sphere, Triangle1 and Triangle2. From these graphs, one can see the maximum total intensity for the destructive interference is of particle form 1, i.e., rectangle. We also see that the rectangular particle has the least total intensity in constructive interference when compared to other particles. This makes the rectangular particle an ideal choice for integration.

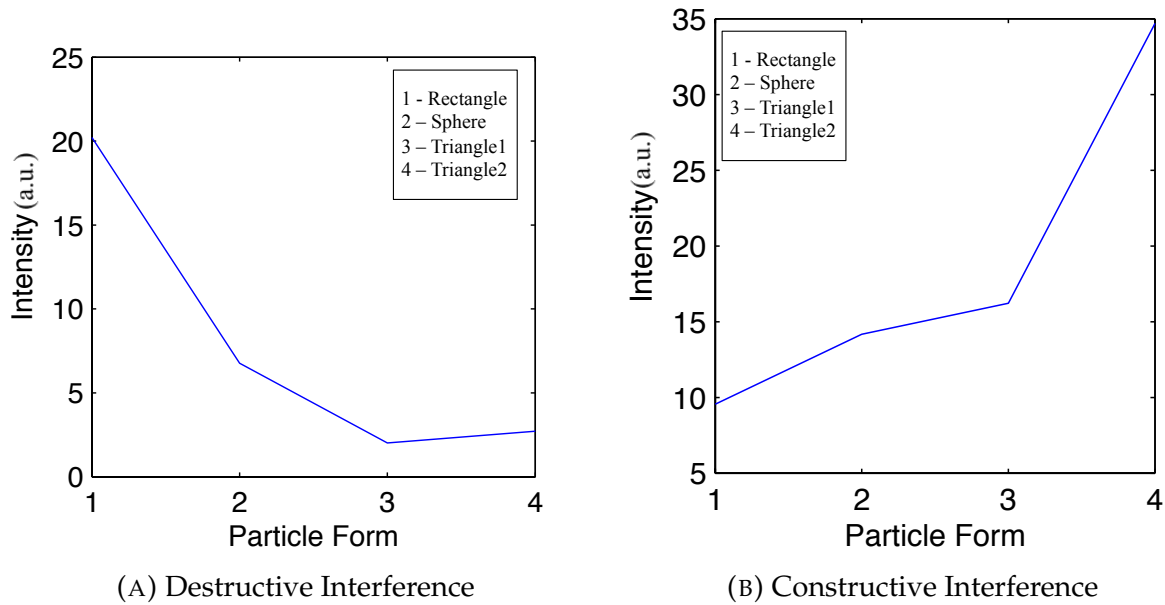


FIGURE A.3: Total intensity is calculated for different nano-particles are considered where the surface area is $15,000 \text{ nm}^2$ when observed in air. Rectangular particle with a $b=150 \text{ nm}$ and $h=100 \text{ nm}$, sphere of radius = 69.10 nm , Triangle1 of $b=200$ and $h=150$ and Triangle2 of $b=100 \text{ nm}$ and $h=100 \text{ nm}$ are considered where b and h means base and height respectively.

A.2 Selection of Material of Nano-Particle

As the shape of the nano particle is determined, now for the same rectangular nano particle of base 150 nm and height 100 nm , the material of the nano particle is modified. This helps us in determining the best possible radiation pattern where we can get the maximum radiated/ scattered light by the nano particle. Different materials are used for these simulations that have exactly the same configuration. The materials used for the simulations are:

- Gold
- Platinum
- Silver
- Aluminium
- Chromium

These metals were chosen as they are precious and have varied optical properties. When the nano particles of these metals were simulated in the CoBiSS configuration with lasers of 600 nm and the radiation patterns can be seen in the Figure A.4 for destructive and constructive interference.

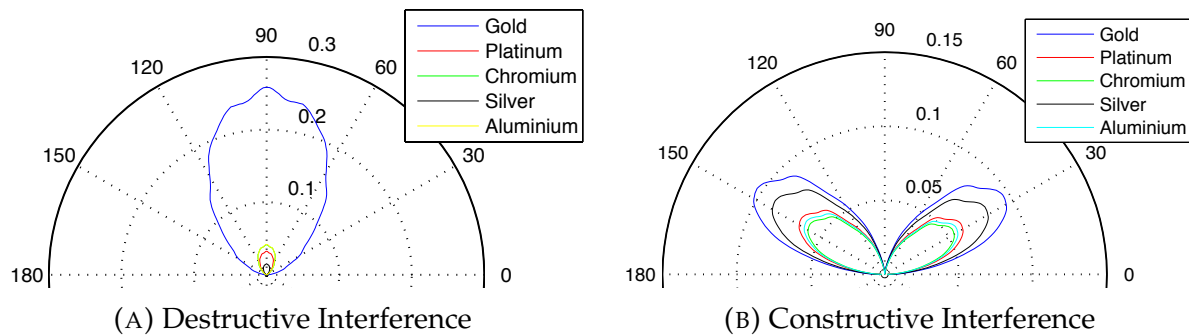


FIGURE A.4: In this calculation a rectangular particle of base 150 nm and height 100 nm is considered. The rectangular particle of different materials like Gold, Platinum, Chromium, Silver and Aluminium are used for simulation.

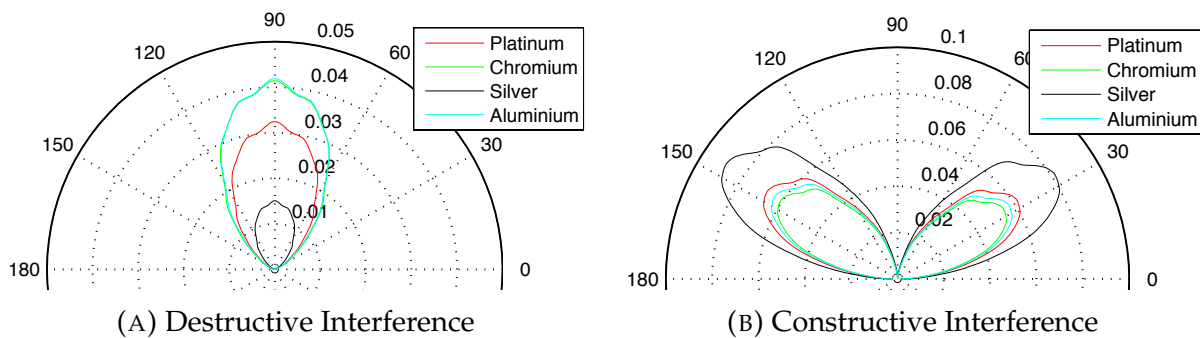


FIGURE A.5: In this calculation a rectangular particle of base 150 nm and height 100 nm is considered. The rectangular particle of different materials like Platinum, Chromium, Silver and Aluminum are used for simulation.

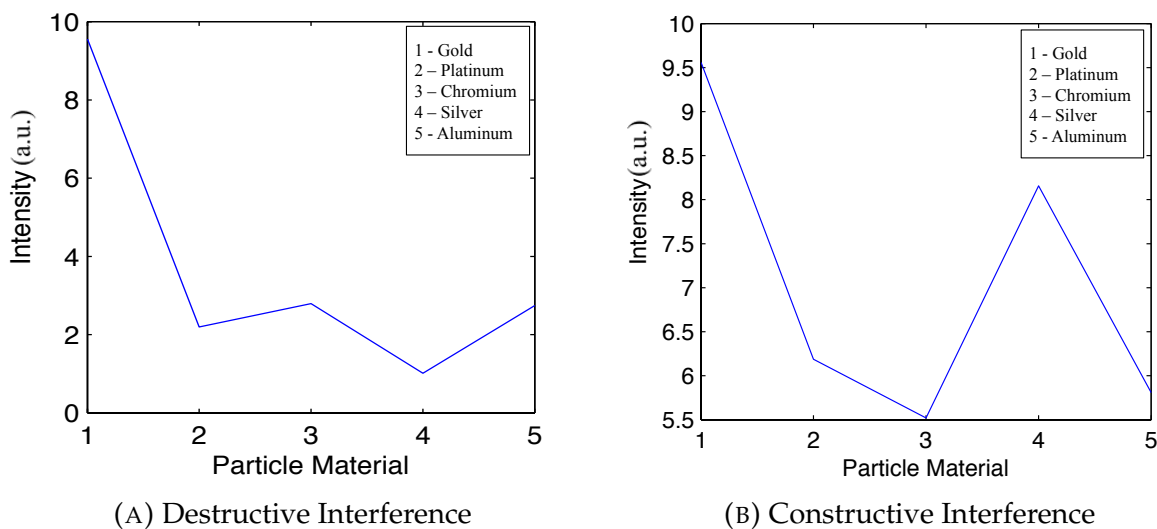


FIGURE A.6: In this calculation a rectangular particle of base 150 nm and height 100 nm is considered. The rectangular particle of different materials like Gold, Platinum, Chromium, Silver and Aluminium are used for simulation. Total Intensity of each material is calculated when observed in air.

In the case of destructive interference, one only sees the domination of Gold nano particle in the radiation pattern. Therefore, understand the behaviour of other nano particle's radiation pattern, the gold nano particle was removed from the plot and can be seen in the Figure A.5.

As we compare the directivity of nano-particles in destructive and constructive interference, the form does not change much. Only the maximum and the intensity changes. For this case also, the nano particles in destructive interference needs to be maximized and constructive interference is required to be minimized.

A plot of total intensities in air for different materials of nano-particles is plotted for destructive and constructive interference. In the Figure A.6, the particle material 1 means the particle is made of Gold followed by Platinum, Chromium, Silver and Aluminium. From these graphs, one sees that the total intensity all the particles in constructive interference is higher than that of destructive interference except for one material i.e. Gold.

This makes Gold as the optimum metal to be used in the nano particles for this device.

A.3 Length variation of Nano-Particle

The Length of the nano particles to be used needs to be decided. For this purpose we have supposed that the heights of the rectangular nano particle will remain constant at 100 and 150 nm respectively. The length of the rectangular nano particle varies from 50 to 250 nm with an interval of 50 nm.

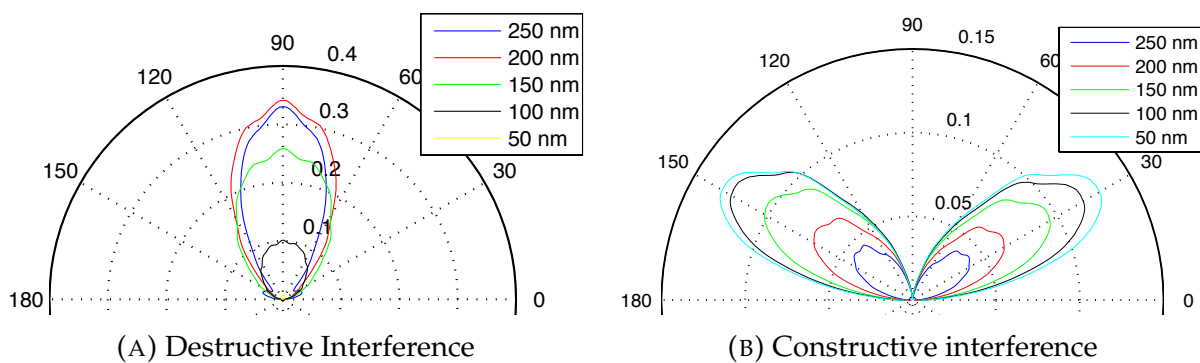
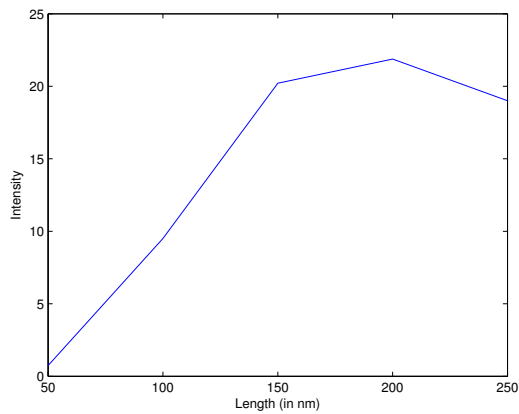
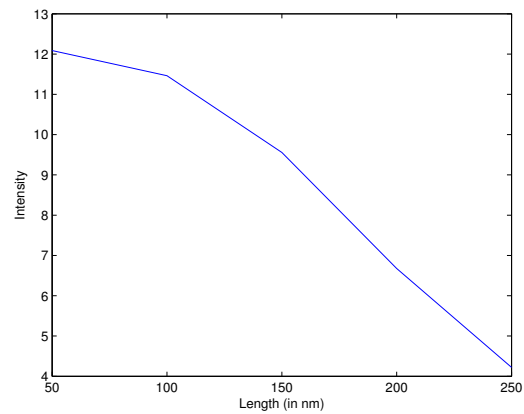


FIGURE A.7: Radiation pattern of a gold rectangular nano-particle of 100 nm in height is used and radiation diagrams are plotted for different base of 50, 100, 150, 200 and 250 nm respectively.

The simulations are performed by varying the length by keeping the height as constant. For the height of 100 and 150 nm, the radiation patterns of varying length can be seen in Figures A.7 and A.9 for destructive and constructive interference. To determine the optimum length the following points needs to be considered :

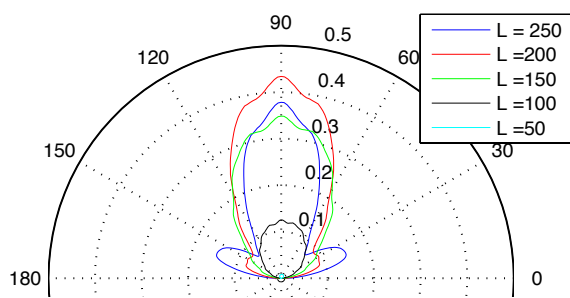


(A) Destructive Interference

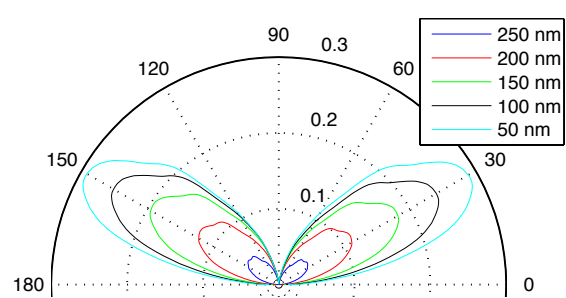


(B) Constructive interference

FIGURE A.8: Total intensity plot of a gold rectangular nano-particle of 100 nm in height is used and radiation diagrams are plotted for different base of 50, 100, 150, 200 and 250 nm respectively.

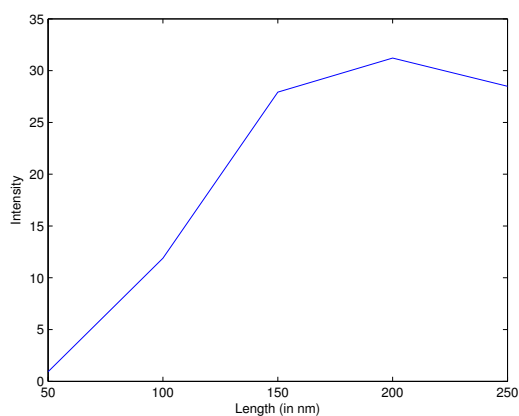


(A) Destructive interference

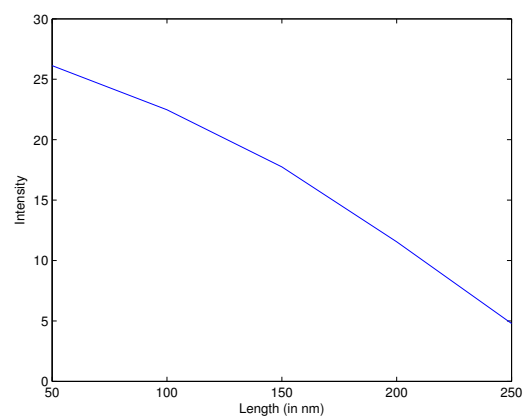


(B) Constructive interference

FIGURE A.9: Radiation pattern of a gold rectangular nano-particle of 150 nm in height is used and radiation diagrams are plotted for different base of 50, 100, 150, 200 and 250 nm respectively.



(A) Destructive Interference



(B) Constructive interference

FIGURE A.10: Total intensity plot of a gold rectangular nano-particle of 150 nm in height is used and radiation diagrams are plotted for different base of 50, 100, 150, 200 and 250 nm respectively.

- The radiation pattern should have a small opening angle. For example, this can be seen in Figure A.7a with the length of particle as 250 nm.
- The length of the particle should be less than the half of effective wavelength of the laser light.

After considering all the points stated above, we can summarize the results along with the explanation as follows:

- For visible region of Light : The minimum wavelength is 400 nm to a maximum of 700 nm. Here, the effective wavelength of the standing wave, formed by two opposite laser, is between 200 to 350 nm. Using these calculations, we can calculate the maximum length of the particle for visible spectrum has to be 100 nm.
- For Near Infrared Region of Light: The range of the Near Infrared wave is between 700 to 900 nm. The effective wavelengths comes in the range of 350 nm to 450 nm. The maximum size of the particle that can be used for making a nano antenna is 175 nm.

But on the contrary, while observing the radiation diagrams one can see that we need to maximize the destructive interference and minimize the constructive interference results. With the help of Figures A.8 and A.10, one observes that maximum in destructive interference is observed at 200 nm length for both cases. We also observe that as the length of the particle increases the intensity value of constructive interference decreases.

When comparing the two results i.e. theoretical and simulated, one finds that it might be better to keep the two in mind. As the simulated results shows good total Intensity graphs for 150 nm and 200 nm and the analytical results show good result below 175 nm for 700 to 900 nm wavelength range. Therefore, we feel it may be a good idea to choose the length of particle as 150 nm as a compromise between the two.

A.4 Height variation of Nano-Particle

The length of the particle has been decided and now its time to decide the height of the particle. This can be decided by the use of the following parameters :

- Capability of manufacturing of nano-particle's height in the laboratory.
- To understand the height criteria of the metal. This helps in determining the maximum height possible (threshold) for manufacturing a nano-particle before it starts to bend on its own weight.
- To minimize the opening angle of the radiation diagram.

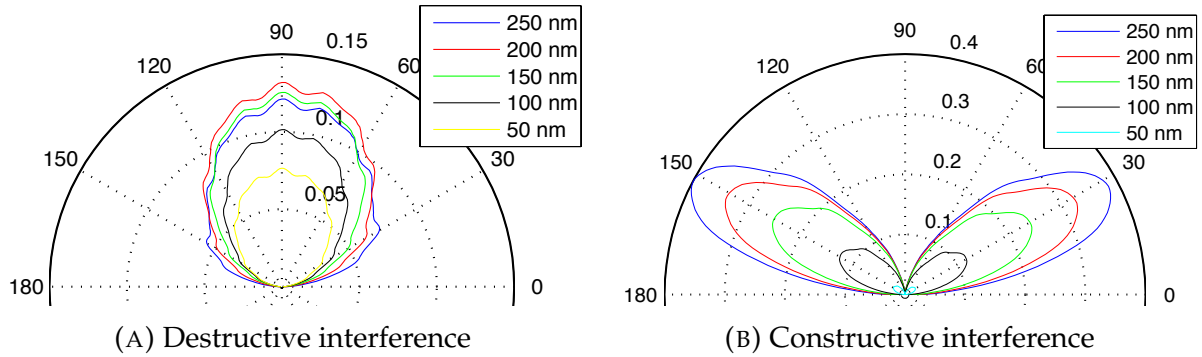


FIGURE A.11: Radiation pattern of a gold rectangular nano-particle of 100 nm in base is used and radiation diagrams are plotted for different height of 50, 100, 150, 200 and 250 nm respectively.

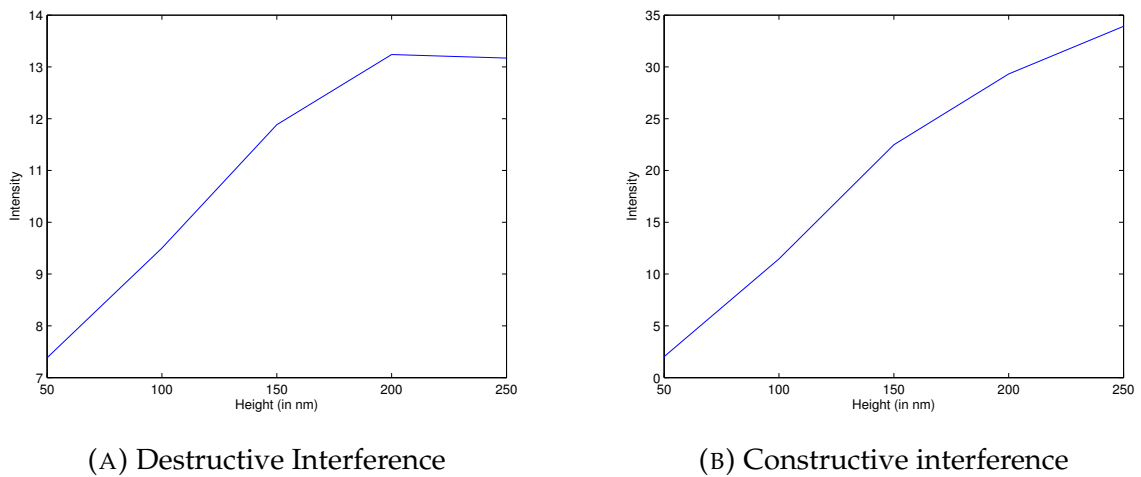


FIGURE A.12: Total intensity plot of a gold rectangular nano-particle of 100 nm in base is used and radiation diagrams are plotted for different heights of 50, 100, 150, 200 and 250 nm respectively.

Here we take an arbitrary value that a nano-particle's height should not be more than 1.5 times the length of the particle (till one can accurately determine the maximum height possible for the nano particle).

By referring to the Figure A.11, one can see the radiation patterns in destructive and constructive interference for different heights which have a constant base size of 100 nm. With the help of theoretical parameter as described, the maximum height possible is 150 nm. With the help of radiation diagrams of destructive and constructive interference, we observe that the intensity increases as the height of the particle increases. This can be observed from the Figure A.12. Using these results we observe that the total intensity of destructive interference is a lot less than the particle present in the constructive interference (almost a factor of 2 for a particle of 250 nm of height). One needs to find the optimum height where the constructive interference part is at least less than or equal to the destructive interference part. One can observe and see that for the height of 50 and 100 nm this holds true.

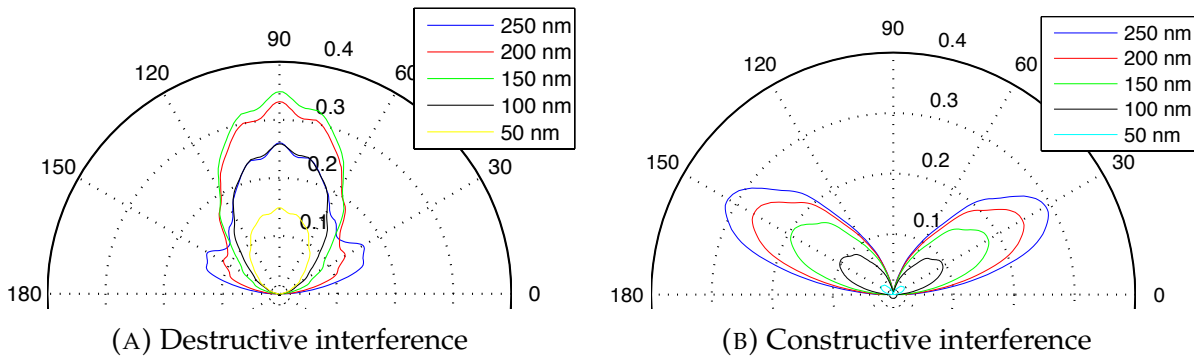


FIGURE A.13: Radiation pattern of a gold rectangular nano-particle of 150 nm in base is used and radiation diagrams are plotted for different height of 50, 100, 150, 200 and 250 nm respectively.

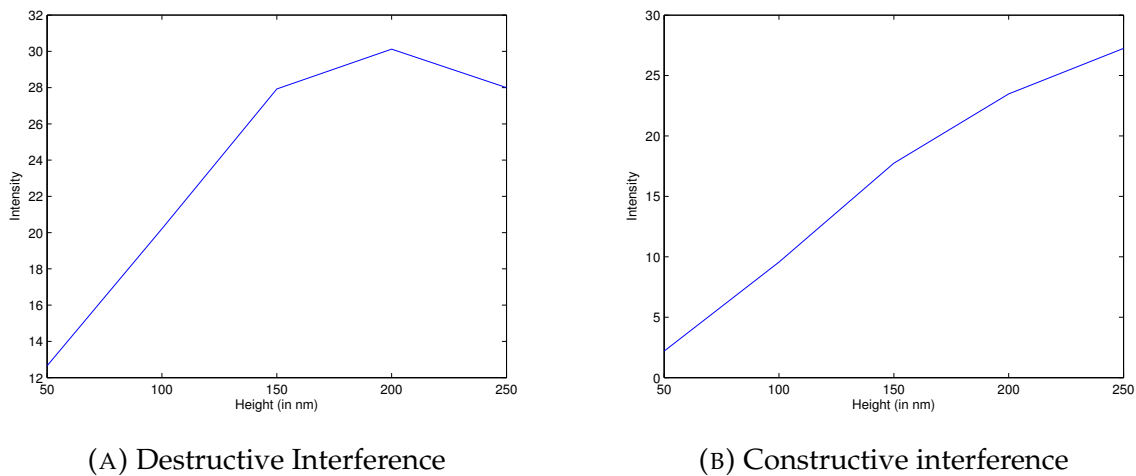


FIGURE A.14: Total intensity plot of a gold rectangular nano-particle of 150 nm in base is used and radiation diagrams are plotted for different heights of 50, 100, 150, 200 and 250 nm respectively.

Figure A.13 represents the radiation patterns in destructive and constructive interference for different heights which have a constant base size of 150 nm. As we need a more directional radiation pattern from the destructive interference, it removes the possibility of using a nano-particle of anything above 150 nm in height as seen from the radiation diagrams in Figure A.13a. We also observe as stated earlier that with the increase in height the total intensity in air also increases (refer to Figure A.14). As we need to maximize the difference between the total intensities of particle from destructive and constructive interference, we observe that shows a linear increase till 150 nm of height. We can use any of the three values namely 50, 100 and 150 nm.

Presently, in the lab new techniques in manufacturing were developed to achieve 100 nm in height and 150 nm would take a bit of extra time. We also would like to reduce the power used by the laser as it will increase in the battery life of the device, therefore we need more intensity irradiated by the nano-particle. So, for this purpose, we have limited our work for the height of 100 nm.

A.5 Test of selected Nano-Particle in Dimer formation

After selecting the nano-particle of base as 150 nm and height 100 nm in height. We were interested to see if can reduce the radiation diagram by using a dimer formation.

For this calculation, we used the height of the particle as 100 nm as in the original particle but we modified the base of new rectangular particle as 75 nm. This was done to keep the total surface area as constant. The total base length of dimers (containing 2 rectangular nano particle) remains constant at 150 nm.

The distance between the two rectangular nano particles (dimer) is modified from 10 nm to 50 nm. This helps in visualizing the radiation pattern of the dimer formation by changing length between the two rectangles. This was done to find the optimum distance where the radiation pattern can become the most directive.

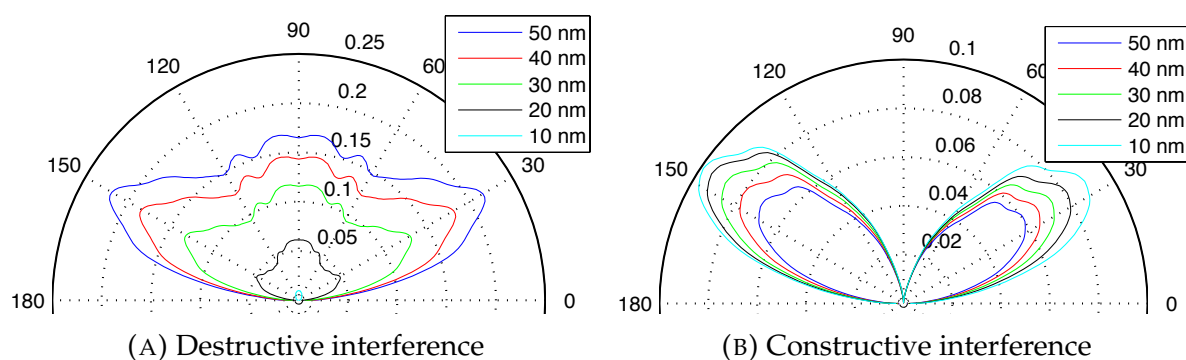


FIGURE A.15: Radiation pattern of two nano-particles of length = 75 nm and height 100 nm are used and the distance between the two are varied from 10,20,30,40 and 50 nm respectively.

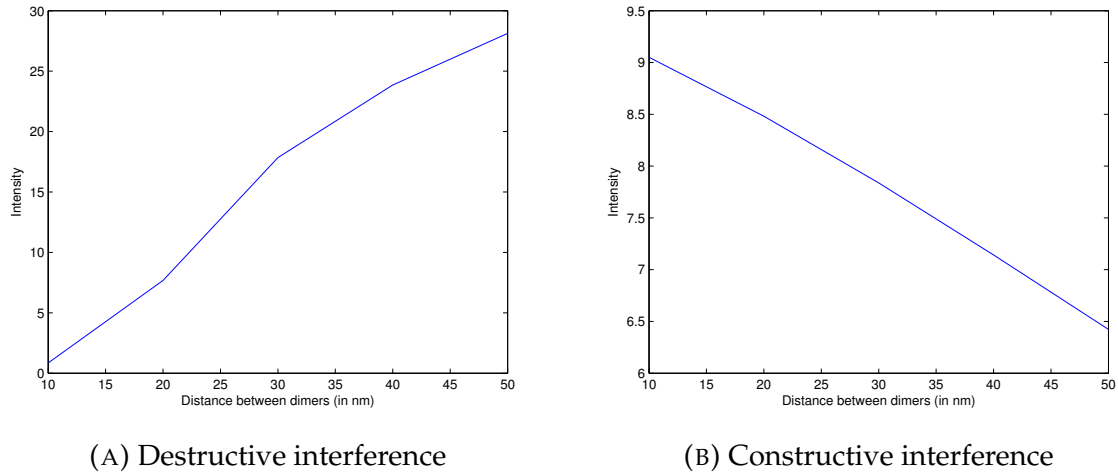


FIGURE A.16: Total Intensity calculation of two nano-particles of length = 75 nm and height 100 nm are used and the distance between the two are varied from 10,20,30,40 and 50 nm respectively in air.

Refer to Figures A.15 and A.16, the dimer radiation pattern and intensity plots show the following results:

- For a nano - particle in destructive interference, as the length between the rectangular nano-particle increase the intensity irradiated also increases. We also observe a contrary effect for when the nano-particle is present in the constructive interference.
- The opening angle increases as the distance between the nano-particle increases.

With the help of the above results and Figures A.15 and A.16, the best possible particle we can use is the rectangle without the dimer formation. This rectangular nano-particle will irradiate more intensity of light and also has a very small opening angle compared to all nano-particles present in the dimer formation.

A.6 Conclusion

With this study of "Selection of Nano-Particle", we have narrowed down the exact particle can be used for the CoBiSS. We simulated various materials that can be used in the nano particle along with the shapes, length and breadth of the nano-particle.

Using this study, we narrowed down that the particles that we can use are Rectangular Gold Nano-Particles of dimensions :

- For Visible Light : Height is 50 nm and Length is 100 nm.
- For Near Infra Red: Height is 100 nm and Length is 150 nm.

A.7 Determination of Width of Nano Particle

We have finished with the definition of the nano-particle in 2D but for manufacturing this particle, one of its key feature is missing that is its breadth. As we have already defined the length and breadth with 2D simulations earlier.

Now few new simulations were performed by varying the breadth from 50 nm to 200 nm in 3D. For these calculations we are always using p-polarized laser light source and also the wavelength here is constant at 600 nm.

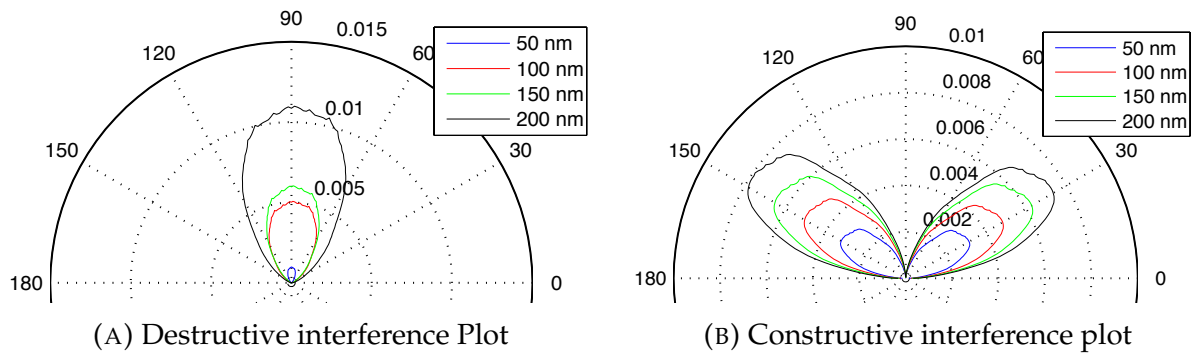


FIGURE A.17: Gold Nano-particle where $L = 150$ nm and $H = 100$ nm with a variation of depth as 50,100,150,200 nm and plotted in XZ plane at the center

To understand the radiation diagrams, one needs to understand the direction nomenclature that is present in the Figure 2.9. We have the height represented by Z axis and base is given by X axis. In this part we are varying the dimensions in Y axis.

In Figure A.17, the XZ plane is represented for the particle and a radiation diagram is built.

Similarly, Figure A.18 represents the YZ plane of observation. When we compare these results with the sections describing selection of height and base (Sections A.4 and A.3). One observes the curves are approximately the same but the intensity values have drastically changed between 2D and 3D observation. This has already been explained as 2D simulation structures have infinite width as compared to 3D simulation.

With these results it might be a good idea to use the width as 150 nm making the two observation plane to view the particle as the same.

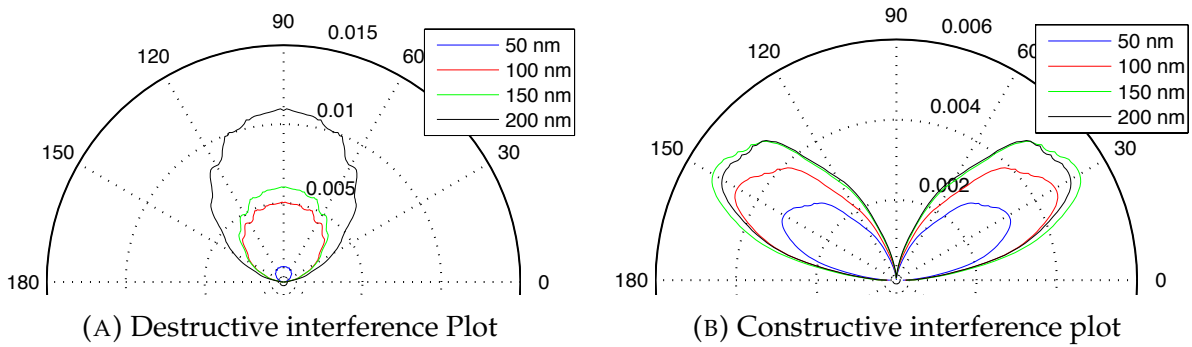


FIGURE A.18: Gold Nano-particle where $L = 150$ nm and $H = 100$ nm with a variation of depth as 50,100,150,200 nm and plotted in YZ plane at the center

When we compare the radiation diagrams of two different interference plots, we find the following :

- Particle present in constructive interference is more dominant as compared to destructive interference.
- Light is distributed in all the directions that creates a constrain in the height of the camera.

As we have seen that the nano-particle is irradiating in all the directions. Now, one needs to determine the ideal height at which the camera needs to be placed so that all the light can be captured by its pixel. Presently, let us consider the that 1 nano-particle irradiates and all its intensity is captured by 1 pixel. This can be visualized using the Figure A.19. For an ease of calculation let us consider the distance between pixels or nano-particle (center to center) is 19 microns (symbolized as 'd' in the Figure A.19). After considering both the radiation diagrams, one sees that the directivity or the maximum opening of intensity distribution is more than 120° and approximately

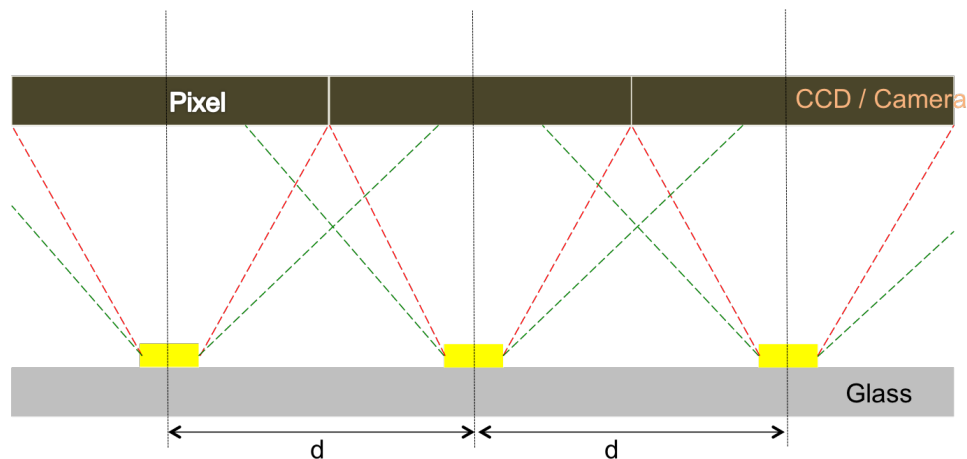


FIGURE A.19: Nano - particle vs Camera Positioning

equal to 160° . For an ease of calculation, we take the maximum opening as 120° . Using these parameters, the ideal height comes out to be 5.48 microns. But, if we consider the opening angle as 160° , then the ideal height will get decreased to 1.68 microns. It was impossible for now to place the camera this ideal height. There is also another problem that the pixel's center needs to coincide with the center of the nano-particle. If there is a small difference then the irradiated light will go to the other pixel and will change the interferometric calculation by adding an error. This meant decreasing the height for the placement of camera even further.

Due to the reasons stated above the height becomes one of the most important constraint. To remove this another calculation was done. In this, we considered that a nano particle irradiates to an surface area of 9 pixels, that is, 3 pixels linearly. Accordingly the distance between nano-particles becomes 57 microns (symbolized as 'd' in the Figure A.19). By using the maximum opening of 120° the ideal height becomes 33 microns and for maximum opening of 160° the height becomes 10.05 microns. It felt achievable but when we calculated the number of sampling points needed by Shannon Criteria, the distance required was more than 7 mm long.

We got a few constraints like

- manufacturing on large surfaces without any small calibration error and each nano-particle to be placed at a distance of 57 microns.
- the intensity of laser required will be more as the threshold of camera intensity needs to be achieved at that height. This will lead to more power consumption and decrease the battery back up of the device.
- the intensity used by the laser is high enough then it can lead to evaporation of the gold nano-particle from the surface and can eventually damage camera and the whole circuit board of the system.

Due to all these constraints we had to drop the idea of using Lomb Scargle Method (described in Section 3.3.4) for calculation which is an integral part of the processing and switch to use the Micro-spectrometer Method (described in Section 3.3.5).

Appendix B

"W" tip - Effect of Peak and Trench

One knows that an electromagnetic wave creates charges while moving in a material that has the effect of creating dipole moments. The material is then no longer electrically neutral and we can see the emergence of local charges. If these charges are observed at a time t (that is to say that the time dependence is fixed in the equations describing the electromagnetic wave) we can see areas of positively and negatively charged as a result of the structural response to the amplitude of the electric field of the wave.

The structure has the particularity to present singularities in its topology, that is, spikes, "specialized" channels:

Under the influence of an electromagnetic wave excitation, there is a surface plasmon mode localized in these singularities (Local Surface Plasmon Resonance: LSPR). In the exaltation of these modes, we can determine the polarity of the function structure of the generated electric field. Based on the work of José Dintinger and Olivier JF Martin entitled "Channel and wedge plasmon modes of metallic V-grooves with finite metal thickness" [111] was along the lines of the electric field according to \vec{e}_x and \vec{e}_z :

This diagram shows the effects of modes of tip channel and on the magnitude of the normalized electric field in projection along the axes \vec{e}_x and \vec{e}_z . We can then determine the local loads present at the structure in their exaltations, blues arrows describing the

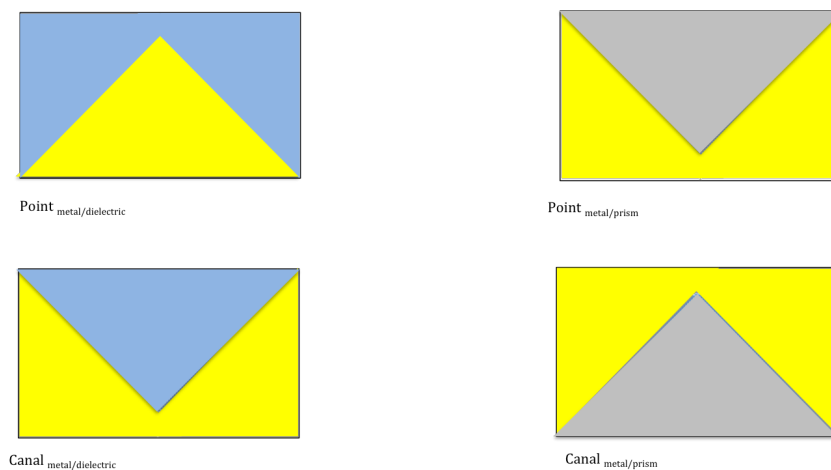


FIGURE B.1: Singularities present at the level of the structure

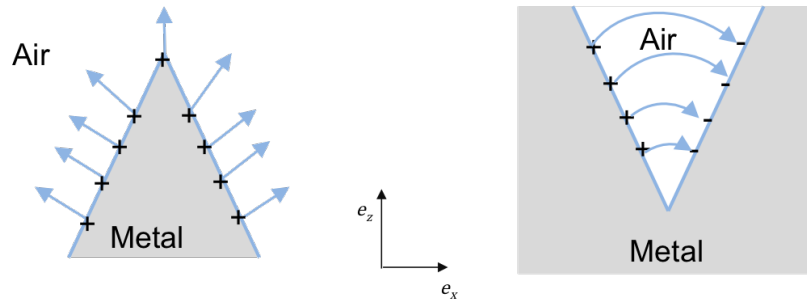


FIGURE B.2: Plasmon Polariton

orientation of the field and the "+" , "-" polarity of the material:

The blues arrows representing the orientation of the electric field, though experiment, we can realize their projections on the axis \vec{e}_x and \vec{e}_z . One then finds patterns in Figure B.2.

Appendix C

Consideration of Devices

Here, most of these devices that were present in the year 2013-2014 were considered. Most of the electronic parts are generic devices which are available of the shelf to anyone.

C.1 Motherboard

A motherboard is the physical arrangement in a computer that contains the computer's basic circuitry and components. On the typical motherboard, the circuitry is imprinted or affixed to the surface of a firm planar surface and usually manufactured in a single step. The computer components included in the motherboard are:

- The microprocessor
- (Optionally) co-processors
- Memory
- basic input/output system (BIOS)
- Expansion slot
- Interconnecting circuitry

Additional components can be added to a motherboard through its expansion slot.[56]

One can see that motherboard is one of the most important device in the electronic integration. This will house the main processor and communicate with other devices using different interfaces. It will also play an important role in integration, specially when we will need to process data and take decisions based on the analysis of data. A table C.1 is created to compare the features of most of the ARM development boards available in the market.

TABLE C.1: Motherboard Comparison

S. NO.	Board Name	Cores and Frequency	RAM	Linux OS	Wi-Fi	Ethernet	USB	GPIO	LCD header	Onboard HDD	Input Voltage and Current	Price (in €)
1.	Pandaboard	4 cores & 2.16 GHz	1 GB	Yes	Yes	Yes	Yes	Yes	Yes	No	5V & 4A	170
2.	Raspberry Pi	1 core & 1 GHz	256 MB	Yes	No	No	Yes	Yes	Yes	No	5V & 2A	30
3.	Pcduino	1 core & 1 GHz	512 MB	Yes	No	Yes	Yes	Yes	No	Yes	5V & 2A	60
4.	Beagleboard Black	2 cores & 1 GHz	512 MB	Yes	No	Yes	Yes	Yes	No	Yes	5V	70
5.	Cotton Candy	2 cores & 1.2 GHz	1 GB	Yes	Yes	No	Yes	No	No	No	5V	200
6.	Nvidia Jetson TK1	4 cores	2 GB	Yes	No	Yes	Yes	Yes	Yes	Yes	12V	270
7.	UDOO Quad	4 cores	1 GB	Yes	Yes	Yes	Yes	Yes	Yes	Yes	12V	135

C.2 Camera

The following table C.2 shows the comparison of cameras that are available in the market with different control method and pixel sizes.

TABLE C.2: Camera Comparison

S. NO.	Camera Name	Sensor Size (mm)	Number of Pixels	Pixel size (μm)	Connection Type	Operating System
1.	Edmund Optics' EO-10012M	6.41 X 4.59	3840 X 2748	1.67 X 1.67	USB, GPIO	Microsoft Windows, Linux For GPIO
2.	Edmund Optics' EO-0414BL	4.5 X 2.8	752 X 480	6 X 6	USB, GPIO	Microsoft Windows, Linux For GPIO
3.	Edmund Optics' EO-1312BL	6.6 X 5.3	1280 X 1024	5.2 X 5.2	USB, GPIO	Microsoft Windows, Linux For GPIO
4.	Edmund Optics' EO-1312M	5.6 X 4.2	2560 X 1920	2.2 X 2.2	USB, GPIO	Microsoft Windows, Linux For GPIO
5.	Thor Labs DCC1545M	6.66 X 5.32	1280 X 1024	5.2 X 5.2	USB	Microsoft Windows
6.	The Imaging Source DMM 72BUC02-ML	5.7 X 4.28	2592 X 1944	2.2 X 2.2	USB	Microsoft Windows, Linux For GPIO
7.	The Imaging Source DMM 42BUC02-ML	4.8 X 2.99	1280 X 796	3.75 X 3.75	USB	Microsoft Windows, Linux For GPIO

8.	The Imaging Source DMM 22BUC02-ML	4.55 X 2.97	752 X 480	6 X 6	USB	Microsoft Windows, Linux
9.	Framos GC1392 XMB - BL - NM - 40	10.2 X 8.3	1392 X 1040	6.45 X 6.45	Ehernet	Microsoft Windows, Linux
10.	RSS Supplied Camera	Not Given	1580 X 1050	19 X 19	USB	Microsoft Windows

C.3 Laser

The following table C.3 shows the comparison of lasers that are available in the market with different wavelength, control method and power output.

TABLE C.3: Laser Comparison

S. NO.	Laser Name	Wavelength (nm)	Maximum Power (mW)	Beam Shape	Connection Type	Operating System
1.	ThorLabs CPS 405	405	4.5	3.8 X 1.8	Power with 2.5" Jack	Not Required
2.	ThorLabs CPS 450	450	4.5	3.2 X 1.0	Power with 2.5" Jack	Not Required
3.	ThorLabs CPS 520	520	4.5	4.6 X 1.7	Power with 2.5" Jack	Not Required
4.	ThorLabs CPS 635R	635	1.2	$\phi = 2.9$	Power with 2.5" Jack	Not Required
5.	ThorLabs CPS 635	635	4.5	4.5 X 1.0	Power with 2.5" Jack	Not Required
6.	ThorLabs CPS 650F	650	4.5	5.0 X 2.4	Power with 2.5" Jack	Not Required
7.	ThorLabs CPS 670F	670	4.5	5.0 X 2.4	Power with 2.5" Jack	Not Required
8.	ThorLabs CPS 192	780	4.5	4.4 X 1.7	Power with 2.5" Jack	Not Required

9.	ThorLabs CPS 780S	780	4.5	3.8 X 1.6	Power with 2.5" Jack	Not Re- quired
10.	MiniLas Evo	488	75 (before fiber cou- pling)	Depends on col- limator used	USB	Microsoft Windows, Linux
11.	MiniLas Evo	515	25 (before fiber cou- pling)	Depends on col- limator used	USB	Microsoft Windows, Linux
12.	MiniLas Evo	640	75 (before fiber cou- pling)	Depends on col- limator used	USB	Microsoft Windows, Linux
13.	MiniLas Evo	660	75 (before fiber cou- pling)	Depends on col- limator used	USB	Microsoft Windows, Linux
14.	MiniLas Evo	685	40 (before fiber cou- pling)	Depends on col- limator used	USB	Microsoft Windows, Linux
15.	MiniLas Evo	785	75 (before fiber cou- pling)	Depends on col- limator used	USB	Microsoft Windows, Linux

Appendix D

OS Selection and Installation for the Development board

Presently, we have 2 different types of Pandaboard ES with Revision B2 and B3. The difference is of the timer present in the two boards. The software supplied with Pandaboard is for the version which has revision B2. For the Pandaboard ES with revision B3, one needs to rebuild the OS.

First of all, the installation of OS for version B2 is explained then for the version B3. For the version B3 a new Ubuntu Desktop version can be compiled to be used rather than the supplied Ubuntu 12.04. The new compiled version is backward compatible and can be used to work for version B2.

OS Installation for Pandaboard version 3

The Linux Ubuntu Desktop 12.04 Operating system that is supplied by the manufacturer is used for this installation.

The installation steps are explained below for Mac OS or Linux OS:

- Copy the ".img" or ".img.gz" file from the CD provided by the manufacturer. This can also be downloaded from: http://omappedia.org/wiki/Prebuilt_ubuntu_binaries.
- Insert a SD MMC card of at least 8 GB in the computer where the prebuild ".img" file is present.
- Find the raw device name (like /dev/mmcblk0 on our computer). This can be identified by the command:


```
$lsblk
```
- If the file is ".img.gz" then extract the files to ".img" format. This can be done by using the command: `$gunzip ubuntu-12.04-preinstalled-desktop-arm+omap4.img.gz`. Before running this command, one needs to make sure that the terminal is commands points in the correct location. In my case, the file is present in downloads then I first run the command: `$cd Downloads/`.

- Now, to copy the disk image files (represented by ".img") to the actual disk (SD MMC), the following command is used : `$sudo dd bs=4M if= ubuntu-12.04-preinstalled-desktop-arm+omap4.img of=/dev/mmcblk0` . This is followed by: `$sudo sync` . To execute the two above commands, one needs to use the privileged root access. Finally, the installation of Operating system can begin for Pandaboard.
- The installation procedure is same as installing Ubuntu on a desktop or laptop.
- After installing the operating system, one needs to add the graphical libraries of Pandaboard to Ubuntu for optimum use. This is done by using the following commands:
 To enable different Repositories on Pandaboard:
`$sudo sed --in-place=.bak -e 's/# \ (deb.*\)/ \1/' /etc/apt/sources.list .`
 For updating the repository:
`$sudo apt-get update.`
 To Add the OMAP4 development repository:
`$sudo apt-get install python-software-properties.`
`$sudo add-apt-repository ppa:tiomap-dev/release.`
`$sudo apt-get update.`
 Finally installing all the Add-ons:
`$sudo apt-get install ubuntu-omap4-extras.`

OS Installation for Pandaboard version 4

The Linux Ubuntu Desktop 16.04 Operating system can be recompiled for the ARM board (Pandaboard)

The installation steps are explained below for Linux OS (64 bit OS) where all the step of installation start at '/' root level:

- ARM Cross Compiler : For GCC

Downloading the ARM Cross-Compiler:

```
$wget -c https://releases.linaro.org/components/
toolchain/binaries/5.3-2016.02/arm-linux-gnueabi/f/
gcc-linaro-5.3-2016.02-x86_64_arm-linux-gnueabi/f.tar.xz.
```

After Downloading the Cross-compiler, it needs to be extracted as:

```
$tar xf
gcc-linaro-5.3-2016.02-x86_64_arm-linux-gnueabi/f.tar.xz.
```

The cross compiler is already compiled for linux it just needs to be used and to

do that, one needs to export the location of the cross compiler for the future use. This can be done by using the following command:

```
$export CC='pwd' /  
gcc-linaro-5.3-2016.02-x86_64_arm-linux-gnueabi/  
bin/arm-linux-gnueabi-
```

- **Bootloader:U-Boot Installation To download the u-boot :**

```
$git clone https://github.com/u-boot/u-boot.
```

After Downloading, we need to find latest patches.

```
$cd u-boot/.
```

```
$git checkout v2016.03 -b tmp.
```

```
$wget -c https://rcn-ee.com/repos/git/  
u-boot-patches/v2016.03/0001.
```

Now after downloading the u-boot patches, the patches need to be applied by using the following command:

```
$patch -p1 <  
0001-omap4-common-uEnv.txt-bootz-n-fixes.patch.
```

Installing all the patched files:

```
$make ARCH=arm CROSS_COMPILE=${CC} distclean.
```

```
$make ARCH=arm CROSS_COMPILE=${CC} omap4_panda _defconfig.
```

```
$make ARCH=arm CROSS_COMPILE=${CC}.
```

- **Linux Kernel Downloading Linux Kernel :**

```
$git clone https://github.com/RobertCNelson/  
armv7-multiplatform.
```

Building the Linux Kernel kernel \$cd armv7-multiplatform.

```
$git checkout origin/v4.1.x -b tmp.
```

```
$/buildkernel.sh.
```

- Ubuntu 16.04 LTS

Downloading the minimal version of Ubuntu OS:

```
$wget -c https://rcn-ee.com/rootfs/eewiki/minfs/
ubuntu-16.04-minimal-armhf-2016-04-22.tar.xz.
```

Extracting the downloaded file:

```
$tar xf ubuntu-16.04-minimal-armhf-2016-04-22.tar.xz.
```

- Setup SD MMC Card

Here the computer identifies the SD MMC card as `/dev/mmcblk0` but the card needs to be unmounted by using the command `$umount /dev/mmcblk0`.

For preparing the SD MMC card the following commands are used:

```
$export DISK=/dev/mmcblk0.
```

For erasing the SD MMC card

```
$sudo dd if=/dev/zero of=${DISK} count=10 bs=1M.
```

To install boot loader, `$cd /`

```
$sudo dd if=./u-boot/MLO of=${DISK} count=1 seek=1 bs=128k.
```

```
$sudo dd if=./u-boot/u-boot.img of=${DISK} count=2 seek=1
bs=384k.
```

Creating the file system for the root file system

Creating the Partition Layout `$sudo sfdisk ${DISK} <<--EOF--`

```
1M, ,L,*
```

```
--EOF--
```

This code can only be executed for util-linux v2.26 or superior.

Creating Format Partition `$mkfs.ext4 -L rootfs -O ^metadata_csum,
^64bit ${DISK}p1 .`

This command is only possible when `mkfs.ext4` is of a version greater or equal to 1.43 and the `metadata_csum` and 64 bit are disabled (using the command shown). Finally, formatting is finished now, we need to mount the SD MMC card for

further use

```
$mount /dev/mmcblk0.
```

- Installing kernel and Root File System of SD MMC

Before starting this procedure, first of all we need to verify and find the exact build version that was created at the end of step Linux Kernel. the reference of this kernel will be said to be `kernel_ver` (this should something similar to 4.X.Y-Z).

Now lets start the Installation process,

```
$cd /.
```

```
$export kernel_version=kernel_ver.
```

To copy Root File system

```
$sudo tar sfvp ./*-*-*-arm-*/armhf-rootfs-*.tar -C
/media/rootfs/.
```

It is needed to set the "uname_r" file in /boot/uEnv.txt file. This is used to tell the which kernel version is present in this built.

```
$sudo sh -c "echo 'uname_r=${kernel_version}' >>
/media/rootfs/boot/uEnv.txt.
```

Lets define this SD MMC card will be used for which Pandasboard ES version.

For the Pandaboard ES

```
$sudo sh -c "echo 'dtb==omap4-panda-es.dtb' >>
/media/rootfs/boot/uEnv.txt".
```

For the version of Pandaboard ES Rev B3

```
$sudo sh -c "echo 'dtb==omap4-panda-es-b3.dtb' >>
/media/rootfs/boot/uEnv.txt".
```

To copy the kernel Image files

```
$sudo cp -v
./arm7-multiplatform/deploy/${kernel_version}.zImage
/media/rootfs/boot/vmlinuz-${kernel_version}.
```

Copying the Kernel Device Tree Binaries

```
$sudo mkdir -p /media/rootfs/boot/dtbs/${kernel_version}/ .
$sudo tar xfv
./armv7-multiplatform/deploy/${kernel_version}-dtbs.tar.gz
-C /media/rootfs/boot/dtbs/${kernel_version}/ .
```

Copying the kernel Modules

```
$sudo tar xfv
./armv7-multiplatform/deploy/${kernel_version}-modules.tar.gz
-C /media/rootfs/ .
```

Creating the file system table (/etc/fstab)

```
$sudo sh -c "echo '/dev/mmcblk0p1 / auto errors=remount-ro
0 1' >> /media/rootfs/etc/fstab".
```

Adding WiFi device drivers To Download the driver package use the following commands:

```
$cd /
$git clone
git://git.kernel.org/pub/scm/linux/kernel/git/
firmware/linux-firmware.git --depth=1.
$sudo mkdir -p /media/rootfs/lib/firmware/ti-connectivity.
$sudo cp -v ./linux-firmware/ti-connectivity/*
/media/rootfs/lib/firmware/ti-connectivity.
```

Enabling Networking

A file named "interfaces" need to be edited and a few lines need to be added. The file is present in the location "/media/rootfs/etc/network/interfaces". The following lines need to be added.

```
auto lo
iface lo inet loopback

auto eth0
iface eth0 inet dhcp
auto wlan0
iface wlan0 inet dhcp
wpa-ssid "ssid"
```

```
wpa-psk "password".
```

The correct essid and password needs to be entered depending on your router settings.

Removing SD card

To remove the SD MMC card please use the following commands: `$sync`

```
$sudo umount /media/rootfs
```

When using Ubuntu 16.04 the username and password are "ubuntu" and "temppwd" respectively.

Appendix E

Article Published

Resolving phase information of the optical local density of state with scattering near-field probes

R. Prasad and R. Vincent*

*Laboratoire de Nanotechnologies et d'Instrumentation Optique, ICD, CNRS UMR 6281,
Université de Technologie de Troyes, 12 Rue Marie Curie, 10004 Troyes, France*

(Received 5 April 2016; revised manuscript received 29 September 2016; published 25 October 2016)

We theoretically discuss the link between the phase measured using a scattering optical scanning near-field microscopy (s-SNOM) and the local density of optical states (LDOS). A remarkable result is that the LDOS information is directly included in the phase of the probe. Therefore by monitoring the spatial variation of the trans-scattering phase, we locally measure the phase modulation associated with the probe and the optical paths. We demonstrate numerically that a technique involving two-phase imaging of a sample with two different sized tips should allow to obtain the image the pLDOS. For this imaging method, numerical comparison with extinction probe measurement shows crucial qualitative and quantitative improvement.

DOI: [10.1103/PhysRevB.94.165440](https://doi.org/10.1103/PhysRevB.94.165440)**I. INTRODUCTION**

The rate of spontaneous emission of a fluorescent emitter is determined both by the internal electronic states and the optical local density of state (LDOS) [1]. Luminescence, i.e., the emission of light by a source, can therefore be tailored through the nanostructuring of its environment, thus modifying the LDOS. Due to this tremendous technological impact at the nanoscale, new applications were designed for its development. This is notably true for energy consumption, which allows the enhanced energy extraction for a localized source such as LED [2], OLED [3], and also for an integrated local photon source [4,5], which makes this of a rising interest in the field of telecommunication information for quantum information processing. Thus imaging the LDOS of fabricated samples becomes essential to characterize optical devices, together with a deeper understanding of light-matter interaction. Despite the general interest, such task remains difficult and few works have been reported, which only partially address the question. The main technique developed in the past decade was based on an indirect measurement, typically by determining the life time of a fluorescence emitter [6–8]. However, this kind of optical characterization is mono frequency and remains very dependent on the quality of the source attached to the scan probe microscopy (SPM) and the resolution is still not really convincing. Nevertheless, a relationship between the electromagnetic LDOS and images obtained by optical scanning near-field microscopy (SNOM) have been identified [9,10]. This has been demonstrated experimentally for a well defined near-field structure [11,12]. Despite this, the theoretical approaches that unify LDOS and SNOM images were ultimately neglecting the cross coupling mechanisms between the tip and the structure itself, leading to the introduction of possible errors in the extraction measurements and misleading the interpretations. Recently, taking advantage of the tip-substrate interaction, we have underlined a link between the modification of the width of absorption cross section resonance of a dipolar plasmonic nanoantenna that is in proximity to a given environment and the variation of the corresponding LDOS [13]. However, to go

further, i.e., for a quantitative measurement, another approach needs to be considered.

Here, first let us present the considered experimental setup, then some elements on LDOS theory and the polarizability probe, followed by a detail derivation of their connections, and finally we will present the schematic idea behind the LDOS-sensitive technique of the phase. The simulations are based on a discrete dipole approximation (DDA) code that we have used previously to study plasmonic and magneto-optical nanostructures [14].

Since the first development of near-field microscopy [15,16], several types of SNOM have been developed, with different setups and near-field probes. Here, we consider a SNOM operating in the scattering mode with an apertureless dielectric probe and the tip is tilted above the sample, see Fig. 1, in order to realize a measure in transmission.

The incident polarized plane wave E_0 at normal incidence has been focalized on the tip's apex from above and the transmitted light is collected through the sample (see Fig. 1). We will call this configuration trans-scattering SNOM mode (TS-SNOM). The probe's apex is considered to be spherical [17], and vibrates vertically at frequency Ω . Signal demodulation at the tip's oscillation frequency along with an interferometric detection yields transmitted field intensity and phase maps, which corresponds to the local field scattered by the tip, for this we derive formal expressions. Before presenting, the LDOS-sensitive technique of phase (LDOS-SP), let us introduce the theoretical framework that is used to derive the formal expression in this study.

II. THEORY

Assuming the scatterer is small enough to be treated as an electric point dipole [14], the dipole moment \mathbf{p} induced by the exciting local field $\mathbf{E}_{\text{loc}}(\mathbf{r})$, at its position \mathbf{r} , is expressed as follows [18]:

$$\mathbf{p}(\mathbf{r}, \omega) = \epsilon_0 \boldsymbol{\alpha}(\mathbf{r}, \omega) \mathbf{E}_{\text{loc}}(\mathbf{r}, \omega) \quad (1)$$

with $\boldsymbol{\alpha}(\mathbf{r}, \omega)$ the dressed polarizability [13], that is in the most generalized situation, a tensor, can be written as

$$\boldsymbol{\alpha}(\mathbf{r}, \omega) = \frac{\boldsymbol{\alpha}_0}{\mathbf{I} - k_0^2 \mathbf{G}_{\text{reg}}(\mathbf{r}, \mathbf{r}, \omega) \boldsymbol{\alpha}_0} \quad (2)$$

*Corresponding author: remi.vincent@utt.fr

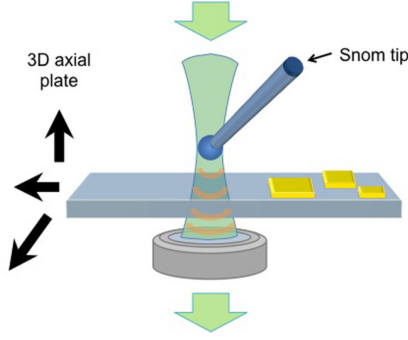


FIG. 1. Trans-scattering-type scanning near-field optical microscopy (TS-SNOM). The wave front illustrates the local field being scattered over the tip and propagating to the detector.

with $\mathbf{G}_{\text{reg}}(\mathbf{r}, \mathbf{r}', \omega)$ as the regular part of the electric dyadic Green function. This Green function connects the electric field between two spatial positions and its own information about its environment. \mathbf{I} is the identity tensor, the wave number in vacuum is $k_0(\omega/c = 2\pi/\lambda)$, and

$$\alpha_0 = 3V(\epsilon - 1)(\epsilon + 2)^{-1} \quad (3)$$

is the quasistatic polarizability of the spherical tip's apex of volume V , with the dielectric constant ϵ .

Now, let us recall that the density of the photonics state $\rho(r, \omega)$ is the trace of the imaginary part of the Green function [19], more precisely its regular part $\mathbf{G}_{\text{reg}}(\mathbf{r}, \mathbf{r}', \omega)$,

$$\rho(\mathbf{r}, \omega) = \frac{6\omega}{\pi c^2} \text{Tr}[\Im[\mathbf{G}_{\text{reg}}(\mathbf{r}, \mathbf{r}, \omega)]] \quad (4)$$

and the partial LDOS (pLDOS), $\rho_{\mathbf{n}}(r, \omega)$, is a component of this LDOS for a given \mathbf{n} direction. Therefore it can be written as

$$\rho_{\mathbf{n}}(\mathbf{r}, \omega) = \frac{6\omega}{\pi c^2} \Im[\mathbf{n} \cdot \mathbf{G}_{\text{reg}}(\mathbf{r}, \mathbf{r}, \omega) \cdot \mathbf{n}]. \quad (5)$$

It can be noted that the pLDOS is the LDOS available for a point dipole, which is oriented along the direction of \mathbf{n} .

III. LDOS-SENSITIVE TECHNIQUE OF PHASE

In our trans-scattering configuration, the vectorial transmitted phase, $\phi_{\text{trans}} = \arg(\mathbf{E}(\mathbf{r}_d, \omega))$, is obtained from the local field that is scattered from the tip and transmitted up to the detector (the direct field being removed by demodulation technique), see Fig. 1. This can be described in terms of the dipolar moment $\mathbf{p}(\mathbf{r}, \omega)$, see Eq. (1), propagating up towards the detector (at position \mathbf{r}_d)

$$\mathbf{E}(\mathbf{r}_d, \omega) = \mathbf{G}(\mathbf{r}_d, \mathbf{r}, \omega) \mathbf{p}(\mathbf{r}, \omega). \quad (6)$$

For a general case, the dipolar moment is a combination of moments in several directions depending on the direction of the local field $\mathbf{E}_{\text{loc}} = E_{\text{loc},x} \mathbf{e}_x + E_{\text{loc},y} \mathbf{e}_y + E_{\text{loc},z} \mathbf{e}_z$, and on the polarizability tensor $\boldsymbol{\alpha}(\mathbf{r})$ as given by Eq. (1). Using the following, let us simplify our analysis to the case of layered non gyrotropic substrates (LNGS). Under this condition, the incoming x -polarized plane wave induces a local field polarized along the x -direction $\mathbf{E}_{\text{loc}} = E_{\text{loc}} \mathbf{e}_x$, and the Green function $\mathbf{G}_{\text{reg}}(\mathbf{r}, \mathbf{r})$ and $\boldsymbol{\alpha}(\mathbf{r})$ are diagonal. Therefore Eq. (6) can

be approximated as follows:

$$\mathbf{E}(\mathbf{r}_d) = \epsilon_0 \mathbf{G}(\mathbf{r}_d, \mathbf{r}) \mathbf{e}_x [\mathbf{e}_x \cdot \boldsymbol{\alpha}(\mathbf{r}) \cdot \mathbf{e}_x] E_{\text{loc}}(\mathbf{r}). \quad (7)$$

This formulation leads to a simple decomposition of the trans-scattered phase, of the transmitted field $\mathbf{E}(\mathbf{r}_d)$ in the direction \mathbf{e}_x ,

$$\phi_{\text{trans}, \mathbf{e}_x} = \arg(\mathbf{E}(\mathbf{r}_d, \omega) \cdot \mathbf{e}_x) = \phi_{G, \mathbf{e}_x} + \phi_{\alpha, \mathbf{e}_x}(\mathbf{r}) + \phi_{E_{\text{loc}}}. \quad (8)$$

In the TS-SNOM mode, the phase in the x direction, $\phi_{\text{trans}, \mathbf{e}_x}$, is the sum of the phase of the total Green function $\phi_{G, \mathbf{e}_x} = \mathbf{e}_x \cdot \mathbf{G}(\mathbf{r}_d, \mathbf{r}) \cdot \mathbf{e}_x$, in the x direction, that is propagating the field from the probe position up to the detector, the phase of the polarizability tensor in the x -direction $\phi_{\alpha, x}(\mathbf{r}, \omega) = \mathbf{e}_x \cdot \arg(\boldsymbol{\alpha}(\mathbf{r}, \omega)) \cdot \mathbf{e}_x$, and the phase of the local field $\phi_{E_{\text{loc}}}$. This last term $\phi_{E_{\text{loc}}}(\mathbf{r})$, being the usual term, is assumed to be measured in general SNOM interferometric technique. Indeed, the dressed polarizability, Eq. (2), which contains the regular part of the total Green function $\mathbf{G}_{\text{reg}}(\mathbf{r}, \mathbf{r}, \omega)$, gives the information about the environment.

A. Phase of the near-field probe

Here, let us focus on the second term, the phase of the polarizability in the x -direction $\phi_{\alpha, \mathbf{e}_x}$ and its link to the LDOS in the x direction, $\rho_{\mathbf{e}_x}(\mathbf{r}, \omega)$, Eq. (5), and call this quantity, probe's phase shift (PPS). Using Eqs. (2) and (3) along with the probe being dielectric and $\text{Arg}(\alpha_0) = 0$, the equation can be written as

$$\begin{aligned} \phi_{\alpha, \mathbf{e}_x}(\mathbf{r}, \omega) &= \mathbf{e}_x \cdot \arg(\boldsymbol{\alpha}(\mathbf{r}, \omega)) \cdot \mathbf{e}_x \quad (9) \\ &= -\mathbf{e}_x \cdot \arg(1 - k_0^2 \mathbf{G}_{\text{reg}}(\mathbf{r}, \mathbf{r}, \omega) \alpha_0(\omega)) \cdot \mathbf{e}_x \quad (10) \\ &= \arctan \frac{k_0^2 \alpha_0 \Im[\mathbf{e}_x \cdot \mathbf{G}_{\text{reg}}(\mathbf{r}, \mathbf{r}, \omega) \cdot \mathbf{e}_x]}{1 - k_0^2 \alpha_0 \Re[\mathbf{e}_x \cdot \mathbf{G}_{\text{reg}}(\mathbf{r}, \mathbf{r}, \omega) \cdot \mathbf{e}_x]}. \quad (11) \end{aligned}$$

A direct observation of this formula, informs us that for a small enough value of the quasi-static polarizability α_0 [i.e., small tip, see Eq. (3)], the previous equation (11), gets reduced to the following:

$$\phi_{\alpha, \mathbf{e}_x}(\mathbf{r}, \omega) \simeq k_0^2 \alpha_0 \Im[\mathbf{e}_x \cdot \mathbf{G}_{\text{reg}}(\mathbf{r}, \mathbf{r}, \omega) \cdot \mathbf{e}_x]. \quad (12)$$

We will see the consequences of this formula in the following sections, where the two cases are explained.

B. In vacuum

It is to be noted that in vacuum $\Im[\mathbf{n} \cdot \mathbf{G}_{\text{reg}, \text{vac}}(\mathbf{r}, \mathbf{r}, \omega) \cdot \mathbf{n}] = k_0/6\pi$ and Eqs. (11) and (12) reduce to the following:

$$\phi_{\alpha_{\text{vac}}, \mathbf{e}_x} \simeq \arctan \left(\frac{k_0^3 \alpha_0}{6\pi} \right) \simeq \frac{k_0^3 \alpha_0}{6\pi}. \quad (13)$$

We observe that the probe phase shift is a nonzero value and that it can have consequences in experimental situations. This phenomenon is due to the radiation losses, included in Eq. (2), and is taken into account by the radiation correction in the dipolar polarizability [13], $\alpha_{\text{vac}} = \alpha_0 (1 - i \frac{k_0^3}{6\pi} \alpha_0)^{-1}$. To illustrate this effect, we have plotted in Fig. 2, its dependence with the probe radius. From this, one can observe the PPS in vacuum has a cubic dependency with the probe's radius, see Eq. (13). It leads to a magnitude of order two proportionality between 25 and 5 nm radius, respectively, and $\phi_{\alpha_{25}, \mathbf{e}_x} \gg \phi_{\alpha_{5}, \mathbf{e}_x}$.

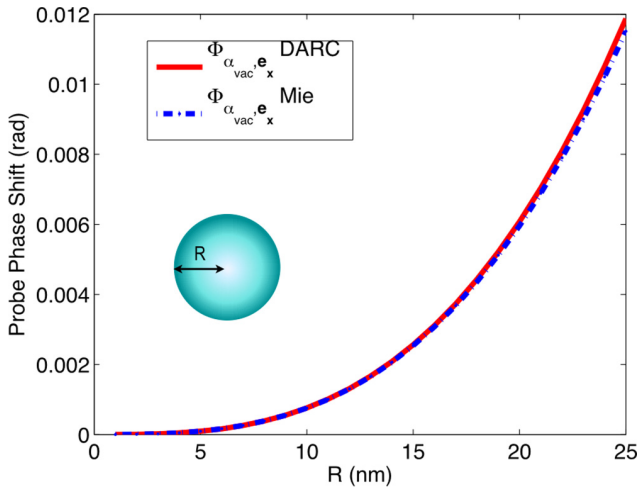


FIG. 2. Vacuum PPS $\phi_{\alpha_{\text{vac}},e_x}$ in the dipolar approximation with radiative correction (DARC), and with Mie calculation, as a function of the probe's radius.

Let us notice here that a 25-nm dielectric probe creates an intrinsic phase shift of around 0.5° . In Fig. 2, a comparison with Mie theory [20] has been added and it shows that till 25-nm-probe radius the dipolar approach shows small deviation with exact Mie solution.

C. In a given environment

In a general situation of an LNGS, Eq. (12), indicates a remarkable result, the probe's phase shift is proportional to the pLDOS,

$$\phi_{\alpha,e_x}(\mathbf{r},\omega) \propto \rho_{e_x}(\mathbf{r},\omega). \quad (14)$$

This is one of the key point of this study. It demonstrates that a measure of the PPS gives us quantitative information about the pLDOS.

Furthermore, using renormalized expressions, we obtain

$$\hat{\phi}_{\alpha,e_x}(\mathbf{r},\omega) \simeq \frac{6\pi}{k_0} \Im[\mathbf{e}_x \cdot \mathbf{G}_{\text{reg}}(\mathbf{r},\mathbf{r},\omega) \cdot \mathbf{e}_x] = \hat{\rho}_{e_x}(\mathbf{r},\omega), \quad (15)$$

an equality between the PPS change $\hat{\phi}_{\alpha,e_x}(\mathbf{r},\omega) = \frac{\phi_{\alpha,e_x}(r,\omega)}{\phi_{\alpha_{\text{vac}},e_x}}$ and the LDOS change $\hat{\rho}_{e_x}(\mathbf{r},\omega) = \frac{\rho_{e_x}(r,\omega)}{\rho_0(\omega)}$. Normalization is done by dividing the PPS and LDOS by their values in free space, i.e., without the environment $\phi_{\alpha_{\text{vac}},e_x}$, or equivalently for large distances from the sample.

To illustrate those analytical results, we simulate an experimental configuration that is made up of a silver film of 10-nm thickness. The numerical calculations are realized using a dipole dipole approximation (DDA) code. The impinging light is an *s*-polarized plane wave at a wavelength of 400 nm, scattering over a spherical particle. The probe is approximated by a dipole [13] and calculations are done at variable distances z above the metallic film. In Fig. 3, we trace the normalized partial LDOS, $\hat{\rho}_{e_x}(\mathbf{r},\omega)$, the phase of the dipolar moment, $\phi_{p,e_x} = \arg(\mathbf{p} \cdot \mathbf{e}_x)$, along with the phase of the local field, $\phi_{E_{\text{loc}}}$ and the normalized PPS, $\hat{\phi}_{\alpha,e_x}$. A 1-nm probe radius is used. The phase of the dipolar moment (PDM) is defined as follows $\phi_{p,e_x} = \phi_{\alpha,e_x} + \phi_{E_{\text{loc}}}$.

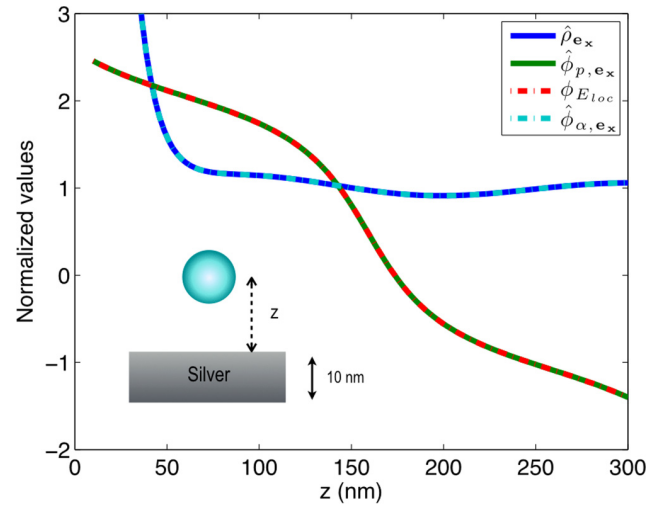


FIG. 3. Normalized partial LDOS $\hat{\rho}_{e_x}(\mathbf{r},\omega)$, phase of the dipolar moment ϕ_{p,e_x} , phase of the local field $\phi_{E_{\text{loc}}}$, and normalized PPS $\hat{\phi}_{\alpha,e_x}$ at a variable distance of a 10-nm silver film, with a dielectric probe of 1 nm radius, at $\lambda = 400$ nm.

In this case, the PDM and the phase of the local field have very small differences, which are related to the polarizability phase. This illustrates the fact that even in the case of a strong LDOS environment, the PPS remains negligible due to the 1 nm probe size. Nevertheless, a comparison of the normalized PPS with the normalized pLDOS shows a perfect agreement as expected from Eq. (15).

D. Polarizability phase extraction method

Based on the results of the previous sections, a polarizability phase extraction method for pLDOS is proposed, see Fig. 4. After measuring the transmitted phase with tips of different size, and calculating the difference, we obtain the phase

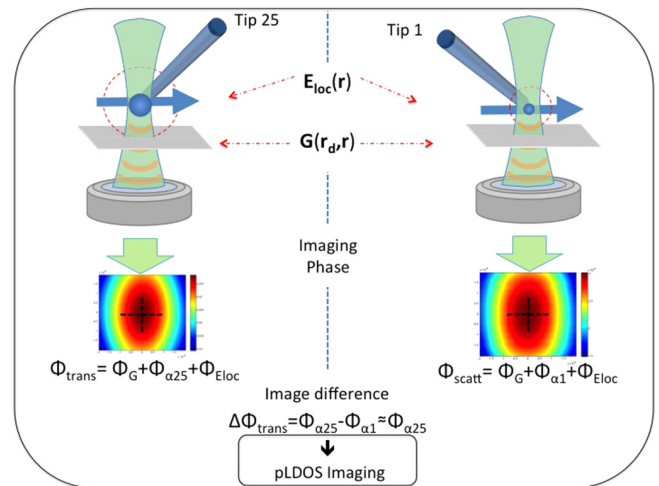


FIG. 4. Illustration of the LDOS phase sensitive (LDOS-SP) technique. It is based on the imaging of the trans-scattering phase map with two different tip sizes that is done sequentially and by normalization of the numerical subtraction, we obtain the map of the pLDOS.

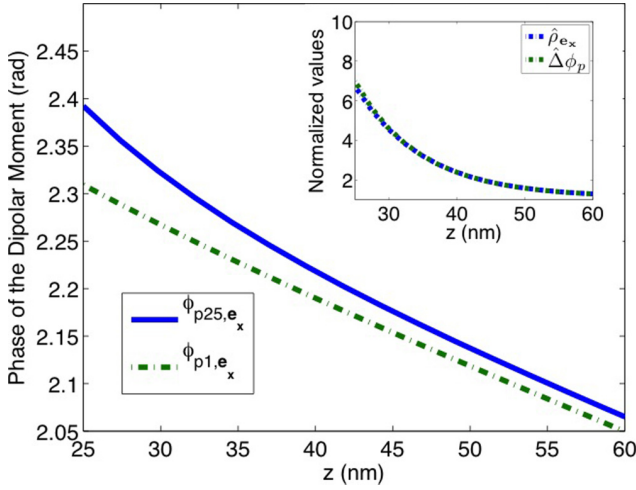


FIG. 5. PDM for two tip radius, $R = 25$ and 1 nm. In insert, normalized pLDOS, and normalized difference of the PDM between the two tip of radius $R = 25$ and 1 nm.

difference of polarizabilities:

$$\phi_{\text{trans}25, \mathbf{e}_x} - \phi_{\text{trans}1, \mathbf{e}_x} = \phi_{p25, \mathbf{e}_x} - \phi_{p1, \mathbf{e}_x} = \phi_{\alpha25, \mathbf{e}_x} - \phi_{\alpha1, \mathbf{e}_x}. \quad (16)$$

Here we assume $\phi_{\alpha25, \mathbf{e}_x} \gg \phi_{\alpha1, \mathbf{e}_x}$, based on the previous results, therefore

$$\phi_{\text{trans}25, \mathbf{e}_x} - \phi_{\text{trans}1, \mathbf{e}_x} \approx \phi_{\alpha25, \mathbf{e}_x} \propto \rho_{\mathbf{e}_x}(\mathbf{r}, \omega). \quad (17)$$

In Fig. 5, the phase of the dipolar moment (PDM) is plotted for two different sizes of the tips, namely, 1 and 25 nm, as a function of the separation distance between the probe and the slab. We observe important phase shift differences between the two tips of up to 0.1 rad ($\simeq 5.5^\circ$) at 25 nm from the surface, revealing strong LDOS effect. Finally, the difference $\Delta\phi_p(z) = \phi_{p25, \mathbf{e}_x} - \phi_{p1, \mathbf{e}_x}$, normalized by its value far from

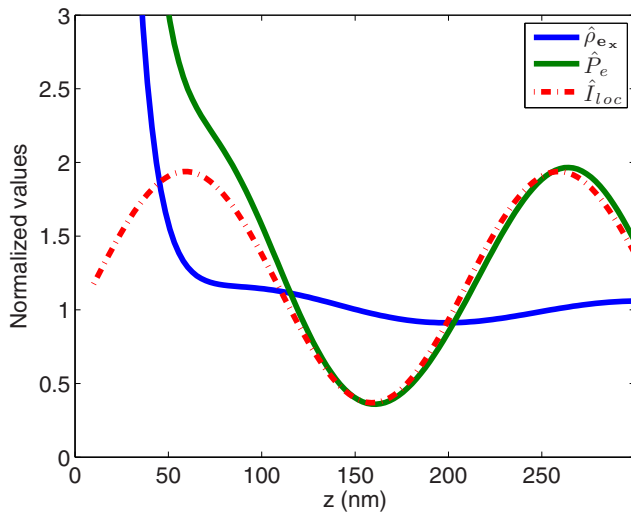


FIG. 6. Normalized extinction, normalized pLDOS, and the normalized local intensity for a 1 nm probe radius at a variable distance of a 10 -nm silver film, at $\lambda = 400$ nm.

the substrate $\hat{\Delta}\phi_p = \Delta\phi_p(z)/\Delta\phi_p(z \rightarrow \infty)$, is plotted in the insert of Fig. 5 and compared to the pLDOS. We find that good adequacies are shown and are in agreement with Eq. (15). In conclusion, simply imaging the trans-scattering phase map with two tip sizes, sequentially would allow us to map the pLDOS by numerical subtraction followed by normalization. In these calculations, a tip of 1 -nm radius was considered, but experimentally it is not accessible. The calculation with a radius that is experimentally accessible is of 5 nm, which could be realized as follows: $\phi_{\text{trans}25, \mathbf{e}_x} - \phi_{\text{trans}5, \mathbf{e}_x} \approx \phi_{\alpha25, \mathbf{e}_x} \propto \rho_{\mathbf{e}_x}(\mathbf{r}, \omega)$. The results are expected to be the same because it is assumed that the PPS, as in the vacuum case, has a cubic dependency with the probe's radius, therefore $\phi_{\alpha25, \mathbf{e}_x} \gg \phi_{\alpha5, \mathbf{e}_x} \gg \phi_{\alpha1, \mathbf{e}_x}$. Finally, as the range of the radius of the tip seems realistic from 5 to 25 nm, the experiment appears to be accessible with the state of the art s-SNOM setup.

E. Comparison with extinction

In order to contrast those results with the extinction technique, a simulation based on the same computation code is realized. The extinction measurement is compared with the pLDOS and discrepancies are shown, see Fig. 6. In this figure, we trace the normalized partial LDOS $\hat{\rho}_{\mathbf{e}_x}(\mathbf{r}, \omega)$ along with extinction efficiency of the particle $P_e(\mathbf{r}, \omega)/P_{e,0}(\mathbf{r}, \omega)$ and the local intensity $I_{\text{loc}}(\mathbf{r})$. We can observe a factor of 2 between the pLDOS and the normalized extinction for a distance of around 50 nm from the surface. These differences are due to the intrication of the local field in the extinction response of the particle, the relation at the origin of this effect is demonstrated in the appendix, and given by

$$P_e(\mathbf{r}, \omega) = \frac{\omega\epsilon_0}{2V} I_{\text{loc}}(\mathbf{r}) [\mathbf{e}_x \text{Im}[\alpha(\omega)] \cdot \mathbf{e}_x]. \quad (18)$$

Aside to this comparison, another remarkable quantity can be resolved, indeed, by dividing the normalized extinction $P_e(\mathbf{r}, \omega)/P_{e,0}(\mathbf{r}, \omega)$ by the normalized pLDOS $\hat{\rho}_{\mathbf{e}_x}(\mathbf{r}, \omega)$ obtained from the LDOS-SP method, we obtain the local intensity $I_{\text{loc}}(\mathbf{r})/I_0$ as follows:

$$\frac{I_{\text{loc}}(\mathbf{r})}{I_0} = \frac{P_e(\mathbf{r}, \omega)/P_{e,0}(\mathbf{r}, \omega)}{\hat{\rho}_{\mathbf{e}_x}(\mathbf{r}, \omega)}. \quad (19)$$

Finally, let us note that the basic idea behind the LDOS-SP method lies in the derived equation (12), which links the PPS and the pLDOS. Therefore any other method that could retrieve the phase of the polarizability would allow us to access the LDOS. For instance, any modulation at the level of the polarizability tensor of the tip (acoustic modulation, anisotropic control, magneto-optic, liquid crystal, etc.) would theoretically allow the same extraction measurement.

IV. CONCLUSIONS

From a theoretical and a numerical analysis point of view, we have confirmed that in an experimental TS-SNOM mode, the extinction and the pLDOS exhibit discrepancies coming from the local field intensity. A framework for the trans-scattering phase of the probe is developed and relationships between the probe's phase shift and the LDOS are established.

These findings have lead us to propose an experimental approach for measuring the LDOS optically and numerical evaluation indicates that it should improve the extinction measurement.

ACKNOWLEDGMENTS

This work was supported by SINPHONIE (ANR-12-NANO-0019) and LABEX ACTION (ANR-11-LABX-01-01) projects funded by Agence Nationale de la Recherche (ANR). Thanks to A. Bruyant for fruitful discussions.

APPENDIX: EXTINCTION BY A NEAR FIELD PROBE

The expression of the dressed polarizability, Eq. (2), can be the starting point to compute the extinction measurement in an arbitrary environment [13]. To carry out this derivation, we start with the expression for the power extracted, i.e., absorbed

and scattered, from the external field \mathbf{E}_{loc} by the probe [21]

$$P_e = \frac{1}{2} \int_V \text{Re}[\mathbf{j}(\mathbf{r}', \omega) \cdot \mathbf{E}_{\text{loc}}^*(\mathbf{r}', \omega)] d^3 \mathbf{r}', \quad (\text{A1})$$

where $\mathbf{j}(\mathbf{r}', \omega) = -i\omega\epsilon_0[\epsilon(\omega) - 1]\mathbf{E}_{\text{loc}}(\mathbf{r}', \omega)$ is the current density induced in the probe. As the electric field is assumed to be uniform inside the probe, and under the assumption of an electrically small probe [13], the extracted power for the probe can be written as

$$P_e = \frac{\omega\epsilon_0}{2V} \text{Im}[\alpha(\omega)\mathbf{E}_{\text{loc}}(\mathbf{r}, \omega) \cdot \mathbf{E}_{\text{loc}}^*(\mathbf{r}, \omega)]. \quad (\text{A2})$$

And using $\mathbf{E}_{\text{loc}} = E_{\text{loc}}\mathbf{e}_x$, this can be rewritten as

$$P_e(\mathbf{r}, \omega) = \frac{\omega\epsilon_0}{2V} I_{\text{loc}}(\mathbf{r})[\mathbf{e}_x \text{Im}[\alpha(\omega)] \cdot \mathbf{e}_x]. \quad (\text{A3})$$

This expression connects the extinction measurement with a cross product between the electric field and a term related to the imaginary part of the polarizability of the probe's tip.

-
- [1] W. L. Barnes, *J. Mod. Opt.* **45**, 661 (1998).
- [2] J. J. Wierer, Jr., A. David, and M. M. Megens, *Nat. Photon.* **3**, 163 (2009).
- [3] K. Saxena, V. K. Jaina, and D. S. Mehtab, *Opt. Mater.* **32**, 221 (2009).
- [4] T. Schröder, A. W. Schell, G. Kewes, T. Aichele, and O. Benson, *Nano Lett.* **11**, 198 (2011).
- [5] A. Laucht, S. Pütz, T. Günthner, N. Hauke, R. Saive, S. Frédérick, M. Bichler, M.-C. Amann, A. W. Holleitner, M. Kaniber, and J. J. Finley, *Phys. Rev. X* **2**, 011014 (2012).
- [6] D. Cao, A. Cazé, M. Calabrese, R. Pierrat, N. Bardou, S. Collin, R. Carminati, V. Krachmalnicoff, and Y. De Wilde, *ACS Photon.* **2**, 189 (2015).
- [7] M. Frimmer, Y. Chen, and A. F. Koenderink, *Phys. Rev. Lett.* **107**, 123602 (2011).
- [8] A. W. Schell, P. Engel, J. F. M. Werra, C. Wolff, K. Busch, and O. Benson, *Nano Lett.* **14**, 2623 (2014).
- [9] R. Carminati and J. J. Sáenz, *Phys. Rev. Lett.* **84**, 5156 (2000).
- [10] G. Colas des Francs, C. Girard, J. C. Weeber, and A. Dereux, *Chem. Phys. Lett.* **345**, 512 (2001).
- [11] C. Chicanne, T. David, R. Quidant, J. C. Weeber, Y. Lacroute, E. Bourillot, A. Dereux, G. Colas des Francs, and C. Girard, *Phys. Rev. Lett.* **88**, 097402 (2002).
- [12] C. Huang, A. Bouhelier, G. Colas Des Francs, G. Legay, J. C. Weeber, and A. Dereux, *Opt. Lett.* **33**, 300 (2008).
- [13] E. Castanie, R. Vincent, R. Pierrat, and R. Carminati, *Intern. J. Opt.* **2012**, 452047 (2012).
- [14] R. Vincent, H. Marinchio, J. J. Saenz, and R. Carminati, *Phys. Rev. B* **90**, 241412(R) (2014).
- [15] A. Lewis, M. Isaacson, A. Harootunian, and A. Muray, *Ultramicroscopy* **13**, 227 (1984).
- [16] D. W. Pohl, W. Denk, and M. Lanz, *Appl. Phys. Lett.* **44**, 651 (1984).
- [17] Y. Oshikane, T. Kataoka, M. Okuda, S. Hara, H. Inoue, and M. Nakano, *Sci. Technol. Adv. Mater.* **8**, 181 (2007).
- [18] G. Colas des Francs, S. Derom, R. Vincent, A. Bouhelier and A. Dereux, *Int. J. Opt.* **2012**, 175162 (2012).
- [19] R. Carminati, A. Cazé, D. Cao, F. Peragut, V. Krachmalnicoff, R. Pierrat, and Y. De Wilde, *Surf. Sci. Rep.* **70**, 1 (2015).
- [20] G. Mie, *Ann. Phys.* **330**, 377 (1908).
- [21] S. Albaladejo *et al.*, *Opt. Express* **18**, 3556 (2010).

Bibliography

- [1] <https://en.wikipedia.org/wiki/Internet>
- [2] <http://www.linux.com/news/who-needs-internet-things>
- [3] <http://www.linux.com/NEWS/21-OPEN-SOURCE-PROJECTS-IOT> 21 Open Source Projects for IoT (Linux.com)
- [4] "Internet of Things Global Standards Initiative". ITU. Retrieved 26 June 2015.
- [5] "Internet of Things Global Standards Initiative". ITU. Retrieved 1 June 2016.
- [6] <https://datafloq.com/read/fog-computing-vital-successful-internet-of-things/1166>
- [7] https://hbr.org/resources/pdfs/comm/verizon/18980_HBR_Verizon_IoT_Nov_14.pdf
- [8] http://www.internet-of-things-research.eu/pdf/Converging_Technologies_for_Smart_Environments_and_Integrated_Ecosystems_IERC_Book_Open_Access_2013.pdf
- [9] http://www.cisco.com/web/solutions/trends/iot/introduction_to_IoT_november.pdf
- [10] <http://cordis.europa.eu/fp7/ict/enet/documents/publications/iot-between-the-internet-revolution.pdf>
- [11] <http://www.vs.inf.ethz.ch/publ/papers/Internet-of-things.pdf>
- [12] <http://www.cognizant.com/InsightsWhitepapers/Reaping-the-Benefits-of-the-Internet-of-Things.pdf>
- [13] "The Supply Chain: Changing at the Speed of Technology". Retrieved 18 September 2015.
- [14] Dave Evans (April 2011). "The Internet of Things: How the Next Evolution of the Internet Is Changing Everything" (PDF). Cisco. Retrieved 15 February 2016.
- [15] "Molluscan eye". Retrieved 26 June 2015.

- [16] More Than 30 Billion Devices Will Wirelessly Connect to the Internet of Everything in 2020, ABI Research
- [17] "Top Five Things to Know about Cisco BiDi Optical Technology White Paper - Cisco". 2014-09-05. Retrieved 2016-05-06. 40-Gbps bidirectional (BiDi) optical technology
- [18] Vongsingthong, S.; Smanchat, S. (2014). "Internet of Things: A review of applications & technologies" (PDF). Suranaree Journal of Science and Technology.
- [19] Kyriazis, D.; Varvarigou, T.; Rossi, A.; White, D.; Cooper, J. (4–7 June 2013). "Sustainable smart city IoT applications: Heat and electricity management & Eco-conscious cruise control for public transportation". IEEE International Symposium and Workshops on a World of Wireless, Mobile and Multimedia Networks (WoWMoM): 1. doi:10.1109/WoWMoM.2013.6583500. ISBN 978-1-4673-5827-9.
- [20] Severi, S.; Abreu, G.; Sottile, F.; Pastrone, C.; Spirito, M.; Berens, F. (23–26 June 2014). "M2M Technologies: Enablers for a Pervasive Internet of Things". The European Conference on Networks and Communications (EUCNC2014).
- [21] Ersue, M.; Romascanu, D.; Schoenwaelder, J.; Sehgal, A. (4 July 2014). "Management of Networks with Constrained Devices: Use Cases". IETF Internet Draft ; draft-ietf-opsawg-coman-use-cases;.
- [22] "STE Security Innovation Awards Honorable Mention: The End of the Disconnect". Retrieved 12 August 2015.
- [23] Davies, Nicola. "How the Internet of Things will enable 'smart buildings'". Extreme Tech.
- [24] Li, Shixing; Wang, Hong; Xu, Tao; Zhou, Guiping (2011). "Application Study on Internet of Things in Environment Protection Field". Lecture Notes in Electrical Engineering Volume. Lecture Notes in Electrical Engineering. 133: 99–106. doi:10.1007/978-3-642-25992-0_13. ISBN 978-3-642-25991-3.
- [25] FIT French Project. "Use case: Sensitive wildlife monitoring". Retrieved 10 July 2014.
- [26] Istepanian, R.; Hu, S.; Philip, N.; Sungoor, A. (30 August – 3 September 2011). "The potential of Internet of m-health Things "m-IoT" for non-invasive glucose level sensing". Annual International Conference of the IEEE Engineering in Medicine and Biology Society (EMBC): 5264. doi:10.1109/IEMBS.2011.6091302. ISBN 978-1-4577-1589-1.

- [27] Swan, Melanie (8 November 2012). "Sensor Mania! The Internet of Things, Wearable Computing, Objective Metrics, and the Quantified Self 2.0". *Sensor and Actuator Networks*. 1 (3): 217–253. doi:10.3390/jsan1030217.
- [28] <http://encyclopedia2.thefreedictionary.com/Optical+Detector>
- [29] <https://www.biocore.com/lifesciences/index.html>
- [30] D. R. Sommers, D. D. Stubbs and W. D. Hunt, "Investigation of SPR technology using Texas Instruments' Spreeta™ sensor," *Proceedings of IEEE Sensors, 2002*, pp. 1244-1249 vol.2. doi: 10.1109/ICSENS.2002.1037294
- [31] http://floralis.fr/us/accueil/floralis_innovation.php
- [32] Clement E. Furlong, Professor, Departments of Medicine (Div. Medical Genetics) & Genome Sciences AOAC, Tacoma, WA 2012
- [33] Vesna Hodnik and Gregor Anderluh*, "Toxin Detection by Surface Plasmon Resonance", *Sensors* 2009, 9, 1339-1354; doi:10.3390/s9031339
- [34] GREGORY DE CRESCENZO, CYRIL BOUCHER, YVES DUROCHER and MARIO JOLICOEUR, "Kinetic Characterization by Surface Plasmon Resonance-Based Biosensors: Principle and Emerging Trends", published in *Cellular and Molecular Bioengineering* (2008) DOI: 10.1007/s12195-008-0035-5
- [35] M. Renault, Y. Hadjar, S. Blaize, A. Bruyant, L. Arnaud, G. Lerondel and P. Royer "Bidimensional near-field sampling Spectrometry", *Opt. Letters* 35,3303-3305 (2010).
- [36] Y. Hadjar, R. Mikael, S. Blaize, A. Bruyant, L. Arnaud, G. Lerondel and P. Royer "BoBiSS: Compact Bidimensional Sampling Spectrometer", in *Imaging and Applied Optics*, OSA Technical Digest (2011), paper FWB6.
- [37] Y. Hadjar, S. Blaize, A. Bruyant, L. Arnaud, G. Lerondel and P. Royer "Compact spectrometer for 2 dimensional sampling", Patent number WO2009127794A1 2009.
- [38] Y. Hadjar, M. Renault, S. Blaize, A. Bruyant, R. Vincent and A. Hmima, "Compact interferometer transducer based on surface plasmon phase resonance", *J. Opt. Soc Am. A*, vol. 32, no. 5, p. 771-777, 2015.
- [39] https://en.wikipedia.org/wiki/Nyquist-Shannon_sampling_theorem#refShannon49
- [40] *Principles of Nano-Optics*, Second Edition, by Lukas Novotny and Bert Hecht.
- [41] M. Quinten, A. Pack, and R. Wannemacher, *Appl. Phys. B* 68, 87 (1999)

- [42] C. Liu, T. Weigel, G. Schweiger, "Structural resonances in a dielectric sphere on a dielectric surface illuminated by an evanescent wave", *Opt. Commun.* 185 (2000) 249-261.
- [43] S. Albaladejo, R. Gómez-Medina, L. S. Froufe-Pérez et al., "Radiative corrections to the polarizability tensor of an electrically small anisotropic dielectric particle," *Optics Express*, vol. 18, no. 4, pp. 3556–3567, 2010.
- [44] B. Knoll and F. Keilmann, *Opt. Commun.* 182, 321-328 (2000).
- [45] C. Girard, A. Dereux, and J.-C. Weeber, *Phys. Rev. E* 58, 1081 (1998)
- [46] E. Castanie, R. Vincent, R. Pierrat, and R. Carminati, *Intern. J. of Opt.* 2012, 452047 (2012).
- [47] W. Lukosz and R. E. Kunz, "Light Emission by magnetic and electric dipoles close to a plane interface. I. Total Radiated power", *Journal of Optical Society of America*, Vol 67, Page no. 1607, No. 12 December 1977.
- [48] W. Lukosz and R. E. Kunz, "Light Emission by magnetic and electric dipoles close to a plane dielectric interface. II. Radiated patterns of perpendicular oriented dipoles", *Journal of Optical Society of America*, Vol 67, Page no. 1615, No.12 December 1977.
- [49] W. Lukosz, "Light Emission by magnetic and electric dipoles close to a plane dielectric interface. III. Radiated patterns of dipoles in arbitrary orientation", *Journal of Optical Society of America*, Vol 69, Page no. 1503, No. 11 November 1979.
- [50] R. Vincent, H. Marinchio, J.J. Saenz, and R. Carminati, *Physical Review B*, 90, 241412(R) (2014).
- [51] J. Schneider, Lecture notes on FDTD, Chapter 3, School of Electrical Engineering and Computer Science, Washington State University.
- [52] <http://www.ece.utah.edu/ece6340/LECTURES/lecture%2014/FDTD.pdf>
- [53] https://en.wikipedia.org/wiki/Finitedifference_timedomain_method
- [54] V.D. Miljkovic, T. Shegai, M. Kall, P. Johansson, "Mode-Specific Directional emission from hybridized particle-on-film plasmons", *Optics Express*, 4 July 2011, Vol. 19, No. 14 Page number 12856-12864
- [55] S. Zhang, K. Bao, N. J. Halas, H. Xu, P. Nordlander, "Substrate-Induced Fano Resonances of a Plasmonic Nanocube: A route to Increased-Sensitivity Localized Surface Plasmon Resonance Sensors Revealed", *Nano Letters* 2011, 11, 1657-1663, Published on March 16, 2011

- [56] <http://whatis.techtarget.com/definition/motherboard>
- [57] <http://whatis.techtarget.com/definition/laser>
- [58] <http://pandaboard.org/content/platform>
- [59] <https://www.raspberrypi.org/products/model-a-plus/>
- [60] <http://www.linksprite.com/linksprite-pcduino/>
- [61] <https://beagleboard.org/black>
- [62] [https://en.wikipedia.org/wiki/Cotton_Candy_\(28single-board_computer\)29](https://en.wikipedia.org/wiki/Cotton_Candy_(28single-board_computer)29)
- [63] <http://www.nvidia.com/object/jetson-tk1-embedded-dev-kit.html>
- [64] <http://www.udoo.org/udoo-dual-and-quad/>
- [65] TJ Donegan. "Casio Exilim EX-H50 First Impressions Review". Retrieved February 23, 2015
- [66] Moynihan, Tom. "CMOS Is Winning the Camera Sensor Battle, and Here's Why". Retrieved 10 April 2015.
- [67] dalsa.com - CCD vs CMOS from Photonics Spectra 2001
- [68] dpreview.com - Sensors By Vincent Bockaert
- [69] <https://eewiki.net/display/linuxonarm/PandaBoard>
- [70] J. Homola, Surface Plasmon Sensors: review vol. 54, 1999
- [71] "Detection of lower hydrocarbons by means of surface plasmon resonance", Takanori Urashi, Tsuyoshi Arakawa, Sensors and Actuators B 76 2001) 32-35, Elsevier Science B.V.
- [72] R.P. Podgorsek, T. Sterkenburgh, J. Wolters, T. Ehrenreich, S. Nischwitz, H. Franke, "Optical gas sensing by evaluating ATR leaky mode spectra", Sensors and Actuators B 39 (1997) 349– 352.
- [73] C.R. Lavers, J.S. Wilkinson, A waveguide-coupled surface- plasmon sensor for an aqueous environment, Sensors and Ac- tuators B 22 (1994) 75–81.
- [74] J. Homola et al, Tuning of spectral opera- tion range of a waveguide surface plasmon resonance sensor, Electron. Lett. 33 (1997) 1246–1248.
- [75] "Theory and Applications of Surface Plasmon Resonance, Resonant Mirror, Resonant Waveguide Grating, and Dual Polarization Interferometry Biosensors", Hikmat N. Daghestani 1 and Billy W. Day 2,*, Sensors 2010, 10, 9630-9646; doi:10.3390/s101109630

- [76] Thomas Lang, Thomas Hirsch*, Christoph Fenzl, Fabian Brandl and Otto S. Wolfbeis, "Surface Plasmon Resonance Sensor for Dissolved and Gaseous Carbon Dioxide.", Institute of Analytical Chemistry, Chemo- and Biosensors, University of Regensburg, 93040 Regensburg, Germany.
- [77] Thomas Lang, Thomas Hirsch,* Christoph Fenzl, Fabian Brandl, and Otto S. Wolfbeis, "Surface Plasmon Resonance Sensor for Dissolved and Gaseous Carbon Dioxide", Published on October 8, 2012 in 2012 American Chemical Society 9085,dx.doi.org/10.1021/ac301673n, Anal. Chem. 2012, 84, 9085–9088
- [78] C.C. Jung, S.B. Saban, S.S. Yee, R.B. Darling, Chemical electrode surface plasmon resonance sensor, *Sensors and Actuators B* 32 (1996) 143 – 147.
- [79] T.M. Chinowsky, S.B. Saban, S.S. Yee, Experimental data from a trace metal sensor combining surface plasmon resonance with anodic stripping voltammetry, *Sensors and Actuators B* 35 (1996) 37–43.
- [80] Takanori Urashi, Tsuyoshi Arakawa, "Detection of lower hydrocarbons by means of surface plasmon resonance", Published on *Sensors and Actuators B* 76 (2001) 32±35
- [81] Dudak, F. C. and Boyacı, İ. H. (2009), Rapid and label-free bacteria detection by surface plasmon resonance (SPR) biosensors. *Biotechnology Journal*, 4: 1003–1011. doi:10.1002/biot.200800316
- [82] Ying-Sing, F., Shi-Hui, S., De-Rong, Z., Piezoelectric crystal for sensing bacteria by immobilizing antibodies on divinyl-sulphone activated poly-m-aminophenol film. *Talanta* 2000,51, 151–158.
- [83] N.E. Agbor, J.P. Cresswell, M.C. Petty, A.P. Monkman, An optical gas sensor based on polyaniline Langmuir-Blodgett films, *Sensors and Actuators B* 41 (1997) 137–141
- [84] "Detection of CO Concentration by Using SnO₂ SPR Apparatus and Common-Path Heterodyne Interferometer", Ke-Ming Chen, Chih-Hsiung Shen, and Jing-Heng published in Chen J. Juang and Y.-C. Huang (eds.), *Intelligent Technologies and Engineering Systems, Lecture Notes in Electrical Engineering* 234, DOI 10.1007/978-1-4614-6747-2_97
- [85] A. B. El-Basaty,^{a*} T. A. El-Brolosy,^b S. Abdalla,^c S. Negm^c R. A. Abdellaa and H. Talaat^b, "Surface plasmon sensor for NO₂ gas", Published on *Surf.Interface Anal.* 2008,40,1623–1626, DOI 10.1002/sia.2980

- [86] Ayushi Paliwal¹, Monika Tomar², Vinay Gupta^{1*}, "Surface Plasmon Resonance Based Optical NO_x Gas Sensor", International Conference on Fiber Optics and Photonics © OSA 2012
- [87] Pegah Abadian, Chase Kelley, Edgar Goluch, "Cellular Analysis and Detection using Surface Plasmon Resonance (SPR) Techniques" published in PubMed on February 2014 with DOI: 10.1021/ac500135s
- [88] R. W. Wood, "On a Remarkable Case of Uneven Distribution of Light in a Diffraction Grating Spectrum", *Proceeding of the Physical Society of London*, vol 18, p. 269, 1902
- [89] U.Fano, "The theory of Anomalous Diffraction Gratings and of Quazi-Stationary Waves on metallic Surfaces (Sommerfeld's Waves)", *J. Opt. Soc Am.*, vol. 31, p. 213-222, 1941.
- [90] R. H. Ritchie, "Plasma losses by Fast Electrons in thin films", *Physical Review*, vol. 106, p. 874, 1957.
- [91] <https://refractiveindex.info/?shelf=main&book=Au&page=Johnson>
- [92] https://kb.lumerical.com/en/ref_scripts_getfdtdindex.html
- [93] https://ece.uwaterloo.ca/~bcui/?page_id=6
- [94] Bohren and Huffman, 1998
- [95] Kelly et al. , 2003
- [96] O. D'Allivy Kelly, "Modélisation de l'influence de la géométrie sur des capteurs plasmoniques à détection de phase", Thesis, Ecole Polytechnique de Montréal.
- [97] Homola J. *Surface Plasmon Resonance Based Sensors*. Berlin: Springer; 2006.
- [98] A K Sharma and G J Mohr, "Theoretical understanding of an alternating dielectric multilayer-based fiber optic SPR sensor and its application to gas sensing " published in *New Journal of Physics* 10 (2008) 023039
- [99] Moharam, M., Grann, E. B., Pommet, D. A., and Gaylord, T., 1995, "Formulation for stable and efficient implementation of the rigorous coupled-wave analysis of binary gratings," *Journal of Optical Society of America A*, 12(5), pp. 1068-1076.
- [100] Moharam, M., Pommet, D. A., Grann, E. B., and Gaylord, T., 1995, "Stable implementation of the rigorous coupled-wave analysis for surface-relief gratings: enhanced transmittance matrix approach," *Journal of Optical Society of America A*, 12(5), pp. 1077-1086.

- [101] https://en.wikipedia.org/wiki/Rigorous_coupled-wave_analysis
- [102] APPLICATION OF RIGOROUS COUPLED-WAVE THEORY FOR STUDYING RADIATIVE PROPERTIES OF MICRO/NANOSTRUCURES AND SILVER NANORODS ON GRATINGS, a thesis presented for Master of Science, School of Mechanical Engineering, Georgia Institute of Technology, August 2011 by Ahmad M. Haider
- [103] Hutter and Fendler, 2004
- [104] Ricardo Téllez Limon, "Light Propagation in integrated chains of metallic nanowires: towards a nano sensing device", Thesis, UTT, Troyes
- [105] K. Kneipp, Surface-Enhanced Raman Scattering: Physics and Applications (Topics in Applied Physics), 2006
- [106] E. Simsek, "Full analytical model for obtaining surface plasmon resonance modes of metal nano particle structures embedded in layered media", Published Optics Express 14 Jan 2010
- [107] E. Simsek, "On the Surface Plasmon Resonance modes of Metal Nano Particle Chains and arrays", Published Springer Plasmonics on 09 Jan 2009
- [108] È.B. Crozier et al. , Experimental measurement of the dispersion relations on the surface plasmon modes of metal nano particle chains., Published Optics Express 17482, on 11 Dec 2007
- [109] C. CAUCHETEUR, « Plasmons de surface : Principes physiques et applications », p. 13, 2014.
- [110] W.H. Weber and G.w. Ford, Propagation of optical excitations by dipolar interactions in metal nano particle chains , Published in Physical Review B 70, 125429, on 30 September 2004
- [111] J. DINTINGER, O. MARTIN, "Channel and wedge plasmon modes of metallic V-grooves with finite metal thickness", p.11,2009
- [112] Origami Plasmonique by M. Proteau, MTE, UTT
- [113] "Interference (holographic) diffraction gratings", by M C Hutley, Journal of Physics E : Scientific Instruments 1976 Volume 9 Printed in Great Britain 01976
- [114] "Diffraction gratings: from principles to applications in high-intensity lasers", NICOLAS BONOD, AND JÉRÔME NEAUPORT, Vol. 8, No. 1 / Advances in Optics and Photonics

-
- [115] https://upload.wikimedia.org/wikipedia/commons/b/b2/Data_Flow_of_the_Internet_Protocol_Suite.PNG
- [116] <http://ecomputernotes.com/computernetworkingnotes/multiple-access/carrier-sense-multiple-access-with-collision-detection>
- [117] <http://phoenix.goucher.edu/kelliher/s2011/cs325/may04.html>
- [118] <https://commons.wikimedia.org/wiki/File%3AClient-server-model.svg>
- [119] <http://www.globalspec.com/reference/81338/203279/chapter-12-mobile-ad-hoc-networks>
- [120] <https://commons.wikimedia.org/wiki/File%3AWSN.svg>

Rohit PRASAD

Doctorat : Matériaux, Mécanique, Optique et Nanotechnologie

Année 2017

Intégration du spectromètre CoBiSS et modélisation de puce (L)SPR pour la détection à travers CoBiSS

Aujourd'hui l'Internet des Objets (IdO) est en pleine évolution, et le dispositif de détection optique tel que présenté ici pourrait être utilisé dans ce domaine. En effet ces dispositifs pourraient être utilisés pour faire des tests pour une analyse comme la surveillance de la santé d'une personne en faisant un test sanguin ou d'autres analyses médicales et utilisés pour surveiller l'environnement en testant l'eau ou de l'air dans les villes, les montagnes, les usines, les rivières. Pour créer le dispositif, on a utilisé une combinaison du spectromètre nommé Spectromètre d'échantillonnage bi-directionnel couplé (CoBiSS) [Brevet WO2009127794A1] et une puce à résonance de plasmon de surface (SPR). Dans le but de l'intégration optique, une nouvelle analyse de l'échantillonnage dans le spectromètre CoBiSS est présentée, suivie de l'intégration du système électronique et optique pour supprimer les pièces mobiles. Il était nécessaire de rendre l'appareil petit et portable. Pour faciliter l'utilisation, une interface graphique a été développée. Pour la détection, une puce SPR a été ajoutée à CoBiSS et une nouvelle puce à résonance de plasmon de surface localisée (LSPR) a été modélisée pour maximiser sa sensibilité. Une nouvelle définition du calcul de sensibilité a été proposée. Cet appareil nécessite l'ajout de fonctionnalisation sur (L)SPR Chip pour la détection et une application finale. Cet appareil pourrait être un « objet » idéale dans l'IdO.

Mots clés : intégration des systèmes (ingénierie) - résonateurs optiques - optique intégrée - capteurs optiques - résonance plasmonique de surface - photonique - nanophotonique - Fourier, spectroscopie par transformée de - optique en champs proche.

Device Integration of the CoBiSS Spectrometer and Modelisation of (L)SPR Chip for the Detection through CoBiSS

As the world is moving towards Internet of Things, an optical detection device is presented that can be utilized in this domain. This device can be used to do tests that use optical detection for analysis like monitoring of Health of a person by doing a blood test or other medical analysis and also be used to monitor environment by testing water or air in cities, mountains, factories, rivers and so on for a practical purpose. To create this optical detection device, a combination of spectrometer named Coupled Bi-Directional Sampling Spectrometer (CoBiSS) [Patent number WO2009127794A1] and Surface Plasmon Resonance (SPR) Chip has been used. For the optical integration, a new analysis of the sampling in the spectrometer CoBiSS is presented. Followed by, Device and Optical Integration of CoBiSS has been done to remove all the moving parts. It was necessary to make the device small that can be handheld and portable. For ease of use a Graphical User interface was developed. For detection, CoBiSS was added with a chip of SPR. A modelisation of SPR chip was done to maximize its sensitivity. A new Localized Surface Plasmon Resonance (LSPR) chip has been proposed to work with CoBiSS. Optimization of LSPR chip has been performed to maximize the sensitivity. A new definition for the calculation of Sensitivity has been proposed. This device needs the addition of functionalization on (L)SPR Chip for detection and a final application. This device could be an ideal "Thing" in Internet of Things.

Keywords: systems integration - optical spectrometers - optical detectors - integrated optics - Surface Plasmon Resonance - photonics - nanophotonics - Fourier transform spectroscopy - near field optics.

Thèse réalisée en partenariat entre :

